Aerodynamic force prediction and breakdown using the Lamb vector in steady compressible flows

Camille Fournis

Doctoral Thesis of Sorbonne Université
Doctoral School of Mechanics, Acoustics, Electronics and Robotics
Speciality: **Fluid Mechanics**

Aerodynamic Force Prediction and Breakdown Using the Lamb Vector in Steady Compressible Flows

Presented by
Camille Fournis

Submitted in fulfillment of the requirements for the degree of
Doctor of Sorbonne Université

Publicly defended on October, 28th 2021 in front of the jury composed of:

Pr. S. Schmitz	Professor, The Pennsylvania State University	Reviewer
Pr. A. Sellier	Professor, École Polytechnique / LadHyX	Reviewer
Pr. P. Cinnella	Professor, Sorbonne Université	Examiner
Dr. S. Trapier	Engineer, AIRBUS	Examiner
Dr. J. Magnaudet	Research Director, CNRS / IMFT	Examiner
Dr. M. Costes	Research Scientist, ONERA	Director
Pr. R. Tognaccini	Professor, Università di Napoli Federico II	Director
Dr. D. Bailly	Research Scientist, ONERA	Examiner
Dr. F. Hervy	Engineer, Direction Générale de l'Armement	Invited

"Si on veut faire quelque chose de différent il faut s'attendre à ne pas rencontrer la compréhension tout de suite."

Boris Vian

Acknowledgements

First of all, I would like to thank Pr. Antoine Sellier and Pr. Sven Schmitz for kindly accepting to review this dissertation. Their remarks on my work have been flattering, relevant, interesting and also insightful on how to further the developments on the Lamb-vector-based approach. I would also like to thank the other members of the jury, Pr. Paola Cinnella, Dr. Simon Trapier, Dr. Jacques Magnaudet and Dr. Franck Hervy for their interesting questions and comments during the defense, and for thoroughly reading this dissertation.

Special thanks must be given to Didier Bailly, Michel Costes and Renato Tognaccini, for their kindness, for their advice, and for outstandingly accompanying me throughout these three years. I have to say that I benefited from an exemplary supervision during this thesis without which the work presented in this dissertation would not have gone that far. In this regard, I would like to emphasize how much the long insightful discussions with Didier have allowed me to overcome the most difficult obstacles of my subject. Michel and Renato, I would like to thank you for the fruitful discussions, for regularly challenging me, and especially for asking me the relevant questions that gave birth to several chapters of this dissertation. Renato, I am very happy to have come to Naples in 2019 for two very useful working weeks. I wish I could have come several times, but the COVID-19 pandemic made it impossible.

I would like to thank all my colleagues and friends at ONERA in Meudon, with whom I often spend very good time. I feel blessed to work within such a positive environment, with people always willing to help, to teach and to pass on their knowledge and experience on various topics. In this regard, my special thanks go to Jean-Luc Hantrais-Gervois, Ilias Petropoulos, Frederic Moens and Antoine Dumont. Beyond the professional aspect, I also made new friends at ONERA, and I thank them for accompanying me during these three years, for supporting me when I was feeling bad, for organising coffee-breaks, afterworks and parties. In this regard, I am very grateful to Jaime Vaquero, Lucas Manueco, Jolan Reynaud, Ilyès Berhouni, Marie Schosseler, Simon Lecler, Ilias Petropoulos, Fulvio Sartor, Simon Bagy, Markus Zauner, Michaël Martin, Julien Lefieux and Camille Castells. Although some have already left, I am glad to pursue the adventure with you at ONERA.

Finally, I would like to thank my relatives for always being present and for giving me the motivation to carry out this work. Thank you to my mother, my sister and my love for coming to the defense and having the courage to listen to me talking about a complicated topic you are definitely not familiar with. Thank you to my father who has ceaselessly been challenging me for pushing my limits further and further. Dad, unfortunately you could not attend the defense but I was feeling your remote support during my presentation. I would also like to thank my maternal grandmother for her love and constant support. I do not forget my paternal grandparents who have already left this world. I dedicate this work to them. Of course, all of this would not have been possible without my friends, with whom I spend my week-ends and holidays. I thank you all for attending the defense, for providing me all your support and more generally for being present at my side. I want to end by saying that I am deeply grateful to Marie Glénat, my love, for loving me, for giving me strength and confidence, and for bearing me during at least half of my thesis.

Table of Contents

Nomenclature

Latin symbols

$\boldsymbol{a}$	acceleration of a fluid particle
c	chord
c_{ref}	reference chord
C_D	drag coefficient
C_{D_i}	lift-induced drag coefficient
C_{D_P}	profile drag coefficient
C_{D_v}	viscous drag coefficient
C_{D_w}	wave drag coefficient
d	distance from the body surface S_b
D	drag
D_i	lift-induced drag
D_P	profile drag
D_v	viscous drag
D_w	wave drag
$\boldsymbol{e}_x, \boldsymbol{e}_y, \boldsymbol{e}_z$	wind-fixed frame
$\boldsymbol{e}_X, \boldsymbol{e}_Y, \boldsymbol{e}_Z$	body-fixed frame
$\boldsymbol{F}$	aerodynamic force
h	specific enthalpy
H	total specific enthalpy
$\boldsymbol{I}$	unit tensor
L	lift
$\boldsymbol{l}$	Lamb vector; $\boldsymbol{\omega} \times \boldsymbol{q}$
M_∞	freestream Mach number
$\boldsymbol{m}_\rho$	compressibility term; $\frac{\boldsymbol{r}}{\mathcal{N}-1} \times \left(\nabla\rho \times \nabla \left(\frac{q^2}{2} \right) \right)$
$\mathcal{N}$	dimension of the physical space
$\boldsymbol{n}$	unit normal pointing outside Ω
$\boldsymbol{N}$	unit normal to the shock surface
$\boldsymbol{n}_{sw}$	unit normal pointing outside Ω_{sw}
p	pressure
P	total pressure (in incompressible flows); $p + \frac{1}{2}\rho q^2$
$\boldsymbol{q}$	velocity vector; $U\boldsymbol{e}_x + v\boldsymbol{e}_y + w\boldsymbol{e}_z$
q^2	velocity squared; $U^2 + v^2 + w^2$
R	perfect gas constant
$\boldsymbol{r}$	position vector
Re	Reynolds number
s	specific entropy
S_e	external surface
S_b	body surface
SW	shock wave surface
T	temperature

U	streamwise velocity component; $U_\infty + u$
$\boldsymbol{U}_\infty$	freestream velocity; $U_\infty \boldsymbol{e}_x$
W	wake plane
W_{sw}	shock wake plane
x, y, z	wind-fixed coordinate system
X, Y, Z	body-fixed coordinate system

Greek symbols

α	angle of attack
$\beta_{\Delta s}$	entropy threshold
β_ω	vorticity threshold
γ	ratio of specific heats
$\delta\Gamma$	wake-induced circulation penalty
$\delta\Gamma^*$	wake-induced compressible circulation penalty
$\delta\boldsymbol{q}$	perturbation velocity vector; $u\boldsymbol{e}_x + v\boldsymbol{e}_y + w\boldsymbol{e}_z$
δq^2	perturbation velocity squared; $u^2 + v^2 + w^2$
ΔH	total specific enthalpy variation with respect to its freestream value
$\Delta\rho$	density variation with respect to its freestream value
Δp	static pressure variation with respect to its freestream value
ΔP	variation in P with respect to its freestream value
Δs	specific entropy variation with respect to its freestream value
ΔT	temperature variation with respect to its freestream value
$\Delta\overline{u}$	irreversible streamwise velocity defect
$\boldsymbol{\Gamma}$	circulation vector; $-\Gamma\boldsymbol{e}_y$
$\boldsymbol{\Gamma}^*$	compressible circulation vector; $-\Gamma^*\boldsymbol{e}_y$
μ	dynamic viscosity
Ω	fluid domain
$\boldsymbol{\omega}$	vorticity vector; $\nabla \times \boldsymbol{q}$
Ω_v	boundary layer region
Ω_{sw}	shock wave region
ρ	density
$\boldsymbol{\tau}$	viscous-stress tensor

Other symbols

∇	gradient operator; $(\partial/\partial x)\,\boldsymbol{e}_x + (\partial/\partial y)\,\boldsymbol{e}_y + (\partial/\partial z)\,\boldsymbol{e}_z$
$\cdot$	scalar product
$\times$	vector product
$\otimes$	tensor product
∞	freestream state
$[\![\bullet]\!]$	jump operator; $\bullet_2 - \bullet_1$

Acronyms

CFD	Computational Fluid Dynamics
CRM	Common Research Model
KJMB	Kutta-Joukowski-Maskell-Betz
NACA	National Advisory Committee for Aeronautics
NASA	National Aeronautics and Space Administration
ONERA	Office National d'Études et de Recherches Aérospatiales
Osw	Oswatitsch
RANS	Reynolds-Averaged Navier Stokes
VdV	Van der Vooren

Introduction

Context

The reduction of operating costs and environmental footprint has been the paradigm of aviation throughout its history. Consequently, improving the performance of aircrafts in terms of fuel consumption has always remained essential. To do so, engineers may work on the propulsion system in order to maximize the engine efficiency. This can be done by increasing the engine bypass ratio. Engineers may also focus on the aircraft structure in order to reduce its weight. This can be done with the use of lightweight materials, for instance carbon-fiber or other composite materials. Finally, they may enhance the aerodynamic performance of the aircraft. This can be done by reducing the drag or resistance, the force caused by friction and pressure at the skin which opposes the aircraft motion.

Before reducing the drag exerted on an aircraft, it is necessary to accurately measure it. That is why scientists and engineers have ceaselessly developed methods able to define, accurately predict and decompose the aerodynamic force acting on an aircraft. This aerodynamic force comprises the drag, already introduced above, and the lift which enables the aircraft to sustain itself into air. The measurement of lift and drag has first been made possible with the use of various experimental methods during wind-tunnel tests. For example, engineers have been using balances in order to measure the net force exerted on a model, pressure probes or pressure-sensitive paint on the skin, five-hole probes in the wake and even laser technologies such as Laser-Doppler-Velocimetry (LDV) and Particle-Image-Velocimetry (PIV). However, wind-tunnel testing is very expensive since it requires a great amount of energy in high-speed tests. Moreover, it provides only limited information on the flow. This motivated the need for numerical methods able to compute the aerodynamic force from Computational Fluid Dynamics (CFD) flow solutions. The most direct approach is the so-called near-field method which consists in integrating the friction and pressure stresses exerted by the fluid on the skin of the aircraft. Hence, this method provides a mechanical breakdown of lift and drag into friction and pressure contributions. Nevertheless, the drag being weaker than the lift by one to two orders of magnitude, the numerical spurious drag generated in the vicinity of the skin may undermine the accuracy of this method. Furthermore, the decomposition provided by the near-field approach does not identify the phenomenological sources of lift and drag.

In this regard, the development of far-field methods becomes paramount in order to phenomenologically decompose the aerodynamic force acting on an aircraft. Rather than the friction and pressure effects exerted by the fluid on the aircraft skin, the far-field approach focuses on the aerodynamic phenomena produced in the fluid by the presence of the aircraft: vortices, viscous boundary layers and wakes or shock waves. Indeed, the fluid undergoes the same force as that it actually exerts on the aircraft. By measuring the stresses in the fluid, one can then equivalently compute the force exerted by the fluid on the aircraft and decompose the drag into three main contributions: the lift-induced drag, related to the presence of vortices due to the generation of lift, the viscous drag, related to the presence of viscous boundary layers and wakes, and the wave drag, related to the presence of shock waves in transonic and supersonic flight. In fact, the knowledge of the aerodynamic phenomena at the origin of drag enables the aerodynamicist to

improve the design of an aircraft. For instance, winglets are added at the tip of the wings in order to mitigate the strength of the tip vortices and hence to reduce the lift-induced drag [1]. The use of laminar wings or riblets has a positive impact on the viscous drag since it allows to reduce the viscous stresses at the skin [2]. Finally, supercritical airfoils undermine the strength of the transonic shock wave and reduce the wave drag, while producing enough lift to sustain the aircraft into air. This drag decomposition is nonetheless artificial since the aforementioned aerodynamic phenomena are all intertwined and interact with each other. For this reason and given the complex physics at work, it is often necessary to model the physics of a specific phenomenon, or even approximate the flow parameters under particular conditions when developing a far-field drag decomposition method.

Far-field formulations have proved their maturity and reliability and have been widely used in recent studies [3, 4]. Their use has most of the time been limited to steady flows, for instance the flow encountered by an aircraft in cruise flight at constant speed and altitude. In fact, the flow becomes unsteady in occasional situations: when the aircraft flies in a turbulent atmosphere, when the flaps are deployed prior to landing, when they are retracted after take-off, upon flow separation due to adverse pressure gradients, or when the transonic shock wave starts buffeting. In this dissertation, the focus will be given to steady flows only. Another crucial characteristic to think about is the compressibility of the flow. It is indeed more common to talk about the compressibility of a fluid, for instance when one compresses the air in a piston. Rigorously speaking, the airflow around an object is always compressible. Yet, at very low flight speed, the airflow around the aircraft can be considered incompressible, i.e. the fluid density remains constant on the trajectory of the fluid particle. At high flight speed, the compressibility is not negligible anymore at all since the fluid density varies along the way. In fact, the compressibility character of the flow greatly increases the intricacy of the various phenomena at work and inevitably has an impact on the lift and the drag exerted on the aircraft. That is why the development of far-field methods able to address such complex flow conditions is still of great interest.

Problem statement

A thorough review of the state-of-the-art of the main existing far-field formulations can be found in the first chapter of this dissertation. The most important ones are summarized thereafter. The first far-field methods were developed at the beginning of the twentieth century by the pioneering aerodynamicists Kutta, Joukowski, Prandtl and Betz [5, 6, 7, 8]. Considering a two-dimensional incompressible inviscid flow, Kutta and Joukowski arrived at the same conclusion that the lift generated by an airfoil is related to the circulation of the fluid flowing around it. Their work constitutes the first definition of the aerodynamic lift using the far-field approach. However, their study was initially rejected by the scientific community on the grounds that, according to Kelvin's theorem, no circulation can be generated in such a flow.

This controversy persisted until Prandtl introduced the concept of effectively inviscid flow, a fluid flow for which the viscosity tends to zero but is not zero [7]: in this case the airfoil effectively generates a circulation. Along with that, Prandtl was the first to introduce the concept of lift-induced drag generated by wings of finite span. His theory is still widely used as a simplified model in low-fidelity simulations but is nonetheless unable to accurately predict the lift and the lift-induced drag in highly complex flows such as the compressible transonic flow encountered by nowadays high-capacity aircrafts. A few years later, Betz [8] investigated the wake of a non-lifting viscous flow. His model allowed him to relate the profile drag (in this case the viscous drag) to the total pressure losses in the viscous wake. Although Betz's formula has until now been largely and successfully used in wind-tunnel wake surveys, its application is however limited to the incompressible regime.

Fifty years later, Maskell [9] addressed the flow around a wing of finite span. His analysis

allowed him to extend the use of Betz's profile drag formula to lifting flows and to define for the first time the lift-induced drag in viscous flows. This drag decomposition is still used today in wind-tunnel experiments and the proposed definition of lift-induced drag has even been applied to compressible flows [10, 11, 12, 13, 14, 15, 16, 17, 18], provided that the wake plane survey is performed far enough downstream of the model. However, Maskell's formula is theoretically valid in incompressible flows only, and its use in compressible flows inevitably yields errors in the measurement of the lift-induced drag.

The limitations of the aforementioned developments justified the need for formulations able to decompose the drag and grasp the intricate flow physics in compressible flows. In this regard, Destarac and Van der Vooren [19, 20, 21] developed a thermodynamic definition of the irreversible drag able to decompose it into viscous and wave drag contributions. The lift-induced drag was nonetheless defined by default, upon subtracting the obtained irreversible drag from the total drag. Thus, the decomposition proposed by Destarac and Van der Vooren relates the viscous drag to the entropy generated within viscous boundary layers and the wave drag to that generated across shock waves but does not directly link the lift-induced drag to its phenomenological sources.

Over the last twenty-five years, several formulations based on the velocity vector were developed [22, 23, 24, 25, 26, 27, 28, 29]. Those formulae all involve moment transformations that allow to eliminate the pressure from the final expression upon introducing the position vector. Wu *et al.* [29] especially developed a Lamb-vector-based aerodynamic force decomposition known as vortex-force theory. The Lamb vector is the cross product of the vorticity vector and the velocity vector, and was first introduced by Lamb [30]. In this formulation, the lift-induced drag was directly defined and related to the Lamb vector field produced in viscous boundary layers and wakes. The lift and the viscous drag were also defined but the application of such a formula remained however limited to incompressible flows. The same authors extended their analysis to compressible flows, but the obtained formulation did not allow to substantially decompose the aerodynamic force into lift, lift-induced drag and profile drag.

The decomposition in compressible transonic flows was made possible very recently by the works of Mele *et al.* [31]. In particular, they investigated the effect of the Mach number on the terms of the decomposition. In fact, CFD simulations emphasized the influence of the compressibility on the lift and the lift-induced drag at high Mach numbers (transonic and supersonic conditions). Besides, they proposed a first Lamb-vector-based definition of the wave drag, but their results were rather unsatisfactory. Moreover, the reference point introduced by the moment transformations was always arbitrarily set on the wake plane. Yet, Kang *et al.* [18] recently highlighted the sensitivity of the terms of the decomposition to the location of this point. Besides, the decomposition of the drag into lift-induced drag and profile drag is also sensitive to the size of the integration domain in three-dimensional flows [18, 32]. In practice, the size of the integration domain was always chosen in order to obtain maximum lift-induced drag. Furthermore, the physical role of the compressibility in lift and drag was not clearly identified. Finally, the obtained results sometimes differed significantly from that provided by the tried-and-tested formulation of Destarac and Van der Vooren [21].

In summary, several far-field methods applicable to compressible flows have been developed so far. On the one hand, the formulation of Destarac and Van der Vooren provides a thermodynamic breakdown of the drag into viscous drag, wave drag and lift-induced drag, but the latter contribution is not directly defined and its physical sources are not clearly identified. On the other hand, the Lamb-vector-based formulation introduced by Mele *et al.* constitutes the first vorticity-based definition able to compute all at once the lift, the lift-induced drag and the profile drag (viscous plus wave drag) in transonic flows. However, this method is sensitive to the location of the reference point and to the size of the integration domain. Furthermore, the physical role of the compressibility in lift and drag is still not clearly identifiable due to the complexity of the mathematical expressions. Finally, no robust definition for the wave drag using the Lamb

vector has been proposed so far. Consequently, all those limitations question the legitimacy of the proposed decomposition and its robustness with regard to its potential use for industrial purposes.

This is what justifies this study. It consists in developing a Lamb-vector-based force decomposition which is invariant to the location of the reference point and to the size of the integration domain everywhere in the flow field. Along with that, the objective is to physically interpret the terms of the decomposition. For this purpose, the new formulation must be able to identify the role of compressibility in lift and drag. The third goal is to develop a method based on the Lamb vector for extracting the wave drag. Finally, the new formulation has to be implemented in a post-processing code in order to be applied to several configurations.

Outline

In the first chapter, the main existing methods for lift and drag breakdown are presented. The focus is first given to the thermodynamic approaches, which allowed to define for the first time the profile drag in incompressible and compressible flows, and later the wave drag in transonic flows. Then, the vortical formulations are examined: those formulations enabled to understand very early the physics responsible for the generation of the lift and the lift-induced drag. Finally, the focus is given to the previous developments on the Lamb-vector-based formulation and the physical insights it provides on lift and drag in incompressible flows.

In the second chapter, the aim is to study the influence of the flow symmetries on the sensitivities of the Lamb-vector-based force decomposition. To do so, it is necessary to study the evolution of the sensitivity to the reference point and the size of the integration domain in various flow regions, in order to identify the regions of sensitivity and those of invariance. It consists in measuring the variations in lift and drag contributions induced by a change in the location of the reference point and the size of the integration domain. Secondly, the aim is to study the influence of the flow symmetries on the invariance in the far field. Indeed, the importance of symmetries was shown by Curie [33]. Their study is now widely spread in physics and they are often used to shed light on invariance properties. In this regard, the focus is given to the behaviour of the sensitive terms in the regions where the flow satisfies the symmetries.

In the third chapter, the aim is to develop a reference-point-invariant Lamb-vector-based formulation. This new formulation has been presented at the *AIAA Scitech 2020 Forum* [34] and published in the *AIAA Journal* [35]. To do so, it is first necessary to symmetrize the flow in the near field in order to establish the same flow conditions as those responsible for the invariance in the far field. It consists in splitting the flow quantities into near-field and far-field components. The reference-point-invariant formulation is then established by integrating the far-field component only, in order to eliminate the sensitive terms of the decomposition. Along with that, it is also necessary to reconstruct the various lift and drag terms in order to properly calculate the aerodynamic force. However, the obtained formulation is nothing but the equivalent invariant form of the decomposition developed by Mele *et al.* [31, 36] and does not clearly identify the physical role of compressibility in lift and drag.

In the fourth chapter, the aim is then to develop a revised Lamb-vector-based formulation identifying the role of compressibility in lift and drag. Indeed, there is little or no coverage of this role in the literature. It first consists in investigating the existing links between the Lamb-vector-based formulation and the classical analyses of Kutta, Joukowski, Maskell and Betz. Notably, a link with the analyses of Kutta-Joukowski and Maskell has already been published as a Technical Note in the *AIAA Journal* [37] while the link with Betz's formula has been presented at the *AIAA Aviation 2021 Forum* [38] and recently submitted to the *AIAA Journal* [39]. In fact, those theories were the first to relate lift and drag to their phenomenological sources. The next step consists in adapting the Lamb-vector-based formulation in order to make it mathematically equivalent to the classical analyses. The revised formulation also has the

advantage to be naturally invariant to the choice of the reference point. Then, an analysis is conducted on the equivalent form of the revised formulation, based this time directly on the classical analyses. Unfortunately, those new formulations are still not able to decompose the profile drag into viscous and wave drag contributions.

Therefore, in the fifth chapter, the aim is to develop a Lamb-vector-based definition of the wave drag. A theoretical comparative study is first conducted in the shock wave wake between famous wave drag extraction methods of the literature and two definitions of the profile drag based on the Lamb vector. This study emphasizes the similarities and differences between the various approaches and highlights the ability of the Lamb-vector-based approach to predict the wave drag. Secondly, it is necessary to identify the shock wave wake in the numerical flow solution in order to separate it from the viscous wake. This is done by means of a physical criterion based on vorticity and entropy. Finally, the wave drag is extracted by integrating on the identified shock wave wake, and compared to the predictions of Oswatitsch [40, 41] and Destarac and Van der Vooren [21].

Communications

The developments contained in this dissertation have been presented in two international conferences. The reference-point-invariant formulation derived in Chapter 3 has been presented at the *AIAA Scitech 2020 Forum* and published in the *AIAA Journal*, and the two novel formulations developed in Chapter 4 have been presented at the *AIAA Aviation 2021 Forum*. An *AIAA Journal* article on these two novel formulations is in preparation.

Conference proceedings

[34] C. Fournis, D. Bailly, and R. Tognaccini, "A reference point invariant Lamb vector based aerodynamic force breakdown in steady compressible flows," in *AIAA Scitech 2020 Forum*, 2020.
[38] C. Fournis, D. Bailly, and R. Tognaccini, "An invariant vortex-force theory related to classical far-field analyses in transonic flows," in *AIAA Aviation 2021 Forum*, p. 2554, 2021.

Peer-reviewed journal articles

[35] C. Fournis, D. Bailly, and R. Tognaccini, "Definition of an invariant Lamb-vector-based aerodynamic force breakdown using far-field flow symmetries," *AIAA Journal*, vol. 59, no. 1, pp. 34–48, 2021.
[37] C. Fournis, D. Bailly, and R. Tognaccini, "Compressibility correction to Kutta-Joukowski and Maskell formulas using vortex-force theory," *AIAA Journal*, vol. 59, no. 2, pp. 758–763, 2021.
[39] C. Fournis, D. Bailly, and R. Tognaccini, "Invariant vortex-force theory extending classical aerodynamic theories to transonic flows," *Submitted to AIAA Journal*.

Chapter 1

Presentation of the Main Existing Methods for Aerodynamic Force Breakdown

The breakdown of the aerodynamic force into lift, lift-induced drag, viscous drag and wave drag is called a far-field decomposition and consists of two main families of formulations: vortical formulations and thermodynamic formulations. In steady flows, all far-field decompositions usually start from the same momentum balance in a control volume of fluid Ω bounded by a closed surface S_e (see Fig.1.1):

$$\boldsymbol{F} = \oint_{S_e} \rho \left(\boldsymbol{U}_\infty - \boldsymbol{q}\right) \left(\boldsymbol{q} \cdot \boldsymbol{n}\right) \mathrm{d}S + \oint_{S_e} \left[\left(p_\infty - p\right) \boldsymbol{n} + \boldsymbol{\tau} \cdot \boldsymbol{n}\right] \mathrm{d}S$$

where $\boldsymbol{\tau}$ is the viscous-stress tensor and $\boldsymbol{n}$ is the unit normal pointing outside the fluid.

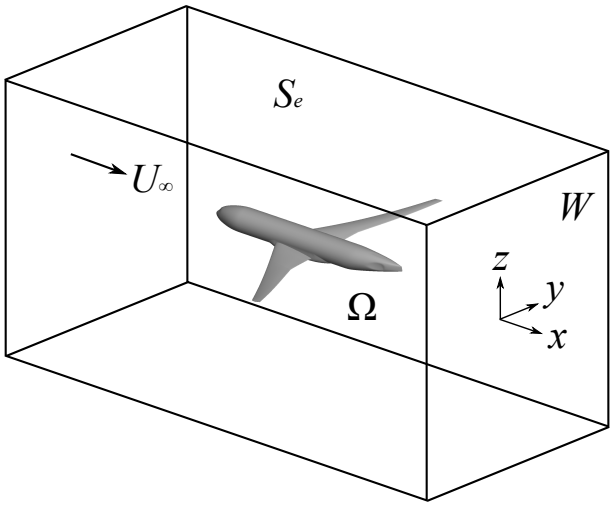

Figure 1.1: Fluid domain and its boundaries

The profile drag is defined as the sum of the viscous and the wave contributions and accounts for the momentum loss caused by the presence of an obstacle in the flow. The viscous drag is generated in the boundary layers whereas the wave drag is produced across shock waves in transonic and supersonic flows. The lift-induced drag is linked to the vortices created by the presence of lifting surfaces and is often called vortex-induced drag.

The need for an accurate determination of those various contributions has led to the development of numerous formulations which are presented hereafter. The focus is first given to the thermodynamic formulations, i.e. the formulations which evaluate the aerodynamic force from

the measurement of the fluid thermodynamic quantities such as pressure, temperature, entropy and total enthalpy. After that, the focus is given to the vortical formulations, i.e. the formulations mainly based on the velocity and vorticity vectors. Finally, a whole section is devoted to the Lamb-vector-based formulation, from its inception to its physical interpretation and numerical applications.

1.1 Thermodynamic formulations

Within the family of thermodynamic formulations, a distinction can be made between the pressure-based formulations (e.g. Betz, Jones and Schmitz), and the entropy-based formulations (e.g. Oswatitsch, Paparone and Tognaccini, Destarac and Van der Vooren). Yet, all those approaches are very similar since the main differences lie in the choice of the variables. They are based on various flow models and were mainly developed to define the profile drag, also called irreversible drag (viscous plus wave drag).

1.1.1 Betz's profile drag definition

One of the first thermodynamic definitions of profile drag in incompressible flows was developed by Betz [8] in 1925 and consisted in assessing the total pressure loss between the inlet and the outlet of a control volume of fluid. In fact, in an incompressible potential flow, the total pressure remains constant. Energy losses within the boundary layers and wakes are then characterized by a loss in total pressure. Betz assumed a flow for which there is no lift and that is almost two-dimensional with parallel streamlines at the measuring point in the wake:

- $L = 0$
- $v = w = 0$

He performed a momentum balance on a wake plane W downstream of the wing (see Fig.1.1) in order to express the profile drag as follows:

$$D_P = \int_W (P_\infty - P)\,\mathrm{d}S + \frac{1}{2}\rho_\infty \int_W \left(U_\infty^2 - U^2\right)\mathrm{d}S \tag{1.1.1}$$

where $P = p + \rho_\infty U^2/2$ is the total pressure and $P_\infty = p_\infty + \rho_\infty U_\infty^2/2$ is the freestream total pressure.

The second integral was addressed by considering a potential flow (producing no drag) with velocity U' and the same mass flow rate as U. This flow is identical to the real flow outside the vortical wake and the total pressure in the vortical wake is the same as that of the real flow outside of it:

$$p + \frac{1}{2}\rho_\infty U'^2 = P_\infty \tag{1.1.2}$$

Equation (1.1.1) was then transformed as

$$D_P = \int_W (P_\infty - P)\,\mathrm{d}S - \frac{1}{2}\rho_\infty \int_W \left(U' - U\right)\left(2U_\infty - U' - U\right)\mathrm{d}S \tag{1.1.3}$$

The second integral of (1.1.3) was neglected in the case of a measuring point taken far enough in the wing wake. A few months later, Taylor [42] derived this expression by adopting the same far-field approximation.

1.1.2 Jones' formulation

In 1936, Jones [43] assumed more restrictive hypotheses and established a formula that could be used in order to experimentally assess the profile drag by wake plane measurements with a Pitot tube. He assumed a non-lifting steady flow on a wake plane where the velocity vector is almost parallel to the freestream and the pressure has almost reached its undisturbed value:

- $L = 0$
- $v = w = 0$
- $p \approx p_\infty$

Applying those conditions to the momentum balance, the profile drag exerted on the body was written as follows:

$$D_P = \rho_\infty \int_W U\left(U_\infty - U\right) \mathrm{d}S \tag{1.1.4}$$

Unfortunately, the assumptions made in this model require that the wake survey be carried out on a plane located far downstream of the body. Yet, Jones wanted to develop a method able to assess the drag generated by a single component of the aircraft. Knowing that the wake gradually merges with the wake of other components downstream, the wake survey must be conducted closer to the body and variations in static pressure must be accounted for on the wake plane. To do so, Jones assumed the total pressure to be conserved between BB and AA (see

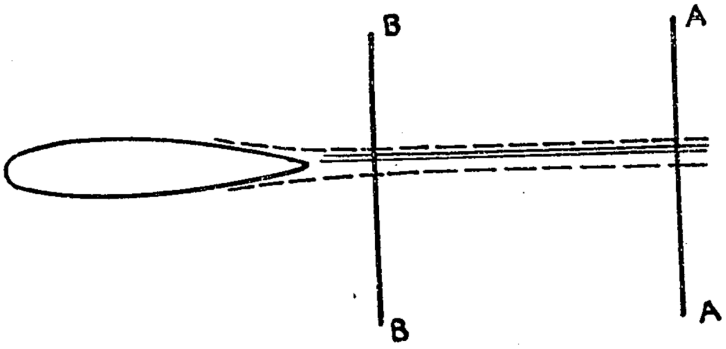

Figure 1.2: Sketch of the two wake planes AA and BB (from [43])

Fig.1.2) and the static pressure on AA to be almost equal to p_∞. Denoting $p_{d_\infty} = \rho_\infty U_\infty^2/2$ the freestream dynamic pressure, $p_d = \rho_\infty U^2/2$ the dynamic pressure on AA and $\Delta p = p_B - p_A$, Jones' formulation finally write

$$D_P = 2\int_{BB} \sqrt{p_d - \Delta p}\left(\sqrt{p_{d_\infty}} - \sqrt{p_d}\right) \mathrm{d}S \tag{1.1.5}$$

1.1.3 Oswatitsch's entropy drag

In the fifties, Oswatitsch [40, 41, 44] derived a famous thermodynamic formula which links the drag to the entropy production and is now referred to as the entropy drag concept. His formula was derived from a momentum balance on a control surface taken far from the body and assuming an isenthalpic flow. Therefore the velocity in the wake was supposed to be very close to $\boldsymbol{U}_\infty$:

- $H = H_\infty$
- $\boldsymbol{q} \approx \boldsymbol{U}_\infty$ in the wake

where $H = h + q^2/2$ is the total specific enthalpy in the wake and $H_\infty = h_\infty + U_\infty^2/2$ is the freestream total specific enthalpy. Oswatitsch substituted the pressure for the specific entropy by assuming that the thermodynamic state differs little from that of the freestream. With his small perturbation approximation, he linearized the second thermodynamic principle as follows:

$$p - p_\infty = \rho_\infty\left(h - h_\infty\right) - \rho_\infty T_\infty\left(s - s_\infty\right) \tag{1.1.6}$$

The linearized version expresses the profile drag D_P as

$$D_P = \rho_\infty T_\infty \oint_{S_e} \Delta s n_x \mathrm{d}S \tag{1.1.7}$$

where $\Delta s = s - s_\infty$ is the increment in specific entropy s. The non-linearized version now referred to as Oswatitsch's entropy drag is given by

$$D_P = \frac{T_\infty}{U_\infty} \oint_{S_e} \Delta s \, (\rho \boldsymbol{q} \cdot \boldsymbol{n}) \, \mathrm{d}S \tag{1.1.8}$$

It is important to remind that the aforementioned definition was established upon adopting restrictive hypotheses. The specific entropy jump Δs is supposed to be small, and the flow is assumed to be in a thermodynamic state close to that of the freestream. That is why the formula provided by (1.1.8) has given satisfaction in transonic flows in which the shock waves are weak. It has also been applied to wind-tunnel wake surveys for extracting the wave drag from the profile drag by means of a criterion based on the transverse vorticity [45].

1.1.4 Paparone and Tognaccini's formulation

In 2003, Paparone and Tognaccini [46] proposed a formulation that is able to decompose the drag into lift-induced, viscous and wave contributions. They considered that S_e extends far away from the body such that:

- $\boldsymbol{\tau} \cdot \boldsymbol{n} \approx \boldsymbol{0}$
- $\Delta p / p_\infty, \ \Delta s / R, \ \Delta H / U_\infty^2 \ll 1$ where $\Delta p = p - p_\infty$ and $\Delta H = H - H_\infty$

Denoting the velocity field as $\boldsymbol{q} = q\boldsymbol{k}$ where $\boldsymbol{k}$ is a unit vector, they expressed the drag as follows:

$$D = \oint_{S_e} \left(\rho_\infty U_\infty^2 \frac{1}{\gamma M_\infty^2} \frac{\Delta p}{p_\infty} n_x + U_\infty f\left(\frac{\Delta p}{p_\infty}, \frac{\Delta s}{R}, \frac{\Delta H}{U_\infty^2} \right) \rho \, (\boldsymbol{q} \cdot \boldsymbol{n}) \, k_x \right) \mathrm{d}S \tag{1.1.9}$$

$$\text{with} \quad f\left(\frac{\Delta p}{p_\infty}, \frac{\Delta s}{R}, \frac{\Delta H}{U_\infty^2} \right) = \sqrt{1 + \frac{2\Delta H}{U_\infty^2} - \frac{2}{(\gamma - 1) M_\infty^2} \left(\left(\left(1 + \frac{\Delta p}{p_\infty} \right) e^{\Delta s / R} \right)^{(\gamma - 1)/\gamma} - 1 \right)}$$

The latter relation holds for a perfect gas only. Again, with a small perturbation approximation, they made a Taylor expansion on f and wrote

$$\begin{aligned}
D = {} & U_\infty \oint_{S_e} \left[\frac{1}{\gamma M_\infty^2} \frac{\Delta s}{R} + \frac{1 + (\gamma - 1) M_\infty^2}{2\gamma^2 M_\infty^4} \left(\frac{\Delta s}{R} \right)^2 \right] \rho \, (\boldsymbol{q} \cdot \boldsymbol{n}) \, k_x \mathrm{d}S \\
& - U_\infty \oint_{S_e} \left[\frac{\Delta H}{U_\infty^2} - \frac{1}{2} \left(\frac{\Delta H}{U_\infty^2} \right)^2 \right] \rho \, (\boldsymbol{q} \cdot \boldsymbol{n}) \, k_x \mathrm{d}S \\
& - U_\infty \oint_{S_e} \left[1 - \frac{1}{\gamma M_\infty^2} \frac{\Delta p}{p_\infty} - \frac{1 + \gamma M_\infty^2}{2\gamma^2 M_\infty^4} \left(\frac{\Delta p}{p_\infty} \right)^2 \right] \rho \, (\boldsymbol{q} \cdot \boldsymbol{n}) \, k_x \mathrm{d}S \\
& - \rho_\infty U_\infty^2 \frac{1}{\gamma M_\infty^2} \oint_{S_e} \frac{\Delta p}{p_\infty} n_x \mathrm{d}S \\
& - U_\infty \oint_{S_e} \left[- \frac{1 + (\gamma - 1) M_\infty^2}{\gamma^2 M_\infty^4} \frac{\Delta p}{p_\infty} \frac{\Delta s}{R} + \frac{1}{\gamma M_\infty^2} \frac{\Delta s}{R} \frac{\Delta H}{U_\infty^2} \right] \rho \, (\boldsymbol{q} \cdot \boldsymbol{n}) \, k_x \mathrm{d}S \\
& + \mathcal{O}\left[\left(\frac{\Delta s}{R} \right)^3, \left(\frac{\Delta H}{U_\infty^2} \right)^3, \left(\frac{\Delta p}{p_\infty} \right)^3 ... \right]
\end{aligned} \tag{1.1.10}$$

The first integral of (1.1.10) is identical to Oswatitsch's formula (1.1.8) at first order: it is then referred to as entropy drag, namely the drag due to the presence of boundary layers and shock waves. The second integral is also involved in the drag generated by irreversible processes although it also accounts for the thrust in power-on conditions [15]. The third and fourth

integrals, linked to the pressure difference, are related to the vortex-induced drag. The last integral is a coupling contribution between entropy, total enthalpy and pressure variations.

The proposed definition of the profile drag is based on the entropy drag and can be expressed with a volume integral upon applying the divergence theorem:

$$D_P = U_\infty \int_\Omega \nabla \cdot \left(\rho g \left(\frac{\Delta s}{R} \right) \boldsymbol{q} \right) \mathrm{d}v \tag{1.1.11}$$

$$\text{with} \quad g\left(\frac{\Delta s}{R} \right) = \frac{1}{\gamma M_\infty^2} \frac{\Delta s}{R} + \frac{1 + (\gamma - 1) M_\infty^2}{2\gamma^2 M_\infty^4} \left(\frac{\Delta s}{R} \right)^2 \tag{1.1.12}$$

The volume Ω is then split into a boundary layer region Ω_v and a shock wave region Ω_{sw} thanks to physical criteria such that the profile drag is decomposed in viscous and wave contributions:

$$D_v = U_\infty \int_{\Omega_v} \nabla \cdot \left(\rho g \left(\frac{\Delta s}{R} \right) \boldsymbol{q} \right) \mathrm{d}v \tag{1.1.13}$$

$$D_w = U_\infty \int_{\Omega_{sw}} \nabla \cdot \left(\rho g \left(\frac{\Delta s}{R} \right) \boldsymbol{q} \right) \mathrm{d}v \tag{1.1.14}$$

1.1.5 Destarac and Van der Vooren's generalization of the entropy drag concept

Actually, the aforementioned definitions are nothing but Taylor expansions of an exact formula applicable to compressible flows of perfect gases developed by Van der Vooren, Sloof and Destarac [19, 20, 21]. In this approach, there is no small perturbation approximation. Rather, it is assumed that there are not any trailing vortices in the flow, hence the drag exerted on the aircraft is only of irreversible nature. The transverse part of the velocity field is zero, the viscous stresses are neglected on a control surface taken far enough from the body and the pressure is equal to its freestream value:

- $\boldsymbol{\tau} \cdot \boldsymbol{n} \approx \boldsymbol{0}$
- $v = w = 0$
- $p = p_\infty$

Hence, with those asumptions:

$$D_P = \oint_{S_e} \rho \left(U_\infty - U \right) \left(\boldsymbol{q} \cdot \boldsymbol{n} \right) \mathrm{d}S \tag{1.1.15}$$

The aim is now to express the velocity deficit $U - U_\infty$ with the thermodynamic quantities. It differs from Oswatitsch's development where the specific entropy is introduced in place of the pressure. The definition of specific entropy and total specific enthalpy variations are given in this case by

$$\Delta s = C_v \ln \left(\left(\frac{T}{T_\infty} \right)^\gamma \right) \tag{1.1.16}$$

$$\Delta H = C_p \left(T - T_\infty \right) + \frac{U^2 - U_\infty^2}{2} \tag{1.1.17}$$

where C_v and C_p are respectively the specific heats at constant volume and pressure. The combination of equations (1.1.16) and (1.1.17) provides an expression of $U - U_\infty = \Delta \overline{u}$ in terms

of specific entropy and total specific enthalpy. Finally, in the case of a flow without trailing vortices the profile drag is defined as

$$D_P = -\oint_{S_e} \Delta\overline{u}\,(\rho\boldsymbol{q}\cdot\boldsymbol{n})\,\mathrm{d}S \tag{1.1.18}$$

$$\text{with}\quad \Delta\overline{u} = U_\infty\sqrt{1+\frac{2\Delta H}{U_\infty^2}-\frac{2}{(\gamma-1)\,M_\infty^2}\left(e^{\Delta s/C_p}-1\right)}-U_\infty \tag{1.1.19}$$

Taylor expansions on the latter expression lead to Oswatitsch's formula (1.1.8) at first order and to Paparone and Tognaccini's formula (1.1.11) at second order. Hence, the domain of applicability of Destarac and Van der Vooren's formulation is wider. The viscous/wave drag bookkeeping is achieved by integrating on the boundaries of Ω_v and Ω_{sw}:

$$D_v = -\oint_{\partial\Omega_v} \Delta\overline{u}\,(\rho\boldsymbol{q}\cdot\boldsymbol{n})\,\mathrm{d}S \tag{1.1.20}$$

$$D_w = -\oint_{\partial\Omega_{sw}} \Delta\overline{u}\,(\rho\boldsymbol{q}\cdot\boldsymbol{n})\,\mathrm{d}S \tag{1.1.21}$$

It is now possible to define a vector $\boldsymbol{f} = \boldsymbol{f}_P + \boldsymbol{f}_i$ in order to express the total drag. The lift-induced drag is computed upon subtracting the profile drag from the total drag with the integration of $\boldsymbol{f}_i$:

$$\boldsymbol{f}_P = -\rho\Delta\overline{u}\boldsymbol{q} \tag{1.1.22}$$

$$\boldsymbol{f}_i = -\rho\,(U-U_\infty-\Delta\overline{u})\,\boldsymbol{q}-(p-p_\infty)\,\boldsymbol{e}_x+\boldsymbol{\tau}\cdot\boldsymbol{e}_x \tag{1.1.23}$$

$$D_i + D_P = \oint_{S_e} (\boldsymbol{f}\cdot\boldsymbol{n})\,\mathrm{d}S \tag{1.1.24}$$

Although this formulation is now widely used in industrial applications, its main drawback lies in the fact that it cannot link the definition of the lift-induced drag to any flow structures or physical phenomena since its magnitude is found only after having computed the profile drag. On the contrary, this latter contribution is defined directly and its irreversible origin is clearly emphasized since it is calculated by assessing the entropy production and total enthalpy dissipation in the flow. It should finally be noted that, unlike the formulations of Betz, Jones and Oswatitsch that were intended for use in wind-tunnel tests, the formulations of Paparone, Tognaccini, Destarac and Van der Vooren were designed to be used in CFD applications.

1.1.6 Schmitz and Coder's partial-pressure-field decomposition

Very recently, Schmitz and Coder [47] developed a partial-pressure-based decomposition of the aerodynamic force in incompressible flows. This work was later extended by Schmitz [48] in compressible flows. Their idea was to split the pressure into a Euler (inviscid) part p_E and a dissipative (viscous) part p_μ. By doing so, they hypothesized that it is possible to decouple the inviscid effects from the viscous effects. In the steady compressible Navier-Stokes equations, the two parts are then separated:

$$\nabla p_E + \rho\nabla\left(\frac{q^2}{2}\right) + \rho\boldsymbol{\omega}\times\boldsymbol{q} = -\nabla p_\mu + \nabla\cdot\boldsymbol{\tau} \tag{1.1.25}$$

where $\boldsymbol{\omega} = \nabla\times\boldsymbol{q}$ is the vorticity vector. Considering an inviscid flow, the right-hand side of (1.1.25) and then the left-hand side are equal to zero. The application of the divergence operator leads to two Poisson equations:

$$\Delta p_E = \nabla\cdot(\rho\boldsymbol{q}\times\boldsymbol{\omega}) - \rho\Delta\left(\frac{q^2}{2}\right) \tag{1.1.26}$$

$$\Delta p_\mu = \nabla\cdot(\nabla\cdot\boldsymbol{\tau}) \tag{1.1.27}$$

which can be solved simultaneously with the converging flow solution [47]. Therefore, the computed p_E and p_μ can be used individually in the momentum balance to decompose the aerodynamic force as follows:

$$\boldsymbol{F} = \boldsymbol{F}_{p_E} + \boldsymbol{F}_{p_\mu,\tau} \tag{1.1.28}$$

with

$$\boldsymbol{F}_{p_E} = -\oint_{S_e} \rho \boldsymbol{q} \left(\boldsymbol{q}\cdot\boldsymbol{n}\right) \mathrm{d}S + \oint_{S_e} \left(p_\infty - p_E\right) \boldsymbol{n} \mathrm{d}S \tag{1.1.29}$$

$$\boldsymbol{F}_{p_\mu,\tau} = \oint_{S_e} \left(p_\infty - p_\mu\right) \boldsymbol{n} \mathrm{d}S + \oint_{S_e} \boldsymbol{\tau}\cdot\boldsymbol{n} \mathrm{d}S \tag{1.1.30}$$

By means of several Taylor expansions on the fluid quantities, Schmitz demonstrated the close relation between $\boldsymbol{F}_{p_E}$ and the works of Kutta-Joukowski and Maskell (see section 1.2) and showed that the drag component of $\boldsymbol{F}_{p_\mu,\tau}$ is closely related to Oswatitsch's formula (1.1.8).

Unlike the previous thermodynamic methods for which the wave drag is mixed with the viscous drag due to the presence of Δs in the expressions, it is in this case mixed with the lift-induced drag because both are contained in the inviscid part $\boldsymbol{F}_{p_E}$. In 2019, Coder and Schmitz [49] introduced a similar splitting for the density field and successfully separated the two drag contributions in inviscid transonic flows.

1.2 Vortical formulations

Within the family of vortical formulations, a distinction can be made between the circulation-based and vorticity-based formulations (a thorough review is available in [50]). The circulation-based formulations evaluate the aerodynamic force from the circulation produced by the wings. They were developed by pioneering aerodynamicists who provided the first models for predicting the lift and the lift-induced drag. The vorticity-based formulations are more recent and relate the aerodynamic force to the velocity and vorticity vectors. Moreover, they are usually applicable to more complex flow conditions.

1.2.1 Kutta-Joukowski theorem

Back in the very beginning of the twentieth century, Kutta in his unpublished thesis from 1902 and later Joukowski [6, 51] in 1906 derived a formula now referred to as the Kutta-Joukowski theorem. They considered the same flow model:

- Two-dimensional flow
- Inviscid potential flow
- Incompressible flow

Their formula relates the lift generated by an airfoil to the circulation of the incompressible flow passing around it:

$$L' = -\rho_\infty U_\infty \Gamma \tag{1.2.1}$$

$$D' = 0 \tag{1.2.2}$$

$$\text{with} \quad \Gamma = \oint_C \boldsymbol{q} \cdot \boldsymbol{t} \mathrm{d}l \tag{1.2.3}$$

where L' is the lift per unit span, Γ is the circulation, C is a closed contour and $\boldsymbol{t}$ is the unit tangent vector.

The proof of this theorem is not presented here because it requires the analysis of the asymptotic field, or complex notions on analytic functions and Joukowski conformal mappings (see [52] p.57-66 and p.91 for more details). This formula provides no drag since it assumes that the flow is inviscid: this is the famous *d'Alembert's paradox*. Yet, the circulation is conserved over time in an inviscid and barotropic flow on which no external forces are exerted according to Kelvin's theorem. Therefore, no circulation should be produced in the conditions presented above and it explains why this theorem was initially left on the sidelines. The circulation of the airfoil is actually set by the Kutta condition (see Fig.1.3) which states that the fluid must leave the airfoil at the trailing edge.

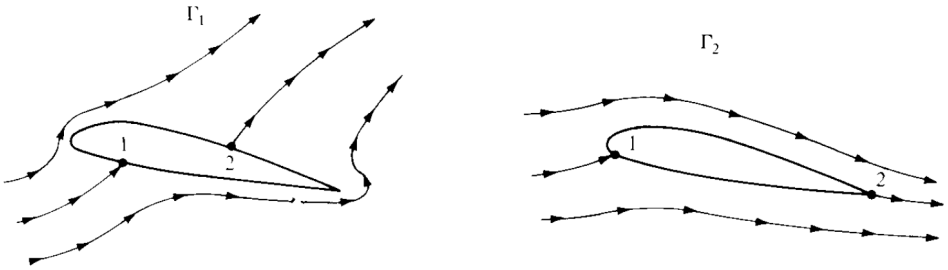

Figure 1.3: Link between circulation and exit point (from [53])

Relation (1.2.1) highlights the necessity for a body to generate a circulation in order to produce the lift. It simply illustrates that the velocity of the flow must be greater on the suction

side than on the pressure side such that a pressure differential is created. Later on, Bryant and Williams [54] studied the case of a rotational flow and stated that equation (1.2.1) may even hold in such a case, provided that the downstream edge of the contour of integration is chosen perpendicular to the velocity vector in the wake.

1.2.2 Joukowski-Filon theorem

In 1926, in parallel with the work of Taylor, Filon [55] derived a drag formula which is the analogue to the Kutta-Joukowski theorem on lift. Denoting Q_ψ what he defined as *"the total outwards flow at infinity"*, the total drag is given by

$$D = \rho_\infty U_\infty Q_\psi \tag{1.2.4}$$

Very recently, Liu et al. [56, 57] generalized the Kutta-Joukowski lift theorem and Filon's drag formula to compressible steady viscous flows and derived a *unified force formula*. They adopted a far-field approximation on the flow quantities:

- $\boldsymbol{q} = \boldsymbol{U}_\infty + \delta\boldsymbol{q}$ with $||\delta\boldsymbol{q}||/U_\infty \ll 1$
- $\rho = \rho_\infty + \Delta\rho$ with $\Delta\rho/\rho_\infty \ll 1$
- $p = p_\infty + \Delta p$ with $\Delta p/p_\infty \ll 1$
- $\mu = \mu_\infty + \Delta\mu$ with $\Delta\mu/\mu_\infty \ll 1$

Moreover the perturbation velocity vector $\delta\boldsymbol{q}$ is given by the following Helmholtz-Hodge decomposition:

$$\delta\boldsymbol{q} = \boldsymbol{q}_\phi + \boldsymbol{q}_\psi = \nabla\phi + \nabla\times\boldsymbol{\psi} \quad \text{with} \quad \nabla\cdot\boldsymbol{\psi} = 0 \tag{1.2.5}$$

where ϕ is the scalar velocity potential and $\boldsymbol{\psi}$ is a vector potential. The theorem is valid for compressible steady viscous flows and is stated as follows:

$$\boldsymbol{F} = (\mathcal{N}-1)\,\rho_\infty\boldsymbol{U}_\infty\times\boldsymbol{\Gamma}_\phi + \rho_\infty\boldsymbol{U}_\infty Q_\psi \tag{1.2.6}$$

where

$$\boldsymbol{\Gamma}_\phi = \oint_{S_e}\boldsymbol{n}\times\nabla\phi\,\mathrm{d}S \tag{1.2.7}$$

$$Q_\psi = -\oint_{S_e}(\boldsymbol{n}\times\nabla)\cdot\boldsymbol{\psi}\,\mathrm{d}S \tag{1.2.8}$$

and $\mathcal{N} = 2$ or 3 is the dimension of the physical space. $\boldsymbol{\Gamma}_\phi$ and Q_ψ are independent of the choice of S_e due to the generalized Stokes theorem [57]. Then, the theorem holds in the near field as well even if it was established upon making a small perturbation approximation valid only in the far field. Unfortunately, the quantities involved in equation (1.2.6) are not experimentally observable since they come out of the definition of ϕ and $\boldsymbol{\psi}$.

This issue was bypassed by the same authors upon deriving what they called the *testable unified force formula*. This formula is this time valid only in the far field and is given by

$$\boldsymbol{F} = \rho_\infty\boldsymbol{U}_\infty\times\boldsymbol{\Gamma} + \rho_\infty\boldsymbol{U}_\infty Q_W \tag{1.2.9}$$

with

$$\boldsymbol{\Gamma} = \int_\Omega\boldsymbol{\omega}\mathrm{d}v = \boldsymbol{\Gamma}_\phi + \oint_{S_e}\boldsymbol{n}\times(\nabla\times\boldsymbol{\psi})\,\mathrm{d}S \tag{1.2.10}$$

$$Q_W = \frac{1}{\mathcal{N}-1}\int_W(z\omega_y - y\omega_z)\,\mathrm{d}S \tag{1.2.11}$$

Here, W is the downstream boundary of S_e perpendicular to the freestream and lies in the asymptotic far field.

The above-stated theorem provides a generalization of the Kutta-Joukowski formula and Filon's drag expression in the case of compressible steady viscous flows. It should be noted, however, that this formulation cannot provide any drag breakdown but only an expression of the total drag in terms of vorticity components.

1.2.3 Prandtl's induced drag formula

At the same period as Betz's, Ludwig Prandtl's works on boundary layers allowed him to lift the veil on *d'Alembert's paradox*. He actually considered an effectively inviscid flow for which $\mu \to 0$ but $\mu \neq 0$. In this case the Kutta condition is indeed satisfied by the fluid and the production of circulation is consigned to the very thin boundary layers, the vorticity being generated on the body surface [58]. More recent studies held at the end of the twentieth century by Wu *et al.* [59, 60, 61] on the *boundary vorticity flux* even relate the production of vorticity to the tangent pressure gradient following the works of Lighthill [62] and the discussion given by Batchelor [63] thirty years earlier. Finally, numerical studies have been led very recently in order to illustrate the role of viscosity in vorticity and lift generation [64, 65].

With his way of examining, Prandtl also asserted that *"the fluid leaves the body along a line called the line of separation, forming the generation of a surface of scission such that the speeds are not the same on both sides of the surface, thus forming a vortical layer"* [7]. This vortical layer is what is commonly called a vortex sheet. In a real viscous flow, the vortex sheet is of finite width. Along with the vortex sheet generated in the body wake, the lifting surface is replaced by a distribution of vortices referred to as attached vortices (see Fig.1.4a). This distribution is responsible for the generation of the circulation around the body. Prandtl considered the following flow model:

- $\boldsymbol{q} = \begin{pmatrix} U_\infty & 0 & w \end{pmatrix}^T$
- Inviscid flow
- Incompressible flow

In this case the Bernoulli theorem applies, then the total pressure is conserved and Prandtl expressed the force acting on a wing solely in terms of the vortex force:

$$\boldsymbol{F} = \rho_\infty \int_\Omega \boldsymbol{q} \times \boldsymbol{\omega} \mathrm{d}v \tag{1.2.12}$$

Considering Prandtl's assumptions [7] and denoting b the wing span, it is possible to express

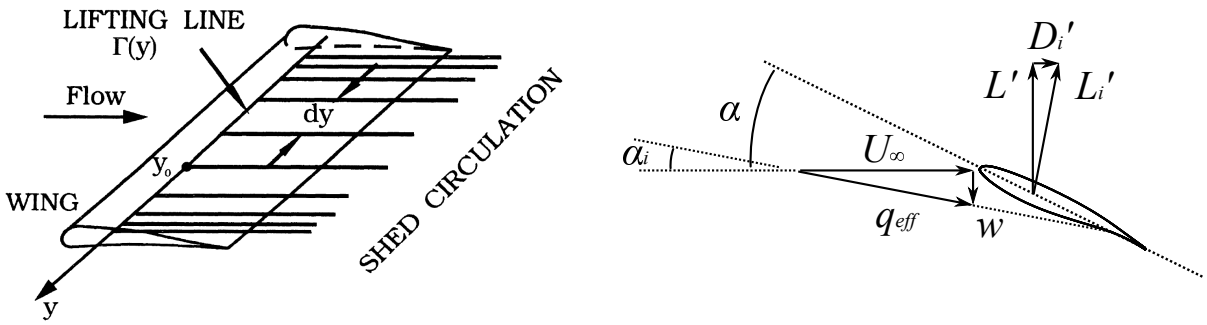

(a) Distribution of vortices on the wing (from [66])

(b) Induced downsweep w

Figure 1.4: The lifting line theory

the downsweep (see Fig.1.4b) produced by the vortices in the flow by means of the Biot-Savart law:

$$w(y_0) = \frac{1}{4\pi}\int_{-b}^{b}\frac{\mathrm{d}\Gamma}{\mathrm{d}y}\frac{\mathrm{d}y}{y_0 - y} = -U_\infty \tan\left(\alpha_i\left(y_0\right)\right) \approx -U_\infty \alpha_i\left(y_0\right) \tag{1.2.13}$$

Moreover, the lift-induced drag D_i can be expressed upon using the Kutta-Joukowski theorem (1.2.1) and equation (1.2.13) such that

$$D_i \approx \int_{-b}^{b} L'\left(y_0\right)\alpha_i\left(y_0\right)\mathrm{d}y = \rho_\infty U_\infty \int_{-b}^{b}\Gamma\left(y_0\right)\alpha_i\left(y_0\right)\mathrm{d}y = -\rho_\infty\int_{-b}^{b}\Gamma\left(y_0\right)w(y_0)\mathrm{d}y \tag{1.2.14}$$

Writing the circulation Γ as a Laurent series of expansion, a lengthy but not difficult integral calculus yields the very first known lift-induced drag definition now referred to as Prandtl's lift-induced drag formula:

$$C_{D_i} = \frac{C_L^2}{\pi \mathcal{AR} e} \tag{1.2.15}$$

where $C_{D_i} = 2D_i/\left(\rho_\infty U_\infty^2 S\right)$ is the lift-induced drag coefficient, $C_L = 2L/\left(\rho_\infty U_\infty^2 S\right)$ is the lift coefficient, S is a surface of reference, $\mathcal{AR} = b^2/S$ is the wing aspect ratio and e is the Oswald factor with $e \leq 1$ ($e = 1$ for an elliptic spanwise lift distribution).

It is then clear that this drag component appears due to the fact that the wing is of finite span. Furthermore, a more slender wing produces less lift-induced drag since it is inversely proportional to $\mathcal{AR}$: it explains why the use of winglets at the tip of the wings reduces this drag contribution. Indeed, those devices increase the aspect ratio of the wing without increasing too much the bending moment caused by its weight.

1.2.4 Maskell's formula

Although Prandtl's formula has remained so far a cornerstone in aerodynamics, the ever more pressing need for formulations able to deal with viscous and high-lifting flows encouraged aerodynamicists to wage further research on more accurate lift-induced drag predictions. Maskell [9] proposed in 1972 a formula that can compute the profile drag and the lift-induced drag in incompressible flows. His analysis is applicable to wake surveys in wind-tunnel experiments for which the measurements must be confined to the vortical wake. He pointed out that a consistent decomposition of the drag is ensured when the two contributions do not depend on the location of the wake plane, a constraint that is still a great issue for several other formulae. He adopted the same approach as Betz's without assuming a parallel flow in order to derive the following breakdown:

$$D_P = \int_W \left(P_\infty - P\right)\mathrm{d}S - \frac{1}{2}\rho_\infty\int_W \left(U' - U\right)\left(2\left(U_\infty + u^*\right) - U' - U\right)\mathrm{d}S \tag{1.2.16}$$

$$D_i = \frac{1}{2}\rho_\infty\int_W \left(v^2 + w^2\right)\mathrm{d}S \tag{1.2.17}$$

where u^* is a wake-blockage velocity. Then, Maskell introduced two scalar functions $\psi\left(y,z\right)$ and $\phi\left(y,z\right)$ in order to express the transverse velocity components as follows:

$$v = \frac{\partial\phi}{\partial y} + \frac{\partial\psi}{\partial z} \tag{1.2.18}$$

$$w = \frac{\partial\phi}{\partial z} - \frac{\partial\psi}{\partial y} \tag{1.2.19}$$

with

$$\frac{\partial^2\psi}{\partial y^2} + \frac{\partial^2\psi}{\partial z^2} = -\omega_x \tag{1.2.20}$$

$$\frac{\partial^2\phi}{\partial y^2} + \frac{\partial^2\phi}{\partial z^2} = \sigma \tag{1.2.21}$$

where ω_x is the streamwise component of the vorticity vector and σ is a source term. Denoting W_v the vortical wake, Maskell's lift-induced drag formula is then given by (a proof is provided in [67])

$$D_i = \frac{1}{2}\rho_\infty \int_{W_v} \psi \omega_x \mathrm{d}S - \frac{1}{2}\rho_\infty \int_W \phi\sigma \mathrm{d}S \tag{1.2.22}$$

In practice, the second integral can often be neglected such that the lift-induced drag integral can be limited to the vortical part of the wake W_v. This formula is still widely used in experimental fluid dynamics [12, 68, 69, 70] and a link with the lifting line theory can be found in several studies [11, 15, 71].

1.3 Definition and application of the Lamb-vector-based force formula

Despite the great number of drag formulations, and even though Destarac and Van der Vooren's decomposition already proved to give accurate results when applied to industrial cases [72], it is still lacking an in-depth physical insight of the origin of the lift-induced drag in compressible flows. Indeed, it defines the profile drag along with a viscous and wave drag breakdown but the lift-induced drag is only deduced by subtraction which understrikes once again the difficulty to directly define the lift-induced drag in a complex flow [73]. Moreover, Destarac and Van der Vooren's formulation cannot compute the lift. In this regard, vortical formulations are more suited to define the lift and the lift-induced drag since they are generated by the presence of vortices. Yet, those presented above require that restrictive hypotheses be made and may not be applicable to more complex flows. That is precisely where the Lamb-vector-based formulation may help.

1.3.1 An unconventional force formula

The Lamb-vector-based aerodynamic force breakdown also belongs to the family of the vortical formulations since it involves the Lamb vector $\boldsymbol{l}$ which is defined as the cross-product between the vorticity vector and the velocity vector:

$$\boldsymbol{l} = \boldsymbol{\omega} \times \boldsymbol{q} \tag{1.3.1}$$

Following the same approach as Prandtl, Saffman [74] expressed the total force acting on a body solely in terms of the vortex force (1.2.12). Unfortunately, the extension to viscous flows had to await the development of Wu *et al.* [29, 75] conducted fifteen years later.

In order to derive the Lamb-vector-based aerodynamic force breakdown in viscous flows, the pressure must be eliminated from the final formula such that the total force is solely expressed by means of the velocity vector and its derivatives. In their works, Prandtl and Saffman used the hypothesis of inviscid flow and applied the Bernoulli equation. In the case of viscous flows, the pressure is eliminated by applying the *derivative moment transformations* (DMT) (A.1) and (A.2) (see Appendix A). According to Wu *et al.* [29], this kind of unconventional expressions are nothing but a generalization of the integration by parts in three dimensions, using the curl and divergence operators on vector fields, and allow for a better understanding of the local flow structures responsible for the lift and the drag.

Those relations previously found trace in several textbooks [63, 74, 76] where the total force was expressed by means of the *vorticity moment theorem*. As derived in more recent books for $\mathcal{N}$-dimensional flows, the force formula involves the vortex impulse which is actually the volume integral of the first moment of the vorticity vector (see Wu [77] or Wu *et al.* [75, 78] for instance). The force was then linked to the growth rate of the area delimited by the bound vortex, the tip vortices and the starting vortex. It provides a generalization of the work conducted by Von Kármán and Sears [79] on airfoil theory. Wu and Wu [61, 80] also used *derivative moment transformations* in order to express the force acting on a body in terms of *boundary vorticity fluxes* that provide more in-depth physical insights on how the aerodynamic force is produced on the body surface. Later on, Noca *et al.* [22, 23, 24] developed several force formulae, namely the *impulse equation*, the *momentum equation* and the *flux equation* to experimentally and numerically determine the aerodynamic force acting on a cylinder using only the velocity vector and its partial derivatives. Finally, Wu *et al.* [26] tested another formula applicable to unsteady incompressible viscous flows on a fish-like body while Zhu *et al.* [25, 27] extended the application of those formulations to compressible flows.

The aforementioned developments provided new techniques for predicting the drag and the lift in complex flows using only the velocity vector and its derivatives. However, no formulation

could decompose the drag into lift-induced and profile contributions. Hence and for the sake of conciseness, all those analyses are not presented in further details in this dissertation. The first Lamb-vector-based formulation able to decompose the aerodynamic force in viscous flows was proposed by Wu *et al.* [75] in 2007.

1.3.2 Incompressible version

Derivation of the formula and decomposition of the force

Assuming a uniform flow at infinity, Wu *et al.* [75] started from the incompressible Navier-Stokes equations in order to express the acceleration of a fluid particle:

$$\rho_\infty \boldsymbol{a} = \rho_\infty \frac{\partial \boldsymbol{q}}{\partial t} + \rho_\infty \boldsymbol{l} + \nabla\left(\rho_\infty \frac{q^2}{2}\right) = -\nabla p + \nabla \cdot \boldsymbol{\tau} \tag{1.3.2}$$

In the far-field approach, the total aerodynamic force is expressed as follows:

$$\boldsymbol{F} = -\rho_\infty \int_\Omega \boldsymbol{a} \mathrm{d}v + \oint_{S_e} (-p\boldsymbol{I} + \boldsymbol{\tau}) \cdot \boldsymbol{n} \mathrm{d}S \tag{1.3.3}$$

Upon using the first DMT (A.1), (1.3.3) becomes

$$\boldsymbol{F} = -\frac{\rho_\infty}{\mathcal{N}-1} \int_\Omega \boldsymbol{r} \times (\nabla \times \boldsymbol{a}) \, \mathrm{d}v + \frac{\rho_\infty}{\mathcal{N}-1} \oint_{\partial\Omega} \boldsymbol{r} \times (\boldsymbol{n} \times \boldsymbol{a}) \, \mathrm{d}S + \oint_{S_e} (-p\boldsymbol{I} + \boldsymbol{\tau}) \cdot \boldsymbol{n} \mathrm{d}S \tag{1.3.4}$$

The substitution of $\boldsymbol{a}$ for the left part of equation (1.3.2) yields

$$\boldsymbol{F} = -\frac{\rho_\infty}{\mathcal{N}-1} \int_\Omega \boldsymbol{r} \times \left(\nabla \times \left(\frac{\partial \boldsymbol{q}}{\partial t} + \boldsymbol{l}\right)\right) \mathrm{d}v + \frac{\rho_\infty}{\mathcal{N}-1} \oint_{\partial\Omega} \boldsymbol{r} \times (\boldsymbol{n} \times \boldsymbol{a}) \, \mathrm{d}S + \oint_{S_e} (-p\boldsymbol{I} + \boldsymbol{\tau}) \cdot \boldsymbol{n} \mathrm{d}S \tag{1.3.5}$$

where $\partial\Omega = S_b \cup S_e$. Using again the first DMT (A.1) on the first integral in the right-hand side of equation (1.3.5), one can retrieve the vortex force first recognized by Prandtl [7]:

$$\begin{aligned} -\frac{\rho_\infty}{\mathcal{N}-1} \int_\Omega \boldsymbol{r} \times \left(\nabla \times \left(\frac{\partial \boldsymbol{q}}{\partial t} + \boldsymbol{l}\right)\right) \mathrm{d}v = &- \frac{\rho_\infty}{\mathcal{N}-1} \int_\Omega \boldsymbol{r} \times \frac{\partial \boldsymbol{\omega}}{\partial t} \mathrm{d}v \\ &- \rho_\infty \int_\Omega \boldsymbol{l} \mathrm{d}v \\ &- \frac{\rho_\infty}{\mathcal{N}-1} \oint_{\partial\Omega} \boldsymbol{r} \times (\boldsymbol{n} \times \boldsymbol{l}) \, \mathrm{d}S \end{aligned} \tag{1.3.6}$$

The second integral of equation (1.3.5) is expressed upon replacing $\boldsymbol{a}$ by the right part of equation (1.3.2):

$$\frac{\rho_\infty}{\mathcal{N}-1} \oint_{\partial\Omega} \boldsymbol{r} \times (\boldsymbol{n} \times \boldsymbol{a}) \, \mathrm{d}S = \frac{\rho_\infty}{\mathcal{N}-1} \oint_{S_b} \boldsymbol{r} \times (\boldsymbol{n} \times \boldsymbol{a}) \, \mathrm{d}S + \frac{1}{\mathcal{N}-1} \oint_{S_e} \boldsymbol{r} \times (\boldsymbol{n} \times (-\nabla p + \nabla \cdot \boldsymbol{\tau})) \, \mathrm{d}S \tag{1.3.7}$$

The application of the second DMT (A.2) yields

$$\frac{\rho_\infty}{\mathcal{N}-1} \oint_{\partial\Omega} \boldsymbol{r} \times (\boldsymbol{n} \times \boldsymbol{a}) \, \mathrm{d}S = \frac{\rho_\infty}{\mathcal{N}-1} \oint_{S_b} \boldsymbol{r} \times (\boldsymbol{n} \times \boldsymbol{a}) \, \mathrm{d}S + \oint_{S_e} p\boldsymbol{n} \mathrm{d}S + \frac{1}{\mathcal{N}-1} \oint_{S_e} \boldsymbol{r} \times (\boldsymbol{n} \times \nabla \cdot \boldsymbol{\tau}) \, \mathrm{d}S \tag{1.3.8}$$

The pressure is then eliminated in (1.3.5). Finally, the *advection form* of the total force can be defined as follows:

$$\boldsymbol{F} = \boldsymbol{F}_{\rho l} + \boldsymbol{F}_{\partial\Omega} + \boldsymbol{F}_\tau + \boldsymbol{F}_b + \boldsymbol{F}_t \tag{1.3.9}$$

with

$$\boldsymbol{F}_{\rho l} = -\rho_\infty \int_\Omega \boldsymbol{l} \mathrm{d}v \tag{1.3.10}$$

$$\boldsymbol{F}_{\partial\Omega} = -\frac{\rho_\infty}{\mathcal{N}-1} \oint_{\partial\Omega} \boldsymbol{r} \times (\boldsymbol{n} \times \boldsymbol{l}) \, \mathrm{d}S \tag{1.3.11}$$

$$\boldsymbol{F}_\tau = \oint_{S_e} \boldsymbol{\tau} \cdot \boldsymbol{n} \mathrm{d}S + \frac{1}{\mathcal{N}-1} \oint_{S_e} \boldsymbol{r} \times (\boldsymbol{n} \times \nabla \cdot \boldsymbol{\tau}) \, \mathrm{d}S \tag{1.3.12}$$

$$\boldsymbol{F}_b = \frac{\rho_\infty}{\mathcal{N}-1} \oint_{S_b} \boldsymbol{r} \times (\boldsymbol{n} \times \boldsymbol{a}) \, \mathrm{d}S \tag{1.3.13}$$

$$\boldsymbol{F}_t = -\frac{\rho_\infty}{\mathcal{N}-1} \int_\Omega \boldsymbol{r} \times \frac{\partial \boldsymbol{\omega}}{\partial t} \mathrm{d}v \tag{1.3.14}$$

In the case of an incompressible steady viscous flow, $\boldsymbol{F}_t = \boldsymbol{0}$ and the no-slip condition states that the velocity is zero on the wall such that $\boldsymbol{F}_b = \boldsymbol{0}$. Moreover, on the wall the Lamb vector $\boldsymbol{l} = \boldsymbol{\omega} \times \boldsymbol{q}$ is also equal to zero, hence $\boldsymbol{F}_{\partial\Omega}$ is limited to S_e. Finally, the term $\boldsymbol{F}_\tau$ is negligible in the case of high Reynolds number flows when S_e is taken far enough from the body surface and boundary layers [81]. Equation (1.3.9) then becomes

$$\boldsymbol{F} = \boldsymbol{F}_{\rho l} + \boldsymbol{F}_{S_e} \tag{1.3.15}$$

with

$$\boldsymbol{F}_{S_e} = -\frac{\rho_\infty}{\mathcal{N}-1} \oint_{S_e} \boldsymbol{r} \times (\boldsymbol{n} \times \boldsymbol{l}) \, \mathrm{d}S \tag{1.3.16}$$

The lift component of $\boldsymbol{F}_{S_e}$ was shown to be equal to zero in the wake [75]. The decomposition into lift, profile drag and lift-induced drag proposed by Wu *et al.* [75] is given by

$$L = \boldsymbol{F}_{\rho l} \cdot \boldsymbol{e}_z \tag{1.3.17}$$

$$D_i = \boldsymbol{F}_{\rho l} \cdot \boldsymbol{e}_x \tag{1.3.18}$$

$$D_P = \boldsymbol{F}_{S_e} \cdot \boldsymbol{e}_x \tag{1.3.19}$$

It is important to note that this formulation depends on the Lamb vector only, and the only assumption made in the present analysis is that the fluid must be newtonian and the flow incompressible: this formulation can therefore be used in aerodynamics and hydrodynamics [82].

First applications to steady numerical cases

Yang *et al.* (2007)

This decomposition was later applied to a slender delta-wing by Yang *et al.* [28] to investigate the physics of the Lamb vector field. First of all, they derived transport equations governing the evolution of the dilatation $\nabla \cdot \boldsymbol{q}$ and the vorticity $\boldsymbol{\omega}$ in compressible flows and noticed that the Lamb vector is involved in both, through its divergence in the former and its curl in the latter. The dilatation transport equation is said to govern compressing processes and to contain the vortex-sound theory (see also Mao *et al.* [83]) while the vorticity transport governs the shearing processes. After showing that the production of the Lamb vector on the body surface is linked to enstrophy and boundary vorticity, they noticed that the Lamb vector field is highly localized in the flow as shown in Fig.1.5. It is more localized than the vorticity since it accounts only for the component perpendicular to the velocity, but it displays more complicated patterns since a vortex can contain regions where the Lamb vector is positive and others where it is negative.

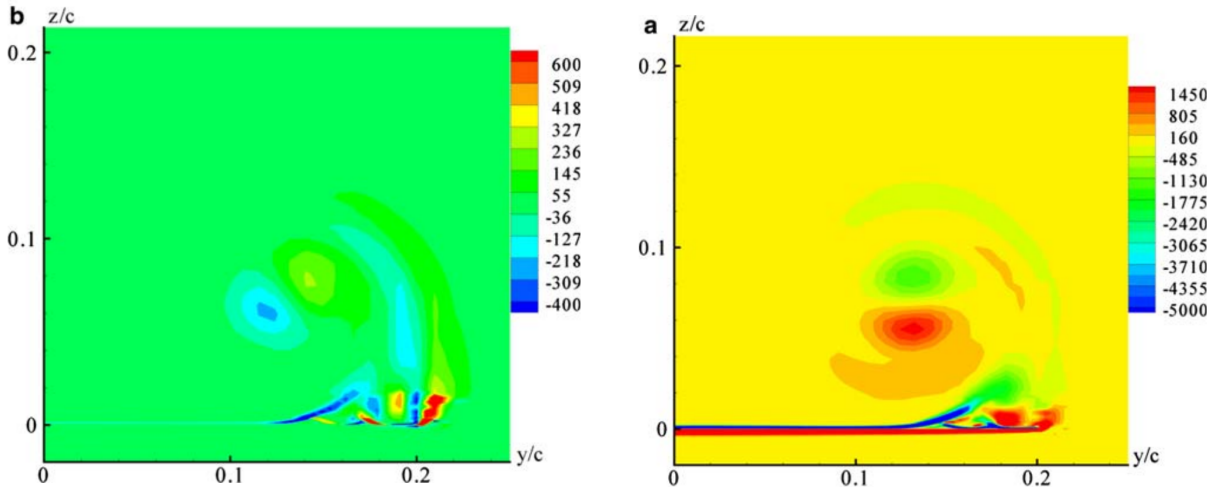

(a) Contour of l_x (b) Contour of l_z

Figure 1.5: Contours of $\boldsymbol{l}$ on a transverse plane at $x/c = 0.8$ (from [28])

Marongiu and Tognaccini (2010)

In 2010, Marongiu and Tognaccini [84] applied the method to steady and unsteady turbulent flows around a NACA0012 airfoil. They first proved that the Lamb-vector-based aerodynamic force breakdown (1.3.15) can be extended to the study of Reynolds-Averaged-Navier-Stokes (RANS) flows provided that all the instantaneous fields are replaced by their averaged value and that the Reynolds stress tensor is included in the term $\boldsymbol{F}_\tau$. Thus, they investigated the sensitivity to the size of the integration domain Ω shown in Fig.1.6. In steady flows, setting $y_S/c = 15$, the total lift coefficient remains constant with x_S while the volume and the surface contributions ($\boldsymbol{F}_{\rho l}$ and $\boldsymbol{F}_{S_e}$) given in the RANS version of (1.3.15) vary linearly. However, the same authors showed that for $y_S/c = 50$, the lift coefficient is solely given by the volume integral of the Lamb vector $\boldsymbol{F}_{\rho l}$. Regarding the drag coefficient, the total value is accurately predicted up to a certain x_S, and the volume contribution $\boldsymbol{F}_{\rho l}$ gradually vanishes such that the drag is entirely given by the surface integral $\boldsymbol{F}_{S_e}$. The loss of accuracy was explained by the poor quality of the CFD solution far downstream. Setting $x_S/c = 0.004$, the lift coefficient progressively reaches its correct value as y_S increases and is fully given by the volume integral $\boldsymbol{F}_{\rho l}$. On the contrary, the drag coefficient is shared between the volume and surface integrals: indeed, it is argued that the position of Σ_I is close to the trailing edge which explains why the volume integral still contributes to the drag. Although it was investigated the weight of the various contributions in the total lift and drag,

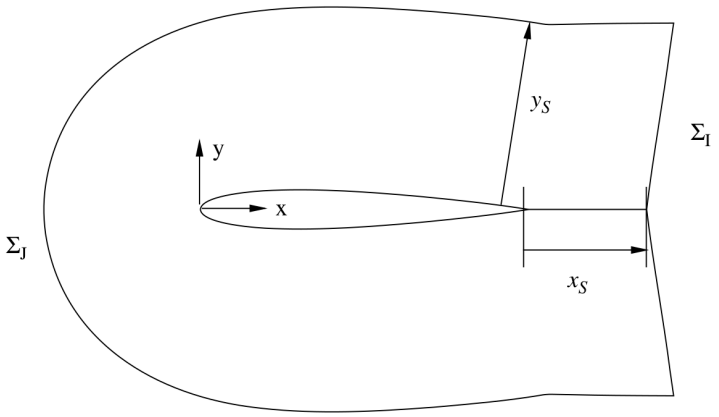

Figure 1.6: Sketch of the control volume and its boundaries (from [84])

no classical breakdown into lift-induced and profile components was clearly tested at that time.

Lift and lift-induced drag predictions

Marongiu *et al.* (2013)

Marongiu *et al.* [81] were the first to compare the definition of the lift-induced drag given by equation (1.3.18) to the so far well-known Prandtl's and Maskell's formulae (1.2.15) and (1.2.22). The numerical application was carried out on an elliptic wing of aspect ratio $\mathcal{AR} = 7$ for which the airfoil section is a NACA0012. Profiles of the components of the Lamb vector with respect to the distance from the wall were provided and confirmed the first impressions of Yang *et al.* [28] that the normal component is dominant. Indeed, $l_z = \omega_x v - \omega_y u$ involves the tangential velocity times the transverse vorticity to the wall. Moreover, it was outlined that the surface integral involved in the definition of the profile drag (1.3.19) can be limited to the section crossing the wake. Besides, it was stated that the Lamb vector associated to the wake vorticity vanishes in the limit of an inviscid flow, making it consistent with the fact that the profile drag is a finite Reynolds number effect. The sensitivity of the force breakdown with respect to the position of

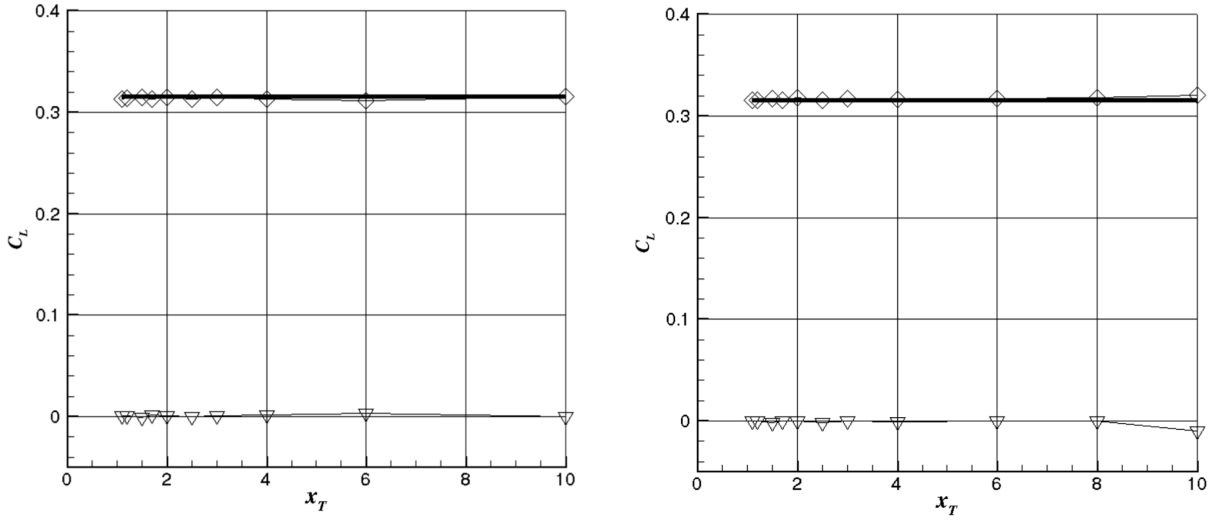

(a) Integration in Ω (b) Integration in boundary layer region

Figure 1.7: C_L VS wake plane position x_T for an elliptic wing with $M_\infty = 0.01$, $Re = 3 \times 10^6$, $\alpha = 4°$. **-** near-field, $-\Diamond-$ $\boldsymbol{F}_{\rho l}$, $-\bigtriangledown-$ $\boldsymbol{F}_{S_e}$ (from [81])

the wake plane was also investigated. The volume and surface contributions of the lift coefficient plotted in Fig.1.7 show that the lift is almost completely computed by the vortex force $\boldsymbol{F}_{\rho l}$ while the surface integral $\boldsymbol{F}_{S_e}$ does not contribute. The drag coefficient shown in Fig.1.8 is not accurately computed when the wake plane is placed too close to the trailing edge. Moreover, the drag breakdown into profile and lift-induced drag components depends on its location: the near wake still contributes to the lift-induced drag. Finally, a better accuracy is ensured when the integration is performed in the boundary layer region, also enclosing the near wake of the wing. The comparison with the lift-induced drag computed by Maskell's formula in Fig.1.9 suggests that the Lamb-vector-based definition is less sensitive to x_T once it has reached its maximum. Moreover, the evolutions are different since the vortex force keeps increasing in the near wake while Maskell's induced drag decreases. The compatibility of the two formulae is improved as well when integrating in the boundary layer region. The comparison with Prandtl's formula (1.2.15) also showed a good agreement with the vortex force. Although the derivation of equation (1.3.15) was conducted without making any hypotheses on the size and shape of the control volume Ω and its external boundary S_e, the first results suggest that the Lamb-vector-based drag breakdown actually depends on its size. Of course the total force remains constant but the decomposition into profile drag and lift-induced drag varies with the extent of the integration domain.

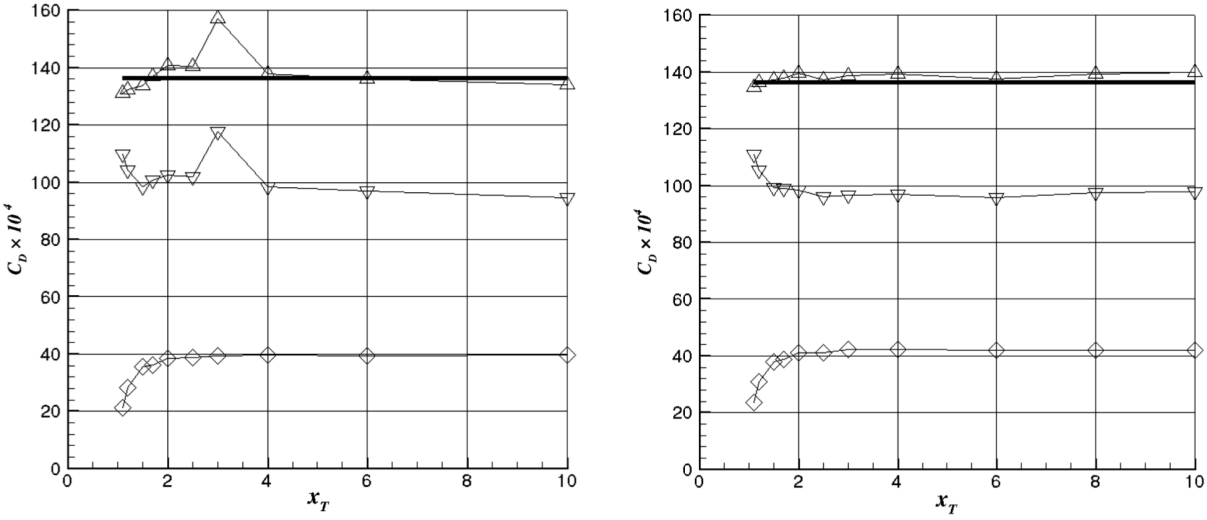

(a) Integration in Ω (b) Integration in boundary layer region

Figure 1.8: C_D VS wake plane position x_T for an elliptic wing with $M_\infty = 0.01$, $Re = 3 \times 10^6$, $\alpha = 4°$. **-** near-field, $-\Diamond-$ $\boldsymbol{F}_{\rho l}$, $-\bigtriangledown-$ $\boldsymbol{F}_{S_e}$, $-\bigtriangleup-$ $\boldsymbol{F}_{\rho l} + \boldsymbol{F}_{S_e}$ (from [81])

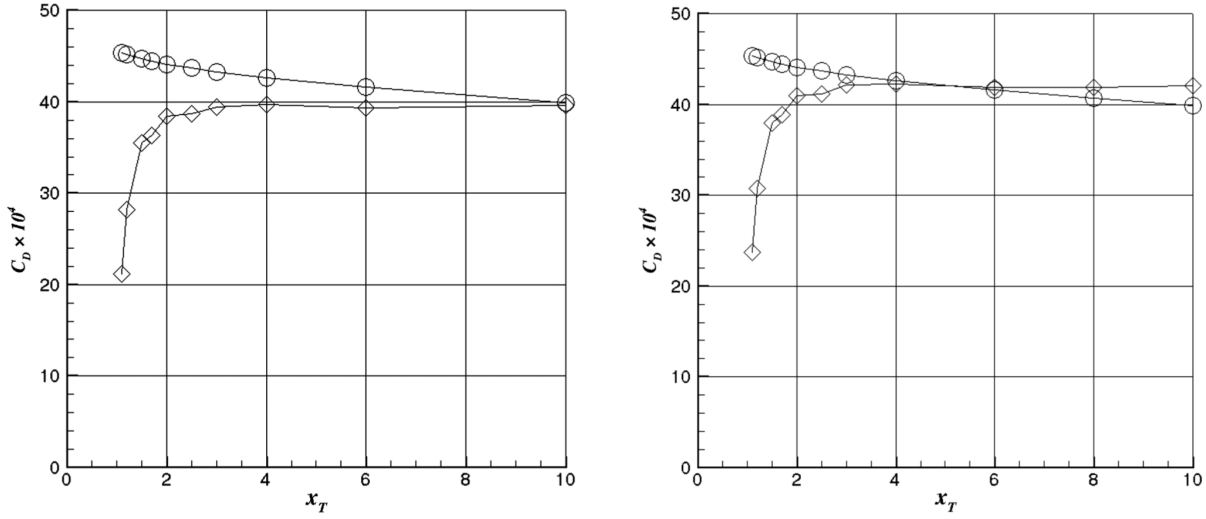

(a) Integration in Ω (b) Integration in boundary layer region

Figure 1.9: Comparison of the Lamb-vector-based definition (1.3.18) and Maskell's formula (1.2.22) VS wake plane position x_T for an elliptic wing with $M_\infty = 0.01$, $Re = 3 \times 10^6$, $\alpha = 4°$. $-\Diamond-$ $\boldsymbol{F}_{\rho l}$, $-\bigcirc-$ Maskell's formula (from [81])

Zou *et al.* (2019)

Very recently, Zou *et al.* [85] investigated the sensitivity of the Lamb-vector-based lift-induced drag formula with the location of the wake plane in incompressible viscous flows around the same elliptic wing as before and around a delta wing of sweep angle $\chi = 76°$. First of all, assuming that S_e is bounded by a wake plane W_v perpendicular to the freestream such that $\boldsymbol{n} = \boldsymbol{e}_x$ and writing the velocity field as $\boldsymbol{q} = \boldsymbol{U}_\infty + \delta\boldsymbol{q}$ with $\delta\boldsymbol{q} = \begin{pmatrix} u & v & w \end{pmatrix}^T$, it is possible to cast the profile drag previously defined by equation (1.3.19) as follows (see [75] p.630):

$$D_P = \frac{\rho_\infty}{\mathcal{N}-1}\boldsymbol{U}_\infty \cdot \int_{W_v} \boldsymbol{\omega} \times \boldsymbol{r}_\perp \mathrm{d}S + \frac{\rho_\infty}{\mathcal{N}-1}\int_{W_v} \boldsymbol{r}_\perp \cdot (\delta\boldsymbol{q} \times \boldsymbol{\omega})\,\mathrm{d}S \tag{1.3.20}$$

where $\boldsymbol{r}_\perp = \begin{pmatrix} 0 & y & z \end{pmatrix}^T$. Cumbersome derivations starting from the Lamb-vector-based lift-

induced drag definition (1.3.18) yield to the following expression [85]:

$$D_i = \frac{\rho_\infty}{\mathcal{N}-1}\int_{W_v} \boldsymbol{\omega}\cdot\boldsymbol{\psi}\mathrm{d}S + \rho_\infty \int_{W_v} \boldsymbol{r}_\perp\cdot(\delta\boldsymbol{q}\times\boldsymbol{\omega})\,\mathrm{d}S + \frac{\rho_\infty}{\mathcal{N}-1}\frac{\mathrm{d}}{\mathrm{d}x}\int_W [\boldsymbol{e}_x\cdot(\boldsymbol{\psi}\times\delta\boldsymbol{q}) + 2u\delta\boldsymbol{q}\cdot\boldsymbol{r}_\perp]\,\mathrm{d}S \tag{1.3.21}$$

where $\boldsymbol{\psi}$ is the vector potential. The evolution of the profile and lift-induced drag contributions

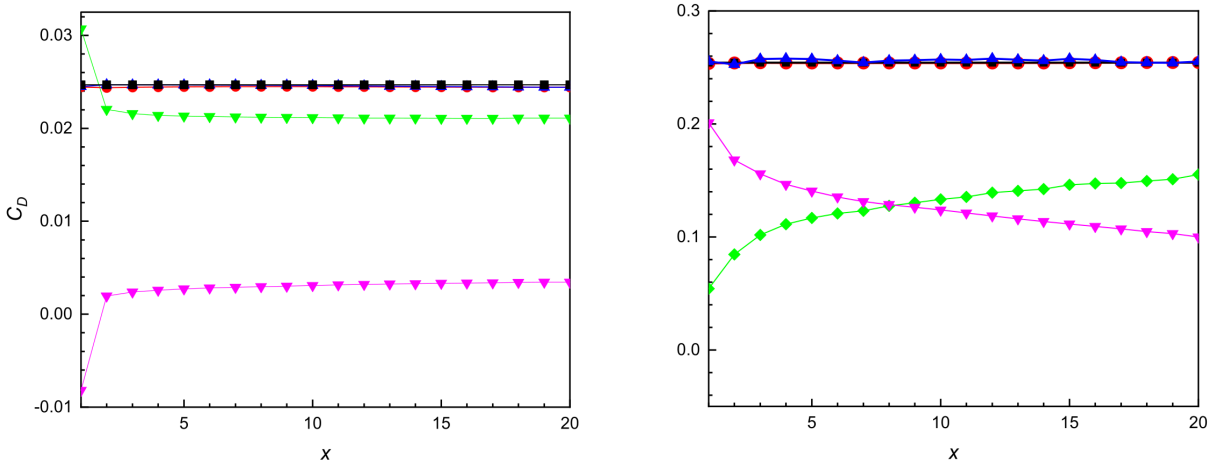

(a) Elliptic wing, $Re = 10^5$, $\alpha = 4°$ (b) Delta wing, $Re = 5\times10^5$, $\alpha = 20°$

Figure 1.10: Evolution of the drag breakdown proposed by Zou *et al.* VS wake plane position x. Magenta curve D_i, green curve D_P, blue curve $D_i + D_P$ (from [85])

with respect to the location of W_v are displayed in Fig.1.10 for the elliptic wing and the delta wing. In both cases, they evolve compensating each other. In the case of the delta wing, the sensitivity of the decomposition to x is much greater. It was argued that the attached flow around the elliptic wing is less dissipated in the wake than that of the detached flow around the delta wing. Indeed, leading edge vortices merge with the free shear layer created downstream of the trailing edge. Fig.1.11 shows the evolution of ω_x in the wake: the tip vortices dissipate quicker in the case of the delta wing. Furthermore, in the case of the elliptic wing, the growth in lift-induced drag occuring in the near wake is explained by the increase in ω_x due to the rolling-up of the vortex sheet. It later stabilizes once the size of the tip vortices becomes constant.

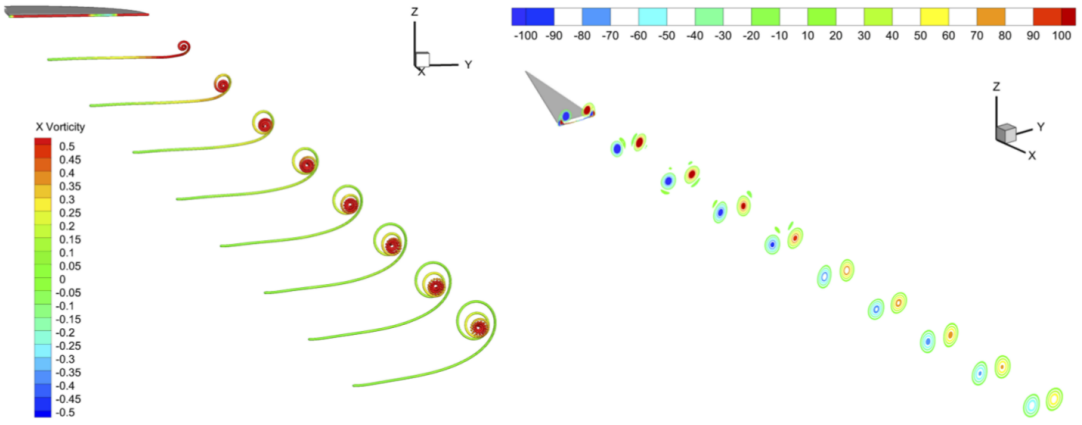

Figure 1.11: Evolution of ω_x VS wake plane position x (from [85])

Finally, the Lamb-vector-based formulation provides a definition of the lift, the lift-induced drag and the profile drag in incompressible steady viscous flows and its applications showed

good agreement with former methods. Therefore, it appeared necessary to extend the formula to compressible flows in order to check if the aerodynamic force generated at higher Mach numbers can be well predicted and decomposed. The aim is of course to apply this breakdown to standard commercial airplanes flying at high altitude in transonic conditions.

1.3.3 Extension to compressible flows

Wu *et al.*'s formulation

An extension of equation (1.3.9) was already derived by Wu *et al.* [75] and adopted by Liu *et al.* [86, 87] in several studies of the various processes and their couplings involved in compressible flows. The derivation of the extended formula is done by following the same steps as before, starting from the compressible Navier-Stokes equations:

$$\rho \boldsymbol{a} = \rho \frac{\partial \boldsymbol{q}}{\partial t} + \rho \boldsymbol{l} - \frac{q^2}{2} \nabla \rho + \nabla \left(\rho \frac{q^2}{2} \right) = -\nabla p + \nabla \cdot \boldsymbol{\tau} \tag{1.3.22}$$

This time, the total aerodynamic force is given by

$$\boldsymbol{F} = -\int_{\Omega} \rho \boldsymbol{a} \mathrm{d}v + \oint_{S_e} (-p\boldsymbol{I} + \boldsymbol{\tau}) \cdot \boldsymbol{n} \mathrm{d}S \tag{1.3.23}$$

The use of the first DMT (A.1) allows to cast (1.3.23) as follows:

$$\boldsymbol{F} = -\frac{1}{\mathcal{N}-1} \int_{\Omega} \boldsymbol{r} \times (\nabla \times (\rho \boldsymbol{a})) \, \mathrm{d}v + \frac{1}{\mathcal{N}-1} \oint_{\partial\Omega} \boldsymbol{r} \times (\boldsymbol{n} \times \rho \boldsymbol{a}) \, \mathrm{d}S + \oint_{S_e} (-p\boldsymbol{I} + \boldsymbol{\tau}) \cdot \boldsymbol{n} \mathrm{d}S \tag{1.3.24}$$

The substitution of $\rho \boldsymbol{a}$ for the left part of equation (1.3.22) yields

$$\begin{aligned} \boldsymbol{F} = &-\frac{1}{\mathcal{N}-1} \int_{\Omega} \boldsymbol{r} \times \left(\nabla \times \left(\rho \frac{\partial \boldsymbol{q}}{\partial t} + \rho \boldsymbol{l} - \frac{q^2}{2} \nabla \rho \right) \right) \mathrm{d}v \\ &+ \frac{1}{\mathcal{N}-1} \oint_{\partial\Omega} \boldsymbol{r} \times (\boldsymbol{n} \times \rho \boldsymbol{a}) \, \mathrm{d}S + \oint_{S_e} (-p\boldsymbol{I} + \boldsymbol{\tau}) \cdot \boldsymbol{n} \mathrm{d}S \end{aligned} \tag{1.3.25}$$

An additional application of the first DMT (A.1) to the first integral in the right-hand side of equation (1.3.25) yields

$$\begin{aligned} -\frac{1}{\mathcal{N}-1} \int_{\Omega} \boldsymbol{r} \times \left(\nabla \times \left(\rho \frac{\partial \boldsymbol{q}}{\partial t} + \rho \boldsymbol{l} - \frac{q^2}{2} \nabla \rho \right) \right) \mathrm{d}v = &- \int_{\Omega} \left(\rho \boldsymbol{l} - \frac{q^2}{2} \nabla \rho \right) \mathrm{d}v \\ &- \frac{1}{\mathcal{N}-1} \oint_{\partial\Omega} \boldsymbol{r} \times \left(\boldsymbol{n} \times \left(\rho \boldsymbol{l} - \frac{q^2}{2} \nabla \rho \right) \right) \mathrm{d}S \\ &- \frac{1}{\mathcal{N}-1} \int_{\Omega} \boldsymbol{r} \times \left(\nabla \times \left(\rho \frac{\partial \boldsymbol{q}}{\partial t} \right) \right) \mathrm{d}v \end{aligned} \tag{1.3.26}$$

The second integral of equation (1.3.25) is expressed upon replacing $\rho \boldsymbol{a}$ by the right part of equation (1.3.22):

$$\begin{aligned} \frac{1}{\mathcal{N}-1} \oint_{\partial\Omega} \boldsymbol{r} \times (\boldsymbol{n} \times \rho \boldsymbol{a}) \, \mathrm{d}S = &\frac{1}{\mathcal{N}-1} \oint_{S_b} \boldsymbol{r} \times (\boldsymbol{n} \times \rho \boldsymbol{a}) \, \mathrm{d}S + \oint_{S_e} p \boldsymbol{n} \mathrm{d}S \\ &+ \frac{1}{\mathcal{N}-1} \oint_{S_e} \boldsymbol{r} \times (\boldsymbol{n} \times \nabla \cdot \boldsymbol{\tau}) \, \mathrm{d}S \end{aligned} \tag{1.3.27}$$

where the second DMT (A.2) has been used. Finally, the compressible expression of the total force is

$$\begin{aligned}\boldsymbol{F} = &-\int_\Omega \left(\rho\boldsymbol{l} - \frac{q^2}{2}\nabla\rho\right)\mathrm{d}v - \frac{1}{\mathcal{N}-1}\oint_{\partial\Omega}\boldsymbol{r}\times\left(\boldsymbol{n}\times\left(\rho\boldsymbol{l} - \frac{q^2}{2}\nabla\rho\right)\right)\mathrm{d}S \\ &+\oint_{S_e}\boldsymbol{\tau}\cdot\boldsymbol{n}\mathrm{d}S + \frac{1}{\mathcal{N}-1}\oint_{S_e}\boldsymbol{r}\times(\boldsymbol{n}\times\nabla\cdot\boldsymbol{\tau})\,\mathrm{d}S \\ &+\frac{1}{\mathcal{N}-1}\oint_{S_b}\boldsymbol{r}\times(\boldsymbol{n}\times\rho\boldsymbol{a})\,\mathrm{d}S - \frac{1}{\mathcal{N}-1}\int_\Omega\boldsymbol{r}\times\left(\nabla\times\left(\rho\frac{\partial\boldsymbol{q}}{\partial t}\right)\right)\mathrm{d}v \end{aligned} \tag{1.3.28}$$

In the case of a compressible steady viscous flow, assuming that S_e retreats far from the body surface such that the viscous stresses are negligible, the compressible version of equation (1.3.15) is given by

$$\boldsymbol{F} = -\int_\Omega \left(\rho\boldsymbol{l} - \frac{q^2}{2}\nabla\rho\right)\mathrm{d}v - \frac{1}{\mathcal{N}-1}\oint_{S_e}\boldsymbol{r}\times\left(\boldsymbol{n}\times\left(\rho\boldsymbol{l} - \frac{q^2}{2}\nabla\rho\right)\right)\mathrm{d}S \tag{1.3.29}$$

The formula is the same except that the Lamb vector $\rho\boldsymbol{l}$ is replaced by its compressible counterpart $\rho\boldsymbol{l} - \frac{q^2}{2}\nabla\rho$. Yet, Liu [88] observed that the surface integral is no longer just a drag component but also contributes to the lift, which makes it tough to define an equivalent breakdown in compressible flows. Moreover, in incompressible flows, the integration could be limited to regions close to the body surface since the Lamb vector is zero everywhere except in the boundary layers and the wake. In compressible flows, this property is lost since $\frac{q^2}{2}\nabla\rho$ may be different from zero even outside those regions as pointed out by Mele and Tognaccini [31].

Breakdown for steady compressible flows

Mele *et al.* (2014, 2016, 2017)

This issue was circumvented by Mele and Tognaccini [31] who applied the first DMT (A.1) to $\frac{q^2}{2}\nabla\rho$ in order to express the aerodynamic force breakdown as follows:

$$\boldsymbol{F} = \boldsymbol{F}_{\rho l} + \boldsymbol{F}_{m_\rho} + \boldsymbol{F}_{S_e} \tag{1.3.30}$$

with

$$\boldsymbol{F}_{\rho l} = -\int_\Omega \rho\boldsymbol{l}\mathrm{d}v \tag{1.3.31}$$

$$\boldsymbol{F}_{m_\rho} = -\frac{1}{\mathcal{N}-1}\int_\Omega\boldsymbol{r}\times\left(\nabla\rho\times\nabla\left(\frac{q^2}{2}\right)\right)\mathrm{d}v = -\int_\Omega\boldsymbol{m}_\rho\mathrm{d}v \tag{1.3.32}$$

$$\boldsymbol{F}_{S_e} = -\frac{1}{\mathcal{N}-1}\oint_{S_e}\boldsymbol{r}\times(\boldsymbol{n}\times\rho\boldsymbol{l})\,\mathrm{d}S \tag{1.3.33}$$

The decomposition into lift and profile and lift-induced drag contributions proposed by Mele and Tognaccini [31] is given by

$$L = \left(\boldsymbol{F}_{\rho l} + \boldsymbol{F}_{m_\rho}\right)\cdot\boldsymbol{e}_z \tag{1.3.34}$$

$$D_i = \left(\boldsymbol{F}_{\rho l} + \boldsymbol{F}_{m_\rho}\right)\cdot\boldsymbol{e}_x \tag{1.3.35}$$

$$D_P = \boldsymbol{F}_{S_e}\cdot\boldsymbol{e}_x \tag{1.3.36}$$

With this formulation, the integrands involved in the volume integrals are different from zero only in the boundary layers, in the wake and downstream of curved shock waves since everywhere else, high Reynolds number flows are actually homoenthalpic and homoentropic. The inviscid Crocco-Vazsonyi equation writes

$$\rho\boldsymbol{l} = \rho T\nabla s - \rho\nabla H \tag{1.3.37}$$

The Lamb vector is then equal to zero in regions where the flow has constant H and constant s. Moreover, the second thermodynamic identity is given by

$$\nabla h = T\nabla s + \frac{\nabla p}{\rho} \tag{1.3.38}$$

Therefore, in regions where the flow is homoenthalpic and homoentropic $\nabla h = -\nabla\left(\frac{q^2}{2}\right)$ such that

$$\rho\nabla\left(\frac{q^2}{2}\right) = -\nabla p \Rightarrow \nabla\rho \times \nabla\left(\frac{q^2}{2}\right) = \mathbf{0} \tag{1.3.39}$$

As a consequence, $\rho\boldsymbol{l}$ and $\boldsymbol{m}_\rho$ are equal to zero everywhere except in boundary layers, behind curved shocks and inside the wakes. Mele and Tognaccini [31] also noticed that setting the reference point for the computation of moments on the wake plane W reduces $\boldsymbol{F}_{S_e}$ to a drag contribution only. It was already proved with different arguments by Wu *et al.* in the incompressible case. Finally, they extended the application of equation (1.3.30) to turbulent flows provided that the instantaneous quantities are replaced by their Favre averaged values.

This force breakdown was then tested on a NACA0012 airfoil [31] and on an elliptic wing [18, 32]. Two-dimensional computations suggest that when the Mach number increases, the lift

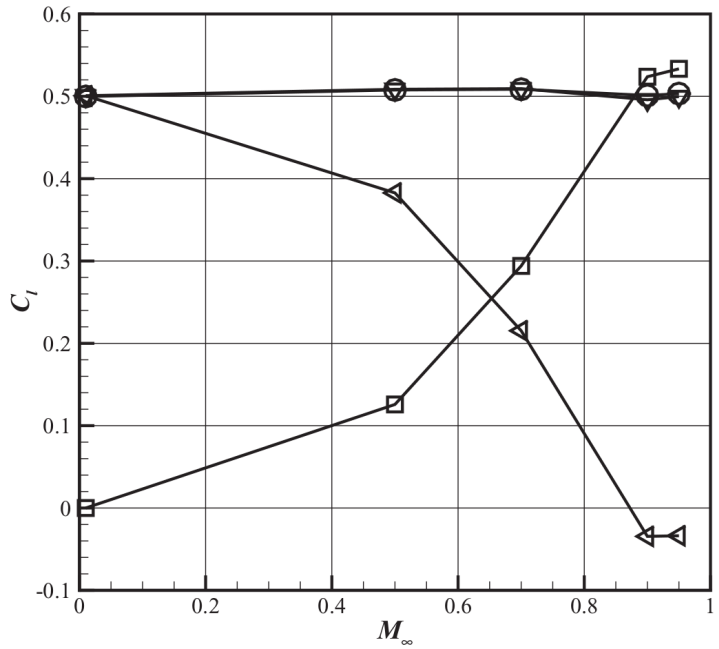

Figure 1.12: Evolution of the lift breakdown proposed by Mele and Tognaccini VS Mach number M_∞, NACA0012 airfoil, $Re = 9 \times 10^6$, $C_L \approx 0.5$. $-\bigcirc-$ near-field, $-\triangleleft-$ $\boldsymbol{F}_{\rho l}$, $-\square-$ $\boldsymbol{F}_{m_\rho}$, $-\triangledown-$ $\boldsymbol{F}_{\rho l} + \boldsymbol{F}_{m_\rho}$ (from [31])

contribution provided by $\boldsymbol{F}_{\rho l}$ decreases in favor of that given by $\boldsymbol{F}_{m_\rho}$ (see Fig.1.12). This tendency had already been noticed by Chang *et al.* [89, 90] who used the projection theory on harmonic functions to determine the aerodynamic force on a delta wing in subsonic and supersonic flows. Fig.1.13 sketches the evolution of the drag breakdown on the NACA0012 airfoil with respect to the freestream Mach number. The total drag is fully computed by the surface integral as in incompressible flows. Moreover, the compressibility term $\boldsymbol{F}_{m_\rho}$ compensates the increase of the vortex force $\boldsymbol{F}_{\rho l}$ up to low transonic Mach numbers. When $M_\infty \to 1$, Mele and Tognaccini [31] asserted that the increasing size of the shock wave region implies an integration performed in zones where the numerical scheme is only first-order accurate, which explains why $\boldsymbol{F}_{m_\rho}$ does not compensate $\boldsymbol{F}_{\rho l}$ anymore. This issue was bypassed by Mele *et al.* [36] who proposed an alternative formula for $\boldsymbol{F}_{m_\rho}$ which avoids the integration in the shock wave region. Additionally,

they noticed that the lift computed by the incompressible definition (1.3.17) of $\boldsymbol{F}_{\rho l}$ is in good agreement with the near-field reference value in transonic and even supersonic conditions.

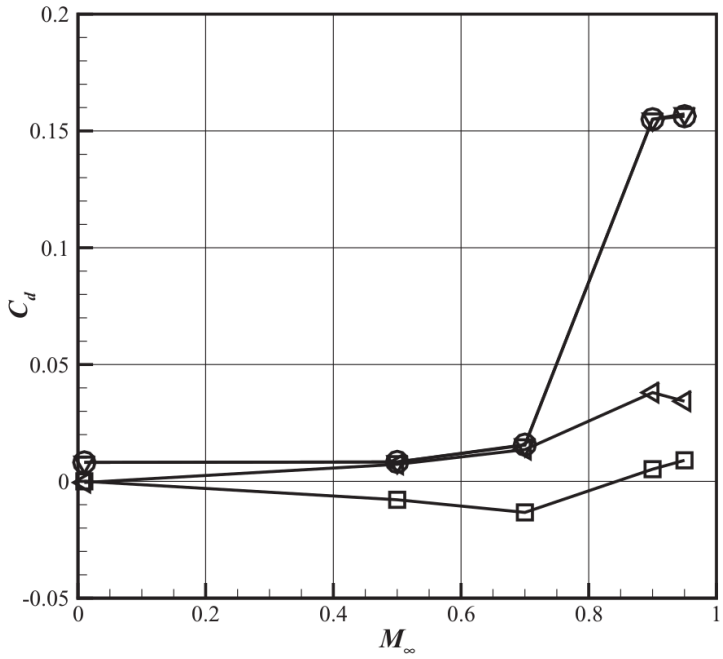

Figure 1.13: Evolution of the drag breakdown proposed by Mele and Tognaccini VS Mach number M_∞, NACA0012 airfoil, $Re = 9 \times 10^6$, $C_L \approx 0.5$. $-\bigcirc-$ near-field, $-\triangleleft-$ $\boldsymbol{F}_{\rho l}$, $-\square-$ $\boldsymbol{F}_{m_\rho}$, $-\triangledown-$ $\boldsymbol{F}_{S_e}$ (from [31])

Depending on the freestream Mach number, the total drag computed in the case of the elliptic wing [32] was more or less accurate when compared to the near-field value as sketched in Fig.1.14. It was shown that the contribution to the lift given by the compressibility term $\boldsymbol{F}_{m_\rho}$ still increases with the Mach number while the contribution of the vortex force $\boldsymbol{F}_{\rho l}$ diminishes. The lift-induced drag computed by the authors consisted in selecting the maximum obtained value of the term $\boldsymbol{F}_{\rho l} + \boldsymbol{F}_{m_\rho}$ and was compared to Prandtl's formula (1.2.15). They concluded that this incompressible inviscid formulation is also able to predict the lift-induced drag in compressible and even transonic flows where strong shocks are present.

Kang *et al.* (2019)

Very recently, Kang *et al.* [18] provided additional results and notably emphasized the sensitivity of the Lamb-vector-based decomposition to the location of the reference point chosen for the computation of moments, and also to the size of the integration domain. Those sensitivities greatly question the robustness of the method although they concluded that the discrepancies in drag prediction are small as long as the reference point is located close to the body skin.

They also compared the profile and lift-induced drag contributions computed by the Lamb-vector-based formula to those calculated by Destarac and Van der Vooren's formulation and Maskell's wake integral: their results are displayed in Fig.1.15. They showed that the surface integral $\boldsymbol{F}_{S_e}$ does not contribute to the lift and gives the total drag in two-dimensional flows, as soon as the wake plane is positioned sufficiently downstream of the trailing edge and the near wake is accounted for. In three-dimensional flows, the total drag is well predicted although some discrepancies can be noted. Moreover, there is a quite satisfactory agreement between the profile drag computed by the Lamb-vector-based formulation and Destarac and Van der Vooren's formula. The lift-induced drag is also close to the one predicted by Maskell's formula.

The same authors also investigated the case of an effectively inviscid flow. Nevertheless, without boundary layers, no vorticity can be generated and then no lift is produced. Therefore,

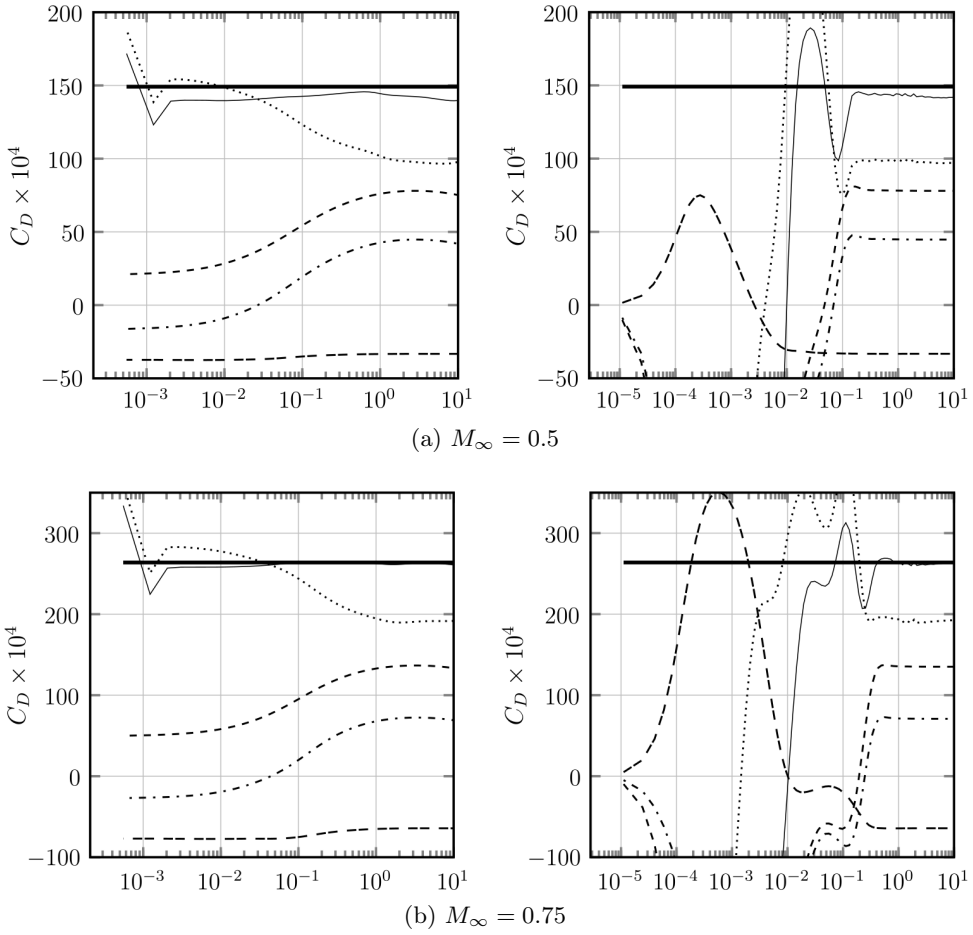

(a) $M_\infty = 0.5$

(b) $M_\infty = 0.75$

Figure 1.14: Evolution of the drag breakdown proposed by Mele *et al.* VS x_S (left) and y_S (right), elliptic wing $Re = 3 \times 10^6$, $\alpha = 4°$. - near-field, $-$ $\boldsymbol{F}_{\rho l} + \boldsymbol{F}_{m_\rho} + \boldsymbol{F}_{S_e}$, $\cdots$ $\boldsymbol{F}_{S_e}$, $-\cdot-$ $\boldsymbol{F}_{\rho l} + \boldsymbol{F}_{m_\rho}$, $---$ $\boldsymbol{F}_{\rho l}$, $--$ $--$ $\boldsymbol{F}_{m_\rho}$ (from [32])

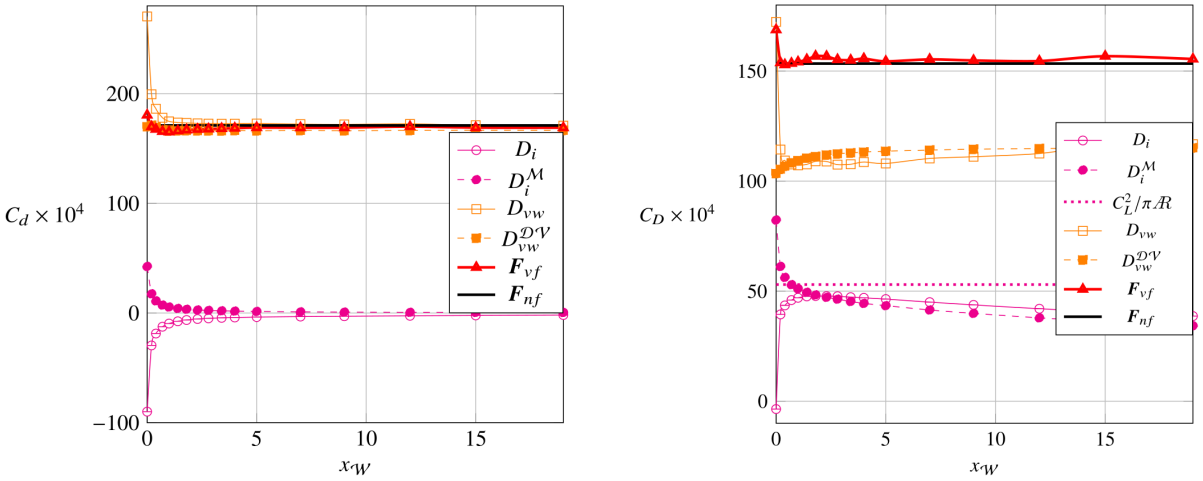

(a) NACA0012 airfoil, $M_\infty = 0.75$, $Re = 6 \times 10^6$, $\alpha = 2°$

(b) Elliptic wing, $M_\infty = 0.5$, $Re = 3 \times 10^6$, $\alpha = 4°$

Figure 1.15: Evolution of the drag breakdown proposed by Kang *et al.* VS wake plane position x_W. $D_i = \boldsymbol{e}_x \cdot (\boldsymbol{F}_{\rho l} + \boldsymbol{F}_{m_\rho})$, $D_i^{\mathcal{M}}$ computed by Maskell's formula, $D_{vw} = \boldsymbol{e}_x \cdot \boldsymbol{F}_{S_e}$, $D_{vw}^{\mathcal{DV}}$ computed by Destarac and Van der Vooren's formula, $\boldsymbol{F}_{vf} = \boldsymbol{F}_{\rho l} + \boldsymbol{F}_{m_\rho} + \boldsymbol{F}_{S_e}$, $\boldsymbol{F}_{nf}$ computed by near-field integration (from [18])

choice was made to add a vortex sheet on the body surface in order to generate the lift. Two-dimensional computations emphasized the fact that the total drag is zero in subsonic conditions and is solely given by the surface integral $\boldsymbol{F}_{S_e}$ in transonic flight. Furthermore, the lift computed on the elliptic wing is in agreement with the one given by the near-field integration. Besides, the computed lift-induced drag is again close to the one computed by Prandtl's formula (1.2.15). The term $\boldsymbol{F}_{\rho l} + \boldsymbol{F}_{m_\rho}$ then seems to systematically predict the lift and the lift-induced drag at subsonic and transonic Mach numbers. Finally, the effect the Reynolds number was investigated: for low Reynolds numbers the vortex force $\boldsymbol{F}_{\rho l}$ produces a thrust contribution which progressively vanishes as Re increases.

Two definitions of the wave drag

Mele *et al.* (2017)

An ambition was then to find a vortical definition of the wave drag generated in transonic and supersonic flows. Indeed, the breakdown (1.3.30) only provides a decomposition into profile and lift-induced drag components, the viscous and wave contributions being mixed altogether. The profile drag can be assessed with the surface integral $\boldsymbol{F}_{S_e}$ limited to the wake section but distinguishing the wake of the boundary layers and the wake of the shock appears to be tough since they progressively merge downstream of the trailing edge. To address this feature, Mele *et al.* [36] proposed to define the wave drag as the surface integral on a plane located downstream of the shock as sketched in Fig.1.16. The viscous and wave drag contributions were then defined as follows:

$$D_w = \boldsymbol{e}_x \cdot \left(-\frac{1}{\mathcal{N}-1} \int_{\mathrm{W_{sw}}} \boldsymbol{r} \times (\boldsymbol{n} \times \rho \boldsymbol{l}) \, \mathrm{d}S \right) \tag{1.3.40}$$

$$D_v = D_P - D_w \tag{1.3.41}$$

This vorticity-based breakdown was compared to the thermodynamic formulation developed by Paparone and Tognaccini [46] on a NACA0012 airfoil for Mach numbers from low subsonic to high transonic conditions (see Fig.1.17). The accuracy of the computed wave drag seems to be excellent although the chart scale chosen does not allow for a neater comparison. The method was also applied to real cruise flight conditions on a NASA Common Research Model (NASA CRM) for several angles of attack and the results were also very satisfactory.

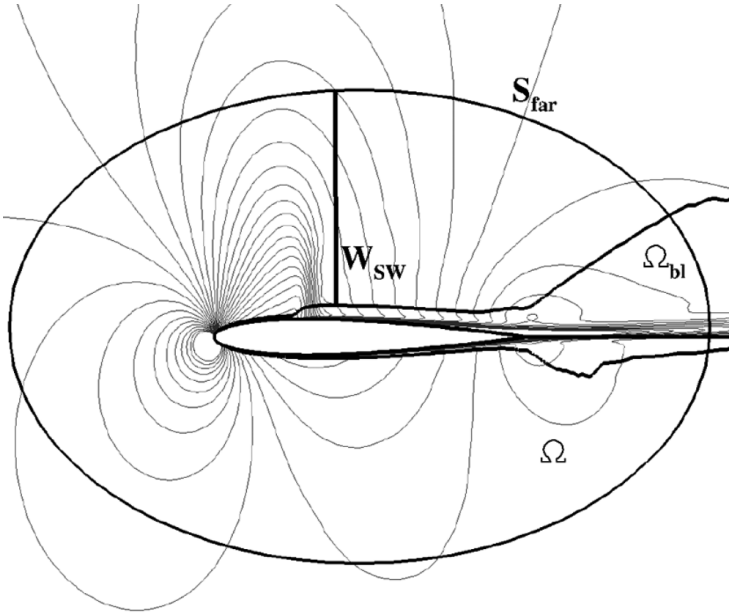

Figure 1.16: Wake plane W_{sw} downstream of the shock wave (from [36])

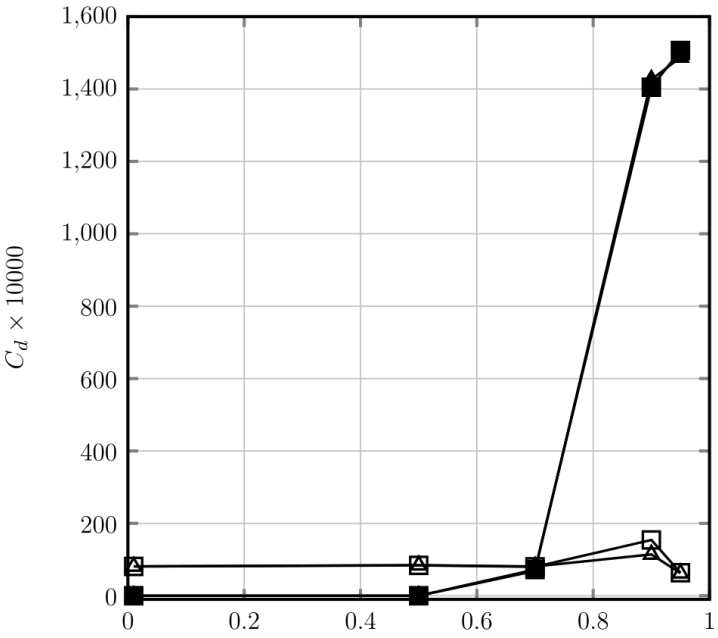

Figure 1.17: Viscous/wave drag breakdown with respect to freestream Mach number. $-\triangle-$ entropy-based viscous drag, $-\blacktriangle-$ entropy-based wave drag, $-\square-$ vorticity-based viscous drag, $-\blacksquare-$ vorticity-based wave drag (from [36])

Ostieri and Tognaccini (2018)

Yet, a few months later, Ostieri and Tognaccini [91] stated that, in spite of the good results, the latter definition provides *"a systematic overprediction of the wave drag at the expense of the viscous contribution"*. They pointed out that transforming the surface integral $\boldsymbol{F}_{S_e}$ which provides the profile drag in a volume integral would be more suited to define the different contributions. To do so, they used the double cross product identity in order to re-express $\boldsymbol{F}_{\partial\Omega_{sw}}$, the force computed on the external boundary $\partial\Omega_{sw}$ of the shock wave region:

$$\begin{aligned}\boldsymbol{F}_{\partial\Omega_{sw}} &= -\frac{1}{\mathcal{N}-1}\oint_{\partial\Omega_{sw}}(\boldsymbol{r}\cdot\rho\boldsymbol{l})\,\boldsymbol{n}\mathrm{d}S + \frac{1}{\mathcal{N}-1}\oint_{\partial\Omega_{sw}}(\boldsymbol{r}\cdot\boldsymbol{n})\,\rho\boldsymbol{l}\mathrm{d}S \\ &= -\frac{1}{\mathcal{N}-1}\int_{\Omega_{sw}}\nabla(\boldsymbol{r}\cdot\rho\boldsymbol{l})\,\mathrm{d}v + \frac{1}{\mathcal{N}-1}\int_{\Omega_{sw}}\nabla\cdot(\boldsymbol{r}\otimes\rho\boldsymbol{l})\,\mathrm{d}v \end{aligned} \tag{1.3.42}$$

where the Gauss and divergence theorems have been applied. The same authors emphasized that the volume Ω_{sw} must enclose the near shock wake in order to account for the Lamb vector field which still contributes to the drag. Fig.1.18 sketches the adopted volume for the computation of the wave drag on a NACA0012 airfoil immersed in a steady flow with $M_\infty = 0.8$, $Re = 9\times10^6$ and $\alpha = 0°$. The computed wave drag plotted in Fig.1.19 increases with y_S before it reaches

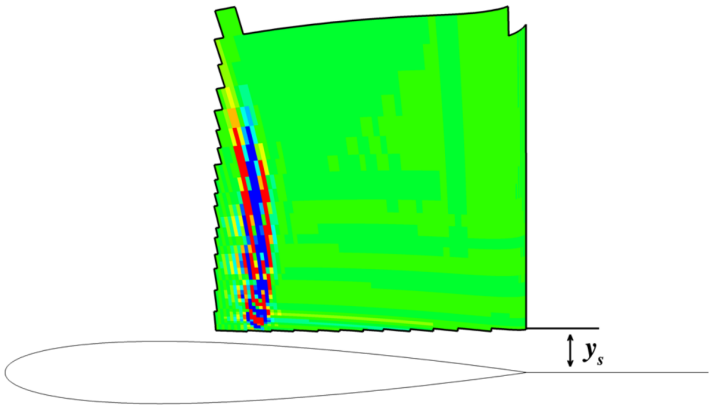

Figure 1.18: Definition of Ω_{sw} (from [91])

the value computed by the thermodynamic method [46]. It was concluded that the results are satisfactory since the wave drag can be accurately predicted in a wide range of y_S values.

1.3.4 Discussion on the physical interpretation in incompressible flows

The Lamb-vector-based formulation seems to correctly predict the lift and the drag along with a decomposition into profile and lift-induced contributions. Furthermore, the results provided by the incompressible analyses of Kutta-Joukowski, Prandtl and Maskell showed to be in quite good agreement with those provided by the Lamb-vector-based formulation, even in compressible regime. Hence it appears necessary to have a formal physical interpretation of the terms involved in the decomposition in order to investigate the existing links between the Lamb-vector-based formulation and former analyses in incompressible flows.

A generalized Kutta-Joukowski theorem

Starting from the expression of the vortex force $\boldsymbol{F}_{\rho l}$ (1.3.18), it is possible to interpret the volume integral in terms of the Kutta-Joukowski theorem (1.2.1) (see Wu *et al.* [75]). Indeed, by applying the curl theorem, the three-dimensional definition of the circulation is given by

$$\boldsymbol{\Gamma} = \oint_{S_e}\boldsymbol{n}\times\boldsymbol{q}\mathrm{d}S = \int_\Omega\boldsymbol{\omega}\mathrm{d}v = -\Gamma\boldsymbol{e}_y \tag{1.3.43}$$

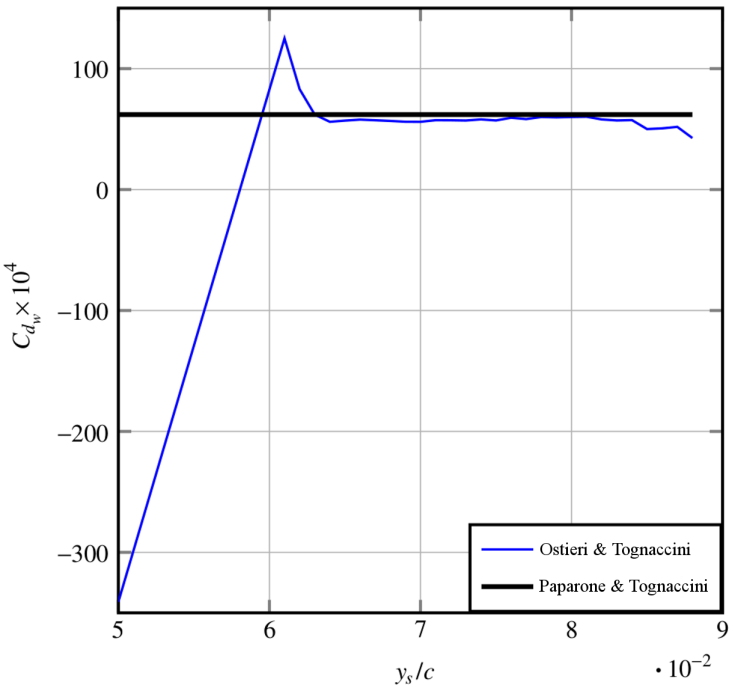

Figure 1.19: Evolution of C_{D_w} on the NACA0012 with the position y_S of the lower surface of the selected shock wave region (from [91])

Therefore, with $\boldsymbol{q} = \boldsymbol{U}_\infty + \delta\boldsymbol{q}$, the vortex force can be decomposed as follows:

$$\begin{aligned}
\boldsymbol{F}_{\rho l} &= \rho_\infty \int_\Omega \boldsymbol{q} \times \boldsymbol{\omega} \mathrm{d}v \\
&= \rho_\infty \boldsymbol{U}_\infty \times \int_\Omega \boldsymbol{\omega} \mathrm{d}v + \rho_\infty \int_\Omega \delta\boldsymbol{q} \times \boldsymbol{\omega} \mathrm{d}v \\
&= \rho_\infty \boldsymbol{U}_\infty \times \boldsymbol{\Gamma} - \rho_\infty \int_\Omega \nabla \cdot \left(\delta\boldsymbol{q} \otimes \delta\boldsymbol{q} - \frac{\delta q^2}{2} \boldsymbol{I} \right) \mathrm{d}v \\
&= \rho_\infty \boldsymbol{U}_\infty \times \boldsymbol{\Gamma} - \rho_\infty \oint_{S_e} \left(\delta\boldsymbol{q} \left(\delta\boldsymbol{q} \cdot \boldsymbol{n} \right) - \frac{\delta q^2}{2} \boldsymbol{n} \right) \mathrm{d}S
\end{aligned} \tag{1.3.44}$$

The expression (1.3.44) was already derived by Marongiu *et al.* [81] in 2013. Schmitz [92] described the surface integral as a finite domain viscous correction to the circulation theory. Indeed, he reminded that the velocity perturbation rapidly decreases in the far field such that when S_e retreats to infinity, the terms inside the integral can be neglected. Moreover, when projecting onto the direction perpendicular to the freestream, a perturbation circulation $\delta\Gamma$ may be defined [47, 92]:

$$\delta\Gamma = \frac{1}{U_\infty} \oint_{S_e} \left(w \left(\delta\boldsymbol{q} \cdot \boldsymbol{n} \right) - \frac{\delta q^2}{2} n_z \right) \mathrm{d}S \tag{1.3.45}$$

The integral can be limited to a wake plane W perpendicular to the freestream such that $\boldsymbol{n} = \boldsymbol{e}_x$. In this case, $\delta\Gamma$ reduces to

$$\delta\Gamma = \frac{1}{U_\infty} \int_W uw \mathrm{d}S \tag{1.3.46}$$

and

$$\boldsymbol{F}_{\rho l} \cdot \boldsymbol{e}_z = -\rho_\infty U_\infty \left(\Gamma + \delta\Gamma \right) \tag{1.3.47}$$

as previously found by Schmitz [92]. In a real flow, the momentum loss caused by the presence of the obstacle implies $u \leq 0$. It suggests that $\delta\Gamma$ can be interpreted as a correction to the lift due to the viscosity of the fluid. The presence of w in the expression may be understood as the influence of the downsweep on the actual lift exerted on the body (see Fig.1.4b).

Link with the lifting line theory

In the expression of the vortex force $\boldsymbol{F}_{\rho l}$, the finite domain viscous term provides a correction to the lift and to the drag: this term is fully non-linear. Its projection on the x-axis yields

$$D_i = \boldsymbol{F}_{\rho l} \cdot \boldsymbol{e}_x = \rho_\infty \int_\Omega (v\omega_z - w\omega_y)\,\mathrm{d}v \tag{1.3.48}$$

This expression involves the downsweep w and the sidesweep v (see Fig.1.20). Considering that the control volume Ω is confined to the vortical regions where $\boldsymbol{\omega} \neq \boldsymbol{0}$, assume that w is weakly dependent on x and z and that v is weakly dependent on x and y. It is nothing but a three-dimensional generalization of the asumptions considered by Prandtl in the case of a two-dimensional flow. Therefore it is possible to express the lift-induced drag as follows:

$$D_i = \rho_\infty \int_{-e}^{e} v\Gamma_z \mathrm{d}z - \rho_\infty \int_{-b}^{b} w\Gamma_y \mathrm{d}y \tag{1.3.49}$$

where e is the width of the body, b is its span, $\Gamma_z = \int_S \omega_z \mathrm{d}x\mathrm{d}y$ is the vertical circulation and $\Gamma_y = \int_S \omega_y \mathrm{d}x\mathrm{d}z$ is the transverse circulation. The second term of (1.3.49) appears in several studies [58, 75, 93] but not the first one. In fact, in Prandtl's lifting line theory, the lift-induced drag was linked to the downsweep induced by the generation of transverse vorticity ω_y or bound circulation Γ directly responsible for the lift. In the Lamb-vector-based formulation, the lift-induced drag is actually related to the same downsweep (second term of equation (1.3.49)) along with the sidesweep due to the presence of boundary layers on the sides (wing tips, fuselage, rudder) and hence the production of vertical vorticity ω_z (first term of equation (1.3.49)).

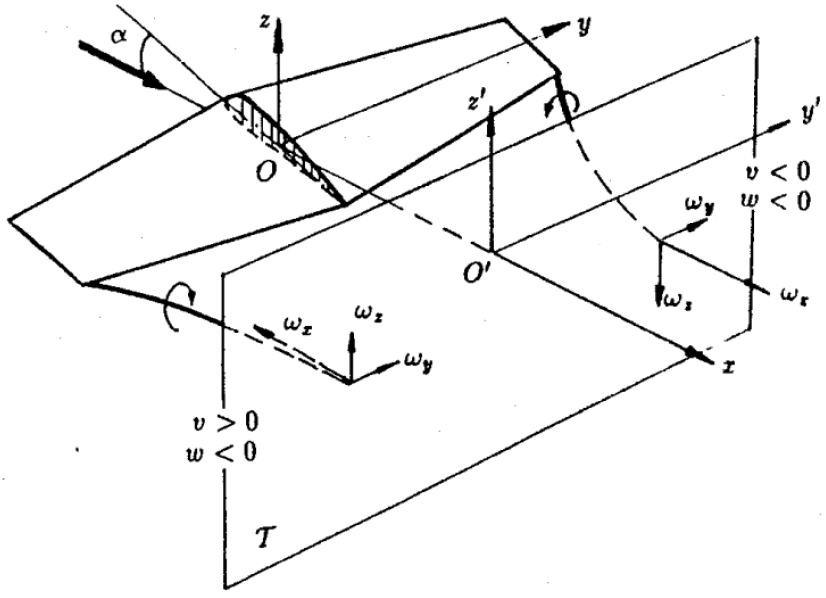

Figure 1.20: Velocities induced by the vertical and transverse vorticity components (adapted from [60])

In (1.3.49), only the transverse vorticity ω_y is involved in the lift whereas the vertical vorticity ω_z produced by the left part of the aircraft is actually compensated by the production on the right part. However, it is possible to show that the term $v\omega_z$ still contributes to the lift-induced drag. Indeed, in Fig.1.20 it is shown that $\omega_z \leq 0$ and $v \leq 0$ for $y \geq 0$ while $\omega_z \geq 0$ and $v \geq 0$ for $y \leq 0$. Therefore $v\omega_z$ is always positive and effectively contributes to the lift-induced drag. It confirms that in three-dimensional flows, not only the downsweep but also the sidesweep is responsible for the drag. It emphasizes the kinematic character of the Lamb vector: it represents

a deviation of the flow perpendicular to the velocity vector and induced by the presence of a vorticity field in shear regions (boundary layers and wakes). Therefore, this deviation of the flow is manifested by the generation of a lift and a vorticity-induced drag.

Link with Betz's and Maskell's wake integrals

In steady incompressible flows, the link between the profile drag integral and Betz's formula was already known [18, 28, 50, 75]. Actually, the Lamb-vector-based force breakdown (1.3.9) is completely equivalent to the force expression which involves the generalized Kutta-Joukowski theorem for predicting the lift, Maskell's formula for the lift-induced drag and Betz's total pressure loss integral for the profile drag. A simple derivation is presented hereafter.

Indeed, if viscous stresses are not negligible, the aerodynamic force can be expressed as follows:

$$\boldsymbol{F} = -\rho_\infty \int_\Omega \boldsymbol{l} \mathrm{d}v - \frac{1}{\mathcal{N}-1} \oint_{S_e} \boldsymbol{r} \times (\boldsymbol{n} \times (\rho_\infty \boldsymbol{l} - \nabla \cdot \boldsymbol{\tau}))\, \mathrm{d}S + \oint_{S_e} \boldsymbol{\tau} \cdot \boldsymbol{n} \mathrm{d}S \tag{1.3.50}$$

The steady incompressible Navier-Stokes equations are

$$\rho_\infty \boldsymbol{l} = -\nabla p - \rho_\infty \nabla \left(\frac{q^2}{2}\right) + \nabla \cdot \boldsymbol{\tau} \quad \Leftrightarrow \quad \rho_\infty \boldsymbol{l} - \nabla \cdot \boldsymbol{\tau} = -\nabla P \tag{1.3.51}$$

where $P = p + \rho_\infty q^2/2$ is the total pressure in incompressible regime. The vortex force $\boldsymbol{F}_{\rho l}$ is then expressed with equation (1.3.44), the total pressure deficit is introduced in the second integral with equation (1.3.51) and the second DMT (A.2) yields

$$\boldsymbol{F} = \rho_\infty \boldsymbol{U}_\infty \times \boldsymbol{\Gamma} - \rho_\infty \oint_{S_e} \left(\delta \boldsymbol{q} \, (\delta \boldsymbol{q} \cdot \boldsymbol{n}) - \frac{\delta q^2}{2} \boldsymbol{n} \right) \mathrm{d}S + \oint_{S_e} (P_\infty - P)\, \boldsymbol{n} \mathrm{d}S + \oint_{S_e} \boldsymbol{\tau} \cdot \boldsymbol{n} \mathrm{d}S \tag{1.3.52}$$

The surface integrations are here limited to the wake plane W with $\boldsymbol{n} = \boldsymbol{e}_x$, provided that the inlet and lateral parts of S_e are located far from the body skin. Indeed, In this case, the projection of $\boldsymbol{F}$ onto the x and z-axes gives

$$L = \underbrace{-\rho_\infty U_\infty \left(\Gamma + \delta\Gamma\right)}_{\text{Generalized KJ theorem}} + \int_W \tau_{xz} \mathrm{d}S \tag{1.3.53}$$

$$D = \underbrace{\frac{1}{2}\rho_\infty \int_W \left(v^2 + w^2 - u^2\right) \mathrm{d}S}_{\text{Maskell's lift-induced drag}} + \underbrace{\int_W \left(P_\infty - P\right) \mathrm{d}S}_{\text{Betz's profile drag}} + \int_W \tau_{xx} \mathrm{d}S \tag{1.3.54}$$

where

$$\boldsymbol{\Gamma} = \oint_{S_e} \boldsymbol{n} \times \delta \boldsymbol{q} \mathrm{d}S = -\Gamma \boldsymbol{e}_y \tag{1.3.55}$$

$$\delta\Gamma = \frac{1}{U_\infty} \int_W uw \mathrm{d}S \tag{1.3.56}$$

In the lift equation, the link with Schmitz's formula [92] is recovered. In equation (1.3.54), Maskell's vortex-induced drag is the same as the one derived in several papers [11, 12, 45, 47] although it is a bit different from the definition (1.2.17) since it contains the square of the streamwise velocity deficit u^2. This equation demonstrates the close relation between the Lamb-vector-based decomposition and former analyses in incompressible flows. The lift is related to the circulation plus a viscous penalty, the lift-induced drag is related to the kinetic energy of the transverse flow, and the profile drag is related to the total pressure losses occuring in the flow. It is important to note that the breakdown introduced by (1.3.54) is applicable in wind-tunnel experiments, as the integrations are performed on the wake plane W downstream of the model.

Chapter summary

A presentation of the main aerodynamic force decomposition methods has been proposed. Thermodynamic methods have proved their capacity to evaluate the profile drag generated by irreversible processes (boundary layers, shocks and wakes). Among these, Destarac and Van der Vooren's formulation definitely appears to be the most robust and advanced method since it provides a breakdown into viscous, wave and lift-induced drag contributions. This model is initially based on the assumption that no trailing vorticity is present in the wake. Yet, the total drag computed by this method is exact whereas former analyses always approximate the flow quantities under particular conditions, thus leading to inevitable errors in the assessment of the total drag. However, Destarac and Van der Vooren's approach is unable to relate the lift-induced drag to its physical sources. Even though its magnitude is evaluated, this contribution is defined by default, after subtracting the viscous and the wave drag from the total drag.

For their part, vortical formulations have proved their ability to evaluate the lift and the lift-induced drag generated by the vortices in the flow. Among these, Maskell's analysis for wake surveys is the most advanced one for predicting the lift-induced drag. Its application has even been extended to compressible flows in several studies. Nevertheless, the vortical formulations presented earlier were all developed assuming restrictive hypotheses: two-dimensional flows, inviscid and/or incompressible flows and small perturbation approximations. Yet, the flow encountered by a high-capacity aircraft in cruise flight is highly compressible and shock waves may also be present on the wings.

The Lamb-vector-based formulation may well be a solution to this problem. In fact, its field of application extends from the incompressible viscous regime to the high-transonic viscous regime. Moreover, the preliminary results are very promising since the formula can decompose the drag into lift-induced and profile contributions, and can also compute the lift. The comparison with the numerical results given by former analyses suggests that the Lamb-vector-based formulation is actually a generalization to compressible viscous flows of the classical vortical formulations. A physical interpretation of the decomposition was made possible by highlighting the mathematical equivalence with the theories of Kutta-Joukowski, Maskell and Betz in incompressible viscous flows. The link with the vortical formulations of Kutta-Joukowski and Maskell comes from a kinematic interpretation of the Lamb vector (through the acceleration of a fluid particle) while the link with the thermodynamic formulation of Betz comes from a dynamic interpretation (through the Navier-Stokes equations). It shows the intricate but remarkable role played by the Lamb vector in fluid mechanics.

However, in spite of those auspicious findings, the Lamb-vector-based decomposition presents sensitivity issues with respect to the location of the reference point chosen for the computation of moments and to the size of the integration domain. Moreover, an equivalent physical interpretation in compressible viscous flows is still lacking. Finally, the possibility to evaluate the wave drag using the Lamb vector and therefore to further decompose the profile drag in viscous and wave contributions remains an open question. For all these reasons, the Lamb-vector-based formulation is not mature enough to be applied as such and to be integrated in industrial calculation chains. This study will therefore focus on the axes of improvement of the formulation. It will first achieve the invariance with respect to the reference point, then identify the role of compressibility in lift and drag and finally introduce a method for extracting the wave drag.

Chapter 2

Study of the Influence of the Flow Symmetries on the Sensitivities of the Lamb-Vector-Based Decomposition

In this chapter, the focus is given to the Lamb-vector-based force decomposition proposed by Mele *et al.* [31, 32, 36]. The first goal is to understand how and why their decomposition varies with a change in the location of the reference point and an increase in the size of the integration domain. As it has been presented in the state-of-the-art, this decomposition is characterized by its sensitivity to those two parameters, which unfortunately undermines its robustness. The second aim is to find out whether the flow symmetries lead to an invariance in the far field.

In the first section, the focus is first given to the sensitivity to the location of the reference point. A theoretical analysis is carried out by proceeding to a shift in the reference point in order to identify the sensitive terms, observe their effects on the decomposition and find a necessary condition for the invariance. Then, the sensitive terms are evaluated with two-dimensional and three-dimensional numerical simulations in order to identify the regions where they are significant and those where they are negligible.

In the second section, the focus is then given to the sensitivity to the size of the integration domain. A theoretical analysis is done by increasing the size of the integration domain in order to describe the transfer occuring between the different terms of the decomposition, find a necessary condition for the invariance and search for an invariant physical quantity. This transfer is later quantified with two-dimensional and three-dimensional numerical simulations in order to determine which terms vary the most and in which flow regions.

In the third section, the aim is to understand how the progressive symmetry properties satisfied by the flow quantities lead to the invariance with respect to the location of the reference point and the size of the integration domain. First of all, two families of symmetries are introduced: the symmetries in the far wake and the symmetries up and downstream of the aircraft. Then, it is shown that the sensitive terms gradually vanish as these far-field symmetries establish.

2.1 Study of the sensitivity to the location of the reference point

So far, the issue of the sensitivity to the location of the reference point was circumvented in several studies [18, 31, 32, 36] by choosing this point on the wake plane W adopted for integration. Unfortunately, it implies to interpolate the flow solution on W, which inevitably leads to errors in the assessment of the total force. Besides, Kang *et al.* [18] noticed this sensitivity on a simple two-dimensional flow. Hence, deliberately prescribing the location of such a point obviously raises the question of the objectiveness and hence the robustness of the force decomposition.

In their study, Kang *et al.* [18] finally concluded that the drag sensitivity to the location of the reference point is not significant as long as the reference point is not chosen too far from the x-axis. Besides, Gao and Wu [94] recently highlighted the invariance of the total aerodynamic force to the location of the reference point but did not focus on the terms of the decomposition. In the present analysis, those observations are confirmed, extended and illustrated on practical test cases.

2.1.1 Identification of the sensitive terms

It is first necessary to identify the terms responsible for the sensitivity to the reference point. The Lamb-vector-based formulation derived by Mele *et al.* [31, 32, 36] is

$$\boldsymbol{F} = \boldsymbol{F}_{\rho l} + \boldsymbol{F}_{m_\rho} + \boldsymbol{F}_{S_e} + \boldsymbol{F}_{\tau} \tag{2.1.1}$$

with

$$\boldsymbol{F}_{\rho l} = -\int_{\Omega} \rho \boldsymbol{l} \mathrm{d}v \tag{2.1.2}$$

$$\boldsymbol{F}_{m_\rho} = \frac{1}{\mathcal{N}-1} \int_{\Omega} \boldsymbol{r} \times \left(\nabla \left(\frac{q^2}{2} \right) \times \nabla \rho \right) \mathrm{d}v \tag{2.1.3}$$

$$\boldsymbol{F}_{S_e} = -\frac{1}{\mathcal{N}-1} \oint_{S_e} \boldsymbol{r} \times (\boldsymbol{n} \times \rho \boldsymbol{l}) \, \mathrm{d}S \tag{2.1.4}$$

$$\boldsymbol{F}_{\tau} = \oint_{S_e} \boldsymbol{\tau} \cdot \boldsymbol{n} \mathrm{d}S + \frac{1}{\mathcal{N}-1} \oint_{S_e} \boldsymbol{r} \times (\boldsymbol{n} \times \nabla \cdot \boldsymbol{\tau}) \, \mathrm{d}S \tag{2.1.5}$$

In high Re flows, $\boldsymbol{F}_{\tau}$ is negligible [28, 84] and the aerodynamic force decomposition proposed by Mele *et al.* [31, 32, 36] is given by

$$L^{\mathrm{Mele}} = \boldsymbol{e}_z \cdot \left(\boldsymbol{F}_{\rho l} + \boldsymbol{F}_{m_\rho} \right) \tag{2.1.6}$$

$$D_i^{\mathrm{Mele}} = \boldsymbol{e}_x \cdot \left(\boldsymbol{F}_{\rho l} + \boldsymbol{F}_{m_\rho} \right) \tag{2.1.7}$$

$$D_P^{\mathrm{Mele}} = \boldsymbol{e}_x \cdot \boldsymbol{F}_{S_e} \tag{2.1.8}$$

In the expression (2.1.1) of the total force, $\boldsymbol{F}_{m_\rho}$, $\boldsymbol{F}_{S_e}$ and $\boldsymbol{F}_{\tau}$ all contain the position vector $\boldsymbol{r}$. It may then explain the sensitivity of these terms to the location of the reference point. The application of the first DMT (A.1) to $\boldsymbol{F}_{m_\rho}$ enables to get an equivalent expression which is more convenient for the analysis to follow:

$$\boldsymbol{F}_{m_\rho} = \int_{\Omega} \frac{q^2}{2} \nabla \rho \mathrm{d}v + \frac{1}{\mathcal{N}-1} \oint_{S_e} \boldsymbol{r} \times \left(\boldsymbol{n} \times \frac{q^2}{2} \nabla \rho \right) \mathrm{d}S \tag{2.1.9}$$

For the sake of exactness, choice is made to keep the term $\boldsymbol{F}_{\tau}$ in this theoretical analysis. In high Re flows however, it is important to keep in mind that $\boldsymbol{F}_{\tau}$ is negligible: it will be the case in the following numerical applications. The cartesian frame remains the same: the coordinates of the flow particles are still measured with respect to the same origin. What changes is the location of the reference point chosen for the computation of moments. In the initial formulation

(2.1.1), the origin of the frame and the reference point of the moments are the same by default. But, if the lever arm $\boldsymbol{r}$ is shifted by a constant vector $\boldsymbol{r}_0$ ($\boldsymbol{r} \to \boldsymbol{r} + \boldsymbol{r}_0$, see Fig.2.1) in (2.1.4), (2.1.5) and (2.1.9), additional terms appear in $\boldsymbol{F}_{m_\rho}$, $\boldsymbol{F}_{S_e}$ and $\boldsymbol{F}_\tau$:

$$\boldsymbol{F}_{m_\rho} = \int_\Omega \frac{q^2}{2}\nabla\rho \mathrm{d}v + \frac{1}{\mathcal{N}-1}\oint_{S_e} \boldsymbol{r} \times \left(\boldsymbol{n} \times \frac{q^2}{2}\nabla\rho\right) \mathrm{d}S + \boldsymbol{r}_0 \times \boldsymbol{R}_{m_\rho} \tag{2.1.10}$$

$$\boldsymbol{F}_{S_e} = -\frac{1}{\mathcal{N}-1}\oint_{S_e} \boldsymbol{r} \times (\boldsymbol{n} \times \rho\boldsymbol{l})\, \mathrm{d}S + \boldsymbol{r}_0 \times \boldsymbol{R}_{S_e} \tag{2.1.11}$$

$$\boldsymbol{F}_\tau = \oint_{S_e} \boldsymbol{\tau} \cdot \boldsymbol{n} \mathrm{d}S + \frac{1}{\mathcal{N}-1}\oint_{S_e} \boldsymbol{r} \times (\boldsymbol{n} \times \nabla \cdot \boldsymbol{\tau})\, \mathrm{d}S + \boldsymbol{r}_0 \times \boldsymbol{R}_\tau \tag{2.1.12}$$

with

$$\boldsymbol{R}_{m_\rho} = \frac{1}{\mathcal{N}-1}\oint_{S_e} \boldsymbol{n} \times \frac{q^2}{2}\nabla\rho \mathrm{d}S \tag{2.1.13}$$

$$\boldsymbol{R}_{S_e} = -\frac{1}{\mathcal{N}-1}\oint_{S_e} \boldsymbol{n} \times \rho\boldsymbol{l} \mathrm{d}S \tag{2.1.14}$$

$$\boldsymbol{R}_\tau = \frac{1}{\mathcal{N}-1}\oint_{S_e} \boldsymbol{n} \times \nabla \cdot \boldsymbol{\tau} \mathrm{d}S \tag{2.1.15}$$

Upon using the curl theorem (A.5), the resulting term $\boldsymbol{R}_{m_\rho}$ can also be expressed with the following volume integral:

$$\boldsymbol{R}_{m_\rho} = \frac{1}{\mathcal{N}-1}\int_\Omega \nabla\left(\frac{q^2}{2}\right) \times \nabla\rho \mathrm{d}v \tag{2.1.16}$$

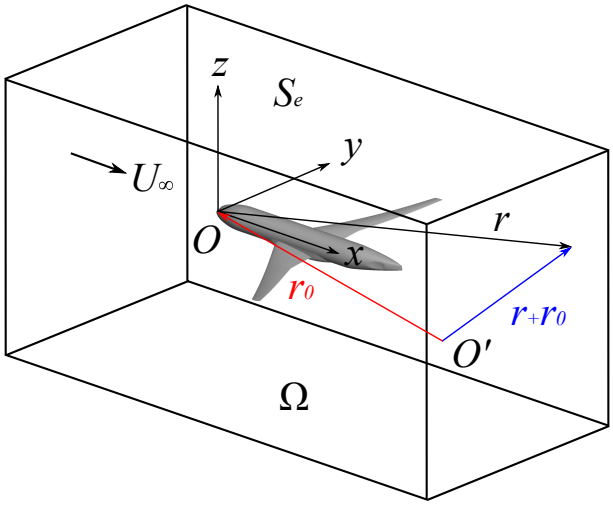

Figure 2.1: Illustration of a change in the reference point

In the expressions of the resulting terms $\boldsymbol{R}_{m_\rho}$, $\boldsymbol{R}_{S_e}$ and $\boldsymbol{R}_\tau$, the integrals are not automatically equal to zero. Consequently, the sensitivity of Mele *et al.*'s force decomposition [31, 32, 36] to the location of the reference point is directly caused by these terms. Moreover, the force contributions $\boldsymbol{F}_{m_\rho}$, $\boldsymbol{F}_{S_e}$ and $\boldsymbol{F}_\tau$ are proportional to the magnitude $\boldsymbol{r}_0$ of the point shift. It means that if the reference point is located close to the origin of the frame (i.e. $||\boldsymbol{r}_0||$ is small), the variations in $\boldsymbol{F}_{m_\rho}$, $\boldsymbol{F}_{S_e}$ and $\boldsymbol{F}_\tau$ are not significant, which confirms Kang *et al.*'s conclusion [18]. On the contrary, if the reference point is located far from the origin of the frame (i.e. $||\boldsymbol{r}_0||$ is big), the variations in $\boldsymbol{F}_{m_\rho}$, $\boldsymbol{F}_{S_e}$ and $\boldsymbol{F}_\tau$ may become so large that the initially proposed decomposition into lift, lift-induced drag and profile drag is totally lost.

It is important to note that $\boldsymbol{F}_\tau$ represents viscous and turbulent stresses, which suggests that it contributes to the profile drag. Therefore, a necessary condition for the invariance of the lift, the lift-induced drag and the profile drag to the location of the reference point is

$$\boldsymbol{R}_{m_\rho} = \boldsymbol{0} \tag{2.1.17a}$$

$$\boldsymbol{R}_{S_e} + \boldsymbol{R}_\tau = \boldsymbol{0} \tag{2.1.17b}$$

In high Re flows, $\boldsymbol{R}_\tau$ is negligible and the condition (2.1.17b) reduces to

$$\boldsymbol{R}_{S_e} = \boldsymbol{0} \tag{2.1.18}$$

2.1.2 Effects on lift and drag contributions

It has been shown that a shift $\boldsymbol{r}_0$ in the location of the reference point gives birth to additional terms which may change the aerodynamic force decomposition. Then, the following analysis will investigate in more details how those additional terms affect the contribution of the various terms to the lift and the drag. By definition, this point shift does not change the magnitude of the total force $\boldsymbol{F}$. Even though this property is self-evident, it is possible to demonstrate it mathematically by analysing the sum of the resulting terms $\boldsymbol{R}_{m_\rho}$, $\boldsymbol{R}_{S_e}$ and $\boldsymbol{R}_\tau$:

$$\boldsymbol{R}_{m_\rho} + \boldsymbol{R}_{S_e} + \boldsymbol{R}_\tau = \frac{1}{\mathcal{N}-1} \oint_{S_e} \boldsymbol{n} \times \left(\nabla \cdot \boldsymbol{\tau} + \frac{q^2}{2} \nabla \rho - \rho \boldsymbol{l} \right) \mathrm{d}S \tag{2.1.19}$$

Then, the steady compressible Navier-Stokes equations can be expressed as follows:

$$\begin{aligned} \rho \boldsymbol{l} + \rho \nabla \left(\frac{q^2}{2} \right) &= -\nabla p + \nabla \cdot \boldsymbol{\tau} \\ \iff \rho \boldsymbol{l} - \frac{q^2}{2} \nabla \rho + \nabla \left(\rho \frac{q^2}{2} \right) &= -\nabla p + \nabla \cdot \boldsymbol{\tau} \\ \iff \nabla \cdot \boldsymbol{\tau} + \frac{q^2}{2} \nabla \rho - \rho \boldsymbol{l} &= -\nabla P \end{aligned} \tag{2.1.20}$$

where $P = p + \rho q^2/2$. Then, using (2.1.20), the sum of the resulting terms (2.1.19) becomes

$$\boldsymbol{R}_{m_\rho} + \boldsymbol{R}_{S_e} + \boldsymbol{R}_\tau = -\frac{1}{\mathcal{N}-1} \oint_{S_e} \boldsymbol{n} \times \nabla P \mathrm{d}S \tag{2.1.21}$$

Here, S_e is a closed surface so $\partial S_e = \varnothing$. Hence, the application of the generalized Stokes theorem (A.6) (see Appendix A) yields

$$\boxed{\boldsymbol{R}_{m_\rho} + \boldsymbol{R}_{S_e} + \boldsymbol{R}_\tau = \boldsymbol{0}} \tag{2.1.22}$$

Therefore it is obvious that the total force $\boldsymbol{F}$ is independent of the location of the reference point.

However, the decomposition of the force $\boldsymbol{F}$ changes with a shift $\boldsymbol{r}_0$. Depending on the direction of this shift (x, y or z-direction), the change undergone by the decomposition is manifested on the drag component, the transverse component or the lift component. Considering first that the shift $\boldsymbol{r}_0$ is exclusively performed in the x-direction, i.e. $\boldsymbol{r}_0 = \begin{pmatrix} x_0 & 0 & 0 \end{pmatrix}^T$, the variation of a contribution, say $\boldsymbol{F}_{S_e}$, is given by

$$\begin{aligned} \boldsymbol{r}_0 \times \boldsymbol{R}_{S_e} &= -\frac{1}{\mathcal{N}-1} \begin{pmatrix} x_0 \\ 0 \\ 0 \end{pmatrix} \times \oint_{S_e} \rho \begin{pmatrix} n_x \\ n_y \\ n_z \end{pmatrix} \times \begin{pmatrix} l_x \\ l_y \\ l_z \end{pmatrix} \mathrm{d}S \\ &= \frac{x_0}{\mathcal{N}-1} \oint_{S_e} \rho \begin{pmatrix} 0 \\ n_x l_y - n_y l_x \\ n_x l_z - n_z l_x \end{pmatrix} \mathrm{d}S \end{aligned} \tag{2.1.23}$$

Therefore, since the x-component of (2.1.23) is zero, a shift in the x-direction has no impact on the drag contribution but may greatly modify the lift and the transverse contributions. This is exactly what was numerically noticed by Kang *et al.* [18] but the lift variations were not significant because the shift in the x-direction was small. Actually, the integral can be limited to the wake plane W where $\boldsymbol{n} = \boldsymbol{e}_x$ since the Lamb vector is zero outside the wake. In this case, (2.1.23) becomes

$$\boldsymbol{r}_0 \times \boldsymbol{R}_{S_e} = \frac{x_0}{\mathcal{N}-1} \int_W \rho \begin{pmatrix} 0 \\ l_y \\ l_z \end{pmatrix} \mathrm{d}S \tag{2.1.24}$$

In the latter expression, nothing suggests that the necessary condition (2.1.18) for the invariance is or will at some point be satisfied since l_y and l_z may remain significant in the wake [28].

Besides, in the case of a shift performed exclusively in the y-direction, i.e. $\boldsymbol{r}_0 = \begin{pmatrix} 0 & y_0 & 0 \end{pmatrix}^T$, the variation of $\boldsymbol{F}_{S_e}$ is given by

$$\begin{aligned} \boldsymbol{r}_0 \times \boldsymbol{R}_{S_e} &= -\frac{1}{\mathcal{N}-1} \begin{pmatrix} 0 \\ y_0 \\ 0 \end{pmatrix} \times \oint_{S_e} \rho \begin{pmatrix} n_x \\ n_y \\ n_z \end{pmatrix} \times \begin{pmatrix} l_x \\ l_y \\ l_z \end{pmatrix} \mathrm{d}S \\ &= \frac{y_0}{\mathcal{N}-1} \oint_{S_e} \rho \begin{pmatrix} n_y l_x - n_x l_y \\ 0 \\ n_y l_z - n_z l_y \end{pmatrix} \mathrm{d}S \end{aligned} \tag{2.1.25}$$

A shift in the y-direction has theoretically no impact on the transverse contribution but may greatly modify the drag and the lift contributions. On W, the variation becomes

$$\boldsymbol{r}_0 \times \boldsymbol{R}_{S_e} = \frac{y_0}{\mathcal{N}-1} \int_W \rho \begin{pmatrix} -l_y \\ 0 \\ 0 \end{pmatrix} \mathrm{d}S \tag{2.1.26}$$

which suggests that in this case, a shift in the y-direction has an impact on the drag contribution only.

Finally, in the case of a shift performed exclusively in the z-direction, i.e. $\boldsymbol{r}_0 = \begin{pmatrix} 0 & 0 & z_0 \end{pmatrix}^T$, the variation of $\boldsymbol{F}_{S_e}$ is given by

$$\begin{aligned} \boldsymbol{r}_0 \times \boldsymbol{R}_{S_e} &= -\frac{1}{\mathcal{N}-1} \begin{pmatrix} 0 \\ 0 \\ z_0 \end{pmatrix} \times \oint_{S_e} \rho \begin{pmatrix} n_x \\ n_y \\ n_z \end{pmatrix} \times \begin{pmatrix} l_x \\ l_y \\ l_z \end{pmatrix} \mathrm{d}S \\ &= \frac{z_0}{\mathcal{N}-1} \oint_{S_e} \rho \begin{pmatrix} n_z l_x - n_x l_z \\ n_z l_y - n_y l_z \\ 0 \end{pmatrix} \mathrm{d}S \end{aligned} \tag{2.1.27}$$

A shift in the z-direction has theoretically no impact on the lift contribution but may greatly modify the drag and the transverse contributions. On W, the variation becomes

$$\boldsymbol{r}_0 \times \boldsymbol{R}_{S_e} = \frac{z_0}{\mathcal{N}-1} \int_W \rho \begin{pmatrix} -l_z \\ 0 \\ 0 \end{pmatrix} \mathrm{d}S \tag{2.1.28}$$

which again suggests that in this case, a shift in the z-direction has an impact on the drag contribution only.

2.1.3 Illustration on practical numerical cases

It has been shown that, depending on the direction of the shift in the location of the reference point, the force decomposition may be impacted primarily on the drag component, the lift

component, the transverse component, or several components at the same time. Therefore, it appears necessary to quantify this impact in practice, in order to identify the regions where the decomposition is the most sensitive, those where it is less and to find out whether invariance is achieved at some point.

From now on, the analysis is restricted to the study of high Re flows such that the contribution of $\boldsymbol{F}_\tau$ and its resulting term $\boldsymbol{R}_\tau$ are negligible. Besides, the plane $y = 0$ being a symmetry plane for the aircraft, the reference point is now shifted in the x and/or z-directions only. The aircraft is assumed to remain in cruise flight, hence the focus is given to the variations in lift and drag contributions only. Therefore, in this case $\boldsymbol{r}_0 = \begin{pmatrix} x_0 & 0 & z_0 \end{pmatrix}^T$. For a given resulting term $\boldsymbol{R} = \begin{pmatrix} R_x & R_y & R_z \end{pmatrix}^T$, the corresponding variation is given by

$$\boldsymbol{r}_0 \times \boldsymbol{R} = \begin{pmatrix} x_0 \\ 0 \\ z_0 \end{pmatrix} \times \begin{pmatrix} R_x \\ R_y \\ R_z \end{pmatrix} = \begin{pmatrix} -z_0 R_y \\ z_0 R_x - x_0 R_z \\ x_0 R_y \end{pmatrix} \tag{2.1.29}$$

In practice the shifts in the location of the reference point are carried out in the body-fixed frame $\boldsymbol{e}_X, \boldsymbol{e}_Y, \boldsymbol{e}_Z$ with

$$\begin{pmatrix} \boldsymbol{e}_X \\ \boldsymbol{e}_Y \\ \boldsymbol{e}_Z \end{pmatrix} = \begin{pmatrix} \cos(\alpha) & 0 & -\sin(\alpha) \\ 0 & 1 & 0 \\ \sin(\alpha) & 0 & \cos(\alpha) \end{pmatrix} \begin{pmatrix} \boldsymbol{e}_x \\ \boldsymbol{e}_y \\ \boldsymbol{e}_z \end{pmatrix} \tag{2.1.30}$$

where α is the angle of attack of the aircraft. If the reference point is shifted in the X-direction by X_0, it is equivalent to a shift $X_0 \cos(\alpha)$ in the x-direction plus a shift $-X_0 \sin(\alpha)$ in the z-direction. If the reference point is now shifted in the Z-direction by Z_0, it is equivalent to a shift $Z_0 \sin(\alpha)$ in the x-direction plus a shift $Z_0 \cos(\alpha)$ in the z-direction.

According to (2.1.29), the variations in lift and drag entailed by a shift in the x and/or z-directions are proportional to R_y, i.e. the y-component of the resulting term of the force contribution. R_y is indeed not equal to zero: the vector resulting from the cross product between the unit normal $\boldsymbol{n}$ and the physical quantities has a nonzero y-component. In the following, the evolutions of $R_{S_e,y}$ and $R_{m_\rho,y}$, the y-components of the resulting terms $\boldsymbol{R}_{S_e}$ and $\boldsymbol{R}_{m_\rho}$, are plotted with respect to the size of the integration domain in the case of the OAT15A airfoil and the NASA CRM (see the convergence in Appendix F).

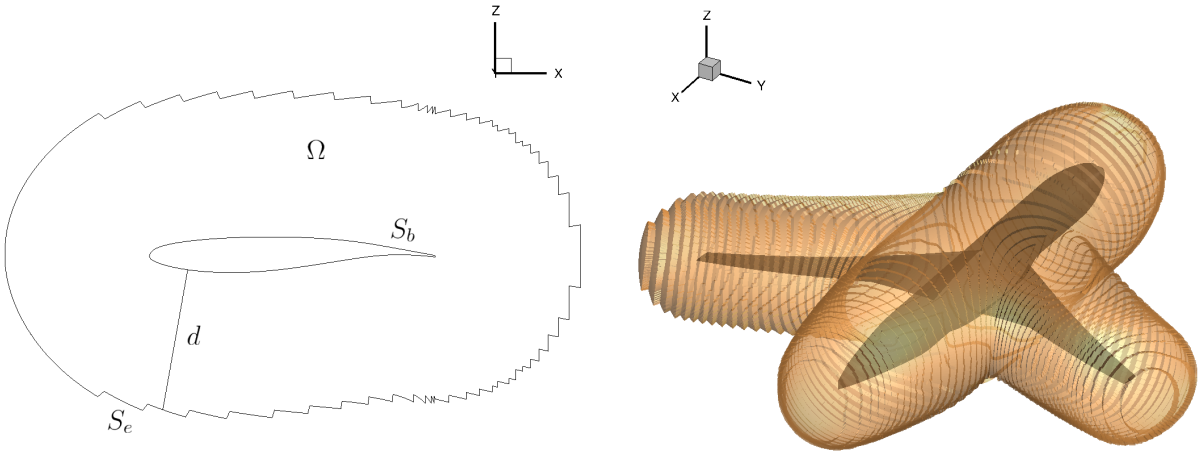

(a) OAT15A airfoil (b) NASA Common Research Model

Figure 2.2: Definition of the size integration domain Ω by the distance d between S_b and S_e

The size of the integration domain is changed in practice by increasing or decreasing the distance to chord ratio d/c (airfoil configurations) or d/c_{ref} (wing and wing-body configurations)

between the cells located on S_e and those on S_b: d is the distance (see Fig.2.2), c is the chord and c_{ref} is the mean aerodynamic chord.

The evolutions on the OAT15A airfoil are plotted in Figs.2.3 and 2.4. Although the evolution of $R_{S_e,y}$ is characterized by a peak at $d/c = 6$ due to grid inaccuracies, it seems that the resulting term tends to zero when the size of the integration domain is increased. As seen from (2.1.13) and (2.1.16), $R_{m_\rho,y}$ can be expressed with a volume integral or a surface integral. Again, some discrepancies due to the grid can be noticed around $d/c = 2$ although both expressions are practically equivalent. Like $R_{S_e,y}$, $R_{m_\rho,y}$ tends to zero in the far field of the airfoil.

The evolutions on the NASA CRM are plotted in Figs.2.5 and 2.6. Like in the two-dimensional case, $R_{S_e,y}$ decreases and seems to vanish in the far field. Regarding $R_{m_\rho,y}$, the two equivalent expressions do not yield the same value although they both become constant in the far field. Only the surface integral expression of (2.1.13) seems to tend to zero as the size of the integration domain is increased. The gap between the two expressions may be caused by numerical errors in the assessment of the volume integral since it requires to compute several times the gradient of the flow quantities.

In order to better appreciate the sensitivity of Mele *et al.*'s decomposition [31, 32, 36] to the location of the reference point, choice was made to perform great shifts, of the order of 25 to 50 reference-chord lengths with respect to the origin of the frame. Figs.2.7 to 2.10 display the evolution of the lift and drag components of $\boldsymbol{F}_{S_e}$ and $\boldsymbol{F}_{m_\rho}$ on the OAT15A airfoil where

$$C_{L_{S_e}} = \frac{2\boldsymbol{F}_{S_e} \cdot \boldsymbol{e}_z}{\rho_\infty U_\infty^2 S} \tag{2.1.31a}$$

$$C_{D_{S_e}} = \frac{2\boldsymbol{F}_{S_e} \cdot \boldsymbol{e}_x}{\rho_\infty U_\infty^2 S} \tag{2.1.31b}$$

and

$$C_{L_{m_\rho}} = \frac{2\boldsymbol{F}_{m_\rho} \cdot \boldsymbol{e}_z}{\rho_\infty U_\infty^2 S} \tag{2.1.32a}$$

$$C_{D_{m_\rho}} = \frac{2\boldsymbol{F}_{m_\rho} \cdot \boldsymbol{e}_x}{\rho_\infty U_\infty^2 S} \tag{2.1.32b}$$

Figs.2.11 to 2.14 show the same quantities in the case of the NASA CRM. It is clear that when the shift in the location of the reference point is performed in the X-direction, the lift component is much more impacted than the drag component. On the contrary, when the shift is performed in the Z-direction, the drag component is much more impacted than the lift component. Actually, a shift in the Z-direction can entail great variations in drag contributions, up to more than 80 drag counts (1 drag count is equivalent to a 10^{-4} increment in the drag coefficient) in the case of $C_{D_{S_e}}$ on the OAT15A airfoil (see Fig.2.7b).

It can also be noticed that $\boldsymbol{F}_{S_e}$ is much more sensitive than $\boldsymbol{F}_{m_\rho}$: it comes from the fact that $R_{S_e,y} \gg R_{m_\rho,y}$ as seen in Figs.2.3 to 2.6. In all the charts, it is obvious that the regions of the flow where the sensitivity to the location of the reference point is the greatest are the regions close to the airfoil and the aircraft, i.e. the near field. Indeed, it corresponds to the region where the resulting terms $R_{S_e,y}$ and $R_{m_\rho,y}$ are still significant. When the size of the integration domain is increased, i.e. S_e extends further away from S_b, this sensitivity is weaker, the gap between the curves tends to zero and the force contributions become invariant in the far field. In fact, it corresponds to the region where $R_{S_e,y}$ and $R_{m_\rho,y}$ tend to zero and where the necessary condition (2.1.17) is satisfied. It means that something may happen in the far field which eliminates the resulting terms and hence the sensitivity: it will be shown in section 2.3 that the invariance is the result of the symmetries which progressively establish in the flow.

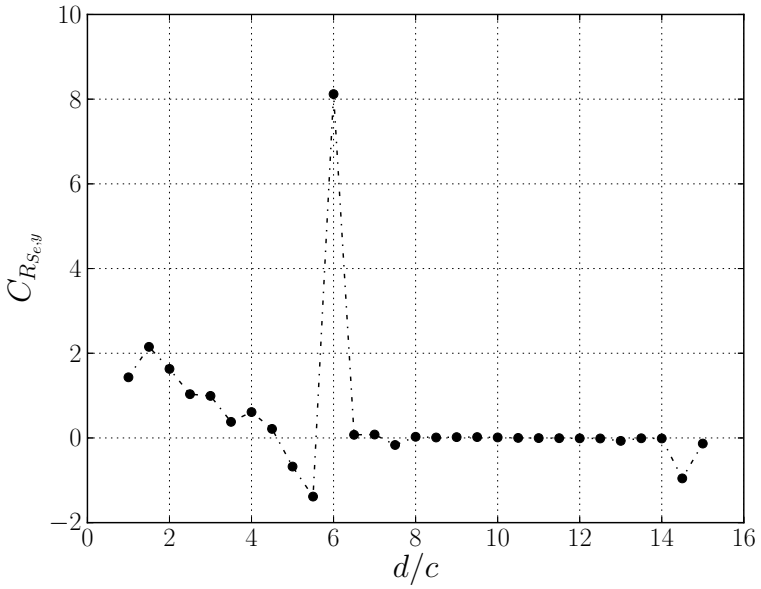

Figure 2.3: Evolution of $C_{R_{S_e,y}} = 2R_{S_e,y}/\rho_\infty U_\infty^2 S$ with respect to the size of the integration domain on the OAT15A airfoil, $M_\infty = 0.724$, $Re = 3 \times 10^6$, $\alpha = 1.15°$

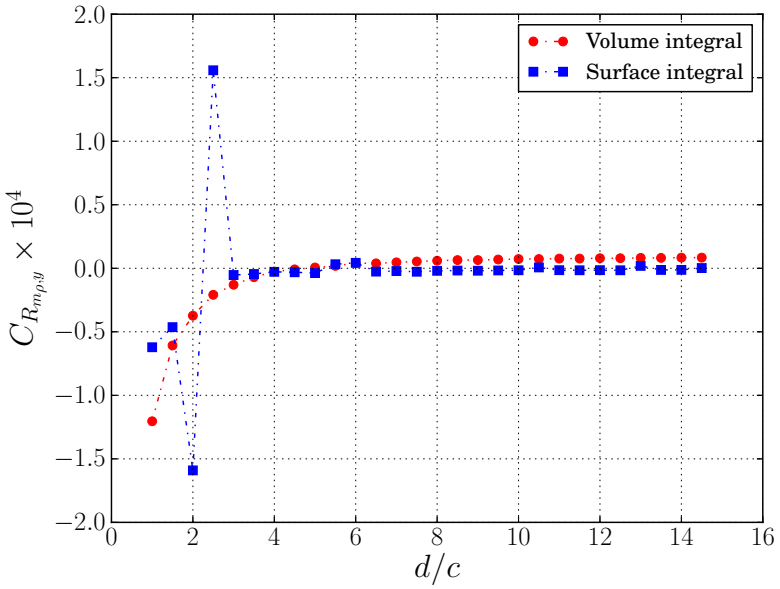

Figure 2.4: Evolution of $C_{R_{m_\rho,y}} = 2R_{m_\rho,y}/\rho_\infty U_\infty^2 S$ with respect to the size of the integration domain on the OAT15A airfoil, $M_\infty = 0.85$, $Re = 3 \times 10^6$, $\alpha = 1.15°$

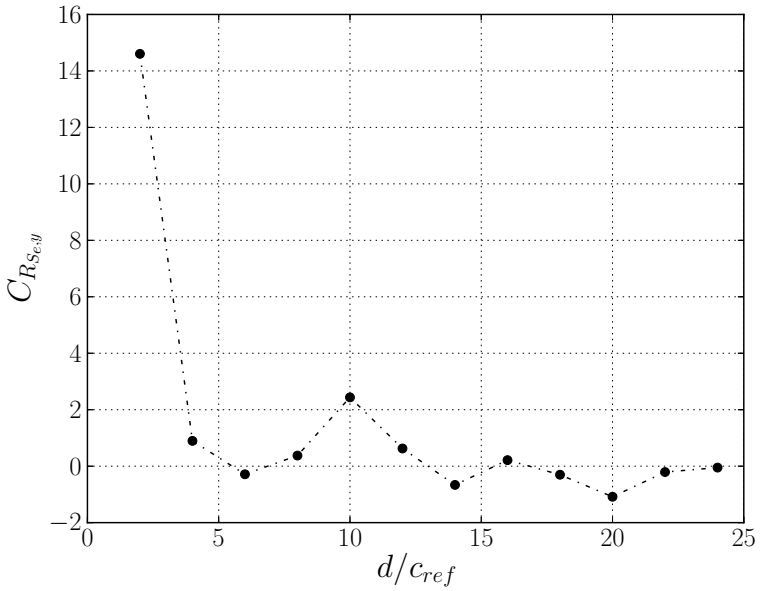

Figure 2.5: Evolution of $C_{R_{S_e,y}} = 2R_{S_e,y}/\rho_\infty U_\infty^2 S$ with respect to the size of the integration domain on the NASA CRM, $M_\infty = 0.85$, $Re = 5 \times 10^6$, $C_L \approx 0.5$

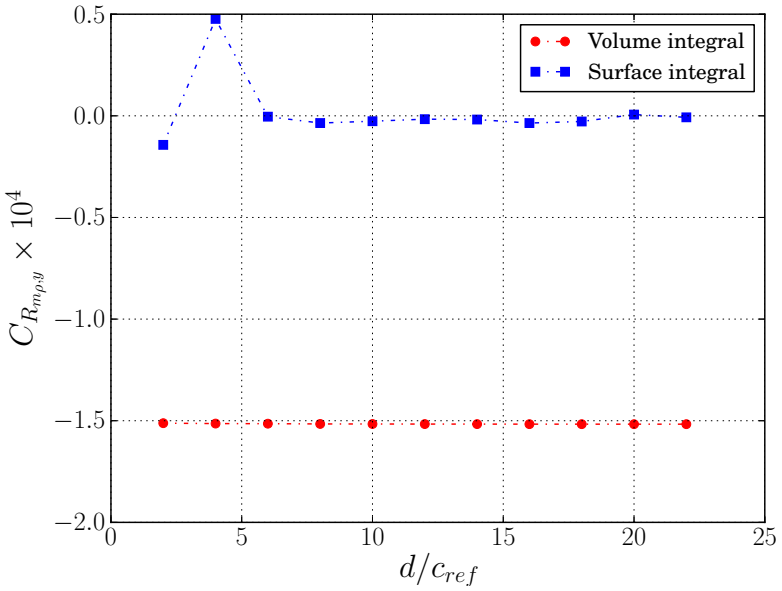

Figure 2.6: Evolution of $C_{R_{m_\rho,y}} = 2R_{m_\rho,y}/\rho_\infty U_\infty^2 S$ with respect to the size of the integration domain on the NASA CRM, $M_\infty = 0.85$, $Re = 5 \times 10^6$, $C_L \approx 0.5$

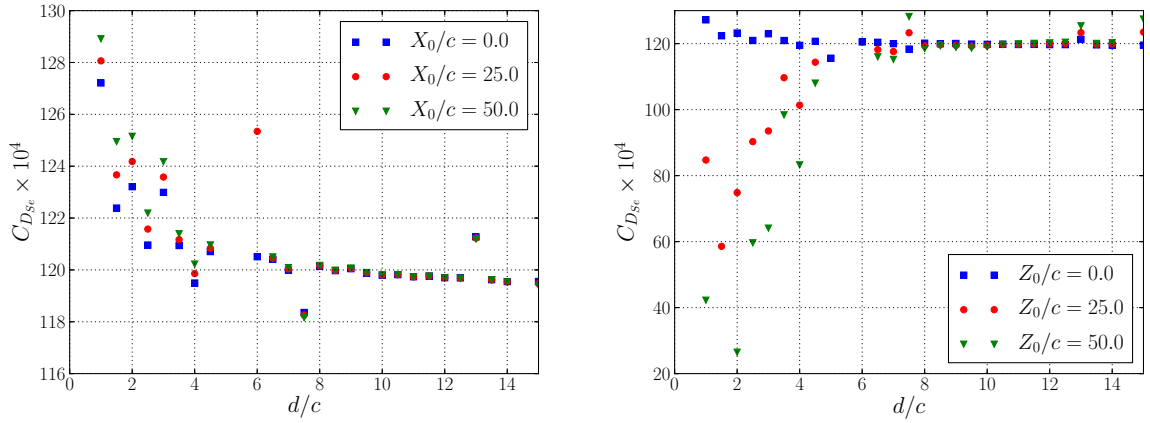

(a) $X \to X + X_0$ (b) $Z \to Z + Z_0$

Figure 2.7: Sensitivity of $C_{D_{S_e}}$ on the OAT15A airfoil, $M_\infty = 0.724$, $Re = 3 \times 10^6$, $\alpha = 1.15°$

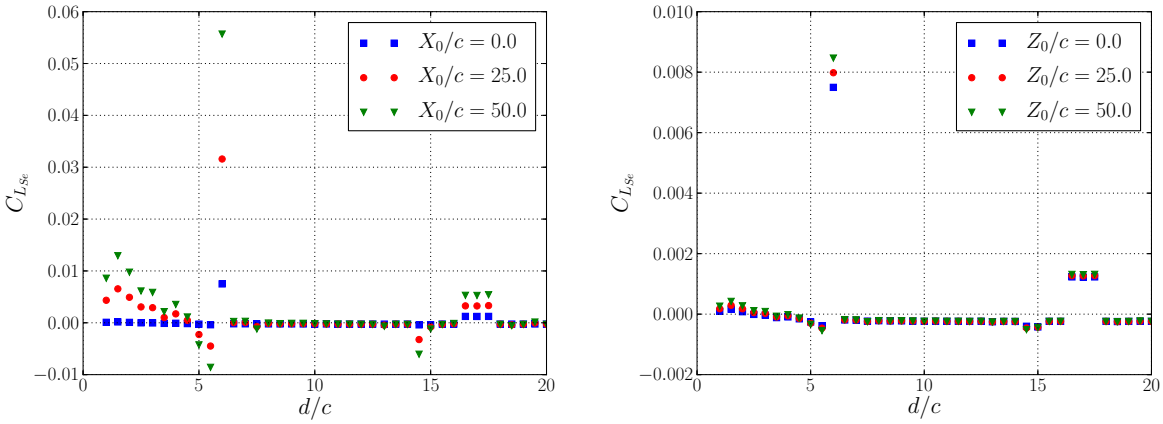

(a) $X \to X + X_0$ (b) $Z \to Z + Z_0$

Figure 2.8: Sensitivity of $C_{L_{S_e}}$ on the OAT15A airfoil, $M_\infty = 0.724$, $Re = 3 \times 10^6$, $\alpha = 1.15°$

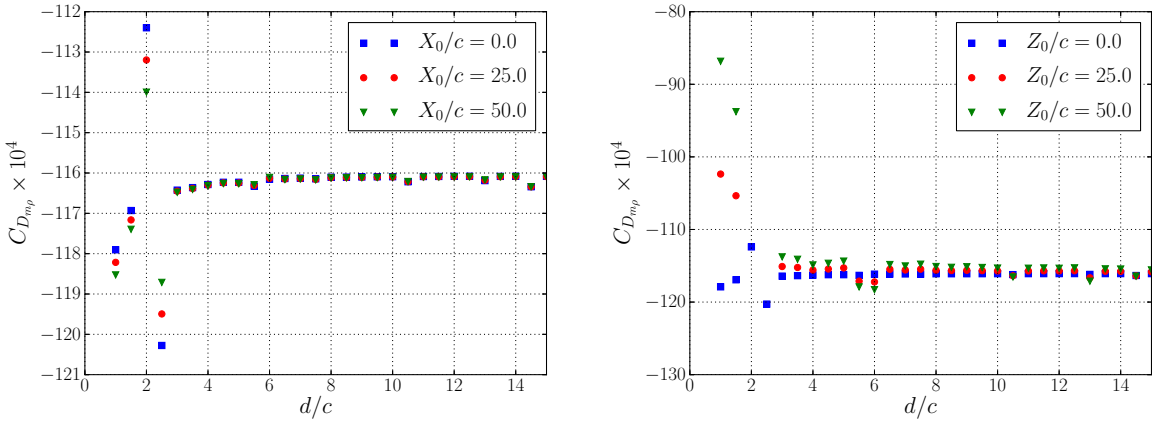

(a) $X \to X + X_0$ (b) $Z \to Z + Z_0$

Figure 2.9: Sensitivity of $C_{D_{m_\rho}}$ on the OAT15A airfoil, $M_\infty = 0.724$, $Re = 3 \times 10^6$, $\alpha = 1.15°$

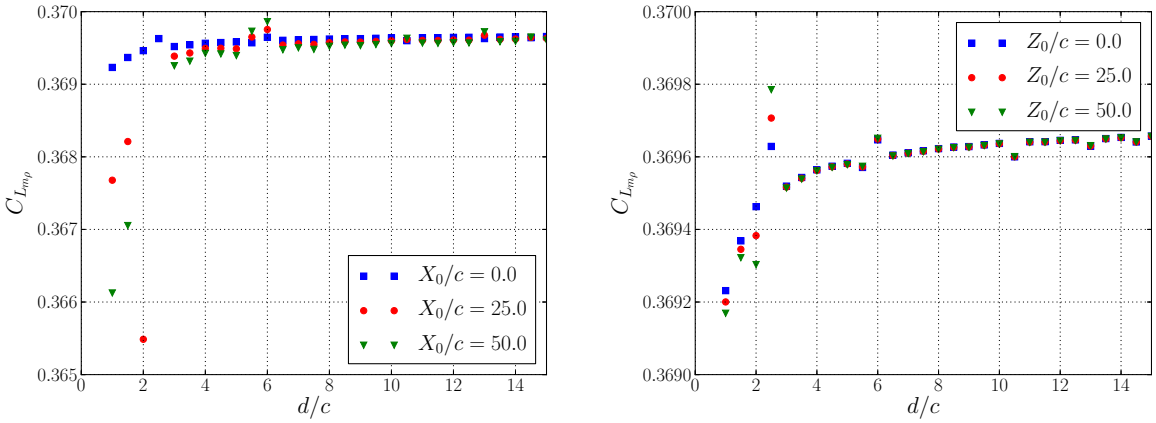

(a) $X \to X + X_0$ (b) $Z \to Z + Z_0$

Figure 2.10: Sensitivity of $C_{L_{m_\rho}}$ on the OAT15A airfoil, $M_\infty = 0.724$, $Re = 3 \times 10^6$, $\alpha = 1.15°$

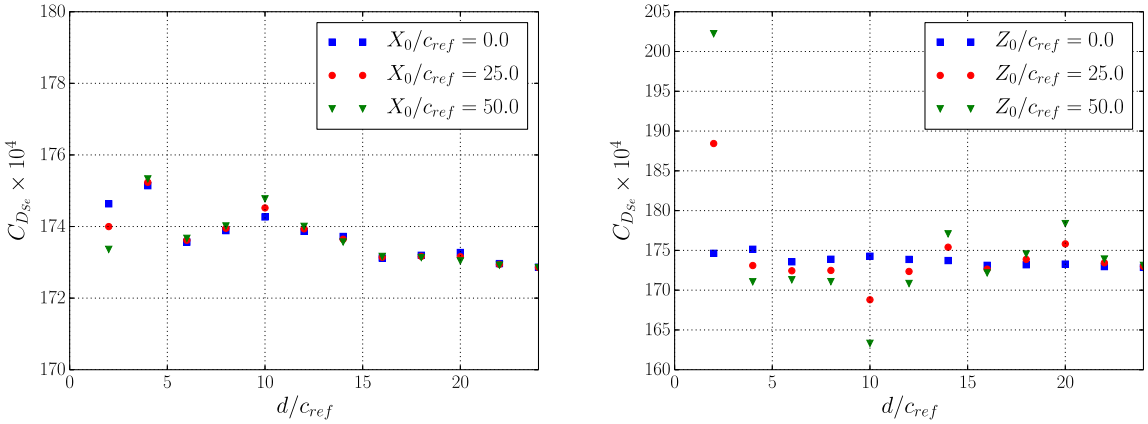

(a) $X \to X + X_0$ (b) $Z \to Z + Z_0$

Figure 2.11: Sensitivity of $C_{D_{S_e}}$ on the NASA CRM, $M_\infty = 0.85$, $Re = 5 \times 10^6$, $C_L \approx 0.5$

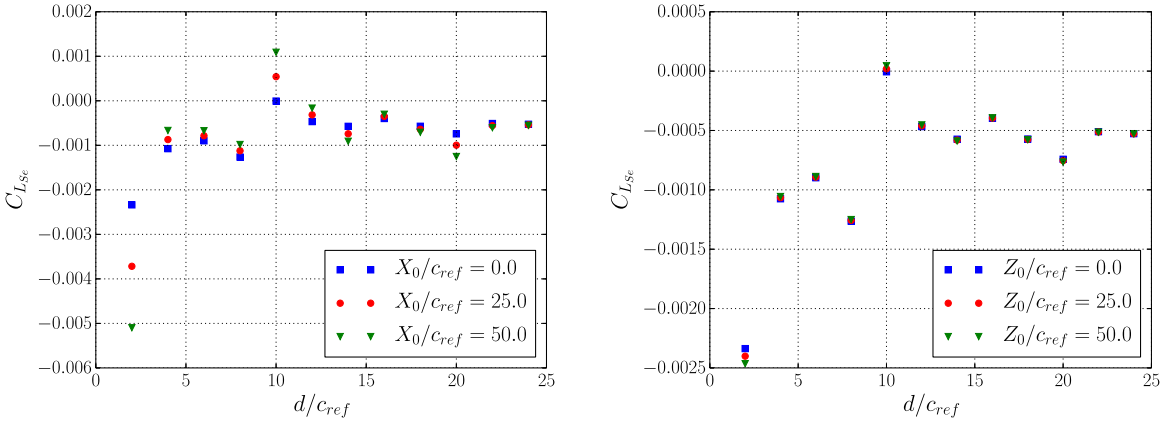

(a) $X \to X + X_0$ (b) $Z \to Z + Z_0$

Figure 2.12: Sensitivity of $C_{L_{S_e}}$ on the NASA CRM, $M_\infty = 0.85$, $Re = 5 \times 10^6$, $C_L \approx 0.5$

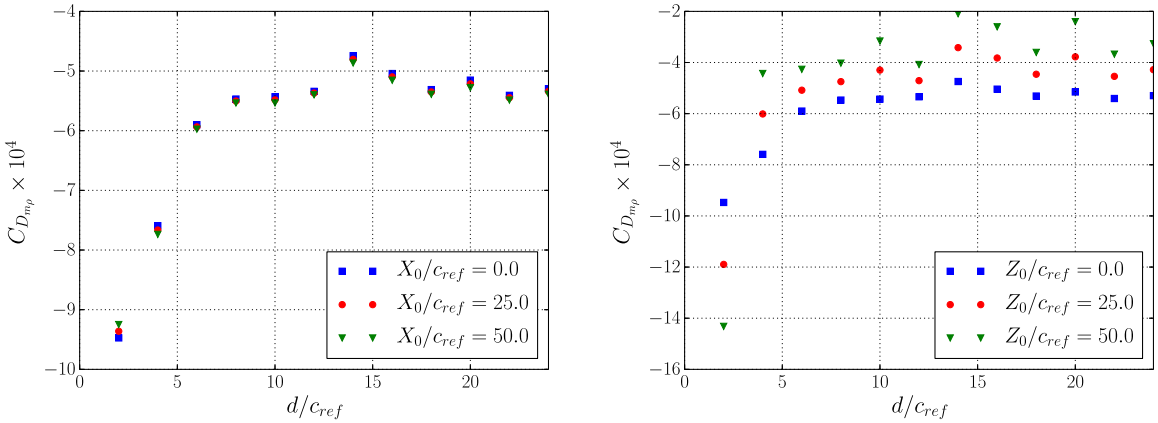

(a) $X \to X + X_0$ (b) $Z \to Z + Z_0$

Figure 2.13: Sensitivity of $C_{D_{m_\rho}}$ on the NASA CRM, $M_\infty = 0.85$, $Re = 5 \times 10^6$, $C_L \approx 0.5$

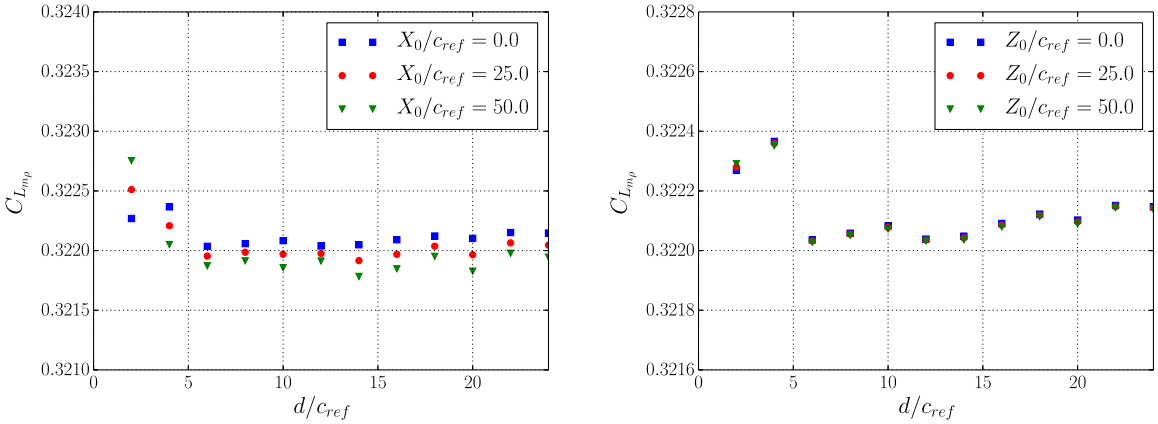

(a) $X \to X + X_0$ (b) $Z \to Z + Z_0$

Figure 2.14: Sensitivity of $C_{L_{m_\rho}}$ on the NASA CRM, $M_\infty = 0.85$, $Re = 5 \times 10^6$, $C_L \approx 0.5$

2.2 Study of the sensitivity to the size of the integration domain

In this section, the focus is this time given to the sensitivity of Mele *et al.*'s force decomposition [31, 32, 36] to the size of the integration domain for a fixed reference point. This sensitivity may undermine the robustness of the decomposition since the choice of the integration domain may be different from one case to another. This feature has been noticed in several studies [18, 32, 81] but seldom put into equation. Only Zou *et al.* [85] managed to theoretically investigate the physics responsible for the sensitivity, but their study was restricted to the case of incompressible flows.

In the present analysis, a Lamb-vector-based momentum balance is performed in order to emphasize the transfer between the various force contributions. Then, another analysis is conducted in order to find a physical quantity which does not depend on the size of the integration domain. Finally, the transfer between the various force contributions is quantified with the help of practical test cases in order to identify which terms are the most sensitive and where they become invariant.

2.2.1 Transfer between the terms of the decomposition

To investigate the sensitivity of Mele *et al.*'s force decomposition to the choice of the integration domain, it is necessary to evaluate the variations in the lift and drag decompositions induced by an increase in the size of this domain. Let Ω^* be the integration domain of increased size (delimited by the solid line in Fig.2.15), S_e^* its external surface and $\Delta\Omega = \Omega^* \setminus \Omega$ the volume extension (delimited by the dotted line and the solid line in Fig.2.15).

By definition, the total aerodynamic force must be independent of the size of the integration domain and can be expressed in Ω or Ω^*. Denoting $\boldsymbol{F}^*_{\rho l}$, $\boldsymbol{F}^*_{m_\rho}$, $\boldsymbol{F}^*_{S_e}$ and $\boldsymbol{F}^*_{\tau}$ the force contributions evaluated in Ω^*, it is possible to express the total aerodynamic force $\boldsymbol{F}$ as follows:

$$\boldsymbol{F} = \boldsymbol{F}^*_{\rho l} + \boldsymbol{F}^*_{m_\rho} + \boldsymbol{F}^*_{S_e} + \boldsymbol{F}^*_{\tau} \tag{2.2.1}$$

with

$$\boldsymbol{F}^*_{\rho l} = -\int_{\Omega^*} \rho \boldsymbol{l} \mathrm{d}v \tag{2.2.2}$$

$$\boldsymbol{F}^*_{m_\rho} = \frac{1}{\mathcal{N}-1}\int_{\Omega^*} \boldsymbol{r} \times \left(\nabla\left(\frac{q^2}{2}\right) \times \nabla\rho\right) \mathrm{d}v \tag{2.2.3}$$

$$\boldsymbol{F}^*_{S_e} = -\frac{1}{\mathcal{N}-1}\oint_{S_e^*} \boldsymbol{r} \times (\boldsymbol{n}^* \times \rho\boldsymbol{l})\, \mathrm{d}S \tag{2.2.4}$$

$$\boldsymbol{F}^*_{\tau} = \oint_{S_e^*} \boldsymbol{\tau}\cdot\boldsymbol{n}^* \mathrm{d}S + \frac{1}{\mathcal{N}-1}\oint_{S_e^*} \boldsymbol{r} \times (\boldsymbol{n}^* \times \nabla\cdot\boldsymbol{\tau})\, \mathrm{d}S \tag{2.2.5}$$

Again, the term $\boldsymbol{F}_\tau$ (respectively $\boldsymbol{F}^*_\tau$) comes from viscous and turbulent stresses and is therefore added to $\boldsymbol{F}_{S_e}$ (respectively $\boldsymbol{F}^*_{S_e}$) in the profile drag contribution. Denoting

$$\Delta\boldsymbol{F}_{\rho l} = \boldsymbol{F}^*_{\rho l} - \boldsymbol{F}_{\rho l} \tag{2.2.6}$$

$$\Delta\boldsymbol{F}_{m_\rho} = \boldsymbol{F}^*_{m_\rho} - \boldsymbol{F}_{m_\rho} \tag{2.2.7}$$

$$\Delta\boldsymbol{F}_{S_e} = \boldsymbol{F}^*_{S_e} - \boldsymbol{F}_{S_e} \tag{2.2.8}$$

$$\Delta\boldsymbol{F}_{\tau} = \boldsymbol{F}^*_{\tau} - \boldsymbol{F}_{\tau} \tag{2.2.9}$$

the variation in $\boldsymbol{F}_{S_e} + \boldsymbol{F}_\tau$ induced by a change in the size of the integration domain is given by

$$\begin{aligned}\Delta\boldsymbol{F}_{S_e} + \Delta\boldsymbol{F}_{\tau} = &\frac{1}{\mathcal{N}-1}\oint_{S_e^*} \boldsymbol{r} \times (\boldsymbol{n}^* \times (\nabla\cdot\boldsymbol{\tau} - \rho\boldsymbol{l}))\, \mathrm{d}S \\ &- \frac{1}{\mathcal{N}-1}\oint_{S_e} \boldsymbol{r} \times (\boldsymbol{n} \times (\nabla\cdot\boldsymbol{\tau} - \rho\boldsymbol{l}))\, \mathrm{d}S + \oint_{S_e^*} \boldsymbol{\tau}\cdot\boldsymbol{n}^* \mathrm{d}S - \oint_{S_e} \boldsymbol{\tau}\cdot\boldsymbol{n} \mathrm{d}S\end{aligned} \tag{2.2.10}$$

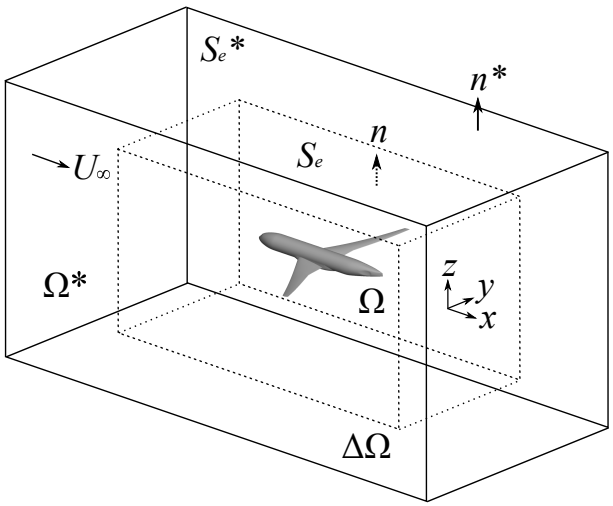

Figure 2.15: Illustration of a change in the size of the integration domain

By applying the first DMT (A.1) to the first line of (2.2.10) and the Gauss theorem (A.5) to the second line, $\Delta \boldsymbol{F}_{S_e} + \Delta \boldsymbol{F}_\tau$ can be expressed with volume integrals on $\Delta\Omega$:

$$\begin{aligned} \Delta \boldsymbol{F}_{S_e} + \Delta \boldsymbol{F}_\tau = &- \int_{\Delta\Omega} (\nabla \cdot \boldsymbol{\tau} - \rho \boldsymbol{l}) \, \mathrm{d}v + \int_{\Delta\Omega} \nabla \cdot \boldsymbol{\tau} \mathrm{d}v \\ &+ \frac{1}{\mathcal{N}-1} \int_{\Delta\Omega} \boldsymbol{r} \times (\nabla \times (\nabla \cdot \boldsymbol{\tau} - \rho \boldsymbol{l})) \, \mathrm{d}v \end{aligned} \tag{2.2.11}$$

The first line of (2.2.11) simply corresponds to $-\Delta \boldsymbol{F}_{\rho l}$. In the second line, reminding that

$$\nabla \times \nabla P = \boldsymbol{0}$$

$-\frac{q^2}{2}\nabla\rho$ can be introduced in place of $\nabla \cdot \boldsymbol{\tau} - \rho \boldsymbol{l}$ by using the steady Navier-Stokes equations (2.1.20):

$$\Delta \boldsymbol{F}_{S_e} + \Delta \boldsymbol{F}_\tau = \int_{\Delta\Omega} \rho \boldsymbol{l} \mathrm{d}v - \frac{1}{\mathcal{N}-1} \int_{\Delta\Omega} \boldsymbol{r} \times \left(\nabla \left(\frac{q^2}{2} \right) \times \nabla \rho \right) \mathrm{d}v \tag{2.2.12}$$

The latter equation then emphasizes the transfer between $\boldsymbol{F}_{S_e} + \boldsymbol{F}_\tau$ and $\boldsymbol{F}_{\rho l} + \boldsymbol{F}_{m_\rho}$ when the size of the integration domain is changed:

$$\boxed{\Delta \boldsymbol{F}_{S_e} + \Delta \boldsymbol{F}_\tau = -\Delta \boldsymbol{F}_{\rho l} - \Delta \boldsymbol{F}_{m_\rho}} \tag{2.2.13}$$

Relation (2.2.13) analytically confirms the invariance of the total aerodynamic force $\boldsymbol{F}$ to the size of the integration domain but clearly shows that the breakdown proposed by Mele *et al.* [31, 32] is sensitive as long as the contributions $\Delta \boldsymbol{F}_{\rho l}$ and $\Delta \boldsymbol{F}_{m_\rho}$ are not equal to zero. Hence, a necessary condition for the invariance of Mele *et al.*'s decomposition [31, 32, 36] is

$$\Delta \boldsymbol{F}_{\rho l} + \Delta \boldsymbol{F}_{m_\rho} = \boldsymbol{0} \tag{2.2.14}$$

2.2.2 Search for an invariant physical quantity

Unfortunately, this necessary condition may not be satisfied in the near field since the flow quantities can still vary a lot in this region. Therefore, it would be desirable to find a physical quantity which remains constant whatever the location of S_e and from which one could possibly define a domain-invariant force decomposition. To do so, it is necessary to transform the volume integrals of (2.2.12) into surface integrals in order to find which quantity is conserved from S_e to S_e^*.

The application of the first DMT (A.1) to the second volume integral of (2.2.12) yields

$$\Delta \boldsymbol{F}_{S_e} + \Delta \boldsymbol{F}_{\tau} = \int_{\Delta\Omega} \left(\rho \boldsymbol{l} - \frac{q^2}{2} \nabla \rho \right) \mathrm{d}v + \frac{1}{\mathcal{N}-1} \oint_{S_e} \boldsymbol{r} \times \left(\boldsymbol{n} \times \frac{q^2}{2} \nabla \rho \right) \mathrm{d}S - \frac{1}{\mathcal{N}-1} \oint_{S_e^*} \boldsymbol{r} \times \left(\boldsymbol{n}^* \times \frac{q^2}{2} \nabla \rho \right) \mathrm{d}S \tag{2.2.15}$$

where the + sign in front of the surface integral in the first line comes from the fact that $\boldsymbol{n}$ is the unit normal pointing outside Ω. Then, by using the relation

$$\rho \boldsymbol{l} - \frac{q^2}{2} \nabla \rho = \nabla \cdot \left(\rho \boldsymbol{q} \otimes \boldsymbol{q} - \rho \frac{q^2}{2} \boldsymbol{I} \right)$$

the volume integral of (2.2.15) can be transformed into surface integrals on S_e and S_e^*:

$$\Delta \boldsymbol{F}_{S_e} + \Delta \boldsymbol{F}_{\tau} = \oint_{S_e^*} \rho \boldsymbol{q} \left(\boldsymbol{q} \cdot \boldsymbol{n}^* \right) \mathrm{d}S - \oint_{S_e^*} \rho \frac{q^2}{2} \boldsymbol{n}^* \mathrm{d}S - \frac{1}{\mathcal{N}-1} \oint_{S_e^*} \boldsymbol{r} \times \left(\boldsymbol{n}^* \times \frac{q^2}{2} \nabla \rho \right) \mathrm{d}S - \oint_{S_e} \rho \boldsymbol{q} \left(\boldsymbol{q} \cdot \boldsymbol{n} \right) \mathrm{d}S + \oint_{S_e} \rho \frac{q^2}{2} \boldsymbol{n} \mathrm{d}S + \frac{1}{\mathcal{N}-1} \oint_{S_e} \boldsymbol{r} \times \left(\boldsymbol{n} \times \frac{q^2}{2} \nabla \rho \right) \mathrm{d}S \tag{2.2.16}$$

Upon applying the second DMT (A.2), it is possible to show that

$$\oint_{S_e} \rho \frac{q^2}{2} \boldsymbol{n} \mathrm{d}S + \frac{1}{\mathcal{N}-1} \oint_{S_e} \boldsymbol{r} \times \left(\boldsymbol{n} \times \frac{q^2}{2} \nabla \rho \right) \mathrm{d}S = -\frac{1}{\mathcal{N}-1} \oint_{S_e} \boldsymbol{r} \times \left(\boldsymbol{n} \times \rho \nabla \left(\frac{q^2}{2} \right) \right) \mathrm{d}S \tag{2.2.17}$$

and $\Delta \boldsymbol{F}_{S_e} + \Delta \boldsymbol{F}_{\tau}$ can be simplified as follows:

$$\Delta \boldsymbol{F}_{S_e} + \Delta \boldsymbol{F}_{\tau} = \oint_{S_e^*} \rho \boldsymbol{q} \left(\boldsymbol{q} \cdot \boldsymbol{n}^* \right) \mathrm{d}S + \frac{1}{\mathcal{N}-1} \oint_{S_e^*} \boldsymbol{r} \times \left(\boldsymbol{n}^* \times \rho \nabla \left(\frac{q^2}{2} \right) \right) \mathrm{d}S - \oint_{S_e} \rho \boldsymbol{q} \left(\boldsymbol{q} \cdot \boldsymbol{n} \right) \mathrm{d}S - \frac{1}{\mathcal{N}-1} \oint_{S_e} \boldsymbol{r} \times \left(\boldsymbol{n} \times \rho \nabla \left(\frac{q^2}{2} \right) \right) \mathrm{d}S \tag{2.2.18}$$

The last step of the demonstration consists in replacing $\Delta \boldsymbol{F}_{S_e} + \Delta \boldsymbol{F}_{\tau}$ by its initial expression (2.2.10). The integrals on S_e^* are moved to the left-hand side of the equal sign and those on S_e are moved to the right-hand side:

$$\begin{aligned} &\oint_{S_e^*} \left[-\rho \boldsymbol{q} \left(\boldsymbol{q} \cdot \boldsymbol{n}^* \right) + \frac{\boldsymbol{r}}{\mathcal{N}-1} \times \left(\boldsymbol{n}^* \times \left(\nabla \cdot \boldsymbol{\tau} - \rho \nabla \left(\frac{q^2}{2} \right) - \rho \boldsymbol{l} \right) \right) + \boldsymbol{\tau} \cdot \boldsymbol{n}^* \right] \mathrm{d}S \\ = &\oint_{S_e} \left[-\rho \boldsymbol{q} \left(\boldsymbol{q} \cdot \boldsymbol{n} \right) + \frac{\boldsymbol{r}}{\mathcal{N}-1} \times \left(\boldsymbol{n} \times \left(\nabla \cdot \boldsymbol{\tau} - \rho \nabla \left(\frac{q^2}{2} \right) - \rho \boldsymbol{l} \right) \right) + \boldsymbol{\tau} \cdot \boldsymbol{n} \right] \mathrm{d}S \end{aligned} \tag{2.2.19}$$

Actually, relation (2.2.19) is nothing but an equivalent expression of the conservation of the momentum between S_e and S_e^*. Indeed, using the steady Navier-Stokes equations

$$\rho \boldsymbol{l} + \rho \nabla \left(\frac{q^2}{2} \right) = -\nabla p + \nabla \cdot \boldsymbol{\tau}$$

and again the second DMT (A.2), relation (2.2.19) is expressed as follows:

$$-\oint_{S_e^*} \rho \boldsymbol{q} \left(\boldsymbol{q} \cdot \boldsymbol{n}^* \right) \mathrm{d}S + \oint_{S_e^*} \left(-p \boldsymbol{I} + \boldsymbol{\tau} \right) \cdot \boldsymbol{n}^* \mathrm{d}S = -\oint_{S_e} \rho \boldsymbol{q} \left(\boldsymbol{q} \cdot \boldsymbol{n} \right) \mathrm{d}S + \oint_{S_e} \left(-p \boldsymbol{I} + \boldsymbol{\tau} \right) \cdot \boldsymbol{n} \mathrm{d}S \tag{2.2.20}$$

Therefore, the physical quantity which remains constant whatever the location of S_e is the momentum of the fluid and (2.2.20) is another evidence that only the total aerodynamic force $\boldsymbol{F}$ is conserved. In fact, the present analysis could not identify any physical quantity from which one could establish a domain-invariant Lamb-vector-based force decomposition. As a matter of fact, it seems that this decomposition will inevitably vary with a change in the size of the integration domain.

2.2.3 Illustration on practical numerical cases

It has been shown that increasing the size of the integration domain leads to a transfer between the various terms of the decomposition. On the one hand, it suggests that there is a transfer between the lift-induced drag and the profile drag. But is this transfer going from the lift-induced drag to the profile drag or the other way around? On the other hand, it raises the question of the lift decomposition: is it always solely given by $\boldsymbol{F}_{\rho l} + \boldsymbol{F}_{m_\rho}$? To answer those questions, RANS computations were performed on the OAT15A airfoil and the NASA Common Research Model wing-fuselage configuration (see the convergence in Appendix F) in order to investigate in practice the evolution of the force decomposition when increasing the size of the integration domain. Here, the reference point coincides with the origin of the frame (at the leading edge of the OAT15A airfoil, at the nose of the NASA CRM).

In the following, the study is once again restricted to high Re flows such that the viscous-turbulent term $\boldsymbol{F}_\tau$ is negligible and will not be accounted for. The lift and drag coefficients are defined as follows:

$$C_{L_{\rho l}} = \frac{2\boldsymbol{F}_{\rho l} \cdot \boldsymbol{e}_z}{\rho_\infty U_\infty^2 S} \tag{2.2.21a}$$

$$C_{D_{\rho l}} = \frac{2\boldsymbol{F}_{\rho l} \cdot \boldsymbol{e}_x}{\rho_\infty U_\infty^2 S} \tag{2.2.21b}$$

As a reminder, Mele *et al.*'s force decomposition [31, 32, 36] is given by

$$C_L^{\text{Mele}} = C_{L_{\rho l}} + C_{L_{m_\rho}} \tag{2.2.22a}$$

$$C_D^{\text{Mele}} = C_{D_{\rho l}} + C_{D_{m_\rho}} + C_{D_{S_e}} \tag{2.2.22b}$$

$$C_{D_i}^{\text{Mele}} = C_{D_{\rho l}} + C_{D_{m_\rho}} \tag{2.2.22c}$$

$$C_{D_P}^{\text{Mele}} = C_{D_{S_e}} \tag{2.2.22d}$$

where $C_{L_{S_e}}$ and $C_{D_{S_e}}$ are defined in (2.1.31), $C_{L_{m_\rho}}$ and $C_{D_{m_\rho}}$ are defined in (2.1.32) and the superscript Mele refers to Mele *et al.*: C_L^{Mele} is the corresponding total lift coefficient, C_D^{Mele} is the total drag coefficient, $C_{D_i}^{\text{Mele}}$ is the lift-induced drag coefficient and $C_{D_P}^{\text{Mele}}$ is the profile drag coefficient.

For the OAT15A airfoil, the evolution of Mele *et al.*'s decomposition with respect to the size of the integration domain is shown in Figs.2.16 and 2.17. C_D^{Mele} remains constant and is in good agreement with the near-field drag coefficient $C_D^{\text{Near-field}}$ (see Fig.2.16a). In this case, the lift-induced drag must technically be equal to zero since this drag contribution is present only in three-dimensional flows around wings of finite span. Yet, it can be noticed that $C_{D_i}^{\text{Mele}}$ is negative and not exactly equal to zero, as already observed by Kang *et al.* [18]. Nevertheless, the magnitude of this contribution tends to zero when increasing the size of the integration domain. Reversely, $C_{D_P}^{\text{Mele}}$ initially overestimates the near-field prediction although it decreases and converges to the same value in the far field. On the contrary, the lift coefficient C_L^{Mele} is not sensitive to the size of the integration domain and is in very good agreement with the near-field lift coefficient $C_L^{\text{Near-field}}$ (see Fig.2.16b). Finally, $C_{L_{S_e}}$ does not contribute to the lift at all although a small discrepancy due to a bad computation of the Lamb vector is noticed at $d/c = 6$.

Hence, the drag decomposition is sensitive to the size of the integration domain in the near field and progressively becomes invariant in the far field. The evolution of the lift-induced drag is investigated in further details in Fig.2.17a: it is clear that the sensitivity of $C_{D_i}^{\text{Mele}}$ to the size of the integration domain comes from $C_{D_{\rho l}}$ when $d/c \leq 2$. In fact, the Lamb vector is nonzero in the boundary layers and in the wake. Here, the increase in the lift-induced drag is caused by the contribution of the Lamb vector in the near wake as it was previously noted by Marongiu *et al.* [81]. On the contrary, $C_{D_{m_\rho}}$ is always constant and for $d/c \geq 2$, it can be seen that its negative contribution is never completely compensated by $C_{D_{\rho l}}$, which explains why the lift-induced drag

is never exactly equal to zero. This might come from regions where the Lamb vector slightly contributes to the thrust in $\boldsymbol{F}_{\rho l}$, as already observed by Kang *et al.* [18], especially at lower Re, and by Ostieri *et al.* in unsteady flows [95]. Regarding the lift decomposition displayed in Fig.2.17b, both $C_{L_{\rho l}}$ and $C_{L_{m_\rho}}$ remain constant and $C_{L_{m_\rho}}$ is responsible for almost 55% of the lift, which suggests that the compressibility plays a great role in the generation of lift in this case.

In conclusion, the analysis on the OAT15A airfoil suggests that the lift is invariant to the size of the integration domain but also that the two-dimensional profile drag of Mele *et al.* [31, 32, 36] is equal to the total drag only in the extreme far field. Therefore, to compute the total drag in two-dimensional flows, it is recommended to account for all the terms of the decomposition $\boldsymbol{F}_{\rho l} + \boldsymbol{F}_{m_\rho} + \boldsymbol{F}_{S_e}$, and not only $\boldsymbol{F}_{S_e}$.

For the NASA CRM, the evolution of Mele *et al.*'s decomposition with respect to the size of the integration domain is shown in Figs.2.18 and 2.19. Like in the two-dimensional case, C_D^{Mele} remains constant and is almost always in very good agreement with the near-field prediction: some discrepancies are noted for $d/c_{ref} \leq 1$. On the contrary, the drag decomposition is again sensitive to the size of the integration domain. Indeed, the transfer going from the profile drag to the lift-induced drag is clearly visible in Fig.2.18a: $C_{D_P}^{\text{Mele}}$ decreases while $C_{D_i}^{\text{Mele}}$ increases for $d/c_{ref} \leq 1$. It is surprising since one usually expects the lift-induced drag to be transferred to the profile drag as a consequence from the diffusion and dissipation of the trailing vortices [85, 96]. Zou *et al.* [85] explained the increase in lift-induced drag by the rolling-up of the vortex sheet in the very near wake, which leads to the formation of the trailing vortices responsible for this drag contribution. This increase in lift-induced drag is in fact caused by the increase in $C_{D_{\rho l}}$ (see Fig.2.19a) and hence by a still significant contribution of the Lamb vector in the vortex sheet [18, 32, 81]. On the contrary, $C_{D_{m_\rho}}$ is much less sensitive and remains almost constant. Anyways, for $d/c_{ref} \geq 1$ the profile drag and the lift-induced drag progressively stabilize and remain constant afterwards. Then the drag decomposition is sensitive to the size of the integration domain in the near field where the flow evolves rapidly, and becomes invariant in the far field where the vortical wake reaches an equilibrium. Nevertheless, the lift-induced drag will inevitably decrease and be transferred to the profile drag further downstream, as the fluid viscosity and the numerical scheme dissipate the trailing vortices.

Again, C_L^{Mele} is almost not sensitive to the size of the integration domain and $C_{L_{S_e}}$ is almost negligible (see Fig.2.18b): for $0.2 \leq d/c_{ref} \leq 0.4$, C_L^{Mele} slightly overestimates the near-field prediction and $C_{L_{S_e}}$ provides a small negative value. As seen in Fig.2.19b, this overestimation of the lift comes from $C_{L_{\rho l}}$ which has still not converged, while $C_{L_{m_\rho}}$ is constant. For $d/c_{ref} \geq 0.4$, C_L^{Mele} is always in perfect agreement with the near-field computation.

In conclusion, the lift is invariant to the size of the integration domain. On the contrary, the drag decomposition is very sensitive when the integration domain is small and progressively stabilizes as its size increases. In two-dimensional flows, the profile drag is systematically overestimated and the lift-induced drag provides a very slight thrust contribution. In fact, the profile drag converges to the near-field drag only in the extreme far field, once the lift-induced drag is equal to zero. In three-dimensional flows, the lift-induced drag and the profile drag evolve due to the transfer going from the latter to the former and become constant only a few reference-chord lengths away from the aircraft. The invariance is achieved in a region where the expansion of the trailing vortices is very slow and balanced by the viscous diffusion inside their cores [85]. It suggests that, in the very near field, the computed drag decomposition does still not correspond to a breakdown into profile drag and lift-induced drag. Further downstream, the lift-induced drag is transferred this time to the profile drag due the dissipation of the vortices. Hence, Mele *et al.*'s drag decomposition [31, 32, 36] is only locally domain-invariant in a specific flow region of the far field. In the next section, it will be shown that the invariance of the drag decomposition in this region is not only caused by the decrease in the magnitude of the Lamb vector, but also to the appearance of symmetries in the flow.

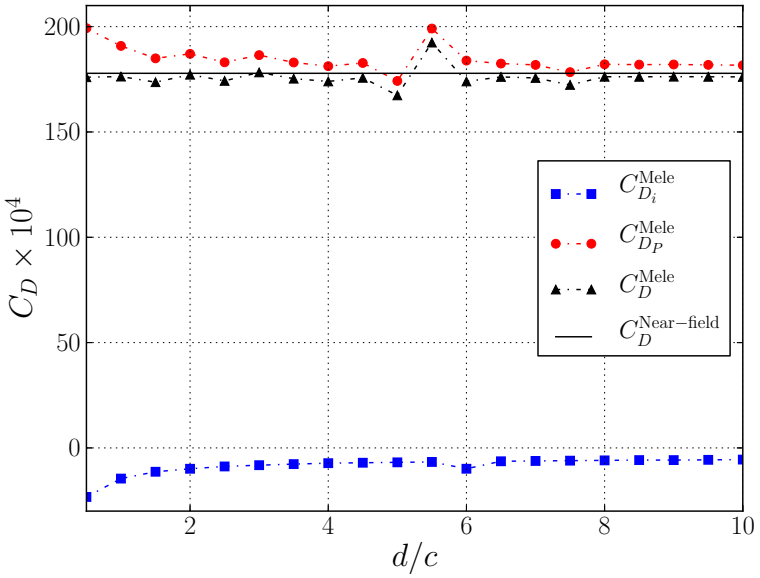

(a) Drag

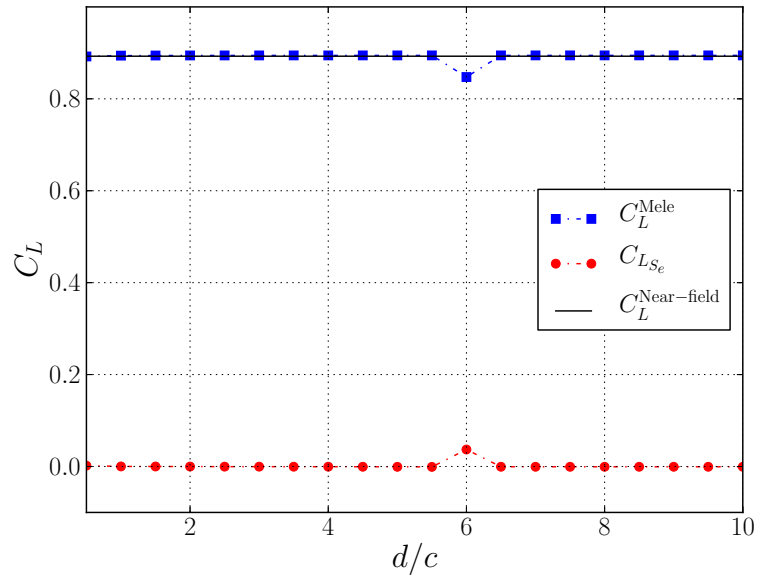

(b) Lift

Figure 2.16: Sensitivity of Mele *et al.*'s decomposition [31, 32, 36] to the size of the integration domain on the OAT15A airfoil, $M_\infty = 0.72$, $Re = 3 \times 10^6$, $\alpha = 2°$

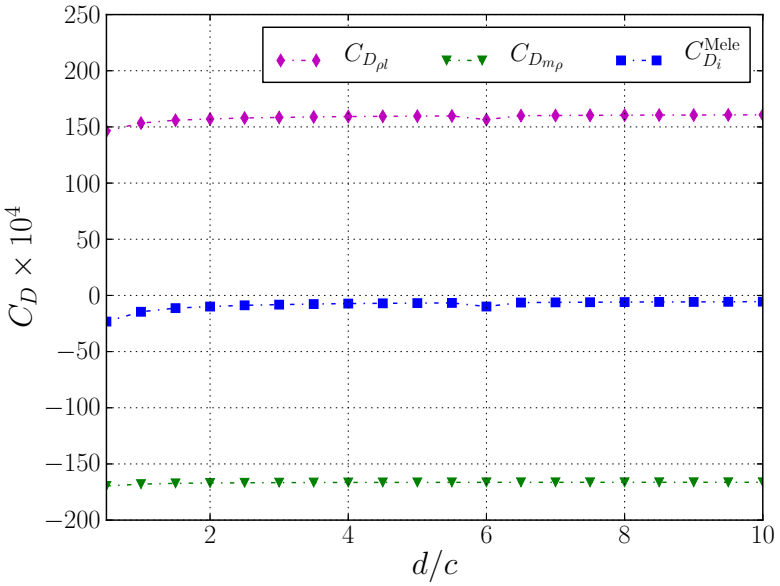

(a) Drag

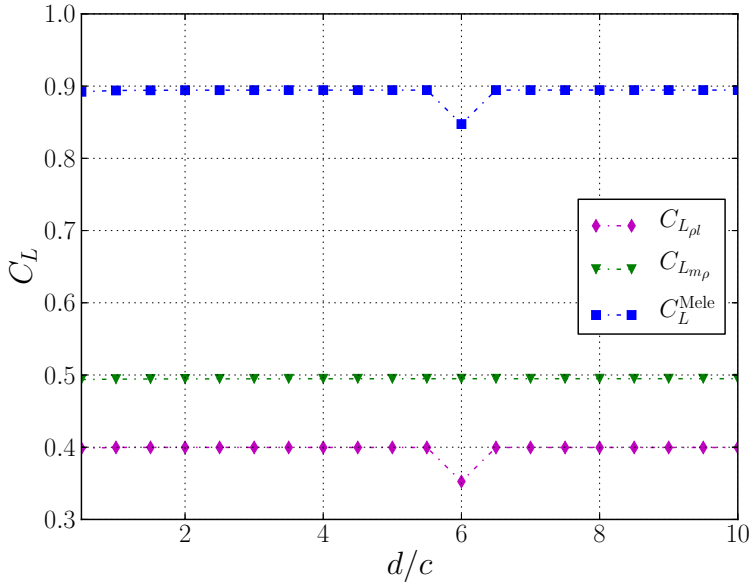

(b) Lift

Figure 2.17: Sensitivity of $\boldsymbol{F}_{\rho l}$ and $\boldsymbol{F}_{m_\rho}$ to the size of the integration domain on the OAT15A airfoil, $M_\infty = 0.72$, $Re = 3 \times 10^6$, $\alpha = 2°$

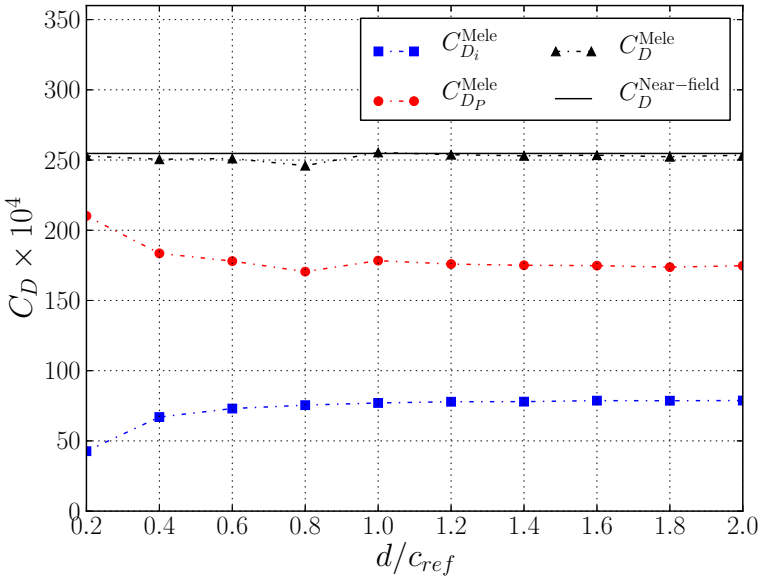

(a) Drag

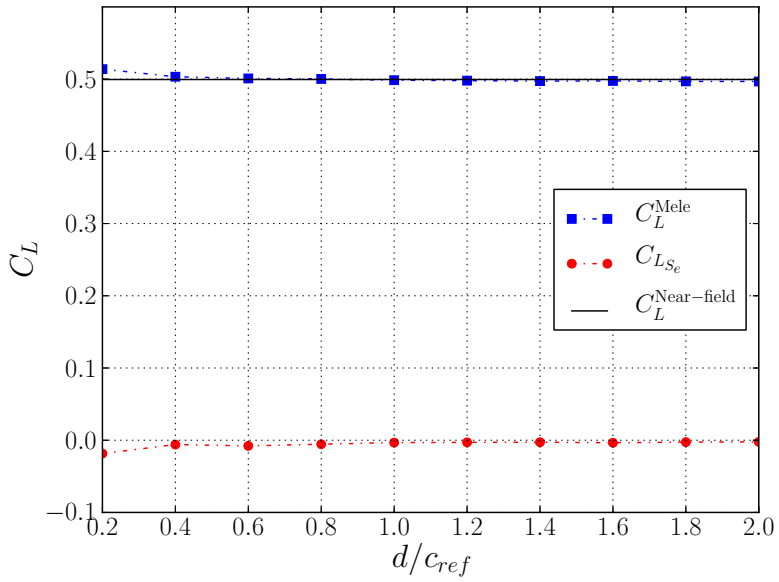

(b) Lift

Figure 2.18: Sensitivity of Mele *et al.*'s decomposition [31, 32, 36] to the size of the integration domain on the NASA CRM, $M_\infty = 0.85$, $Re = 5 \times 10^6$, $C_L \approx 0.5$

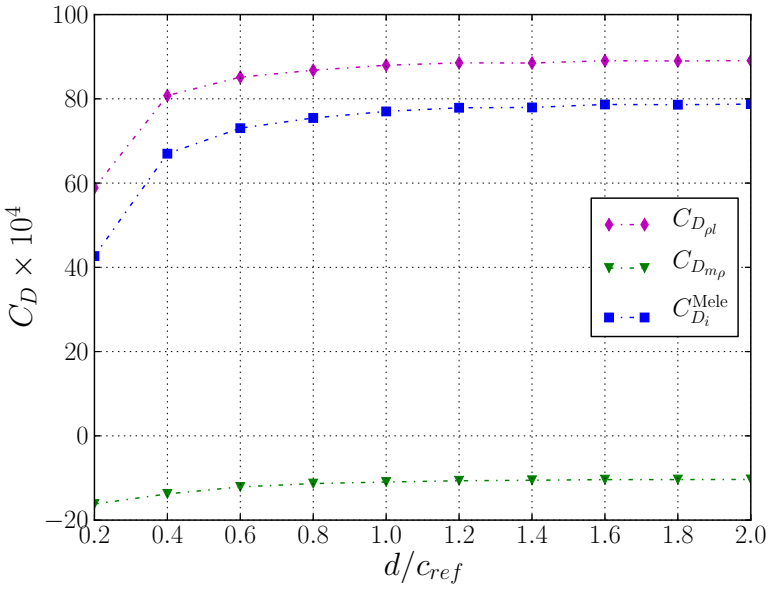

(a) Drag

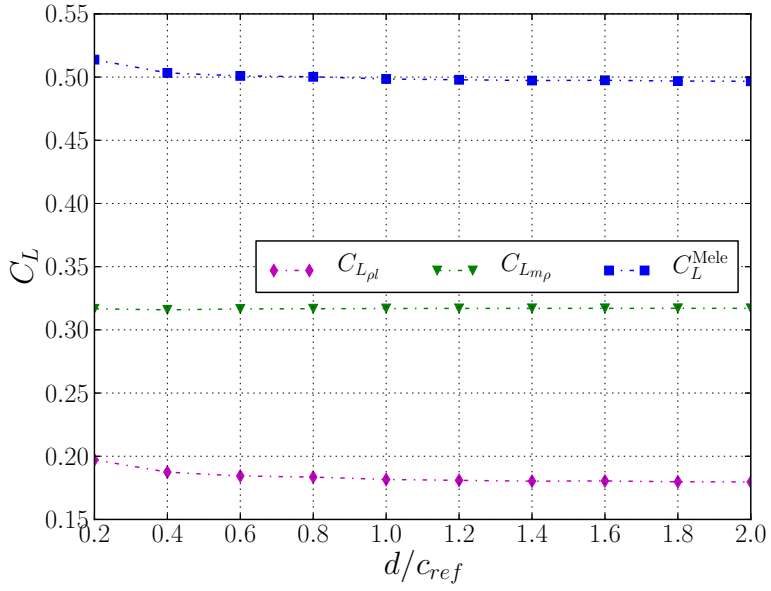

(b) Lift

Figure 2.19: Sensitivity of $\boldsymbol{F}_{\rho l}$ and $\boldsymbol{F}_{m_\rho}$ to the size of the integration domain on the NASA CRM, $M_\infty = 0.85$, $Re = 5 \times 10^6$, $C_L \approx 0.5$

2.3 Influence of the flow symmetries on the invariance in the far field

In section 2.1, it has been shown that Mele *et al.*'s aerodynamic force decomposition [31, 32, 36] is sensitive to the location of the reference point chosen for the computation of moment transformations. In particular, the decomposition is greatly impacted by a shift in the reference point when the size of the integration domain is small, i.e. when the surface integrals containing the position vector $\boldsymbol{r}$, in $\boldsymbol{F}_{S_e}$ and $\boldsymbol{F}_{m_\rho}$, are computed in the near field. On the contrary, the decomposition becomes progressively invariant as the size of the integration domain is increased, i.e. when the same surface integrals are computed in the far field.

Similarly, in section 2.2, it has been shown that, for a fixed reference point, an increase in the size of the integration domain leads to a transfer from the profile drag to the lift-induced drag while the total drag remains constant. In particular, this transfer occurs in the near field and the drag decomposition becomes constant in the far field.

In the present analysis, it is proved that the flow symmetries which progressively establish in the far field are responsible for the invariance to the location of the reference point, and that they partly contribute to the invariance to the size of the integration domain. First of all, two families of symmetries are introduced: the wake symmetries and the upstream-downstream symmetries. Then, their consequences on the previously identified sensitive terms are thoroughly analysed.

2.3.1 Presentation of the wake symmetries

In the Lamb-vector-based force decomposition proposed by Mele *et al.* [31, 32, 36], it has been shown in section 2.1 that the sensitivity of the decomposition to the location of the reference point is caused by the presence of the resulting terms $\boldsymbol{R}_{S_e}$ and $\boldsymbol{R}_{m_\rho}$. Similarly, it has been shown in section 2.2 that the sensitivity to the size of the integration domain is caused by the variations $\Delta\boldsymbol{F}_{\rho l}$ and $\Delta\boldsymbol{F}_{m_\rho}$ in the near field. $\boldsymbol{R}_{S_e}$ and $\Delta\boldsymbol{F}_{\rho l}$ involve the Lamb vector $\boldsymbol{l} = \boldsymbol{\omega} \times \boldsymbol{q}$ while $\boldsymbol{R}_{m_\rho}$ and $\Delta\boldsymbol{F}_{m_\rho}$ contain the quantity $\frac{q^2}{2}\nabla\rho$. In $\boldsymbol{R}_{S_e}$ and $\Delta\boldsymbol{F}_{\rho l}$, the Lamb vector is nonzero only on the portions of S_e and $\Delta\Omega$ crossing the wake. Hence, it is necessary to find the symmetries satisfied by the velocity vector $\boldsymbol{q}$, the vorticity vector $\boldsymbol{\omega}$ and then the Lamb vector in the wake. Besides, since the flow is assumed compressible, it is also necessary to investigate the wake symmetries of the density, the kinetic energy $q^2/2$, the density gradient $\nabla\rho$ and then the quantity $\frac{q^2}{2}\nabla\rho$.

In particular, the study is restricted to the far wake where the symmetries are satisfied. To do so, several hypotheses must be considered:

1. The aircraft is in cruise flight such that there is no side-slip angle.
2. The viscous wake is vertically symmetrical.
3. The vortical wake consists of a counter-rotating vortex pair as observed in numerous studies [97, 98, 99, 100, 101].
4. The wake is steady [102] and the expansion of the trailing vortices is assumed to be slow. Hence, the physical and numerical dissipations of the vortices are not accounted for.
5. The external surface S_e is chosen symmetrical with respect to the horizontal plane $z = 0$ and the vertical plane $y = 0$.

Those assumptions are realistic and often observed in practice. Indeed, the trailing vortices can have a great lifetime in aircraft wakes [101] which explains why each aircraft must respect a specific waiting time prior to take-off and landing on airport runways. In terms of the flow quantities, the aforementioned hypotheses respectively imply the following properties:

1. The velocity vector and the density are symmetrical with respect to the vertical plane $y = 0$.

2. The velocity defect u caused by the boundary layers and shock waves is symmetrical with respect to the horizontal plane $z = 0$.

3. The transverse part of the velocity vector (v, w) is symmetrical with respect to the plane $y = 0$ and antisymmetrical with respect to the plane $z = 0$.

4. The x-derivatives are negligible compared to the y and z-derivatives: $\partial/\partial x \ll \partial/\partial y, \partial/\partial z$.

5. The position vector $\boldsymbol{r}$ and the unit normal $\boldsymbol{n}$ on S_e are symmetrical with respect to the planes $y = 0$ and $z = 0$.

To describe the various symmetry properties, three matrices $\boldsymbol{S}_x$, $\boldsymbol{S}_y$ and $\boldsymbol{S}_z$ are introduced for more convenience:

$$\boldsymbol{S}_x = \begin{pmatrix} -1 & 0 & 0 \\ 0 & 1 & 0 \\ 0 & 0 & 1 \end{pmatrix} \tag{2.3.1}$$

$$\boldsymbol{S}_y = \begin{pmatrix} 1 & 0 & 0 \\ 0 & -1 & 0 \\ 0 & 0 & 1 \end{pmatrix} \tag{2.3.2}$$

$$\boldsymbol{S}_z = \begin{pmatrix} 1 & 0 & 0 \\ 0 & 1 & 0 \\ 0 & 0 & -1 \end{pmatrix} \tag{2.3.3}$$

Hence, in the vortical wake, hypotheses 1 and 2 imply that the velocity vector satisfies the following symmetry properties (see Fig.2.20):

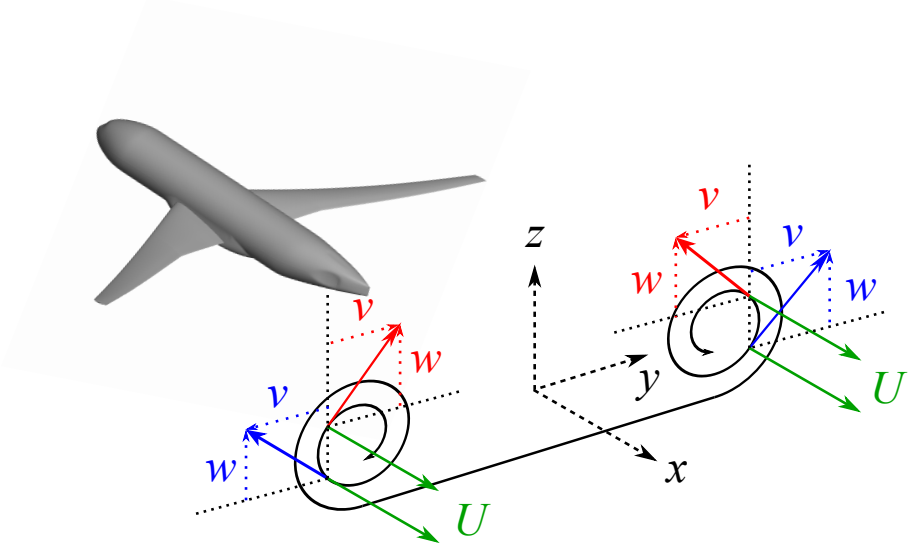

Figure 2.20: Illustration of the symmetries of the velocity vector in the vortical wake

$$\boldsymbol{q}(x, -y, z) = \boldsymbol{S}_y \cdot \boldsymbol{q}(x, y, z) \tag{2.3.4a}$$

$$\boldsymbol{q}(x, y, -z) = \boldsymbol{S}_y \cdot \boldsymbol{q}(x, y, z) \tag{2.3.4b}$$

Besides, the density and the kinetic energy $\frac{q^2}{2}$ satisfy

$$\rho(x, -y, z) = \rho(x, y, z) \tag{2.3.5a}$$

$$\rho(x, y, -z) = \rho(x, y, z) \tag{2.3.5b}$$

and

$$\frac{q^2}{2}(x,-y,z) = \frac{q^2}{2}(x,y,z) \tag{2.3.6a}$$

$$\frac{q^2}{2}(x,y,-z) = \frac{q^2}{2}(x,y,z) \tag{2.3.6b}$$

In order to obtain the symmetry properties satisfied by the Lamb vector in the vortical wake, it is necessary to write those satisfied by the vorticity vector. Yet, the vorticity vector contains the derivatives of the velocity vector:

$$\boldsymbol{\omega} = \begin{pmatrix} \partial w/\partial y - \partial v/\partial z \\ \partial u/\partial z - \partial w/\partial x \\ \partial v/\partial x - \partial u/\partial y \end{pmatrix} \tag{2.3.7}$$

Then, under hypothesis 4, the x-derivatives are negligible and the vorticity vector simply writes as

$$\boldsymbol{\omega} = \begin{pmatrix} \partial w/\partial y - \partial v/\partial z \\ \partial u/\partial z \\ -\partial u/\partial y \end{pmatrix} \tag{2.3.8}$$

The symmetries of the derivatives of the velocity vector are demonstrated in Appendix B. They are summarized here:

$$\frac{\partial \boldsymbol{q}}{\partial x}(x,-y,z) = \boldsymbol{S}_y \cdot \frac{\partial \boldsymbol{q}}{\partial x}(x,y,z) \tag{2.3.9a}$$

$$\frac{\partial \boldsymbol{q}}{\partial y}(x,-y,z) = -\boldsymbol{S}_y \cdot \frac{\partial \boldsymbol{q}}{\partial y}(x,y,z) \tag{2.3.9b}$$

$$\frac{\partial \boldsymbol{q}}{\partial z}(x,-y,z) = \boldsymbol{S}_y \cdot \frac{\partial \boldsymbol{q}}{\partial z}(x,y,z) \tag{2.3.9c}$$

and

$$\frac{\partial \boldsymbol{q}}{\partial x}(x,y,-z) = \boldsymbol{S}_y \cdot \frac{\partial \boldsymbol{q}}{\partial x}(x,y,z) \tag{2.3.10a}$$

$$\frac{\partial \boldsymbol{q}}{\partial y}(x,y,-z) = \boldsymbol{S}_y \cdot \frac{\partial \boldsymbol{q}}{\partial y}(x,y,z) \tag{2.3.10b}$$

$$\frac{\partial \boldsymbol{q}}{\partial z}(x,y,-z) = -\boldsymbol{S}_y \cdot \frac{\partial \boldsymbol{q}}{\partial z}(x,y,z) \tag{2.3.10c}$$

Therefore, using (2.3.9b), (2.3.9c), (2.3.10b) and (2.3.10c), it is possible to express the symmetry properties satisfied by the vorticity vector in the far wake (see Fig.2.21):

$$\boldsymbol{\omega}(x,-y,z) = -\boldsymbol{S}_y \cdot \boldsymbol{\omega}(x,y,z) \tag{2.3.11a}$$

$$\boldsymbol{\omega}(x,y,-z) = \boldsymbol{S}_y \cdot \boldsymbol{\omega}(x,y,z) \tag{2.3.11b}$$

As expected, ω_x is antisymmetrical with respect to the vertical plane $y = 0$ and symmetrical with respect to the horizontal plane $z = 0$ because of the presence of the counter-rotating tip vortices in the wake. Besides, ω_y is the result of the shearing processes occuring in the boundary layers of the horizontal surfaces of the aircraft and is then symmetrical with respect to the plane $y = 0$ and antisymmetrical with respect to the plane $z = 0$. On the contrary, ω_z is the result of the same shearing processes occuring this time in the boundary layers of the vertical surfaces of the aircraft, and is therefore antisymmetrical with respect to the plane $y = 0$ and symmetrical with respect to the plane $z = 0$.

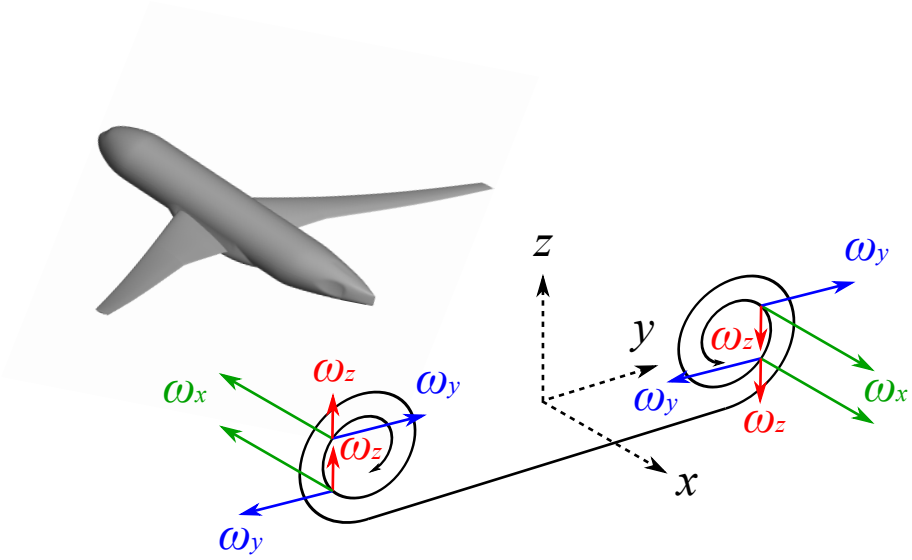

Figure 2.21: Illustration of the symmetries of the vorticity vector in the vortical wake

It is now possible to find out the symmetries satisfied by the Lamb vector in the far wake of an aircraft. As already said in this dissertation, the Lamb vector is the cross product of the vorticity and the velocity:

$$\boldsymbol{l} = \boldsymbol{\omega} \times \boldsymbol{q} = \begin{pmatrix} \omega_y w - \omega_z v \\ \omega_z u - \omega_x w \\ \omega_x v - \omega_y u \end{pmatrix} \tag{2.3.12}$$

Before deriving the symmetries, it is worthwhile keeping in mind the following points:

- The product of two symmetrical quantities yields a symmetrical quantity.
- The product of a symmetrical quantity with an antisymmetrical quantity yields an antisymmetrical quantity.
- The product of two antisymmetrical quantities yields a symmetrical quantity.

Therefore, using the symmetries of the velocity vector (2.3.4), the symmetries of the density field (2.3.5) and the symmetries of the vorticity vector (2.3.11), it is possible to show that $\rho\boldsymbol{l}$ satisfies the following symmetry properties in the far wake (see Fig.2.22):

$$\rho\boldsymbol{l}\,(x,-y,z) = \boldsymbol{S}_y \cdot \rho\boldsymbol{l}\,(x,y,z) \tag{2.3.13a}$$
$$\rho\boldsymbol{l}\,(x,y,-z) = -\boldsymbol{S}_y \cdot \rho\boldsymbol{l}\,(x,y,z) \tag{2.3.13b}$$

Regarding the quantity $\frac{q^2}{2}\nabla\rho$, it is necessary to combine the symmetries of the kinetic energy and the symmetries of the derivatives of the density field which are summarized below (see Fig.2.23, the proof is given in Appendix B):

$$\nabla\rho\,(x,-y,z) = \boldsymbol{S}_y \cdot \nabla\rho\,(x,y,z) \tag{2.3.14a}$$
$$\nabla\rho\,(x,y,-z) = \boldsymbol{S}_z \cdot \nabla\rho\,(x,y,z) \tag{2.3.14b}$$

Indeed, the density field is symmetrical with respect to the vertical plane $y = 0$ and the horizontal plane $z = 0$ in the wake: it entails that only $\partial\rho/\partial y$ is antisymmetrical with respect to the plane $y = 0$, and only $\partial\rho/\partial z$ is antisymmetrical with respect to the plane $z = 0$. Similarly, the gradient

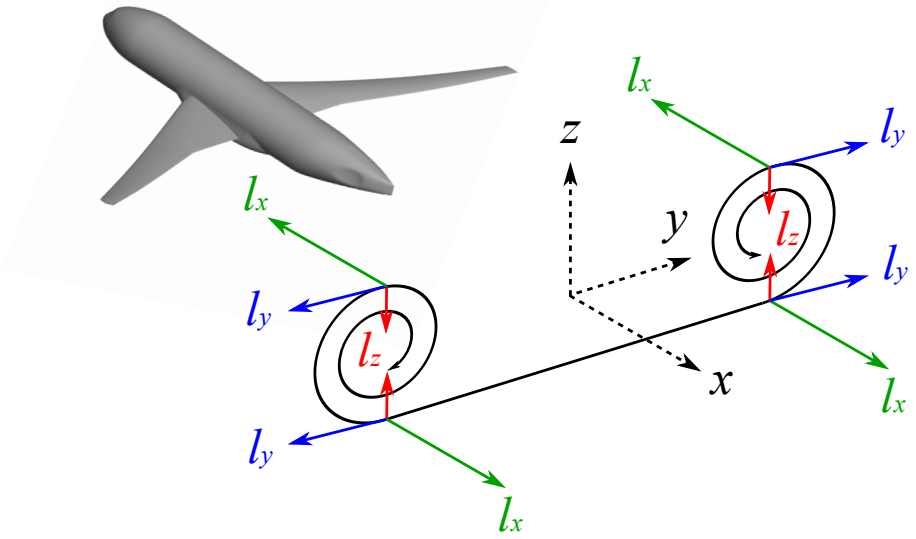

Figure 2.22: Illustration of the symmetries of the Lamb vector in the vortical wake

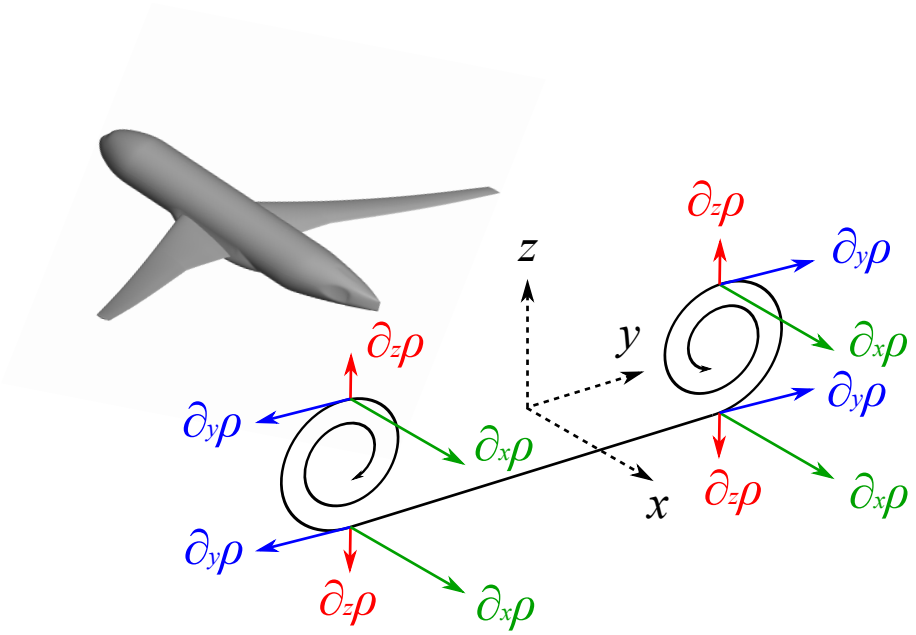

Figure 2.23: Illustration of the symmetries of the density gradient in the vortical wake

of kinetic energy satisfies the same symmetries:

$$\nabla\left(\frac{q^2}{2}\right)(x,-y,z) = \boldsymbol{S}_y \cdot \nabla\left(\frac{q^2}{2}\right)(x,y,z) \tag{2.3.15a}$$

$$\nabla\left(\frac{q^2}{2}\right)(x,y,-z) = \boldsymbol{S}_z \cdot \nabla\left(\frac{q^2}{2}\right)(x,y,z) \tag{2.3.15b}$$

Then, using (2.3.6) and (2.3.14), it can be shown that the quantity $\frac{q^2}{2}\nabla\rho$ satisfies the same

symmetries as $\nabla\rho$ in the far wake:

$$\frac{q^2}{2}\nabla\rho\left(x,-y,z\right) = \boldsymbol{S}_y \cdot \frac{q^2}{2}\nabla\rho\left(x,y,z\right) \tag{2.3.16a}$$

$$\frac{q^2}{2}\nabla\rho\left(x,y,-z\right) = \boldsymbol{S}_z \cdot \frac{q^2}{2}\nabla\rho\left(x,y,z\right) \tag{2.3.16b}$$

Finally, it is also necessary to express the symmetry properties satisfied by the position vector $\boldsymbol{r}$ and the unit normal $\boldsymbol{n}$ on the surface S_e. Under the fifth hypothesis, S_e is chosen symmetrical with respect to the vertical plane $y = 0$ and the horizontal plane $z = 0$. Therefore, $\boldsymbol{r}$ and $\boldsymbol{n}$ satisfy the same symmetries as the quantity $\frac{q^2}{2}\nabla\rho$:

$$\boldsymbol{r}\left(x,-y,z\right) = \boldsymbol{S}_y \cdot \boldsymbol{r}\left(x,y,z\right) \tag{2.3.17a}$$

$$\boldsymbol{r}\left(x,y,-z\right) = \boldsymbol{S}_z \cdot \boldsymbol{r}\left(x,y,z\right) \tag{2.3.17b}$$

and

$$\boldsymbol{n}\left(x,-y,z\right) = \boldsymbol{S}_y \cdot \boldsymbol{n}\left(x,y,z\right) \tag{2.3.18a}$$

$$\boldsymbol{n}\left(x,y,-z\right) = \boldsymbol{S}_z \cdot \boldsymbol{n}\left(x,y,z\right) \tag{2.3.18b}$$

In conclusion, the analysis of the vortical flow downstream of an aircraft enabled to elucidate the symmetries satisfied by the Lamb vector, the gradient of density, the gradient of kinetic energy and the quantity $\frac{q^2}{2}\nabla\rho$ in the far wake. Yet, the quantity $\frac{q^2}{2}\nabla\rho$ is linked to the compressibility of the flow and may be nonzero in other parts of the far field. Hence, the symmetries satisfied in the wake are not necessarily satisfied outside. That is why it is necessary to investigate other symmetries satisfied by this quantity, in particular the far-field symmetries up and downstream of the aircraft.

2.3.2 Presentation of the upstream-downstream symmetries

Indeed, in compressible flows, the presence of an obstacle produces a density gradient upstream of the aircraft. In the present analysis, a new set of symmetries satisfied outside the wake by the quantity $\frac{q^2}{2}\nabla\rho$ between the flow regions up and downstream of the aircraft will be introduced.

In fact, as $|x|$ tends to infinity, the density and the kinetic energy recover their freestream value and therefore become symmetrical with respect to the vertical planes $y = 0$ (since the aircraft is symmetrical) and $x = x_0$ where x_0 approximately corresponds to half of the chord in the case of an airfoil and half of the length of the fuselage in the case of an aircraft. In practice, the exact value of x_0 is not required since the location of the plane $x = x_0$ does not affect the following analyses. Moreover, in the far field, $|x|$ tends to infinity, hence $|x_0| \ll |x|$ and the upstream-downstream symmetries satisfied outside the wake can be expressed with respect to the plane $x = 0$:

$$\rho\left(-x,y,z\right) = \rho\left(x,y,z\right) \tag{2.3.19a}$$

$$\rho\left(x,-y,z\right) = \rho\left(x,y,z\right) \tag{2.3.19b}$$

and

$$\frac{q^2}{2}\left(-x,y,z\right) = \frac{q^2}{2}\left(x,y,z\right) \tag{2.3.20a}$$

$$\frac{q^2}{2}\left(x,-y,z\right) = \frac{q^2}{2}\left(x,y,z\right) \tag{2.3.20b}$$

Therefore, the gradients of density and kinetic energy satisfy the following symmetries (see Appendix B):

$$\nabla\rho\left(-x,y,z\right) = \boldsymbol{S}_x \cdot \nabla\rho\left(x,y,z\right) \tag{2.3.21a}$$
$$\nabla\rho\left(x,-y,z\right) = \boldsymbol{S}_y \cdot \nabla\rho\left(x,y,z\right) \tag{2.3.21b}$$

and

$$\nabla\left(\frac{q^2}{2}\right)\left(-x,y,z\right) = \boldsymbol{S}_x \cdot \nabla\left(\frac{q^2}{2}\right)\left(x,y,z\right) \tag{2.3.22a}$$
$$\nabla\left(\frac{q^2}{2}\right)\left(x,-y,z\right) = \boldsymbol{S}_y \cdot \nabla\left(\frac{q^2}{2}\right)\left(x,y,z\right) \tag{2.3.22b}$$

To illustrate the symmetries fulfilled by the quantity $\frac{q^2}{2}\nabla\rho$ in the far field, several RANS computations were performed. A first simulation was conducted on the fine mesh of the NACA0012 airfoil (see meshes in Appendix F) for a Mach number $M_\infty = 0.8$, a Reynolds number $Re = 3\times10^6$ and $\alpha = 0°$ in order to analyse the case of a symmetrical flow between the suction side and the pressure side. The contours of the x and z-components of $\frac{q^2}{2}\nabla\rho$ are shown in Fig.2.24. In this

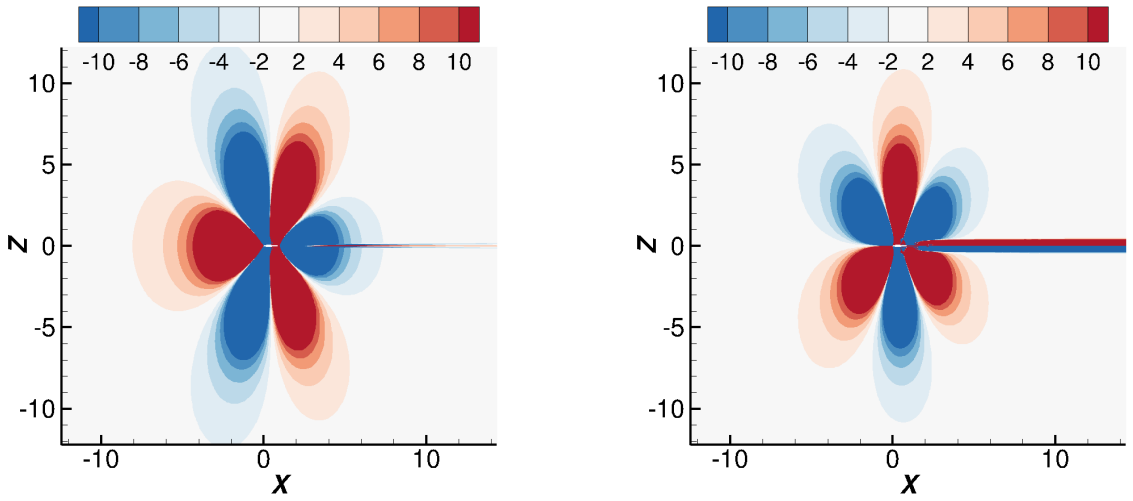

(a) x-component (b) z-component

Figure 2.24: Contours of $\frac{q^2}{2}\nabla\rho$ around the NACA0012 airfoil, $M_\infty = 0.8$, $Re = 9\times10^6$, $\alpha = 0°$

symmetrical case, the flow first undergoes a compression in front of the leading edge which explains why the x-component is positive (see Fig.2.24a). It becomes negative further downstream on both sides of the airfoil when the flow accelerates due to the wall curvature (expansion). Then, the x-component becomes positive when the flow faces an adverse pressure gradient and decelerates (compression). It becomes negative again when the flow is expanded downstream of the trailing edge.

On the suction side of the airfoil, the z-component is negative in front of the leading edge because the fluid particles are less compressed far from the wall than close to the wall (see Fig.2.24b): then the density decreases with z. Further downstream, the z-component becomes positive because the fluid particles are again less expanded far from the wall than close to the wall: this time the density increases with z. Finally, near the trailing edge, the presence of a region of higher pressure explains why the z-component becomes negative. Finally, both components gradually satisfy symmetry properties in the far field with respect to the vertical plane $x = 0$: the x-component is antisymmetrical while the z-component is symmetrical. In this nonlifting

case, it can also be seen that the x-component is symmetrical with respect to the horizontal plane $z = 0$ (see Fig.2.24a) while the z-component is antisymmetrical (see Fig.2.24b).

The phenomena described above are visible when $\alpha \neq 0°$ as well but their location has changed: it is due to the generation of lift. It is illustrated by the flow around the OAT15A airfoil in Fig.2.25 and around the NASA CRM in Fig.2.26. In those cases, as the flow arrives with

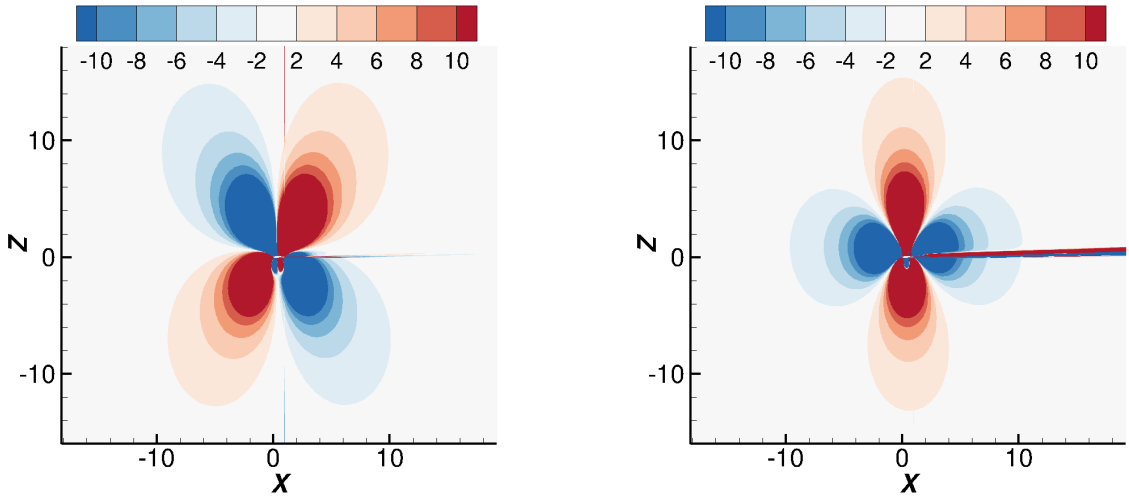

(a) x-component (b) z-component

Figure 2.25: Contours of $\frac{q^2}{2}\nabla\rho$ around the OAT15A airfoil, $M_\infty = 0.72$, $Re = 3 \times 10^6$, $\alpha = 2°$

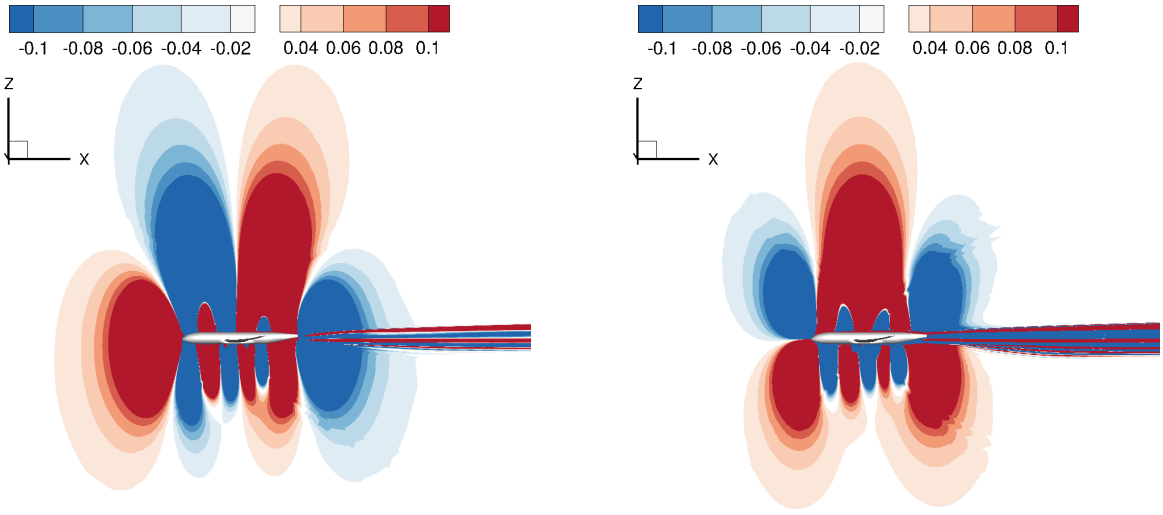

(a) x-component (b) z-component

Figure 2.26: Contours of $\frac{q^2}{2}\nabla\rho$ around the NASA CRM, $M_\infty = 0.85$, $Re = 5 \times 10^6$, $C_L \approx 0.5$

an angle α from the bottom left corner, the compression zone (in red) and the expansion zone (in blue) respectively in front of the leading edge and downstream of the trailing edge are moved downwards: they are now located under the pressure side (see Fig.2.25a). As a consequence the symmetries observed in the symmetrical case are modified: unlike the nonlifting case, the x-component of $\frac{q^2}{2}\nabla\rho$ becomes this time antisymmetrical with respect to the horizontal plane $z = 0$ in the far field while the z-component becomes symmetrical. Yet, the quantity $\frac{q^2}{2}\nabla\rho$ still

satisfies the same symmetry properties as before with respect to the planes $x = 0$ and $y = 0$:

$$\frac{q^2}{2}\nabla\rho\left(-x,y,z\right) = \boldsymbol{S}_x \cdot \frac{q^2}{2}\nabla\rho\left(x,y,z\right) \tag{2.3.23a}$$

$$\frac{q^2}{2}\nabla\rho\left(x,-y,z\right) = \boldsymbol{S}_y \cdot \frac{q^2}{2}\nabla\rho\left(x,y,z\right) \tag{2.3.23b}$$

Finally, if S_e is chosen symmetrical with respect to these two planes, the position vector $\boldsymbol{r}$ and the unit normal $\boldsymbol{n}$ satisfy the same symmetries as the quantity $\frac{q^2}{2}\nabla\rho$:

$$\boldsymbol{r}\left(-x,y,z\right) = \boldsymbol{S}_x \cdot \boldsymbol{r}\left(x,y,z\right) \tag{2.3.24a}$$

$$\boldsymbol{r}\left(x,-y,z\right) = \boldsymbol{S}_y \cdot \boldsymbol{r}\left(x,y,z\right) \tag{2.3.24b}$$

and

$$\boldsymbol{n}\left(-x,y,z\right) = \boldsymbol{S}_x \cdot \boldsymbol{n}\left(x,y,z\right) \tag{2.3.25a}$$

$$\boldsymbol{n}\left(x,-y,z\right) = \boldsymbol{S}_y \cdot \boldsymbol{n}\left(x,y,z\right) \tag{2.3.25b}$$

In conclusion, it has been shown that the Lamb vector, the gradients of density and kinetic energy and the quantity $\frac{q^2}{2}\nabla\rho$ progressively fulfill symmetry properties in the far wake. Moreover, $\nabla\rho$, $\nabla\left(\frac{q^2}{2}\right)$ and $\frac{q^2}{2}\nabla\rho$ also satisfy symmetries between the upstream and downstream flow regions in the far field whereas the Lamb vector is zero outside the wake. Therefore, as the resulting terms $\boldsymbol{R}_{S_e}$ and $\Delta\boldsymbol{F}_{\rho l}$ contain the Lamb vector only, their contribution will be impacted only by the symmetries in the far wake. On the contrary, the resulting terms $\boldsymbol{R}_{m_\rho}$ and $\Delta\boldsymbol{F}_{m_\rho}$ contain the quantities $\nabla\left(\frac{q^2}{2}\right)\times\nabla\rho$ and $\frac{q^2}{2}\nabla\rho$, hence their contribution will be impacted by the symmetries in the far wake and the symmetries up and downtream the aircraft. In the following, the influence of the symmetries on the sensitive terms $\boldsymbol{R}_{S_e}$, $\boldsymbol{R}_{m_\rho}$, $\Delta\boldsymbol{F}_{\rho l}$ and $\Delta\boldsymbol{F}_{m_\rho}$ will be analysed. In particular, it will be shown that the appearance of symmetries eliminates the contributions of $\boldsymbol{R}_{S_e}$, $\boldsymbol{R}_{m_\rho}$ and $\Delta\boldsymbol{F}_{\rho l}$.

2.3.3 Symmetry properties of the cross products

$\boldsymbol{R}_{S_e}$ is the surface integral of $\boldsymbol{n}\times\rho\boldsymbol{l}$, $\boldsymbol{R}_{m_\rho}$ can be expressed as the surface integral of $\boldsymbol{n}\times\frac{q^2}{2}\nabla\rho$ or the volume integral of $\nabla\left(\frac{q^2}{2}\right)\times\nabla\rho$ and $\Delta\boldsymbol{F}_{m_\rho}$ is the volume integral of $\boldsymbol{r}\times\left(\nabla\left(\frac{q^2}{2}\right)\times\nabla\rho\right)$. Hence, before analysing the consequences of the appearance of symmetries on the sensititive terms in the far field, it is necessary to write the symmetry properties satisfied by a vector resulting from a cross product.

The symmetry properties of the Lamb vector, the gradients of density and kinetic energy, the quantity $\frac{q^2}{2}\nabla\rho$, the position vector $\boldsymbol{r}$ and the unit normal $\boldsymbol{n}$ are summarized below:

$$\left.\begin{aligned}\rho\boldsymbol{l}\left(x,-y,z\right) &= \boldsymbol{S}_y\cdot\rho\boldsymbol{l}\left(x,y,z\right)\\ \rho\boldsymbol{l}\left(x,y,-z\right) &= -\boldsymbol{S}_y\cdot\rho\boldsymbol{l}\left(x,y,z\right)\end{aligned}\right\}\quad\text{in the far wake} \tag{2.3.26}$$

$$\begin{aligned}\nabla\rho\left(-x,y,z\right) &= \boldsymbol{S}_x\cdot\nabla\rho\left(x,y,z\right) \quad \text{outside the wake}\\ \nabla\rho\left(x,-y,z\right) &= \boldsymbol{S}_y\cdot\nabla\rho\left(x,y,z\right)\\ \nabla\rho\left(x,y,-z\right) &= \boldsymbol{S}_z\cdot\nabla\rho\left(x,y,z\right) \quad \text{in the far wake}\end{aligned} \tag{2.3.27}$$

$$\begin{aligned}\nabla\left(\frac{q^2}{2}\right)\left(-x,y,z\right) &= \boldsymbol{S}_x\cdot\nabla\left(\frac{q^2}{2}\right)\left(x,y,z\right) \quad \text{outside the wake}\\ \nabla\left(\frac{q^2}{2}\right)\left(x,-y,z\right) &= \boldsymbol{S}_y\cdot\nabla\left(\frac{q^2}{2}\right)\left(x,y,z\right)\\ \nabla\left(\frac{q^2}{2}\right)\left(x,y,-z\right) &= \boldsymbol{S}_z\cdot\nabla\left(\frac{q^2}{2}\right)\left(x,y,z\right) \quad \text{in the far wake}\end{aligned} \tag{2.3.28}$$

$$\boxed{\begin{aligned}
&\frac{q^2}{2}\nabla\rho\left(-x,y,z\right) = \boldsymbol{S}_x \cdot \frac{q^2}{2}\nabla\rho\left(x,y,z\right) \quad \text{outside the wake}\\
&\frac{q^2}{2}\nabla\rho\left(x,-y,z\right) = \boldsymbol{S}_y \cdot \frac{q^2}{2}\nabla\rho\left(x,y,z\right)\\
&\frac{q^2}{2}\nabla\rho\left(x,y,-z\right) = \boldsymbol{S}_z \cdot \frac{q^2}{2}\nabla\rho\left(x,y,z\right) \quad \text{in the far wake}
\end{aligned}} \tag{2.3.29}$$

$$\boxed{\begin{aligned}
&\boldsymbol{n}\left(-x,y,z\right) = \boldsymbol{S}_x \cdot \boldsymbol{n}\left(x,y,z\right)\\
&\boldsymbol{n}\left(x,-y,z\right) = \boldsymbol{S}_y \cdot \boldsymbol{n}\left(x,y,z\right)\\
&\boldsymbol{n}\left(x,y,-z\right) = \boldsymbol{S}_z \cdot \boldsymbol{n}\left(x,y,z\right)
\end{aligned}} \tag{2.3.30}$$

$$\boxed{\begin{aligned}
&\boldsymbol{r}\left(-x,y,z\right) = \boldsymbol{S}_x \cdot \boldsymbol{r}\left(x,y,z\right)\\
&\boldsymbol{r}\left(x,-y,z\right) = \boldsymbol{S}_y \cdot \boldsymbol{r}\left(x,y,z\right)\\
&\boldsymbol{r}\left(x,y,-z\right) = \boldsymbol{S}_z \cdot \boldsymbol{r}\left(x,y,z\right)
\end{aligned}} \tag{2.3.31}$$

First of all, let $\boldsymbol{f}$ and $\boldsymbol{g}$ be two vectors which satisfy the same symmetry properties as those of the gradient of density, the gradient of kinetic energy, the quantity $\frac{q^2}{2}\nabla\rho$ and the unit normal $\boldsymbol{n}$ (see (2.3.27) for instance). The cross product of $\boldsymbol{f}$ and $\boldsymbol{g}$ writes as follows:

$$\boldsymbol{f}\times\boldsymbol{g} = \begin{pmatrix} f_y g_z - f_z g_y \\ f_z g_x - f_x g_z \\ f_x g_y - f_y g_x \end{pmatrix} \tag{2.3.32}$$

Then, it follows that $\boldsymbol{f}\times\boldsymbol{g}$ satisfies the following symmetries in the far field:

$$\left(\boldsymbol{f}\times\boldsymbol{g}\right)\left(-x,y,z\right) = -\boldsymbol{S}_x \cdot \left(\boldsymbol{f}\times\boldsymbol{g}\right)\left(x,y,z\right) \quad \text{outside the wake} \tag{2.3.33a}$$
$$\left(\boldsymbol{f}\times\boldsymbol{g}\right)\left(x,-y,z\right) = -\boldsymbol{S}_y \cdot \left(\boldsymbol{f}\times\boldsymbol{g}\right)\left(x,y,z\right) \tag{2.3.33b}$$
$$\left(\boldsymbol{f}\times\boldsymbol{g}\right)\left(x,y,-z\right) = -\boldsymbol{S}_z \cdot \left(\boldsymbol{f}\times\boldsymbol{g}\right)\left(x,y,z\right) \quad \text{in the far wake} \tag{2.3.33c}$$

with $\boldsymbol{f}\times\boldsymbol{g} = \boldsymbol{n}\times\frac{q^2}{2}\nabla\rho$ or $\nabla\left(\frac{q^2}{2}\right)\times\nabla\rho$. It is also possible to find the symmetry properties satisfied by the quantities $\boldsymbol{r}\times\left(\nabla\left(\frac{q^2}{2}\right)\times\nabla\rho\right)$ and $\boldsymbol{r}\times\left(\boldsymbol{n}\times\frac{q^2}{2}\nabla\rho\right)$ in the far field. To do so, it is more convenient to use the rule of the double cross product

$$\boldsymbol{r}\times\left(\boldsymbol{f}\times\boldsymbol{g}\right) = \left(\boldsymbol{r}\cdot\boldsymbol{g}\right)\boldsymbol{f} - \left(\boldsymbol{r}\cdot\boldsymbol{f}\right)\boldsymbol{g} \tag{2.3.34}$$

and the matrix writing format for the scalar product and the transposed matrix product

$$\boldsymbol{f}\cdot\boldsymbol{g} = \boldsymbol{f}^T\cdot\boldsymbol{g} \tag{2.3.35}$$
$$\left(\boldsymbol{S}\cdot\boldsymbol{f}\right)^T = \boldsymbol{f}^T\cdot\boldsymbol{S}^T \tag{2.3.36}$$

where $\boldsymbol{S}$ is any of the symmetry matrices presented earlier. Then, with $\boldsymbol{r}$, $\boldsymbol{f}$ and $\boldsymbol{g}$ satisfying symmetry properties with respect to a random plane, and having that $\boldsymbol{S}^T\cdot\boldsymbol{S} = \boldsymbol{I}$, the symmetrical double cross product can be written as

$$\begin{aligned}
\boldsymbol{S}\cdot\boldsymbol{r}\times\left(\boldsymbol{S}\cdot\boldsymbol{f}\times\boldsymbol{S}\cdot\boldsymbol{g}\right) &= \left(\boldsymbol{r}^T\cdot\boldsymbol{S}^T\cdot\boldsymbol{S}\cdot\boldsymbol{g}\right)\boldsymbol{S}\cdot\boldsymbol{f} - \left(\boldsymbol{r}^T\cdot\boldsymbol{S}^T\cdot\boldsymbol{S}\cdot\boldsymbol{f}\right)\boldsymbol{S}\cdot\boldsymbol{g}\\
&= \boldsymbol{S}\cdot\left\{\left(\boldsymbol{r}^T\cdot\boldsymbol{S}^T\cdot\boldsymbol{S}\cdot\boldsymbol{g}\right)\boldsymbol{f} - \left(\boldsymbol{r}^T\cdot\boldsymbol{S}^T\cdot\boldsymbol{S}\cdot\boldsymbol{f}\right)\boldsymbol{g}\right\}\\
&= \boldsymbol{S}\cdot\left(\boldsymbol{r}\times\left(\boldsymbol{f}\times\boldsymbol{g}\right)\right)
\end{aligned} \tag{2.3.37}$$

Similarly, having that $\boldsymbol{S}_x^T\cdot\boldsymbol{S}_x = \boldsymbol{S}_y^T\cdot\boldsymbol{S}_y = \boldsymbol{S}_z^T\cdot\boldsymbol{S}_z = \boldsymbol{I}$, and using (2.3.27), (2.3.28), (2.3.29), (2.3.30) and (2.3.31), then the symmetry properties of the quantities $\boldsymbol{r}\times\left(\nabla\left(\frac{q^2}{2}\right)\times\nabla\rho\right)$ and

$\boldsymbol{r} \times \left(\boldsymbol{n} \times \frac{q^2}{2}\nabla\rho\right)$ in the far field are given by

$$(\boldsymbol{r} \times (\boldsymbol{f} \times \boldsymbol{g}))(-x, y, z) = \boldsymbol{S}_x \cdot (\boldsymbol{r} \times (\boldsymbol{f} \times \boldsymbol{g}))(x, y, z) \quad \text{outside the wake} \tag{2.3.38a}$$
$$(\boldsymbol{r} \times (\boldsymbol{f} \times \boldsymbol{g}))(x, -y, z) = \boldsymbol{S}_y \cdot (\boldsymbol{r} \times (\boldsymbol{f} \times \boldsymbol{g}))(x, y, z) \tag{2.3.38b}$$
$$(\boldsymbol{r} \times (\boldsymbol{f} \times \boldsymbol{g}))(x, y, -z) = \boldsymbol{S}_z \cdot (\boldsymbol{r} \times (\boldsymbol{f} \times \boldsymbol{g}))(x, y, z) \quad \text{in the far wake} \tag{2.3.38c}$$

with $\boldsymbol{f} \times \boldsymbol{g} = \boldsymbol{n} \times \frac{q^2}{2}\nabla\rho$ or $\nabla\left(\frac{q^2}{2}\right) \times \nabla\rho$.

Regarding the quantity $\boldsymbol{n} \times \rho\boldsymbol{l}$, $\boldsymbol{n}$ satisfies (2.3.30) and $\rho\boldsymbol{l}$ satisfies (2.3.26) in the far wake. The cross product is then written as follows:

$$\boldsymbol{n} \times \rho\boldsymbol{l} = \rho \begin{pmatrix} n_y l_z - n_z l_y \\ n_z l_x - n_x l_z \\ n_x l_y - n_y l_x \end{pmatrix} \tag{2.3.39}$$

Yet, in the far wake the velocity field can be approximated as $\boldsymbol{q} = (U_\infty + u)\,\boldsymbol{e}_x + v\boldsymbol{e}_y + w\boldsymbol{e}_z$ such that $|u/U_\infty|, |v/U_\infty|, |w/U_\infty| \ll 1$. In this case, the Lamb vector consists of a first-order and a second-order term:

$$\boldsymbol{l} = \underbrace{\begin{pmatrix} 0 \\ \omega_z U_\infty \\ -\omega_y U_\infty \end{pmatrix}}_{\text{first order}} + \underbrace{\begin{pmatrix} \omega_y w - \omega_z v \\ \omega_z u - \omega_x w \\ \omega_x v - \omega_y u \end{pmatrix}}_{\text{second order}} \tag{2.3.40}$$

Besides, in the far wake the direction of the flow is almost parallel to that of the freestream, hence the region where the Lamb vector is nonzero coincides with a portion of S_e where $\boldsymbol{n} \approx \boldsymbol{e}_x$. Therefore, at first order $l_x \ll l_y, l_z$ and $n_y, n_z \ll n_x$ [34, 35]. Hence, it follows that, at first order:

$$\boldsymbol{n} \times \rho\boldsymbol{l} = \rho \begin{pmatrix} n_y l_z - n_z l_y \\ -n_x l_z \\ n_x l_y \end{pmatrix} \tag{2.3.41}$$

In the far wake, using (2.3.26) and (2.3.30), it is then possible to write the symmetries of the cross product $\boldsymbol{n} \times \rho\boldsymbol{l}$:

$$(\boldsymbol{n} \times \rho\boldsymbol{l})(x, -y, z) = -\boldsymbol{S}_y \cdot (\boldsymbol{n} \times \rho\boldsymbol{l})(x, y, z) \tag{2.3.42a}$$
$$(\boldsymbol{n} \times \rho\boldsymbol{l})(x, y, -z) = -\boldsymbol{S}_z \cdot (\boldsymbol{n} \times \rho\boldsymbol{l})(x, y, z) \tag{2.3.42b}$$

and using (2.3.31), those of the double cross product $\boldsymbol{r} \times (\boldsymbol{n} \times \rho\boldsymbol{l})$:

$$(\boldsymbol{r} \times (\boldsymbol{n} \times \rho\boldsymbol{l}))(x, -y, z) = \boldsymbol{S}_y \cdot (\boldsymbol{r} \times (\boldsymbol{n} \times \rho\boldsymbol{l}))(x, y, z) \tag{2.3.43a}$$
$$(\boldsymbol{r} \times (\boldsymbol{n} \times \rho\boldsymbol{l}))(x, y, -z) = \boldsymbol{S}_z \cdot (\boldsymbol{r} \times (\boldsymbol{n} \times \rho\boldsymbol{l}))(x, y, z) \tag{2.3.43b}$$

The symmetry properties derived in this part will now be introduced in the integrals in order to emphasize the influence of the flow symmetries on the sensitive terms of Mele *et al.*'s decomposition [31, 32, 36].

2.3.4 Consequences on the sensitive terms

Consequences on the resulting terms $\boldsymbol{R}_{S_e}$ and $\boldsymbol{R}_{m_\rho}$

In the present analysis, it will be explained how Mele *et al.*'s aerodynamic force decomposition becomes totally independent of the location of the reference point in the far field. To do so, it is necessary to focus on the resulting terms $\boldsymbol{R}_{S_e}$ and $\boldsymbol{R}_{m_\rho}$ responsible for the sensitivity to the

reference point (see section 2.1), and especially to investigate how they are impacted by the appearance of symmetries.

Let S_w represent the part of S_e crossing the wake: S_w is not a wake plane and then $\boldsymbol{n} \neq \boldsymbol{e}_x$ on it. The integral in the term $\boldsymbol{R}_{S_e}$ can be limited to S_w since the Lamb vector is zero everywhere else:

$$\begin{aligned}\boldsymbol{R}_{S_e} &= -\frac{1}{\mathcal{N}-1}\int_{S_w} \boldsymbol{n}\times\rho\boldsymbol{l}\mathrm{d}S \\ &= -\frac{1}{\mathcal{N}-1}\int_{S_w}^{y\geq 0} \boldsymbol{n}\times\rho\boldsymbol{l}\mathrm{d}S - \frac{1}{\mathcal{N}-1}\int_{S_w}^{y\leq 0} \boldsymbol{n}\times\rho\boldsymbol{l}\mathrm{d}S\end{aligned} \tag{2.3.44}$$

Then the second integral for $y \leq 0$ is equivalently expressed for $y \geq 0$ by using the symmetry properties (2.3.42a) satisfied in the far wake:

$$\boldsymbol{R}_{S_e} = -\frac{1}{\mathcal{N}-1}\left(\boldsymbol{I}-\boldsymbol{S}_y\right)\cdot\int_{S_w}^{y\geq 0} \boldsymbol{n}\times\rho\boldsymbol{l}\mathrm{d}S \tag{2.3.45}$$

The same splitting is performed with the z-coordinate and using the symmetry properties (2.3.42b), $\boldsymbol{R}_{S_e}$ is finally written as follows:

$$\boldsymbol{R}_{S_e} = -\frac{1}{\mathcal{N}-1}\underbrace{\left(\boldsymbol{I}-\boldsymbol{S}_y\right)\cdot\left(\boldsymbol{I}-\boldsymbol{S}_z\right)}_{=\boldsymbol{0}}\cdot\int_{S_w}^{y,z\geq 0} \boldsymbol{n}\times\rho\boldsymbol{l}\mathrm{d}S = \boldsymbol{0} \tag{2.3.46}$$

Therefore $\boldsymbol{R}_{S_e}$ vanishes in the far wake which explains why $\boldsymbol{F}_{S_e}$ becomes invariant with respect to the location of the reference point. Moreover, by using the same method, it is possible to split the integral in $\boldsymbol{F}_{S_e}$ into contributions for $y \geq 0$, $y \leq 0$, $z \geq 0$ and $z \leq 0$. By using the symmetry properties (2.3.43) of the double cross product $\boldsymbol{r}\times(\boldsymbol{n}\times\rho\boldsymbol{l})$ in the far wake, $\boldsymbol{F}_{S_e}$ is expressed as

$$\boldsymbol{F}_{S_e} = -\frac{1}{\mathcal{N}-1}\left(\boldsymbol{I}+\boldsymbol{S}_y\right)\cdot\left(\boldsymbol{I}+\boldsymbol{S}_z\right)\int_{S_w}^{y,z\geq 0} \boldsymbol{r}\times\left(\boldsymbol{n}\times\rho\boldsymbol{l}\right)\mathrm{d}S \tag{2.3.47}$$

Yet, it turns out that

$$\left(\boldsymbol{I}+\boldsymbol{S}_y\right)\cdot\left(\boldsymbol{I}+\boldsymbol{S}_z\right) = \begin{pmatrix}4&0&0\\0&0&0\\0&0&0\end{pmatrix} \tag{2.3.48}$$

Hence, the symmetries satisfied by the Lamb vector and the unit normal in the far wake reduce $\boldsymbol{F}_{S_e}$ to a drag contribution only:

$$\boldsymbol{F}_{S_e} = -\frac{4}{\mathcal{N}-1}\left(\int_{S_w}^{y,z\geq 0} \boldsymbol{r}\times\left(\boldsymbol{n}\times\rho\boldsymbol{l}\right)\mathrm{d}S\right)\cdot\boldsymbol{e}_x \tag{2.3.49}$$

Unlike $\boldsymbol{R}_{S_e}$, the integral in $\boldsymbol{R}_{m_\rho}$ must be split into a wake contribution on S_w and a contribution on the rest $S_e \setminus S_w$ since $\frac{q^2}{2}\nabla\rho$ is nonzero in and outside the wake:

$$\boldsymbol{R}_{m_\rho} = \frac{1}{\mathcal{N}-1}\int_{S_w} \boldsymbol{n}\times\frac{q^2}{2}\nabla\rho\mathrm{d}S + \frac{1}{\mathcal{N}-1}\int_{S_e\setminus S_w} \boldsymbol{n}\times\frac{q^2}{2}\nabla\rho\mathrm{d}S \tag{2.3.50}$$

As for $\boldsymbol{R}_{S_e}$, the two integrals are split into a contribution for $y \geq 0$ and another for $y \leq 0$. Therefore, using the symmetry properties (2.3.33b) for $\boldsymbol{n}\times\frac{q^2}{2}\nabla\rho$, it is possible to write $\boldsymbol{R}_{m_\rho}$ as follows:

$$\begin{aligned}\boldsymbol{R}_{m_\rho} &= \frac{1}{\mathcal{N}-1}\left(\boldsymbol{I}-\boldsymbol{S}_y\right)\cdot\int_{S_w}^{y\geq 0} \boldsymbol{n}\times\frac{q^2}{2}\nabla\rho\mathrm{d}S \\ &\quad + \frac{1}{\mathcal{N}-1}\left(\boldsymbol{I}-\boldsymbol{S}_y\right)\cdot\int_{S_e\setminus S_w}^{y\geq 0} \boldsymbol{n}\times\frac{q^2}{2}\nabla\rho\mathrm{d}S\end{aligned} \tag{2.3.51}$$

The first integral on S_w is split into contributions for $z \geq 0$ and $z \leq 0$ in order to use the symmetry properties (2.3.33c) of $\boldsymbol{n} \times \frac{q^2}{2}\nabla\rho$ with respect to the plane $z = 0$ in the wake. Then, the second integral on $S_e \setminus S_w$ is split into contributions for $x \geq 0$ and $x \leq 0$ in order to use the symmetry properties (2.3.33a) of $\boldsymbol{n} \times \frac{q^2}{2}\nabla\rho$, satisfied up and downstream of the aircraft with respect to the plane $x = 0$. Finally, $\boldsymbol{R}_{m_\rho}$ is expressed as

$$\begin{aligned}\boldsymbol{R}_{m_\rho} = &\frac{1}{\mathcal{N}-1}\underbrace{(\boldsymbol{I}-\boldsymbol{S}_y)\cdot(\boldsymbol{I}-\boldsymbol{S}_z)}_{=\boldsymbol{0}}\cdot\int_{S_w}^{y,z\geq 0}\boldsymbol{n}\times\frac{q^2}{2}\nabla\rho\mathrm{d}S\\ &+\frac{1}{\mathcal{N}-1}\underbrace{(\boldsymbol{I}-\boldsymbol{S}_x)\cdot(\boldsymbol{I}-\boldsymbol{S}_y)}_{=\boldsymbol{0}}\cdot\int_{S_e\setminus S_w}^{x,y\geq 0}\boldsymbol{n}\times\frac{q^2}{2}\nabla\rho\mathrm{d}S=\boldsymbol{0}\end{aligned} \tag{2.3.52}$$

Therefore $\boldsymbol{R}_{m_\rho}$ also vanishes in the far field which explains why $\boldsymbol{F}_{m_\rho}$ also becomes invariant with respect to the location of the reference point. Besides, one must keep in mind that $\boldsymbol{F}_{m_\rho}$ consists of a volume and a surface integral according to (2.1.9). The surface integral is then split in the same way as $\boldsymbol{R}_{m_\rho}$ by using the symmetry properties (2.3.38) of the double cross product $\boldsymbol{r}\times\left(\boldsymbol{n}\times\frac{q^2}{2}\nabla\rho\right)$ in the far field and $\boldsymbol{F}_{m_\rho}$ is expressed as follows:

$$\begin{aligned}\boldsymbol{F}_{m_\rho} = &\int_\Omega\frac{q^2}{2}\nabla\rho\mathrm{d}v\\ &+\frac{1}{\mathcal{N}-1}(\boldsymbol{I}+\boldsymbol{S}_y)\cdot(\boldsymbol{I}+\boldsymbol{S}_z)\cdot\int_{S_w}^{y,z\geq 0}\boldsymbol{r}\times\left(\boldsymbol{n}\times\frac{q^2}{2}\nabla\rho\right)\mathrm{d}S\\ &+\frac{1}{\mathcal{N}-1}(\boldsymbol{I}+\boldsymbol{S}_x)\cdot(\boldsymbol{I}+\boldsymbol{S}_y)\cdot\int_{S_e\setminus S_w}^{x,y\geq 0}\boldsymbol{r}\times\left(\boldsymbol{n}\times\frac{q^2}{2}\nabla\rho\right)\mathrm{d}S\end{aligned} \tag{2.3.53}$$

Having that

$$(\boldsymbol{I}+\boldsymbol{S}_x)\cdot(\boldsymbol{I}+\boldsymbol{S}_y)=\begin{pmatrix}0&0&0\\0&0&0\\0&0&4\end{pmatrix} \tag{2.3.54}$$

it means that the wake symmetries with respect to the planes $y = 0$ and $z = 0$ again reduce the surface integral on S_w to a drag contribution only, while the upstream-downstream symmetries with respect to the planes $x = 0$ and $y = 0$ reduce the surface integral on $S_e \setminus S_w$ to a lift contribution only:

$$\begin{aligned}\boldsymbol{F}_{m_\rho} = &\int_\Omega\frac{q^2}{2}\nabla\rho\mathrm{d}v\\ &+\frac{4}{\mathcal{N}-1}\left(\int_{S_w}^{y,z\geq 0}\boldsymbol{r}\times\left(\boldsymbol{n}\times\frac{q^2}{2}\nabla\rho\right)\mathrm{d}S\right)\boldsymbol{e}_x\\ &+\frac{4}{\mathcal{N}-1}\left(\int_{S_e\setminus S_w}^{x,y\geq 0}\boldsymbol{r}\times\left(\boldsymbol{n}\times\frac{q^2}{2}\nabla\rho\right)\mathrm{d}S\right)\boldsymbol{e}_z\end{aligned} \tag{2.3.55}$$

In the end, it has been shown that the appearance of flow symmetries eliminates the resulting terms $\boldsymbol{R}_{S_e}$ and $\boldsymbol{R}_{m_\rho}$ such that the necessary condition (2.1.17) for the invariance to the location of the reference point is fulfilled. It explains why Mele *et al.*'s decomposition [31, 32, 36] becomes reference-point-invariant in the far field. Moreover, it has been observed that the wake symmetries reduce the surface integrals in $\boldsymbol{F}_{S_e}$ and $\boldsymbol{F}_{m_\rho}$ to a drag contribution, while the upstream-downstream symmetries reduce them to a lift contribution. Those insights will actually be crucial for the development of a Lamb-vector-based force decomposition completely invariant to the location of the reference point everywhere in the flow field. In the following, the influence of the symmetries on the terms $\Delta\boldsymbol{F}_{\rho l}$ and $\Delta\boldsymbol{F}_{m_\rho}$ will be investigated.

Consequences on the terms $\Delta \boldsymbol{F}_{\rho l}$ and $\Delta \boldsymbol{F}_{m_\rho}$

In the present analysis, it will be shown that the appearance of symmetries, expecially the wake symmetries, partially explains why Mele *et al.*'s decomposition progressively becomes invariant to the size of the integration domain. Here, it is necessary to focus on the effects of the symmetries on the terms $\Delta \boldsymbol{F}_{\rho l}$ and $\Delta \boldsymbol{F}_{m_\rho}$ which are responsible for the sensitivity in the near field. In this case, the invariance to the size of the integration domain is achieved faster in practice than the invariance to the reference point (see section 2.2). Therefore, the velocity field cannot be linearized as in the previous analysis and the Lamb vector satisfies the symmetry properties (2.3.13) initially derived in subsection 2.3.1.

Let $\Delta\Omega_w$ be the part of the volume extension $\Delta\Omega$ which crosses the wake. Then, the volume integral in the term $\Delta \boldsymbol{F}_{\rho l}$ can be limited to $\Delta\Omega_w$ since this term contains only the Lamb vector:

$$\Delta \boldsymbol{F}_{\rho l} = -\int_{\Delta\Omega_w} \rho \boldsymbol{l} \mathrm{d}v \tag{2.3.56}$$

The next step consists in splitting the integral into contributions for $y \geq 0$, $y \leq 0$, $z \geq 0$ and $z \leq 0$. Then, by using the symmetry properties (2.3.13) satisfied by the Lamb vector in the far wake, $\Delta \boldsymbol{F}_{\rho l}$ is expressed as

$$\Delta \boldsymbol{F}_{\rho l} = -\underbrace{(\boldsymbol{I} + \boldsymbol{S}_y) \cdot (\boldsymbol{I} - \boldsymbol{S}_y)}_{=0} \cdot \int_{\Delta\Omega_w}^{y,z\geq 0} \rho \boldsymbol{l} \mathrm{d}v = \boldsymbol{0} \tag{2.3.57}$$

Regarding the term $\Delta \boldsymbol{F}_{m_\rho}$, the volume integral is split into a wake contribution on $\Delta\Omega_w$ and another one on $\Delta\Omega \setminus \Delta\Omega_w$:

$$\Delta \boldsymbol{F}_{m_\rho} = \frac{1}{\mathcal{N}-1} \int_{\Delta\Omega_w} \boldsymbol{r} \times \left(\nabla \left(\frac{q^2}{2} \right) \times \nabla \rho \right) \mathrm{d}v + \frac{1}{\mathcal{N}-1} \int_{\Delta\Omega \setminus \Delta\Omega_w} \boldsymbol{r} \times \left(\nabla \left(\frac{q^2}{2} \right) \times \nabla \rho \right) \mathrm{d}v \tag{2.3.58}$$

Then the first integral on $\Delta\Omega_w$ is split into contributions for $y \geq 0$, $y \leq 0$, $z \geq 0$ and $z \leq 0$ and the second integral into contributions for $y \geq 0$, $y \leq 0$, $x \geq 0$ and $x \leq 0$. With the use of the symmetry properties (2.3.38) with respect to $y = 0$ and $z = 0$ on the first integral and those with respect to $x = 0$ and $y = 0$ on the second integral, it is possible to write $\Delta \boldsymbol{F}_{m_\rho}$ as follows:

$$\begin{aligned} \Delta \boldsymbol{F}_{m_\rho} = & \frac{1}{\mathcal{N}-1} (\boldsymbol{I} + \boldsymbol{S}_y) \cdot (\boldsymbol{I} + \boldsymbol{S}_z) \cdot \int_{\Delta\Omega_w}^{y,z\geq 0} \boldsymbol{r} \times \left(\nabla \left(\frac{q^2}{2} \right) \times \nabla \rho \right) \mathrm{d}v \\ & + \frac{1}{\mathcal{N}-1} (\boldsymbol{I} + \boldsymbol{S}_x) \cdot (\boldsymbol{I} + \boldsymbol{S}_y) \cdot \int_{\Delta\Omega \setminus \Delta\Omega_w}^{x,y\geq 0} \boldsymbol{r} \times \left(\nabla \left(\frac{q^2}{2} \right) \times \nabla \rho \right) \mathrm{d}v \end{aligned} \tag{2.3.59}$$

Finally,

$$\begin{aligned} \Delta \boldsymbol{F}_{m_\rho} = & \frac{4}{\mathcal{N}-1} \left(\int_{\Delta\Omega_w}^{y,z\geq 0} \boldsymbol{r} \times \left(\nabla \left(\frac{q^2}{2} \right) \times \nabla \rho \right) \mathrm{d}v \right) \boldsymbol{e}_x \\ & + \frac{4}{\mathcal{N}-1} \left(\int_{\Delta\Omega \setminus \Delta\Omega_w}^{x,y\geq 0} \boldsymbol{r} \times \left(\nabla \left(\frac{q^2}{2} \right) \times \nabla \rho \right) \mathrm{d}v \right) \boldsymbol{e}_z \neq \boldsymbol{0} \end{aligned} \tag{2.3.60}$$

In the end, it was shown that $\Delta \boldsymbol{F}_{\rho l}$ progressively disappears because of the symmetries satisfied by the Lamb vector in the wake so that the vortex force $\boldsymbol{F}_{\rho l}$ does not contribute anymore to the lift and the drag in the far field. However, the study of the symmetries has not enabled to determine why $\boldsymbol{F}_{m_\rho}$ quickly becomes constant: indeed, the symmetries satisfied in the far field by the quantity $\boldsymbol{r} \times \left(\nabla \left(\frac{q^2}{2} \right) \times \nabla \rho \right)$ do not yield $\Delta \boldsymbol{F}_{m_\rho} = \boldsymbol{0}$ and the necessary condition for the invariance (2.2.14) is theoretically not satisfied. Yet, it was observed in section 2.2 that the sensitivity of the lift and the lift-induced drag to the size of the integration domain is mostly caused by the evolution of $\boldsymbol{F}_{\rho l}$ whereas $\boldsymbol{F}_{m_\rho}$ is almost constant.

Chapter summary

A theoretical analysis has emphasized the appearance of additional terms in the force decomposition when proceeding to a shift in the reference point. It has been shown that these additional terms are responsible for the sensitivity of the decomposition to the location of this point. Then, numerical simulations have evidenced that the sensitivity to the reference point is more important when the size of the integration domain is small, because the magnitude of the additional terms is still significant in the near field. On the contrary, they have suggested that the decomposition becomes invariant when the size of the integration domain is increased, because the magnitude of these terms tends to zero in the far field.

Then, for a fixed reference point, another theoretical analysis has highlighted the transfer occuring between the various force contributions when increasing the size of the integration domain. It has been shown that only the total force remains constant whereas the contributions responsible for the lift-induced drag and the profile drag are likely to vary. It has later been confirmed by numerical simulations: they featured the transfer from the profile drag to the lift-induced drag in the near field of the aircraft. Yet, they have also suggested that the profile drag and the lift-induced drag progressively reach a constant value in the far field.

Finally, the role of the flow symmetries on the invariance in the far field has been proved. First of all, two sets of symmetries have been introduced: the symmetries in the wake and the symmetries up and downstream of the aircraft. Then, it has been shown that the symmetries eliminate the additional terms resulting from a shift in the reference point, therefore explaining how Mele *et al.*'s decomposition [31, 32, 36] becomes reference-point-invariant in the far field. Moreover, it has also been shown that the Lamb vector does not contribute anymore to the aerodynamic force in the presence of those symmetries in the far field, which partially, if not largely, explains how Mele *et al.*'s decomposition becomes domain-invariant.

In conclusion, the sensitivities to the reference point and the integration domain inevitably question the objectiveness of the method: how to legitimately define the lift-induced drag and the profile drag if both depend on such parameters? Fortunately, the study of the flow symmetries highlighted the mechanisms that bring the decomposition to become invariant in the far field. In fact, the control volume must be such that its external boundaries lie in regions where the symmetries are fulfilled. Unfortunately, this implies that the grid on which the surface integrals are computed is coarser which inevitably leads to errors in the assessment of the lift and the drag. Thus, it is crucial to find a method which makes the decomposition invariant everywhere. In the next chapter, a method based on flow symmetrization will be implemented in order to develop a reference-point-invariant Lamb-vector-based aerodynamic force decomposition.

Chapter 3

Development of a Reference-Point-Invariant Lamb-Vector-Based Decomposition by Flow Symmetrization

It has been shown that Mele *et al.*'s decomposition [31, 32, 36] is sensitive to the location of the reference point in the near field and is invariant in the far field. The aim of this chapter is to develop a new formulation which provides a decomposition invariant everywhere in the flow field, i.e. whatever the size of the integration domain.

In the first section, the flow is first symmetrized in order to set up in the near field the same symmetry properties it fulfills in the far field, and hence be in the same flow conditions as those responsible for the invariance to the reference point. In particular, the flow quantities are split into a near-field component and a far-field component which satisfies the symmetries.

In the second section, the new formulation is established. To do so, only the far-field component is accounted for and introduced in the integrals of the terms responsible for the sensitivity. Then, it is shown that the new expressions eliminate the sensitive terms and hence ensure the invariance of the decomposition to the location of the reference point everywhere in the flow field. Finally, the lift and drag contributions of each term are reconstructed by introducing the far-field components in the integrals containing the position vector.

In the third section, the new formulation is tested on the OAT15A airfoil and the NASA CRM in order to compare the results with those obtained with the sensitive formulation. Eventually, the decomposition provided by the new formulation is compared to that provided by the thermodynamic approach of Destarac and Van der Vooren [21].

3.1 Flow symmetrization in the near field

It has been proved that the invariance of Mele *et al.*'s decomposition [31, 32, 36] to the location of the reference point appears in the far field where the flow satisfies symmetries. In order to develop a reference-point-invariant formulation, it is then necessary to isolate the flow quantities which satisfy the far-field symmetries everywhere in the flow field.

To do so, the flow quantities are split into a near-field component and a far-field component: this is what is called the flow symmetrization. The principle is first explained on a one-dimensional function of a single variable. Then, it is applied to the flow quantities and the far-field component is defined such that it fulfills the previously introduced symmetries (see section 2.3).

3.1.1 Illustration with a one-dimensional example

In section 2.1, it has been shown that the Lamb vector and the quantities $\frac{q^2}{2}\nabla\rho$ and $\nabla\left(\frac{q^2}{2}\right)\times\nabla\rho$ are involved in the terms responsible for the sensitivity to the location of the reference point. In section 2.3, it has been proved that the invariance is achieved as soon as they satisfy symmetry properties in the far field. It suggests that these flow quantities can be decomposed into a part which does not satisfy the symmetries and is theoretically expected to disappear in the far field, and another one which satisfies the symmetries everywhere in the flow and persists in the far field. The former part is from now on referred to as the near-field component and the latter part as the far-field component.

To illustrate this point, let us analyse the case of a function φ of a single variable ξ. It can be shown that φ is uniquely decomposed into a symmetrical part φ_s and an antisymmetrical part φ_a as follows:

$$\varphi(\xi) = \varphi_s(\xi) + \varphi_a(\xi) \tag{3.1.1}$$

with

$$\varphi_s(\xi) = \frac{1}{2}\left(\varphi(\xi) + \varphi(-\xi)\right) \tag{3.1.2}$$

$$\varphi_a(\xi) = \frac{1}{2}\left(\varphi(\xi) - \varphi(-\xi)\right) \tag{3.1.3}$$

In fact, it is clearly seen that

$$\varphi_s(-\xi) = \varphi_s(\xi) \tag{3.1.4}$$

$$\varphi_a(-\xi) = -\varphi_a(\xi) \tag{3.1.5}$$

In section 2.1, it has been evidenced that the sensitivity to the location of the reference point is caused by the presence of the position vector $\boldsymbol{r}$ in the integrals of $\boldsymbol{F}_{S_e}$ and $\boldsymbol{F}_{m_\rho}$:

$$\boldsymbol{F}_{S_e} = -\frac{1}{\mathcal{N}-1}\oint_{S_e}\boldsymbol{r}\times(\boldsymbol{n}\times\rho\boldsymbol{l})\,\mathrm{d}S \tag{3.1.6}$$

$$\boldsymbol{F}_{m_\rho} = \int_\Omega \frac{q^2}{2}\nabla\rho\mathrm{d}v + \frac{1}{\mathcal{N}-1}\oint_{S_e}\boldsymbol{r}\times\left(\boldsymbol{n}\times\frac{q^2}{2}\nabla\rho\right)\mathrm{d}S \tag{3.1.7}$$

or

$$\boldsymbol{F}_{m_\rho} = \frac{1}{\mathcal{N}-1}\int_\Omega \boldsymbol{r}\times\left(\nabla\left(\frac{q^2}{2}\right)\times\nabla\rho\right)\mathrm{d}v \tag{3.1.8}$$

In the case of the one-dimensional function φ, those integrals are represented by

$$\int_{-a}^{a}\xi\varphi(\xi)\,\mathrm{d}\xi$$

where φ may represent $\boldsymbol{n} \times \rho\boldsymbol{l}$, $\boldsymbol{n} \times \frac{q^2}{2}\nabla\rho$ or $\nabla\left(\frac{q^2}{2}\right) \times \nabla\rho$, and ξ represents $\boldsymbol{r}$. The interval $[-a, a]$ is centered on zero and represents a surface S_e chosen symmetrical with respect to the planes $x = 0$, $y = 0$ and $z = 0$ in three dimensions. In this case, changing the location of the reference point comes down to replacing ξ by $\xi + \xi_0$. Let us define the integral $I(\xi_0)$ as follows:

$$I(\xi_0) = \int_{-a}^{a} (\xi + \xi_0)\, \varphi(\xi)\, \mathrm{d}\xi \tag{3.1.9}$$

Therefore, the invariance to the location of the reference point is ensured when

$$I(\xi_0) = I(0) \tag{3.1.10}$$

By using the decomposition of φ in (3.1.1), it is possible to develop the integral in (3.1.9):

$$\begin{aligned} I(\xi_0) &= \int_{-a}^{a} \xi\varphi(\xi)\, \mathrm{d}\xi + \xi_0 \int_{-a}^{a} \varphi(\xi)\, \mathrm{d}\xi \\ &= I(0) + \xi_0 \int_{-a}^{a} \varphi_s(\xi)\, \mathrm{d}\xi + \xi_0 \int_{-a}^{a} \varphi_a(\xi)\, \mathrm{d}\xi \end{aligned} \tag{3.1.11}$$

Using the variable shift $\chi = -\xi$, it is possible to show that the integral of φ_a is zero:

$$\begin{aligned} \int_{-a}^{a} \varphi_a(\xi)\, \mathrm{d}\xi &= \int_{-a}^{0} \varphi_a(\xi)\, \mathrm{d}\xi + \int_{0}^{a} \varphi_a(\xi)\, \mathrm{d}\xi \\ &= -\int_{a}^{0} \varphi_a(-\chi)\, \mathrm{d}\chi + \int_{0}^{a} \varphi_a(\xi)\, \mathrm{d}\xi \\ &= \int_{a}^{0} \varphi_a(\chi)\, \mathrm{d}\chi + \int_{0}^{a} \varphi_a(\xi)\, \mathrm{d}\xi \\ &= -\int_{0}^{a} \varphi_a(\chi)\, \mathrm{d}\chi + \int_{0}^{a} \varphi_a(\xi)\, \mathrm{d}\xi \\ &= 0 \end{aligned} \tag{3.1.12}$$

Hence, $I(\xi_0) = I(0)$ and the invariance is achieved as soon as $\varphi_s(\xi) = 0$. For Mele *et al.*'s decomposition [31, 32, 36], $\varphi_s(\xi) = 0$ in the far field, hence the flow quantities $\boldsymbol{n} \times \rho\boldsymbol{l}$, $\boldsymbol{n} \times \frac{q^2}{2}\nabla\rho$ and $\nabla\left(\frac{q^2}{2}\right) \times \nabla\rho$ become antisymmetrical as φ_a, the resulting terms $\boldsymbol{R}_{S_e}$ and $\boldsymbol{R}_{m_\rho}$ are eliminated and the invariance is achieved. However, those quantities do not enjoy the same properties in the near field since the magnitude of φ_s is still significant there.

Therefore, in order to enforce the invariance everywhere in the flow field, it is necessary to account only for the antisymmetrical part in the integrals containing the position vector $\boldsymbol{r}$. However, the flow quantities involved in Mele *et al.*'s decomposition are vectorial quantities which depend on the three cartesian coordinates x, y and z. As a consequence, it is not convenient to talk about their symmetrical and antisymmetrical parts: rather, those quantities are split into a near-field component and a far-field component. The near-field component is expected to vanish in the far field while the far-field component persists and satisfies the symmetry properties derived earlier.

3.1.2 Breakdown of the flow quantities into near-field and far-field components

In section 2.3, two different families of symmetries have been presented: the wake symmetries and the upstream-downstream symmetries. Therefore, it is necessary to analyse separately the two cases since the flow quantities will be split differently depending on the symmetries the far-field component must satisfy in the flow field.

In subsection 2.3.1, it has been shown that the Lamb vector progressively fulfills symmetry properties in the far wake. Later on, in subsection 2.3.3, it has been shown that l_y and l_z are first-order terms while l_x is a second-order term and is negligible. Then in the far wake:

$$\boldsymbol{l} \approx \boldsymbol{l}_\perp = \begin{pmatrix} 0 \\ l_y \\ l_z \end{pmatrix} \tag{3.1.13}$$

where $\boldsymbol{l}_\perp$ represents the transverse part of the Lamb vector. Under those considerations and using the initial symmetry properties (2.3.13) satisfied by $\rho\boldsymbol{l}$ in the far wake, it is possible to show that, still in the far wake, $\rho\boldsymbol{l}$ now satisfies the following symmetries:

$$\rho\boldsymbol{l}\left(x,-y,z\right) = \boldsymbol{S}_y \cdot \rho\boldsymbol{l}\left(x,y,z\right) \tag{3.1.14a}$$

$$\rho\boldsymbol{l}\left(x,y,-z\right) = \boldsymbol{S}_z \cdot \rho\boldsymbol{l}\left(x,y,z\right) \tag{3.1.14b}$$

Therefore, in the near field, the Lamb vector must be split into a near-wake component $\rho\boldsymbol{l}_{nw}$ and a far-wake component $\rho\boldsymbol{l}_{fw}$ which satisfies (3.1.14) everywhere in the flow field (see [35] for further details):

$$\rho\boldsymbol{l} = \rho\boldsymbol{l}_{nw} + \rho\boldsymbol{l}_{fw} \tag{3.1.15}$$

where

$$\rho\boldsymbol{l}_{nw} = \rho\boldsymbol{l} - \rho\boldsymbol{l}_{fw} \tag{3.1.16}$$

$$\begin{aligned}\rho\boldsymbol{l}_{fw} = \frac{1}{4}\big[&\rho\boldsymbol{l}_\perp\left(x,y,z\right) + \boldsymbol{S}_y \cdot \rho\boldsymbol{l}_\perp\left(x,-y,z\right) \\ &+\boldsymbol{S}_z \cdot \rho\boldsymbol{l}_\perp\left(x,y,-z\right) + \boldsymbol{S}_{yz} \cdot \rho\boldsymbol{l}_\perp\left(x,-y,-z\right)\big]\end{aligned} \tag{3.1.17}$$

and $\boldsymbol{S}_{yz} = \boldsymbol{S}_y \cdot \boldsymbol{S}_z = \boldsymbol{S}_z \cdot \boldsymbol{S}_y$. Using the definition (3.1.17), it is possible to show that $\rho\boldsymbol{l}_{fw}$ satisfies everywhere in the flow field the same symmetries (3.1.14) satisfied by $\rho\boldsymbol{l}$ only in the far wake. Indeed, given that $\boldsymbol{S}_y^2 = \boldsymbol{S}_z^2 = \boldsymbol{I}$, switching y for $-y$ and z for $-z$ yields

$$\begin{aligned}\rho\boldsymbol{l}_{fw}\left(x,-y,z\right) &= \frac{1}{4}\big[\rho\boldsymbol{l}_\perp\left(x,-y,z\right) + \boldsymbol{S}_y \cdot \rho\boldsymbol{l}_\perp\left(x,y,z\right) \\ &\quad +\boldsymbol{S}_z \cdot \rho\boldsymbol{l}_\perp\left(x,-y,-z\right) + \boldsymbol{S}_{yz} \cdot \rho\boldsymbol{l}_\perp\left(x,y,-z\right)\big] \\ &= \frac{1}{4}\big[\boldsymbol{S}_y^2 \cdot \rho\boldsymbol{l}_\perp\left(x,-y,z\right) + \boldsymbol{S}_y \cdot \rho\boldsymbol{l}_\perp\left(x,y,z\right) \\ &\quad +\boldsymbol{S}_y^2 \cdot \boldsymbol{S}_z \cdot \rho\boldsymbol{l}_\perp\left(x,-y,-z\right) + \boldsymbol{S}_y \cdot \boldsymbol{S}_z \cdot \rho\boldsymbol{l}_\perp\left(x,y,-z\right)\big] \\ &= \frac{1}{4}\boldsymbol{S}_y \cdot \big[\boldsymbol{S}_y \cdot \rho\boldsymbol{l}_\perp\left(x,-y,z\right) + \rho\boldsymbol{l}_\perp\left(x,y,z\right) \\ &\quad +\boldsymbol{S}_{yz} \cdot \rho\boldsymbol{l}_\perp\left(x,-y,-z\right) + \boldsymbol{S}_z \cdot \rho\boldsymbol{l}_\perp\left(x,y,-z\right)\big] \\ &= \boldsymbol{S}_y \cdot \rho\boldsymbol{l}_{fw}\left(x,y,z\right)\end{aligned} \tag{3.1.18a}$$

and

$$\begin{aligned}\rho\boldsymbol{l}_{fw}\left(x,y,-z\right) &= \frac{1}{4}\big[\rho\boldsymbol{l}_\perp\left(x,y,-z\right) + \boldsymbol{S}_y \cdot \rho\boldsymbol{l}_\perp\left(x,-y,-z\right) \\ &\quad +\boldsymbol{S}_z \cdot \rho\boldsymbol{l}_\perp\left(x,y,z\right) + \boldsymbol{S}_{yz} \cdot \rho\boldsymbol{l}_\perp\left(x,-y,z\right)\big] \\ &= \frac{1}{4}\big[\boldsymbol{S}_z^2 \cdot \rho\boldsymbol{l}_\perp\left(x,y,-z\right) + \boldsymbol{S}_y \cdot \boldsymbol{S}_z^2 \cdot \rho\boldsymbol{l}_\perp\left(x,-y,-z\right) \\ &\quad +\boldsymbol{S}_z \cdot \rho\boldsymbol{l}_\perp\left(x,y,z\right) + \boldsymbol{S}_y \cdot \boldsymbol{S}_z \cdot \rho\boldsymbol{l}_\perp\left(x,-y,z\right)\big] \\ &= \frac{1}{4}\boldsymbol{S}_z \cdot \big[\boldsymbol{S}_z \cdot \rho\boldsymbol{l}_\perp\left(x,y,-z\right) + \boldsymbol{S}_{yz} \cdot \rho\boldsymbol{l}_\perp\left(x,-y,-z\right) \\ &\quad +\rho\boldsymbol{l}_\perp\left(x,y,z\right) + \boldsymbol{S}_y \cdot \rho\boldsymbol{l}_\perp\left(x,-y,z\right)\big] \\ &= \boldsymbol{S}_z \cdot \rho\boldsymbol{l}_{fw}\left(x,y,z\right)\end{aligned} \tag{3.1.18b}$$

Along with the Lamb vector, it is also necessary to decompose the quantity $\frac{q^2}{2}\nabla\rho$ into near-field and far-field components. This quantity is not limited to the wake as $\rho\boldsymbol{l}$ and also satisfies symmetries outside the wake in the far field. Therefore, its decomposition into near-field and far-field components depends on the symmetries the far-field component must satisfy

$$\frac{q^2}{2}\nabla\rho = \left.\frac{q^2}{2}\nabla\rho\right|_{nf} + \begin{cases} \left.\frac{q^2}{2}\nabla\rho\right|_{fw} \\ \left.\frac{q^2}{2}\nabla\rho\right|_{ud} \end{cases} \tag{3.1.19}$$

Here the near-field component is $\left.\frac{q^2}{2}\nabla\rho\right|_{nf}$ while the far-field component can be defined either as a far-wake component

$$\begin{aligned}\left.\frac{q^2}{2}\nabla\rho\right|_{fw} = \frac{1}{4}\Bigg[&\frac{q^2}{2}\nabla\rho\left(x,y,z\right) + \boldsymbol{S}_y\cdot\frac{q^2}{2}\nabla\rho\left(x,-y,z\right) \\ &+\boldsymbol{S}_z\cdot\frac{q^2}{2}\nabla\rho\left(x,y,-z\right) + \boldsymbol{S}_{yz}\cdot\frac{q^2}{2}\nabla\rho\left(x,-y,-z\right)\Bigg]\end{aligned} \tag{3.1.20}$$

or as an upstream-downstream component

$$\begin{aligned}\left.\frac{q^2}{2}\nabla\rho\right|_{ud} = \frac{1}{4}\Bigg[&\frac{q^2}{2}\nabla\rho\left(x,y,z\right) + \boldsymbol{S}_x\cdot\frac{q^2}{2}\nabla\rho\left(-x,y,z\right) \\ &+\boldsymbol{S}_y\cdot\frac{q^2}{2}\nabla\rho\left(x,-y,z\right) + \boldsymbol{S}_{xy}\cdot\frac{q^2}{2}\nabla\rho\left(-x,-y,z\right)\Bigg]\end{aligned} \tag{3.1.21}$$

with $\boldsymbol{S}_{xy} = \boldsymbol{S}_x\cdot\boldsymbol{S}_y = \boldsymbol{S}_y\cdot\boldsymbol{S}_x$. The far-wake component satisfies the wake symmetries while the upstream-downstream component satisfies the symmetries up and downstream of the aircraft (see relation (2.3.29) in subsection 2.3.3). Indeed, as it has been shown for $\rho\boldsymbol{l}$, by switching x for $-x$, y for $-y$ or z for $-z$ in (3.1.20) and (3.1.21), it is possible to show that they satisfy those symmetries everywhere in the flow field:

$$\left.\frac{q^2}{2}\nabla\rho\right|_{fw}\left(x,-y,z\right) = \boldsymbol{S}_y\cdot\left.\frac{q^2}{2}\nabla\rho\right|_{fw}\left(x,y,z\right) \tag{3.1.22a}$$

$$\left.\frac{q^2}{2}\nabla\rho\right|_{fw}\left(x,y,-z\right) = \boldsymbol{S}_z\cdot\left.\frac{q^2}{2}\nabla\rho\right|_{fw}\left(x,y,z\right) \tag{3.1.22b}$$

while

$$\left.\frac{q^2}{2}\nabla\rho\right|_{ud}\left(-x,y,z\right) = \boldsymbol{S}_x\cdot\left.\frac{q^2}{2}\nabla\rho\right|_{ud}\left(x,y,z\right) \tag{3.1.22c}$$

$$\left.\frac{q^2}{2}\nabla\rho\right|_{ud}\left(x,-y,z\right) = \boldsymbol{S}_y\cdot\left.\frac{q^2}{2}\nabla\rho\right|_{ud}\left(x,y,z\right) \tag{3.1.22d}$$

In the case of a two-dimensional flow, the expressions of the far-field quantities can actually be simplified since the flow is limited to the plane $y = 0$ and hence the y-component of $\rho\boldsymbol{l}$ and $\frac{q^2}{2}\nabla\rho$ is identically zero. Then, the implementation in a post-processing code can be facilitated with the far-field components of $\rho\boldsymbol{l}$ and $\frac{q^2}{2}\nabla\rho$ defined as follows:

$$\rho\boldsymbol{l}_{fw} = \frac{1}{2}\left[\rho\boldsymbol{l}_\perp\left(x,0,z\right) + \boldsymbol{S}_z\cdot\rho\boldsymbol{l}_\perp\left(x,0,-z\right)\right] \tag{3.1.23}$$

and

$$\left.\frac{q^2}{2}\nabla\rho\right|_{fw} = \frac{1}{2}\left[\frac{q^2}{2}\nabla\rho\left(x,0,z\right) + \boldsymbol{S}_z\cdot\frac{q^2}{2}\nabla\rho\left(x,0,-z\right)\right] \tag{3.1.24}$$

while

$$\left.\frac{q^2}{2}\nabla\rho\right|_{ud} = \frac{1}{2}\left[\frac{q^2}{2}\nabla\rho\left(x,0,z\right) + \boldsymbol{S}_x \cdot \frac{q^2}{2}\nabla\rho\left(-x,0,z\right)\right] \tag{3.1.25}$$

Of course, the initial definitions of the far-field components given in (3.1.17), (3.1.20) and (3.1.21) can be implemented as such in the post-processing code in the two-dimensional case as well, but the simplified expressions presented above may greatly ease the work of the developer.

In the end, $\rho\boldsymbol{l}$ has been decomposed as a near-wake component and a far-wake component while $\frac{q^2}{2}\nabla\rho$ has been decomposed as a near-field component and a far-field component which can take the form of a far-wake component or an upstream-downstream component. In both cases, the near-field components are expected to vanish in the far field, and it has been shown that the far-field components satisfy the symmetries everywhere in the flow field. Yet, the flow quantities involved in the resulting terms and the force contributions are the cross products between the position vector $\boldsymbol{r}$ and/or the unit normal $\boldsymbol{n}$, $\rho\boldsymbol{l}$ and $\frac{q^2}{2}\nabla\rho$. Then, it is necessary to derive the symmetries of these cross products.

3.1.3 Symmetry properties of the cross products

In the case of a surface S_e chosen symmetrical with respect to the planes $x = 0$, $y = 0$ and $z = 0$, the unit normal $\boldsymbol{n}$ satisfies the symmetry properties (2.3.30), and it is possible to express the symmetries of the single cross products (the proof is the same as in subsection 2.3.3):

$$\left(\boldsymbol{n} \times \rho\boldsymbol{l}_{fw}\right)\left(x,-y,z\right) = -\boldsymbol{S}_y \cdot \left(\boldsymbol{n} \times \rho\boldsymbol{l}_{fw}\right)\left(x,y,z\right) \tag{3.1.26a}$$

$$\left(\boldsymbol{n} \times \rho\boldsymbol{l}_{fw}\right)\left(x,y,-z\right) = -\boldsymbol{S}_z \cdot \left(\boldsymbol{n} \times \rho\boldsymbol{l}_{fw}\right)\left(x,y,z\right) \tag{3.1.26b}$$

and

$$\left(\boldsymbol{n} \times \left.\frac{q^2}{2}\nabla\rho\right|_{fw}\right)\left(x,-y,z\right) = -\boldsymbol{S}_y \cdot \left(\boldsymbol{n} \times \left.\frac{q^2}{2}\nabla\rho\right|_{fw}\right)\left(x,y,z\right) \tag{3.1.27a}$$

$$\left(\boldsymbol{n} \times \left.\frac{q^2}{2}\nabla\rho\right|_{fw}\right)\left(x,y,-z\right) = -\boldsymbol{S}_z \cdot \left(\boldsymbol{n} \times \left.\frac{q^2}{2}\nabla\rho\right|_{fw}\right)\left(x,y,z\right) \tag{3.1.27b}$$

while

$$\left(\boldsymbol{n} \times \left.\frac{q^2}{2}\nabla\rho\right|_{ud}\right)\left(-x,y,z\right) = -\boldsymbol{S}_x \cdot \left(\boldsymbol{n} \times \left.\frac{q^2}{2}\nabla\rho\right|_{ud}\right)\left(x,y,z\right) \tag{3.1.27c}$$

$$\left(\boldsymbol{n} \times \left.\frac{q^2}{2}\nabla\rho\right|_{ud}\right)\left(x,-y,z\right) = -\boldsymbol{S}_y \cdot \left(\boldsymbol{n} \times \left.\frac{q^2}{2}\nabla\rho\right|_{ud}\right)\left(x,y,z\right) \tag{3.1.27d}$$

Similarly, the position vector $\boldsymbol{r}$ satisfies the symmetry properties (2.3.31), and it is possible to express the symmetries of the double cross products:

$$\left(\boldsymbol{r} \times \left(\boldsymbol{n} \times \rho\boldsymbol{l}_{fw}\right)\right)\left(x,-y,z\right) = \boldsymbol{S}_y \cdot \left(\boldsymbol{r} \times \left(\boldsymbol{n} \times \rho\boldsymbol{l}_{fw}\right)\right)\left(x,y,z\right) \tag{3.1.28a}$$

$$\left(\boldsymbol{r} \times \left(\boldsymbol{n} \times \rho\boldsymbol{l}_{fw}\right)\right)\left(x,y,-z\right) = \boldsymbol{S}_z \cdot \left(\boldsymbol{r} \times \left(\boldsymbol{n} \times \rho\boldsymbol{l}_{fw}\right)\right)\left(x,y,z\right) \tag{3.1.28b}$$

and

$$\left(\boldsymbol{r} \times \left(\boldsymbol{n} \times \left.\frac{q^2}{2}\nabla\rho\right|_{fw}\right)\right)\left(x,-y,z\right) = \boldsymbol{S}_y \cdot \left(\boldsymbol{r} \times \left(\boldsymbol{n} \times \left.\frac{q^2}{2}\nabla\rho\right|_{fw}\right)\right)\left(x,y,z\right) \tag{3.1.29a}$$

$$\left(\boldsymbol{r} \times \left(\boldsymbol{n} \times \left.\frac{q^2}{2}\nabla\rho\right|_{fw}\right)\right)\left(x,y,-z\right) = \boldsymbol{S}_z \cdot \left(\boldsymbol{r} \times \left(\boldsymbol{n} \times \left.\frac{q^2}{2}\nabla\rho\right|_{fw}\right)\right)\left(x,y,z\right) \tag{3.1.29b}$$

while

$$\left(\boldsymbol{r}\times\left(\boldsymbol{n}\times\frac{q^2}{2}\nabla\rho\Big|_{ud}\right)\right)(-x,y,z)=\boldsymbol{S}_x\cdot\left(\boldsymbol{r}\times\left(\boldsymbol{n}\times\frac{q^2}{2}\nabla\rho\Big|_{ud}\right)\right)(x,y,z) \tag{3.1.29c}$$

$$\left(\boldsymbol{r}\times\left(\boldsymbol{n}\times\frac{q^2}{2}\nabla\rho\Big|_{ud}\right)\right)(x,-y,z)=\boldsymbol{S}_y\cdot\left(\boldsymbol{r}\times\left(\boldsymbol{n}\times\frac{q^2}{2}\nabla\rho\Big|_{ud}\right)\right)(x,y,z) \tag{3.1.29d}$$

Those symmetry properties are fundamental for the analyses to follow: it will be shown that the symmetries of the single cross products eliminate the resulting terms responsible for the sensitivity to the location of the reference point, and those of the double cross products will be used to reconstruct the lift and drag components of the various contributions to the total force.

3.2 Definition of the reference-point-invariant decomposition

The study of the flow symmetries (see section 2.3) has not only provided an explanation for the invariance of Mele *et al.*'s decomposition [31, 32, 36] to the location of the reference point in the far field: it has also provided the necessary insights for the development of a new decomposition that is invariant everywhere in the flow field. Indeed, in section 3.1, the flow quantities have been decomposed into a near-field component and a far-field component which satisfies the far-field symmetries everywhere in the flow field.

In the following, the invariance to the location of the reference point is achieved by introducing only the far-field component in the integrals so that the resulting terms responsible for the sensitivity are identically zero. Yet, accounting solely for the far-field component may change the contribution of the various integrals to the total force. Hence, the force contributions must be reconstructed with the appropriate far-field components in order to preserve the contribution of the integral and ensure its invariance to the reference point. Eventually, the final expression of the invariant decomposition is presented.

3.2.1 Proof of the invariance to the location of the reference point

First of all, it is necessary to check that the previously defined far-field components guarantee the elimination of the resulting terms $\boldsymbol{R}_{m_\rho}$ and $\boldsymbol{R}_{S_e}$

$$\boldsymbol{R}_{m_\rho} = \frac{1}{\mathcal{N}-1}\oint_{S_e} \boldsymbol{n}\times\frac{q^2}{2}\nabla\rho \mathrm{d}S \tag{3.2.1}$$

$$\boldsymbol{R}_{S_e} = -\frac{1}{\mathcal{N}-1}\oint_{S_e} \boldsymbol{n}\times\rho\boldsymbol{l} \mathrm{d}S \tag{3.2.2}$$

and hence the invariance of the decomposition to the location of the reference point. To do so, only the far-field components of $\rho\boldsymbol{l}$ and $\frac{q^2}{2}\nabla\rho$ are introduced in the integrals.

For the resulting term $\boldsymbol{R}_{S_e}$, the far-field component of $\rho\boldsymbol{l}$ is the far-wake component $\rho\boldsymbol{l}_{fw}$ defined in (3.1.17). When replacing $\rho\boldsymbol{l}$ by $\rho\boldsymbol{l}_{fw}$ in (3.2.2), and using the symmetry properties (3.1.26), it is possible to show that the resulting term is zero (the proof is the same as in subsection 2.3.4):

$$\oint_{S_e} \boldsymbol{n}\times\rho\boldsymbol{l}_{fw}\mathrm{d}S = \underbrace{(\boldsymbol{I}-\boldsymbol{S}_y)\cdot(\boldsymbol{I}-\boldsymbol{S}_z)}_{=\boldsymbol{0}}\cdot\int_{S_e}^{y,z\geq 0}\boldsymbol{n}\times\rho\boldsymbol{l}_{fw}\mathrm{d}S = \boldsymbol{0} \tag{3.2.3}$$

For the resulting term $\boldsymbol{R}_{m_\rho}$, the far-field component of $\frac{q^2}{2}\nabla\rho$ may be the far-wake component or the upstream-downstream component, defined in (3.1.20) and (3.1.21). When replacing $\frac{q^2}{2}\nabla\rho$ by the far-wake component in (3.2.1), and using the symmetry properties (3.1.27a) and (3.1.27b), it is possible to show that the resulting term is zero:

$$\oint_{S_e} \boldsymbol{n}\times\frac{q^2}{2}\nabla\rho\bigg|_{fw}\mathrm{d}S = \underbrace{(\boldsymbol{I}-\boldsymbol{S}_y)\cdot(\boldsymbol{I}-\boldsymbol{S}_z)}_{=\boldsymbol{0}}\cdot\int_{S_e}^{y,z\geq 0}\boldsymbol{n}\times\frac{q^2}{2}\nabla\rho\bigg|_{fw}\mathrm{d}S = \boldsymbol{0} \tag{3.2.4}$$

Similarly, when replacing by the upstream-downstream component this time, and using the symmetry properties (3.1.27c) and (3.1.27d), it can be shown that

$$\oint_{S_e} \boldsymbol{n}\times\frac{q^2}{2}\nabla\rho\bigg|_{ud}\mathrm{d}S = \underbrace{(\boldsymbol{I}-\boldsymbol{S}_x)\cdot(\boldsymbol{I}-\boldsymbol{S}_y)}_{=\boldsymbol{0}}\cdot\int_{S_e}^{x,y\geq 0}\boldsymbol{n}\times\frac{q^2}{2}\nabla\rho\bigg|_{ud}\mathrm{d}S = \boldsymbol{0} \tag{3.2.5}$$

Hence, the far-field components defined earlier eliminate the resulting terms responsible for the sensitivity to the location of the reference point and the invariance is achieved everywhere in the flow field. The aim is now to introduce these far-field components in the expression of the various contributions to the total force in order to reconstruct their lift and drag components.

3.2.2 Reconstruction of the aerodynamic force

Indeed, it has been shown in subsection 2.3.4 that the far-field symmetries preserve one component of the force contribution at a time: the wake symmetries conserve the drag component while the lift component is eliminated and the upstream-downstream symmetries conserve the lift component while the drag component is eliminated. That is why it is necessary to reconstruct the lift and the drag components of a given force contribution with the appropriate far-field quantity.

Let us first analyse the case of $\boldsymbol{F}_{S_e}$. According to Mele *et al.* [31, 32, 36] and Kang *et al.* [18], this contribution is responsible for the profile drag and no lift, and only the transverse part of the Lamb vector $\boldsymbol{l}_\perp$ is involved as soon as l_x becomes negligible in the wake:

$$\boldsymbol{F}_{S_e} = -\frac{1}{\mathcal{N}-1}\oint_{S_e} \boldsymbol{r}\times(\boldsymbol{n}\times\rho\boldsymbol{l}_\perp)\,\mathrm{d}S \tag{3.2.6}$$

When replacing $\rho\boldsymbol{l}_\perp$ by the far-wake component $\rho\boldsymbol{l}_{fw}$ in (3.2.6), and using the symmetry properties (3.1.28) of the double cross product this time, it is possible to show that the obtained integral is, indeed, only a drag component:

$$\begin{aligned}-\frac{1}{\mathcal{N}-1}\oint_{S_e} \boldsymbol{r}\times(\boldsymbol{n}\times\rho\boldsymbol{l}_{fw})\,\mathrm{d}S &= -\frac{1}{\mathcal{N}-1}(\boldsymbol{I}+\boldsymbol{S}_y)\cdot(\boldsymbol{I}+\boldsymbol{S}_z)\int_{S_e}^{y,z\geq 0}\boldsymbol{r}\times(\boldsymbol{n}\times\rho\boldsymbol{l}_{fw})\,\mathrm{d}S\\ &= -\frac{1}{\mathcal{N}-1}\begin{pmatrix}4&0&0\\0&0&0\\0&0&0\end{pmatrix}\int_{S_e}^{y,z\geq 0}\boldsymbol{r}\times(\boldsymbol{n}\times\rho\boldsymbol{l}_{fw})\,\mathrm{d}S\end{aligned} \tag{3.2.7}$$

The next step consists in introducing the expression (3.1.17) of $\rho\boldsymbol{l}_{fw}$ in (3.2.7) in order to obtain an integration on the entirety of S_e. To do so, it is necessary to proceed to the coordinate shifts $y\to -y$ and/or $z\to -z$ in order to integrate in $(x,-y,z)$, $(x,y,-z)$ and $(x,-y,-z)$. Then the application of the symmetry properties (2.3.30) and (2.3.31) of $\boldsymbol{r}$ and $\boldsymbol{n}$ yields

$$\begin{aligned}-\frac{1}{\mathcal{N}-1}\oint_{S_e} \boldsymbol{r}\times(\boldsymbol{n}\times\rho\boldsymbol{l}_{fw})\,\mathrm{d}S = -\frac{1}{\mathcal{N}-1}\begin{pmatrix}1&0&0\\0&0&0\\0&0&0\end{pmatrix}\Bigg\{&\int_{S_e}^{y,z\geq 0}\boldsymbol{r}\times(\boldsymbol{n}\times\rho\boldsymbol{l}_\perp)\,\mathrm{d}S\\ &+\int_{S_e}^{y\leq 0,z\geq 0}\boldsymbol{S}_y\cdot\boldsymbol{r}\times(\boldsymbol{S}_y\cdot\boldsymbol{n}\times\boldsymbol{S}_y\cdot\rho\boldsymbol{l}_\perp)\,\mathrm{d}S\\ &+\int_{S_e}^{y\geq 0,z\leq 0}\boldsymbol{S}_z\cdot\boldsymbol{r}\times(\boldsymbol{S}_z\cdot\boldsymbol{n}\times\boldsymbol{S}_z\cdot\rho\boldsymbol{l}_\perp)\,\mathrm{d}S\\ &+\int_{S_e}^{y,z\leq 0}\boldsymbol{S}_{yz}\cdot\boldsymbol{r}\times(\boldsymbol{S}_{yz}\cdot\boldsymbol{n}\times\boldsymbol{S}_{yz}\cdot\rho\boldsymbol{l}_\perp)\,\mathrm{d}S\Bigg\}\end{aligned} \tag{3.2.8}$$

Then, by following the same method as in subsection 2.3.3 (see relation (2.3.37)), the latter expression simplifies as follows:

$$\begin{aligned}-\frac{1}{\mathcal{N}-1}\oint_{S_e} \boldsymbol{r}\times(\boldsymbol{n}\times\rho\boldsymbol{l}_{fw})\,\mathrm{d}S = -\frac{1}{\mathcal{N}-1}\begin{pmatrix}1&0&0\\0&0&0\\0&0&0\end{pmatrix}\Bigg\{&\int_{S_e}^{y,z\geq 0}\boldsymbol{r}\times(\boldsymbol{n}\times\rho\boldsymbol{l}_\perp)\,\mathrm{d}S\\ &+\boldsymbol{S}_y\cdot\int_{S_e}^{y\leq 0,z\geq 0}\boldsymbol{r}\times(\boldsymbol{n}\times\rho\boldsymbol{l}_\perp)\,\mathrm{d}S\\ &+\boldsymbol{S}_z\cdot\int_{S_e}^{y\geq 0,z\leq 0}\boldsymbol{r}\times(\boldsymbol{n}\times\rho\boldsymbol{l}_\perp)\,\mathrm{d}S\\ &+\boldsymbol{S}_{yz}\cdot\int_{S_e}^{y,z\leq 0}\boldsymbol{r}\times(\boldsymbol{n}\times\rho\boldsymbol{l}_\perp)\,\mathrm{d}S\Bigg\}\end{aligned} \tag{3.2.9}$$

Finally, having that

$$\begin{pmatrix}1&0&0\\0&0&0\\0&0&0\end{pmatrix}\cdot\boldsymbol{S}_y=\begin{pmatrix}1&0&0\\0&0&0\\0&0&0\end{pmatrix}\cdot\boldsymbol{S}_z=\begin{pmatrix}1&0&0\\0&0&0\\0&0&0\end{pmatrix}\cdot\boldsymbol{S}_{yz}=\begin{pmatrix}1&0&0\\0&0&0\\0&0&0\end{pmatrix} \tag{3.2.10}$$

it is possible to write the integral as

$$\begin{aligned}-\frac{1}{\mathcal{N}-1}\oint_{S_e}\boldsymbol{r}\times(\boldsymbol{n}\times\rho\boldsymbol{l}_{fw})\,\mathrm{d}S&=-\frac{1}{\mathcal{N}-1}\begin{pmatrix}1&0&0\\0&0&0\\0&0&0\end{pmatrix}\left\{\int_{S_e}^{y,z\geq0}\boldsymbol{r}\times(\boldsymbol{n}\times\rho\boldsymbol{l}_\perp)\,\mathrm{d}S\right.\\&\quad+\int_{S_e}^{y\leq0,z\geq0}\boldsymbol{r}\times(\boldsymbol{n}\times\rho\boldsymbol{l}_\perp)\,\mathrm{d}S\\&\quad+\int_{S_e}^{y\geq0,z\leq0}\boldsymbol{r}\times(\boldsymbol{n}\times\rho\boldsymbol{l}_\perp)\,\mathrm{d}S\\&\quad\left.+\int_{S_e}^{y,z\leq0}\boldsymbol{r}\times(\boldsymbol{n}\times\rho\boldsymbol{l}_\perp)\,\mathrm{d}S\right\}\\&=-\frac{1}{\mathcal{N}-1}\left(\boldsymbol{e}_x\cdot\oint_{S_e}\boldsymbol{r}\times(\boldsymbol{n}\times\rho\boldsymbol{l}_\perp)\,\mathrm{d}S\right)\boldsymbol{e}_x\\&=(\boldsymbol{e}_x\cdot\boldsymbol{F}_{S_e})\,\boldsymbol{e}_x\end{aligned} \tag{3.2.11}$$

The obtained contribution is only the drag component of $\boldsymbol{F}_{S_e}$ as expected. There is no need to reconstruct the lift component in this case since $\boldsymbol{F}_{S_e}$ does not contribute.

Let us now analyse the case of $\boldsymbol{F}_{m_\rho}$. Unlike $\boldsymbol{F}_{S_e}$, this contribution is responsible for part of the lift and part of the lift-induced drag in the decomposition proposed by Mele *et al.* [31, 32, 36]:

$$\boldsymbol{F}_{m_\rho}=\int_\Omega\frac{q^2}{2}\nabla\rho\mathrm{d}v+\frac{1}{\mathcal{N}-1}\oint_{S_e}\boldsymbol{r}\times\left(\boldsymbol{n}\times\frac{q^2}{2}\nabla\rho\right)\mathrm{d}S \tag{3.2.12}$$

Therefore, it is here necessary to reconstruct the lift and the drag contributions of the surface integral. For the drag contribution, the method is the same as that applied to $\boldsymbol{F}_{S_e}$: $\frac{q^2}{2}\nabla\rho$ is replaced by the far-wake component and by following the same steps as before, the surface integral is expressed as follows:

$$\frac{1}{\mathcal{N}-1}\oint_{S_e}\boldsymbol{r}\times\left(\boldsymbol{n}\times\frac{q^2}{2}\nabla\rho\Big|_{fw}\right)\mathrm{d}S=\frac{1}{\mathcal{N}-1}\left(\boldsymbol{e}_x\cdot\oint_{S_e}\boldsymbol{r}\times\left(\boldsymbol{n}\times\frac{q^2}{2}\nabla\rho\right)\mathrm{d}S\right)\boldsymbol{e}_x \tag{3.2.13}$$

For the lift contribution, the steps to follow are the same but $\frac{q^2}{2}\nabla\rho$ is replaced this time by the upstream-downstream component in the surface integral of (3.2.12). When using the symmetry properties (3.1.29c) and (3.1.29d), it is possible to show that the obtained integral is only a lift component:

$$\begin{aligned}\frac{1}{\mathcal{N}-1}\oint_{S_e}\boldsymbol{r}\times\left(\boldsymbol{n}\times\frac{q^2}{2}\nabla\rho\Big|_{ud}\right)\mathrm{d}S&=\frac{1}{\mathcal{N}-1}\left(\boldsymbol{I}+\boldsymbol{S}_x\right)\cdot\left(\boldsymbol{I}+\boldsymbol{S}_y\right)\int_{S_e}^{x,y\geq0}\boldsymbol{r}\times\left(\boldsymbol{n}\times\frac{q^2}{2}\nabla\rho\Big|_{ud}\right)\mathrm{d}S\\&=\frac{1}{\mathcal{N}-1}\begin{pmatrix}0&0&0\\0&0&0\\0&0&4\end{pmatrix}\int_{S_e}^{x,y\geq0}\boldsymbol{r}\times\left(\boldsymbol{n}\times\frac{q^2}{2}\nabla\rho\Big|_{ud}\right)\mathrm{d}S\end{aligned} \tag{3.2.14}$$

It is now necessary to replace $\frac{q^2}{2}\nabla\rho\Big|_{ud}$ by its expression (3.1.21) and proceed to the coordinate shifts $x\to-x$ and/or $y\to-y$ in order to integrate in $(-x,y,z)$, $(x,-y,z)$ and $(-x,-y,z)$

and obtain an integration on the entirety of S_e. Then, with the application of the symmetry properties (2.3.30) and (2.3.31) of $\boldsymbol{r}$ and $\boldsymbol{n}$, and the method introduced in relation (2.3.37), the integral is transformed as

$$\begin{aligned}\frac{1}{\mathcal{N}-1}\oint_{S_e}\boldsymbol{r}\times\left(\boldsymbol{n}\times\frac{q^2}{2}\nabla\rho\Big|_{ud}\right)\mathrm{d}S = \frac{1}{\mathcal{N}-1}\begin{pmatrix}0&0&0\\0&0&0\\0&0&1\end{pmatrix}\Bigg\{&\int_{S_e}^{x,y\geq 0}\boldsymbol{r}\times\left(\boldsymbol{n}\times\frac{q^2}{2}\nabla\rho\right)\mathrm{d}S\\ &+\boldsymbol{S}_x\cdot\int_{S_e}^{x\leq 0,y\geq 0}\boldsymbol{r}\times\left(\boldsymbol{n}\times\frac{q^2}{2}\nabla\rho\right)\mathrm{d}S\\ &+\boldsymbol{S}_y\cdot\int_{S_e}^{x\geq 0,y\leq 0}\boldsymbol{r}\times\left(\boldsymbol{n}\times\frac{q^2}{2}\nabla\rho\right)\mathrm{d}S\\ &+\boldsymbol{S}_{xy}\cdot\int_{S_e}^{x,y\leq 0}\boldsymbol{r}\times\left(\boldsymbol{n}\times\frac{q^2}{2}\nabla\rho\right)\mathrm{d}S\Bigg\}\end{aligned}\tag{3.2.15}$$

Finally, having that

$$\begin{pmatrix}0&0&0\\0&0&0\\0&0&1\end{pmatrix}\cdot\boldsymbol{S}_x=\begin{pmatrix}0&0&0\\0&0&0\\0&0&1\end{pmatrix}\cdot\boldsymbol{S}_y=\begin{pmatrix}0&0&0\\0&0&0\\0&0&1\end{pmatrix}\cdot\boldsymbol{S}_{xy}=\begin{pmatrix}0&0&0\\0&0&0\\0&0&1\end{pmatrix}\tag{3.2.16}$$

it is possible to write the integral as

$$\begin{aligned}\frac{1}{\mathcal{N}-1}\oint_{S_e}\boldsymbol{r}\times\left(\boldsymbol{n}\times\frac{q^2}{2}\nabla\rho\Big|_{ud}\right)\mathrm{d}S &= \frac{1}{\mathcal{N}-1}\begin{pmatrix}0&0&0\\0&0&0\\0&0&1\end{pmatrix}\Bigg\{\int_{S_e}^{x,y\geq 0}\boldsymbol{r}\times\left(\boldsymbol{n}\times\frac{q^2}{2}\nabla\rho\right)\mathrm{d}S\\ &\quad+\int_{S_e}^{x\leq 0,y\geq 0}\boldsymbol{r}\times\left(\boldsymbol{n}\times\frac{q^2}{2}\nabla\rho\right)\mathrm{d}S\\ &\quad+\int_{S_e}^{x\geq 0,y\leq 0}\boldsymbol{r}\times\left(\boldsymbol{n}\times\frac{q^2}{2}\nabla\rho\right)\mathrm{d}S\\ &\quad+\int_{S_e}^{x,y\leq 0}\boldsymbol{r}\times\left(\boldsymbol{n}\times\frac{q^2}{2}\nabla\rho\right)\mathrm{d}S\Bigg\}\\ &=\frac{1}{\mathcal{N}-1}\left(\boldsymbol{e}_z\cdot\oint_{S_e}\boldsymbol{r}\times\left(\boldsymbol{n}\times\frac{q^2}{2}\nabla\rho\right)\mathrm{d}S\right)\boldsymbol{e}_z\end{aligned}\tag{3.2.17}$$

The obtained contribution is only the lift component of the surface integral of $\boldsymbol{F}_{m_\rho}$ as expected.

In conclusion, the drag contribution of $\boldsymbol{F}_{S_e}$ and the surface contribution of $\boldsymbol{F}_{m_\rho}$ to the total force $\boldsymbol{F}$ have been recovered upon replacing $\rho\boldsymbol{l}$ and $\frac{q^2}{2}\nabla\rho$ by their far-field components in the integrals containing the position vector. The expressions are summarized below:

$$-\frac{1}{\mathcal{N}-1}\oint_{S_e}\boldsymbol{r}\times(\boldsymbol{n}\times\rho\boldsymbol{l}_{fw})\,\mathrm{d}S=-\frac{1}{\mathcal{N}-1}\left(\boldsymbol{e}_x\cdot\oint_{S_e}\boldsymbol{r}\times(\boldsymbol{n}\times\rho\boldsymbol{l}_\perp)\,\mathrm{d}S\right)\boldsymbol{e}_x\tag{3.2.18}$$

$$\frac{1}{\mathcal{N}-1}\oint_{S_e}\boldsymbol{r}\times\left(\boldsymbol{n}\times\frac{q^2}{2}\nabla\rho\Big|_{fw}\right)\mathrm{d}S=\frac{1}{\mathcal{N}-1}\left(\boldsymbol{e}_x\cdot\oint_{S_e}\boldsymbol{r}\times\left(\boldsymbol{n}\times\frac{q^2}{2}\nabla\rho\right)\mathrm{d}S\right)\boldsymbol{e}_x\tag{3.2.19}$$

$$\frac{1}{\mathcal{N}-1}\oint_{S_e}\boldsymbol{r}\times\left(\boldsymbol{n}\times\frac{q^2}{2}\nabla\rho\Big|_{ud}\right)\mathrm{d}S=\frac{1}{\mathcal{N}-1}\left(\boldsymbol{e}_z\cdot\oint_{S_e}\boldsymbol{r}\times\left(\boldsymbol{n}\times\frac{q^2}{2}\nabla\rho\right)\mathrm{d}S\right)\boldsymbol{e}_z\tag{3.2.20}$$

3.2.3 Implementation in the case of unsymmetrical surfaces

The aforementioned developments have been carried out considering a surface S_e that is symmetrical with respect to the planes $x=0$, $y=0$ and $z=0$, such that the position vector $\boldsymbol{r}$

and the unit normal $\boldsymbol{n}$ satisfy symmetry properties. It should be noted, however, that the way the flow symmetrization is implemented in the post-processing code allows the method to be applied to unsymmetrical surfaces as well, on which $\boldsymbol{r}$ and $\boldsymbol{n}$ do not necessarily satisfy symmetries. It is due to the fact that, in the post-processing code, it is impossible to evaluate the flow quantities in $(-x, y, z)$, $(x, -y, z)$ or $(x, y, -z)$ since the structured grid cells are identified by their (i, j, k) indices and not by their cartesian coordinates. Then, the far-field components of the flow quantities are not directly defined as such in the code.

Rather, say for $\boldsymbol{F}_{S_e}$, it is necessary to replace $\rho \boldsymbol{l}_{fw}$ by its expression (3.1.17) and proceed to the variable shifts $y \to -y$ and $z \to -z$ in order to write the integral in the following form on S_e:

$$\begin{aligned} -\frac{1}{\mathcal{N}-1}\oint_{S_e} \boldsymbol{r} \times (\boldsymbol{n} \times \rho \boldsymbol{l}_{fw})\,\mathrm{d}S = -\frac{1}{4\,(\mathcal{N}-1)} \Bigg\{ &\oint_{S_e} \boldsymbol{r} \times (\boldsymbol{n} \times \rho \boldsymbol{l}_{\perp})\,\mathrm{d}S \\ &+ \oint_{S_e} \boldsymbol{S}_y \cdot \boldsymbol{r} \times (\boldsymbol{S}_y \cdot \boldsymbol{n} \times \boldsymbol{S}_y \cdot \rho \boldsymbol{l}_{\perp})\,\mathrm{d}S \\ &+ \oint_{S_e} \boldsymbol{S}_z \cdot \boldsymbol{r} \times (\boldsymbol{S}_z \cdot \boldsymbol{n} \times \boldsymbol{S}_z \cdot \rho \boldsymbol{l}_{\perp})\,\mathrm{d}S \\ &+ \oint_{S_e} \boldsymbol{S}_{yz} \cdot \boldsymbol{r} \times (\boldsymbol{S}_{yz} \cdot \boldsymbol{n} \times \boldsymbol{S}_{yz} \cdot \rho \boldsymbol{l}_{\perp})\,\mathrm{d}S \Bigg\} \end{aligned} \tag{3.2.21}$$

With the method presented in subsection 2.3.3 (see relation (2.3.37)) and having that

$$\boldsymbol{I} + \boldsymbol{S}_y + \boldsymbol{S}_z + \boldsymbol{S}_{yz} = \begin{pmatrix} 4 & 0 & 0 \\ 0 & 0 & 0 \\ 0 & 0 & 0 \end{pmatrix} \tag{3.2.22}$$

the integral yields only the drag component of $\boldsymbol{F}_{S_e}$ as expected.

Similarly, in the case of $\boldsymbol{F}_{m_\rho}$, it is necessary to replace the far-wake component by its expression (3.1.20) and proceed to the variables shifts $y \to -y$ and $z \to -z$, and replace the upstream-downstream component by its expression (3.1.21) and proceed to the variables shifts $x \to -x$ and $y \to -y$ in order to obtain

$$\begin{aligned} \frac{1}{\mathcal{N}-1}\oint_{S_e} \boldsymbol{r} \times \left(\boldsymbol{n} \times \frac{q^2}{2}\nabla\rho\bigg|_{fw}\right)\mathrm{d}S = \frac{1}{4\,(\mathcal{N}-1)} \Bigg\{ &\oint_{S_e} \boldsymbol{r} \times \left(\boldsymbol{n} \times \frac{q^2}{2}\nabla\rho\right)\mathrm{d}S \\ &+ \oint_{S_e} \boldsymbol{S}_y \cdot \boldsymbol{r} \times \left(\boldsymbol{S}_y \cdot \boldsymbol{n} \times \boldsymbol{S}_y \cdot \frac{q^2}{2}\nabla\rho\right)\mathrm{d}S \\ &+ \oint_{S_e} \boldsymbol{S}_z \cdot \boldsymbol{r} \times \left(\boldsymbol{S}_z \cdot \boldsymbol{n} \times \boldsymbol{S}_z \cdot \frac{q^2}{2}\nabla\rho\right)\mathrm{d}S \\ &+ \oint_{S_e} \boldsymbol{S}_{yz} \cdot \boldsymbol{r} \times \left(\boldsymbol{S}_{yz} \cdot \boldsymbol{n} \times \boldsymbol{S}_{yz} \cdot \frac{q^2}{2}\nabla\rho\right)\mathrm{d}S \Bigg\} \end{aligned} \tag{3.2.23}$$

and

$$\begin{aligned} \frac{1}{\mathcal{N}-1}\oint_{S_e} \boldsymbol{r} \times \left(\boldsymbol{n} \times \frac{q^2}{2}\nabla\rho\bigg|_{ud}\right)\mathrm{d}S = \frac{1}{4\,(\mathcal{N}-1)} \Bigg\{ &\oint_{S_e} \boldsymbol{r} \times \left(\boldsymbol{n} \times \frac{q^2}{2}\nabla\rho\right)\mathrm{d}S \\ &+ \oint_{S_e} \boldsymbol{S}_x \cdot \boldsymbol{r} \times \left(\boldsymbol{S}_x \cdot \boldsymbol{n} \times \boldsymbol{S}_x \cdot \frac{q^2}{2}\nabla\rho\right)\mathrm{d}S \\ &+ \oint_{S_e} \boldsymbol{S}_y \cdot \boldsymbol{r} \times \left(\boldsymbol{S}_y \cdot \boldsymbol{n} \times \boldsymbol{S}_y \cdot \frac{q^2}{2}\nabla\rho\right)\mathrm{d}S \\ &+ \oint_{S_e} \boldsymbol{S}_{xy} \cdot \boldsymbol{r} \times \left(\boldsymbol{S}_{xy} \cdot \boldsymbol{n} \times \boldsymbol{S}_{xy} \cdot \frac{q^2}{2}\nabla\rho\right)\mathrm{d}S \Bigg\} \end{aligned} \tag{3.2.24}$$

Again, using the method of subsection 2.3.3 in (2.3.37), the first integral yields only the drag component and the second yields the lift component since

$$\boldsymbol{I} + \boldsymbol{S}_x + \boldsymbol{S}_y + \boldsymbol{S}_{xy} = \begin{pmatrix} 0 & 0 & 0 \\ 0 & 0 & 0 \\ 0 & 0 & 4 \end{pmatrix} \tag{3.2.25}$$

In the post-processing code, it is therefore necessary to move to the calculation step which is described in the aforementioned relations: hence all the integrals on the right-hand side are calculated, summed and their sum is eventually divided by 4 (the number of integrals). As a consequence, this implementation process is applicable to any kind of surfaces, no matter whether they are symmetrical are not, even if the method was initially developed for symmetrical ones only.

3.2.4 Presentation of the final invariant formulation

Subsonic flows

The flow symmetrization in the near field has allowed to split the flow quantities and has led to the definition of far-field quantities with which the resulting terms are eliminated and the force contributions reconstructed. In this study, the force decomposition initially proposed by Mele *et al.* [31, 32, 36] has then been made completely invariant to the location of the reference point. The equivalent reference-point-invariant version of this formulation is defined as follows in subsonic flows:

$$\boxed{\begin{aligned} L_{\text{inv}}^{\text{Mele}} &= \left(\boldsymbol{F}_{\rho l} + \boldsymbol{F}_{m_\rho}^{\text{inv}}\right) \cdot \boldsymbol{e}_z && (3.2.26) \\ D_{i,\text{inv}}^{\text{Mele}} &= \left(\boldsymbol{F}_{\rho l} + \boldsymbol{F}_{m_\rho}^{\text{inv}}\right) \cdot \boldsymbol{e}_x && (3.2.27) \\ D_{P,\text{inv}}^{\text{Mele}} &= \boldsymbol{F}_{S_e}^{\text{inv}} \cdot \boldsymbol{e}_x && (3.2.28) \end{aligned}}$$

with

$$\boxed{\begin{aligned} \boldsymbol{F}_{\rho l} &= -\int_\Omega \rho \boldsymbol{l} \mathrm{d}v && (3.2.29) \\ \boldsymbol{F}_{m_\rho}^{\text{inv}} &= \int_\Omega \frac{q^2}{2} \nabla\rho \mathrm{d}v + \frac{1}{\mathcal{N}-1} \oint_{S_e} \boldsymbol{r} \times \left(\boldsymbol{n} \times \frac{q^2}{2} \nabla\rho \Big|_{fw} \right) \mathrm{d}S \\ &\quad + \frac{1}{\mathcal{N}-1} \oint_{S_e} \boldsymbol{r} \times \left(\boldsymbol{n} \times \frac{q^2}{2} \nabla\rho \Big|_{ud} \right) \mathrm{d}S && (3.2.30) \\ \boldsymbol{F}_{S_e}^{\text{inv}} &= -\frac{1}{\mathcal{N}-1} \oint_{S_e} \boldsymbol{r} \times (\boldsymbol{n} \times \rho \boldsymbol{l}_{fw}) \, \mathrm{d}S && (3.2.31) \end{aligned}}$$

In this decomposition, $\boldsymbol{F}_{m_\rho}^{\text{inv}}$ is expressed with a surface integral. Mele and Tognaccini [31] noticed that this form implies that the integration is not limited to the boundary layers and the near wake. Rather, an expression based on a single volume integral is better suited:

$$\boldsymbol{F}_{m_\rho} = \frac{1}{\mathcal{N}-1} \int_\Omega \boldsymbol{r} \times \left(\nabla \left(\frac{q^2}{2} \right) \times \nabla\rho \right) \mathrm{d}v \tag{3.2.32}$$

The invariant form of the latter expression is obtained after defining the far-field components of

$\boldsymbol{f} = \nabla\left(\frac{q^2}{2}\right) \times \nabla\rho$:

$$\begin{aligned}\boldsymbol{f}_{fw} = \frac{1}{4}\left[\boldsymbol{f}\left(x,y,z\right) - \boldsymbol{S}_y \cdot \boldsymbol{f}\left(x,-y,z\right)\right.\\ \left.-\boldsymbol{S}_z \cdot \boldsymbol{f}\left(x,y,-z\right) + \boldsymbol{S}_{yz} \cdot \boldsymbol{f}\left(x,-y,-z\right)\right]\end{aligned} \tag{3.2.33}$$

$$\begin{aligned}\boldsymbol{f}_{ud} = \frac{1}{4}\left[\boldsymbol{f}\left(x,y,z\right) - \boldsymbol{S}_x \cdot \boldsymbol{f}\left(-x,y,z\right)\right.\\ \left.-\boldsymbol{S}_y \cdot \boldsymbol{f}\left(x,-y,z\right) + \boldsymbol{S}_{xy} \cdot \boldsymbol{f}\left(-x,-y,z\right)\right]\end{aligned} \tag{3.2.34}$$

and

$$\boxed{\begin{aligned}\boldsymbol{F}_{m_\rho}^{\text{inv}} = \frac{1}{\mathcal{N}-1}\int_\Omega \boldsymbol{r} \times \left(\nabla\left(\frac{q^2}{2}\right) \times \nabla\rho\right)_{fw} \mathrm{d}v\\ + \frac{1}{\mathcal{N}-1}\int_\Omega \boldsymbol{r} \times \left(\nabla\left(\frac{q^2}{2}\right) \times \nabla\rho\right)_{ud} \mathrm{d}v\end{aligned}} \tag{3.2.35}$$

In practice, it is recommended to use the expression based on the single volume integral because it yields more accurate lift and drag predictions than the expression involving the surface integral. In the case of an unsymmetrical surface S_e, the volume Ω is unsymmetrical as well and $\boldsymbol{r}$ does not necessarily satisfies symmetries in Ω. In this case, the invariance to the reference point is achieved with the same implementation procedure as that described in subsection 3.2.3.

Transonic flows

In transonic flows, shock waves are present on the fuselage and the suction side of the wing (see Fig.F.13 in Appendix F): in such conditions, Mele *et al.* [36] adapted their formulation in order to avoid the integration in the shock wave region Ω_{sw} where the computation of $\boldsymbol{F}_{m_\rho}$ was seen to be inaccurate (see Fig.1.13). Its alternative expression in transonic flows is the following:

$$\begin{aligned}\boldsymbol{F}_{m_\rho}^{\text{trans}} = \frac{1}{\mathcal{N}-1}\int_{\Omega\setminus\Omega_{sw}} \boldsymbol{r} \times \left(\nabla\left(\frac{q^2}{2}\right) \times \nabla\rho\right)\mathrm{d}v + \oint_{\partial\Omega_{sw}} \left(\rho\frac{q^2}{2}\boldsymbol{n}_{sw} - \rho\boldsymbol{q}\left(\boldsymbol{q}\cdot\boldsymbol{n}_{sw}\right)\right)\mathrm{d}S\\ + \frac{1}{\mathcal{N}-1}\oint_{\partial\Omega_{sw}} \boldsymbol{r} \times \left(\boldsymbol{n}_{sw} \times \frac{q^2}{2}\nabla\rho\right)\mathrm{d}S + \int_{\Omega_{sw}} \rho\boldsymbol{l}\mathrm{d}v\end{aligned} \tag{3.2.36}$$

where $\partial\Omega_{sw}$ is the closed surface bounding the shock wave volume Ω_{sw} and $\boldsymbol{n}_{sw}$ is the unit normal pointing outwards. The reason why $\boldsymbol{F}_{m_\rho}$ is inaccurate in transonic flows and the derivation of $\boldsymbol{F}_{m_\rho}^{\text{trans}}$ will be addressed in the next chapter.

In the second line of (3.2.36), a surface integral on $\partial\Omega_{sw}$ contains the position vector $\boldsymbol{r}$. The surface $\partial\Omega_{sw}$ is actually an unsymmetrical surface, on which $\boldsymbol{r}$ and $\boldsymbol{n}_{sw}$ do not necessarily satisfy symmetries, but thanks to the implementation procedure presented in subsection 3.2.3, the invariance of $\boldsymbol{F}_{m_\rho}^{\text{trans,inv}}$ to the location of the reference point is nevertheless guaranteed:

$$\begin{aligned}\boldsymbol{F}_{m_\rho}^{\text{trans,inv}} = \oint_{\partial\Omega_{sw}} \left(\rho\frac{q^2}{2}\boldsymbol{n}_{sw} - \rho\boldsymbol{q}\left(\boldsymbol{q}\cdot\boldsymbol{n}_{sw}\right)\right)\mathrm{d}S + \int_{\Omega_{sw}} \rho\boldsymbol{l}\mathrm{d}v\\ + \frac{1}{\mathcal{N}-1}\int_{\Omega\setminus\Omega_{sw}} \boldsymbol{r}^{\text{sym}} \times \left(\nabla\left(\frac{q^2}{2}\right) \times \nabla\rho\right)_{fw} \mathrm{d}v\\ + \frac{1}{\mathcal{N}-1}\int_{\Omega\setminus\Omega_{sw}} \boldsymbol{r}^{\text{sym}} \times \left(\nabla\left(\frac{q^2}{2}\right) \times \nabla\rho\right)_{ud} \mathrm{d}v\\ + \frac{1}{\mathcal{N}-1}\oint_{\partial\Omega_{sw}} \boldsymbol{r}^{\text{sym}} \times \left(\boldsymbol{n}_{sw}^{\text{sym}} \times \frac{q^2}{2}\nabla\rho\Big|_{fw}\right)\mathrm{d}S\\ + \frac{1}{\mathcal{N}-1}\oint_{\partial\Omega_{sw}} \boldsymbol{r}^{\text{sym}} \times \left(\boldsymbol{n}_{sw}^{\text{sym}} \times \frac{q^2}{2}\nabla\rho\Big|_{ud}\right)\mathrm{d}S\end{aligned} \tag{3.2.37}$$

where $\boldsymbol{r}^{\mathrm{sym}}$ and $\boldsymbol{n}^{\mathrm{sym}}$ are the symmetrized versions of $\boldsymbol{r}$ and $\boldsymbol{n}$ implemented in the post-processing code which satisfy symmetries on $\partial\Omega_{sw}$. Hence, in transonic flows, the reference-point-invariant version of Mele *et al.*'s decomposition is defined as follows:

$$\boxed{\begin{aligned} L_{\mathrm{inv}}^{\mathrm{Mele}} &= \left(\boldsymbol{F}_{\rho l} + \boldsymbol{F}_{m_\rho}^{\mathrm{trans,inv}}\right) \cdot \boldsymbol{e}_z \qquad (3.2.38)\\ D_{i,\mathrm{inv}}^{\mathrm{Mele}} &= \left(\boldsymbol{F}_{\rho l} + \boldsymbol{F}_{m_\rho}^{\mathrm{trans,inv}}\right) \cdot \boldsymbol{e}_x \qquad (3.2.39)\\ D_{P,\mathrm{inv}}^{\mathrm{Mele}} &= \boldsymbol{F}_{S_e}^{\mathrm{inv}} \cdot \boldsymbol{e}_x \qquad (3.2.40) \end{aligned}}$$

3.3 Application to practical numerical cases

In the following, the reference-point-invariant version of Mele *et al.*'s decomposition is applied to the same test cases as the sensitive formulation (see subsection 2.1.3): on the OAT15A airfoil and on the NASA CRM in order to check that the proposed formulation is indeed invariant to the reference point on two-dimensional and three-dimensional test cases.

Later on, the invariant decomposition is compared to the thermodynamic decomposition proposed by Destarac and Van der Vooren [21] in order to compare the predictions of the lift-induced drag and profile drag to those provided by a tried-and-tested method already widely used in the industry.

3.3.1 Application to the OAT15A airfoil

The reference-point-invariant formulation of Mele *et al.*'s decomposition is here applied to the same flow conditions around the OAT15A airfoil as in subsection 2.1.3: $M_\infty = 0.724$, $Re = 3{\times}10^6$ and $\alpha = 1.15°$. Once again, choice was made to perform great shifts in the location of the reference point, of the order of 25 and 50 chord lengths in the X and Z-directions, in order to make sure that the flow symmetrization method presented earlier is effective.

The evolutions of $\boldsymbol{F}^{\text{inv}}_{S_e}$ and $\boldsymbol{F}^{\text{inv}}_{m_\rho}$ with respect to the reference point are displayed in Figs.3.1, 3.2 and 3.3 for an integration domain of increasing size. The aim is to compare the present results to those previously shown in subsection 2.1.3 with the sensitive formulation: that is why $\boldsymbol{F}^{\text{inv}}_{m_\rho}$ is computed here with the surface integral in (3.2.30). The lift and drag coefficient are defined as follows:

$$C^{\text{inv}}_{L_{m_\rho}} = \frac{2\boldsymbol{F}^{\text{inv}}_{m_\rho} \cdot \boldsymbol{e}_z}{\rho_\infty U_\infty^2 S} \tag{3.3.1}$$

$$C^{\text{inv}}_{D_{m_\rho}} = \frac{2\boldsymbol{F}^{\text{inv}}_{m_\rho} \cdot \boldsymbol{e}_x}{\rho_\infty U_\infty^2 S} \tag{3.3.2}$$

$$C^{\text{inv}}_{D_{S_e}} = \frac{2\boldsymbol{F}^{\text{inv}}_{S_e} \cdot \boldsymbol{e}_x}{\rho_\infty U_\infty^2 S} \tag{3.3.3}$$

Only the drag component of $\boldsymbol{F}^{\text{inv}}_{S_e}$ is shown here: its lift component is identically zero because of the symmetries fulfilled by the far-field component of the Lamb vector in the far wake (see subsection 3.2.2). The axes limits have been kept identical to those used in the figures relative to the sensitive formulation in order to better appreciate how well the sensitivity is eliminated by the invariant formulation. In the charts, the three curves correspond to the various locations of the reference point.

First of all, it can be clearly seen in Figs.3.1a and 3.2a that the evolutions of $\boldsymbol{F}^{\text{inv}}_{S_e}$ and $\boldsymbol{F}^{\text{inv}}_{m_\rho}$ are blurred by some discrepancies at one or several locations in the far field, due to numerical errors in the assesment of the surface integrals. Indeed, those integrals contain double cross products involving among else the unit normal and the gradient of the flow quantities, and their evaluation on an ever coarser grid may become inaccurate.

Nevertheless, this issue has been noticed on the sensitive formulation as well. Moreover, the new formulation guarantees a strict invariance to the reference point since the three curves are merged and have all the same evolution. Those results confirm that the reference-point-invariant version of Mele *et al.*'s decomposition is perfectly effective in the case of two-dimensional flows.

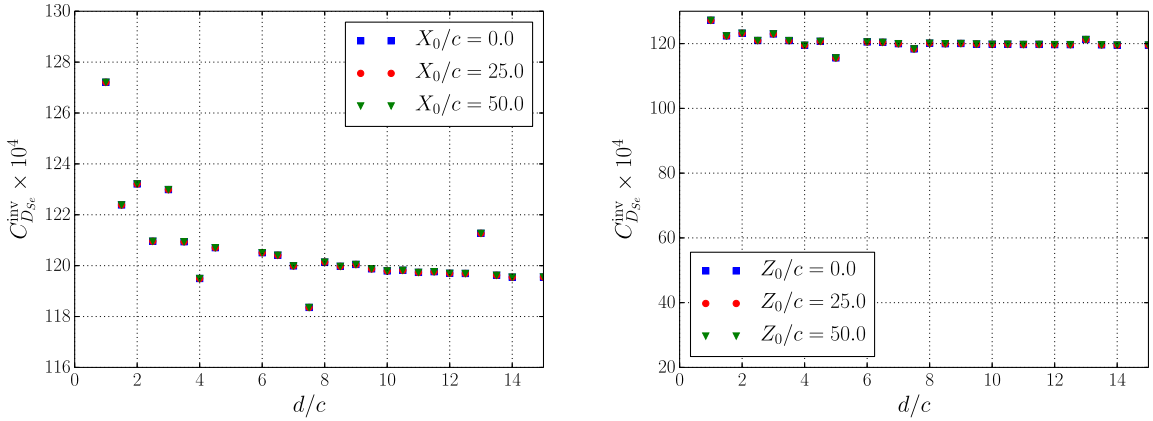

(a) $X \to X + X_0$ (b) $Z \to Z + Z_0$

Figure 3.1: Invariance of $C^{\text{inv}}_{D_{Se}}$ on the OAT15A airfoil, $M_\infty = 0.724$, $Re = 3 \times 10^6$, $\alpha = 1.15°$

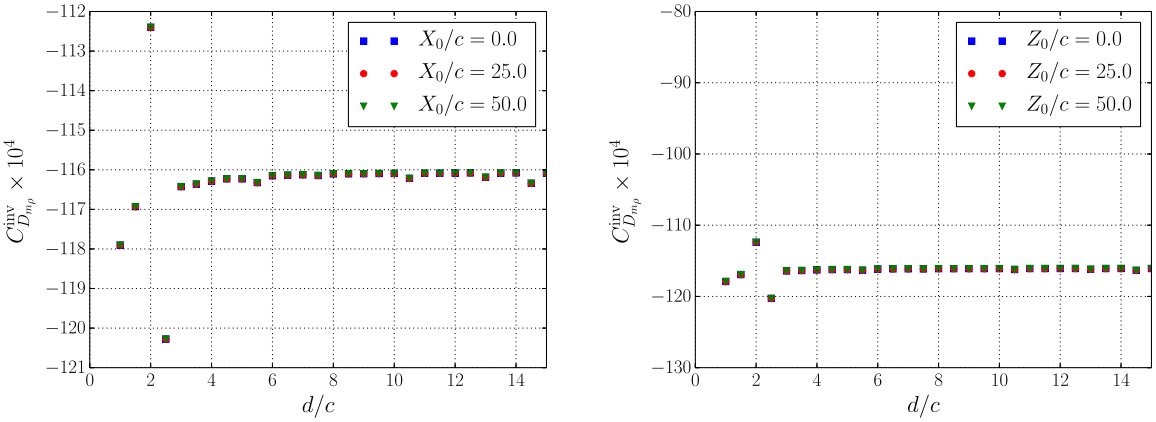

(a) $X \to X + X_0$ (b) $Z \to Z + Z_0$

Figure 3.2: Invariance of $C^{\text{inv}}_{D_{m_\rho}}$ on the OAT15A airfoil, $M_\infty = 0.724$, $Re = 3 \times 10^6$, $\alpha = 1.15°$

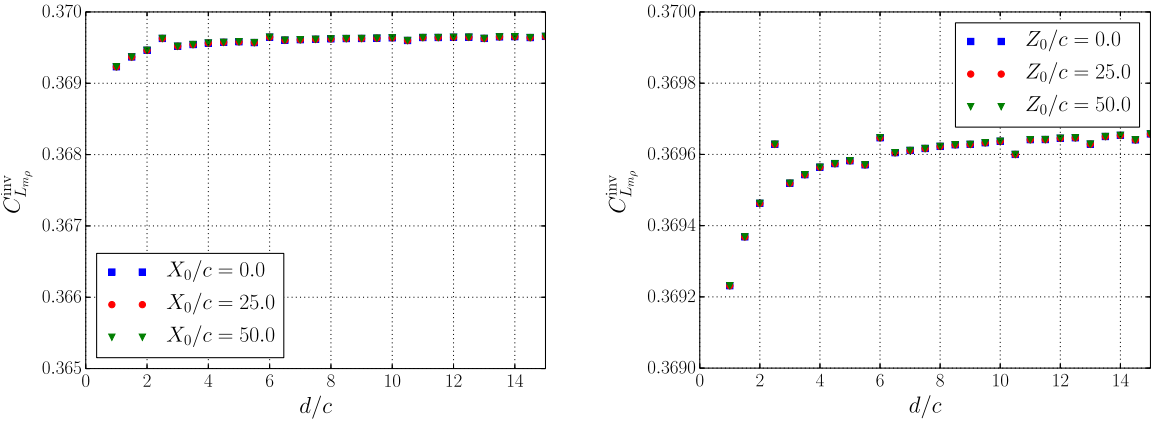

(a) $X \to X + X_0$ (b) $Z \to Z + Z_0$

Figure 3.3: Invariance of $C^{\text{inv}}_{L_{m_\rho}}$ on the OAT15A airfoil, $M_\infty = 0.724$, $Re = 3 \times 10^6$, $\alpha = 1.15°$

3.3.2 Application to the NASA Common Research Model

The invariant formulation is now applied to the same transonic cruise flight conditions around the NASA CRM as before: $M_\infty = 0.85$, $Re = 5 \times 10^6$ and $C_L \approx 0.5$. The shifts in the location of the reference point are the same as in the two-dimensional case: of the order of 25 and 50 reference-chord lengths in the X and Z-directions ($c_{ref} = 7.00532$ m in this case).

The evolutions of $\boldsymbol{F}_{S_e}^{\text{inv}}$ and $\boldsymbol{F}_{m_\rho}^{\text{inv}}$ with respect to the reference point are displayed in Figs.3.4, 3.5 and 3.6 for an integration domain of increasing size. Again, $\boldsymbol{F}_{m_\rho}^{\text{inv}}$ is evaluated with the surface integral in (3.2.30) in order to directly compare the results to those presented in subsection 2.1.3. The definitions of the lift and drag coefficients are the same as in the case of the OAT15A airfoil. In this three-dimensional case, the discrepancies due to the numerical errors seem to be less pronounced than in the two-dimensional case. Once again, the new formulation guarantees a strict invariance to the location of the reference point which acknowledges that the reference-point-invariant version of Mele *et al.*'s decomposition is perfectly effective in the case of three-dimensional flows as well.

In the end, a new invariant aerodynamic force decomposition based on the Lamb vector has been developed and successfully applied to compressible steady viscous flows around the OAT15A airfoil and the NASA CRM. Initially, it has been shown that the decomposition proposed by Mele *et al.* [31, 32, 36] is sensitive to the location of the reference point. Moreover, the sensitivity of $\boldsymbol{F}_{S_e}$ and $\boldsymbol{F}_{m_\rho}$ to the size of the integration domain also varies with a shift in the location of this point (see subsection 2.1.3). On the contrary, the new formulation proposed here guarantees that the sensitivity of $\boldsymbol{F}_{S_e}^{\text{inv}}$ and $\boldsymbol{F}_{m_\rho}^{\text{inv}}$ with respect to the size of the integration domain is the same whatever the location of the reference point.

It is then possible to objectively decompose the lift and the drag with the Lamb vector. In particular, it is now possible to objectively investigate the physical evolution of the decomposition with respect to the size of the integration domain, whatever the location of the reference point. Furthermore, the aerodynamic force decomposition provided by this method may now be compared to former ones.

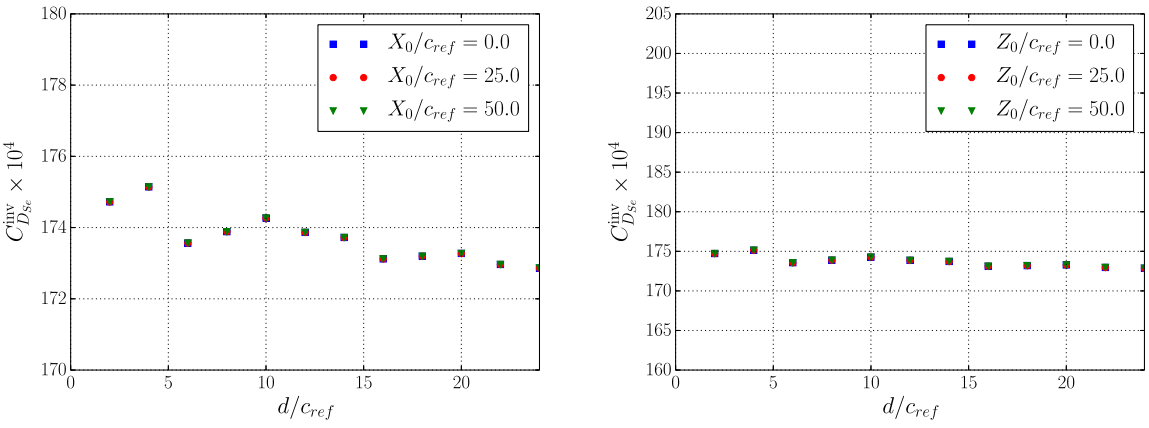

(a) $X \to X + X_0$ (b) $Z \to Z + Z_0$

Figure 3.4: Invariance of $C_{D_{Se}}^{\text{inv}}$ on the NASA CRM, $M_\infty = 0.85$, $Re = 5 \times 10^6$, $C_L \approx 0.5$

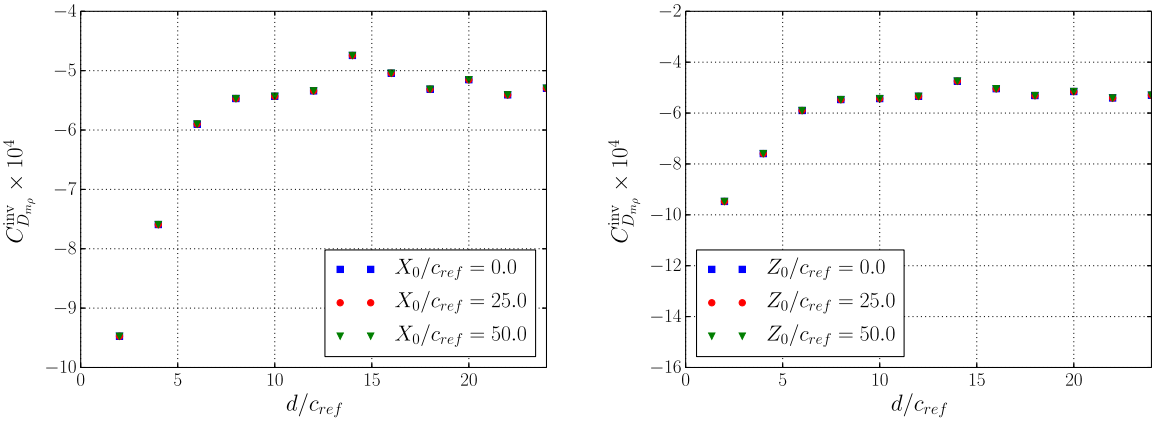

(a) $X \to X + X_0$ (b) $Z \to Z + Z_0$

Figure 3.5: Invariance of $C^{\text{inv}}_{D_{m_\rho}}$ on the NASA CRM, $M_\infty = 0.85$, $Re = 5 \times 10^6$, $C_L \approx 0.5$

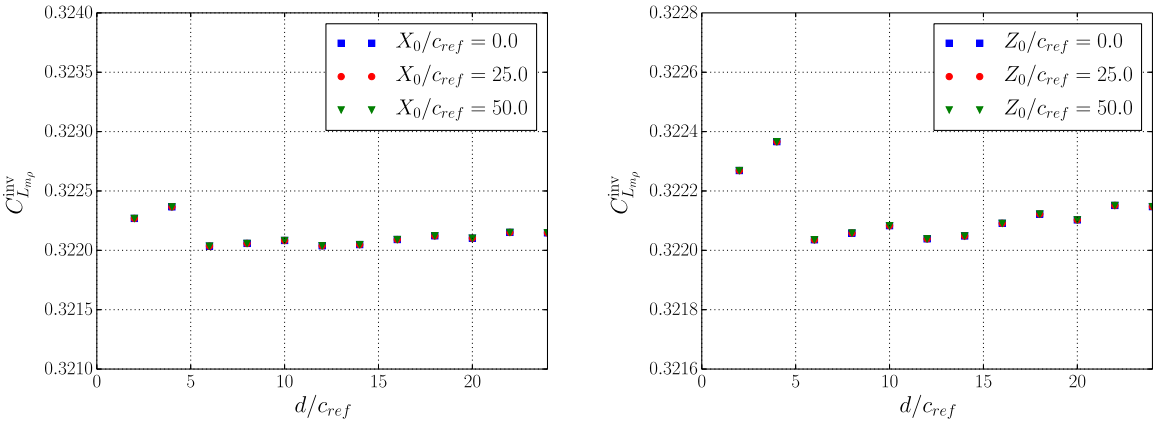

(a) $X \to X + X_0$ (b) $Z \to Z + Z_0$

Figure 3.6: Invariance of $C^{\text{inv}}_{L_{m_\rho}}$ on the NASA CRM, $M_\infty = 0.85$, $Re = 5 \times 10^6$, $C_L \approx 0.5$

3.3.3 Comparison with Destarac and Van der Vooren's formulation

It is interesting to compare the drag decomposition of the new invariant Lamb-vector-based formulation to that calculated by the thermodynamic approach of Destarac and Van der Vooren [21]. Indeed, this thermodynamic formulation is now widely used in industrial projects, owing to its unprecedented robustness and applicability to transonic flows. In the present analysis, both formulations are once again applied to the NASA CRM wing-fuselage configuration in transonic cruise flight conditions: $M_\infty = 0.85$, $Re = 5 \times 10^6$, $C_L \approx 0.5$.

Yet, the previous computations of $\boldsymbol{F}_{m_\rho}$ and $\boldsymbol{F}_{m_\rho}^{\text{inv}}$ did not avoid the shock wave region, which could potentially lead to erroneous lift and drag predictions. The aim is now to obtain accurate results in order to compare them to the thermodynamic decomposition. Then, the contribution of $\boldsymbol{F}_{m_\rho}$ is computed using the invariant transonic version $\boldsymbol{F}_{m_\rho}^{\text{trans,inv}}$ defined in (3.2.37) such that the lift, the lift-induced drag and the profile drag are evaluated using the transonic reference-point-invariant formulation given in (3.2.38), (3.2.39) and (3.2.40).

The evolutions of the lift and the drag with respect to the size of the integration domain are displayed in Fig.3.7. The superscript VdV refers to the drag contributions computed with the thermodynamic formulation of Destarac and Van der Vooren [21]. In Fig.3.7a, the profile drag coefficient $C_{D_P}^{\text{VdV}}$ and the lift-induced drag coefficient $C_{D_i}^{\text{VdV}}$ are constant and represented by horizontal lines: actually, the profile drag is computed on the contours of the shock wave region and the boundary layer region which are volumes of constant size. Hence, the lift-induced drag is also a constant because the total drag coefficient C_D^{VdV} does not depend on the size of the integration domain and $C_{D_i}^{\text{VdV}} = C_D^{\text{VdV}} - C_{D_P}^{\text{VdV}}$. In the present analysis $C_{D_P}^{\text{VdV}}$ and $C_{D_i}^{\text{VdV}}$ are taken as reference for the comparison with the drag decomposition provided by the Lamb-vector-based formulation.

It can be seen in Fig.3.7a that the total drag computed by the Lamb-vector-based formulation is in very good agreement with that calculated by the thermodynamic approach starting from $d/c_{ref} \geq 1$. Similarly, the computed lift stabilizes for $d/c_{ref} \geq 1.6$ and is in quite good agreement with the near-field prediction (see Fig.3.7b). On the contrary, it seems that the Lamb-vector-based drag decomposition never reaches the thermodynamic one: the computed lift-induced drag is always lower while the profile drag is always higher.

It is better seen in Fig.3.8. The lift-induced drag increases until it reaches a maximum value at $d/c_{ref} = 1.6$ but is still around 13 counts lower than the thermodynamic reference (see Fig.3.8a). Similarly, the profile drag decreases until it reaches a local minimum value at $d/c_{ref} = 1.8$ but is still 13 counts higher than the thermodynamic prediction (see Fig.3.8b). It suggests that, although the total drag is the same, the drag decomposition provided by the Lamb-vector-based formulation is different from the thermodynamic one and that the physics at stake in the various drag contributions may also differ from one formulation to another.

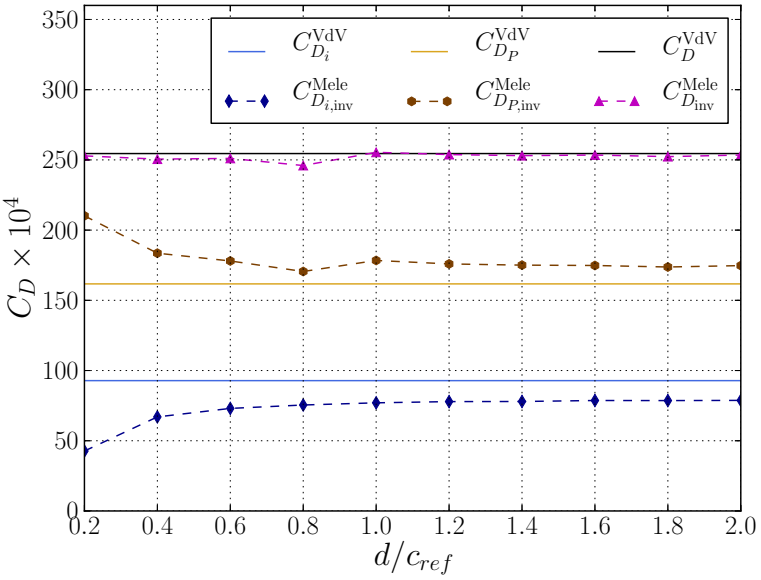

(a) Drag

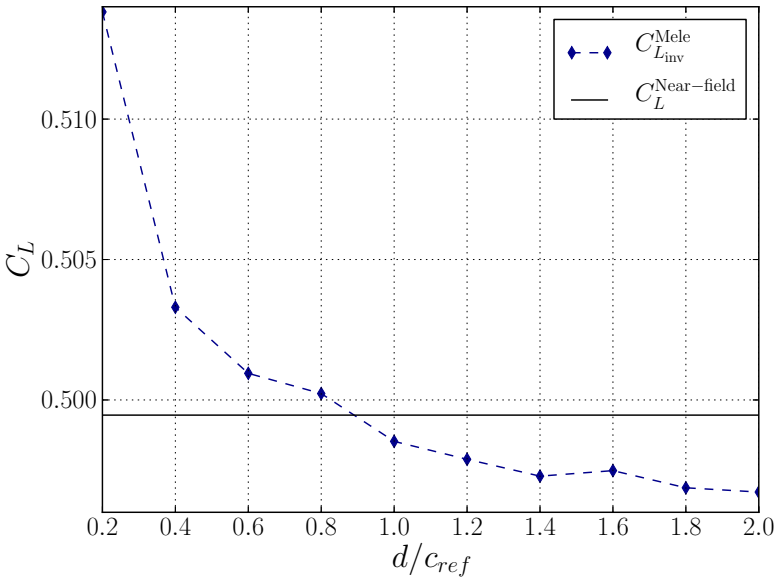

(b) Lift

Figure 3.7: Evolution of the aerodynamic force breakdown with respect to the size of the integration domain: comparison between the reference-point-invariant version of Mele *et al.*'s formulation and Destarac and Van der Vooren's formulation [21] on the NASA CRM, $M_\infty = 0.85$, $Re = 5 \times 10^6$, $C_L \approx 0.5$

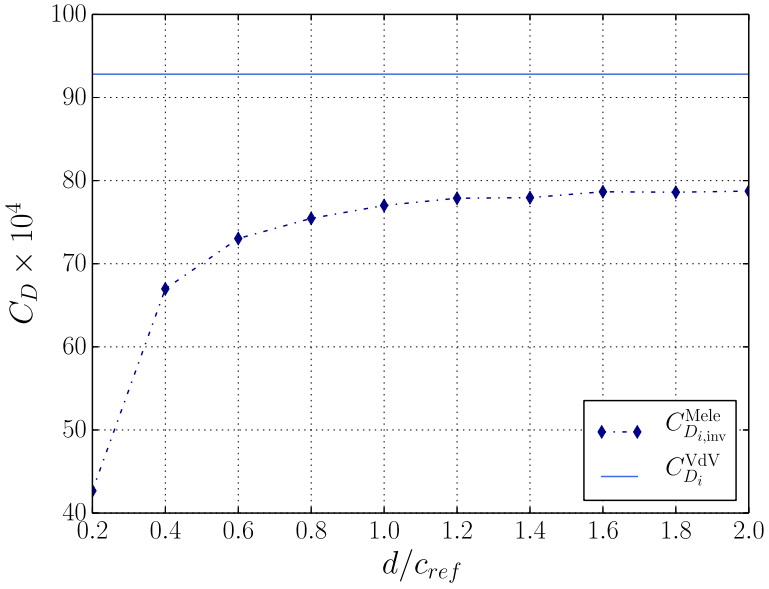

(a) Lift-induced drag

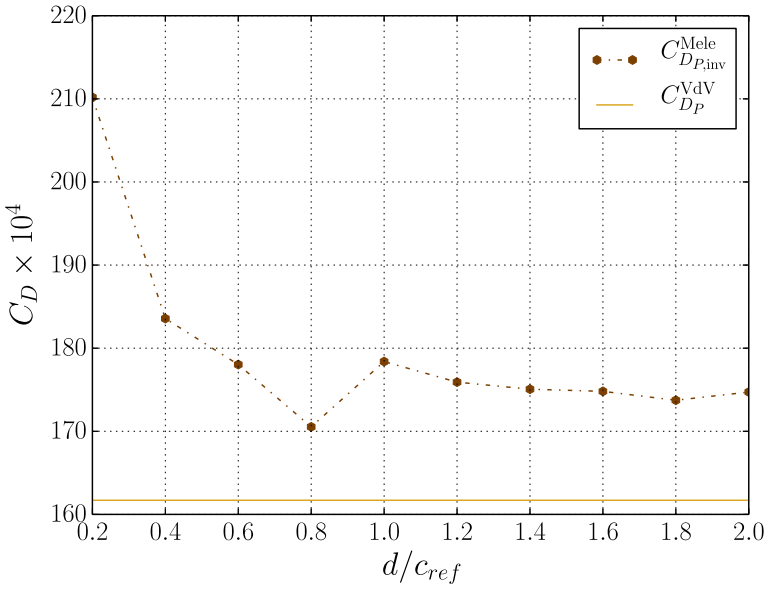

(b) Profile drag

Figure 3.8: Evolution of the lift-induced drag and the profile drag with respect to the size of the integration domain: comparison between the reference-point-invariant version of Mele *et al.*'s formulation and Destarac and Van der Vooren's formulation [21] on the NASA CRM, $M_\infty = 0.85$, $Re = 5 \times 10^6$, $C_L \approx 0.5$

Chapter summary

A symmetrization of the flow has been performed in order to decompose the flow quantities into near-field and far-field components. The far-field components have been defined such that they satisfy the symmetries in the wake or the symmetries up and downstream of the aircraft.

Then, only the far-field components have been accounted for in the integrals of the terms resulting from a shift in the location of the reference point. By doing so, the flow in the near field has been given the same symmetry properties as those it naturally fulfills in the far field. In particular, it has been shown that the resulting terms are identically equal to zero, which guarantees the invariance to the reference point everywhere in the flow field. Later on, the contributions of the integrals containing the position vector have been reconstructed each time with the appropriate far-field component, in order to conserve the invariance to the reference point, and recover the lift or the drag component of the initial integral.

The flow symmetrization method has also proved to be applicable in practice to unsymmetrical surfaces on which the position vector and the unit normal do not necessarily satisfy symmetries. Consequently, this method can be applied to the case of transonic flows, for which there is an additional surface integral containing the position vector on the contour of the shock wave region.

Thus, an exact reference-point-invariant version of Mele *et al.*'s aerodynamic force decomposition [31, 32, 36] has been devised:

Subsonic flows

$$L_{\text{inv}}^{\text{Mele}} = \left(\boldsymbol{F}_{\rho l} + \boldsymbol{F}_{m_\rho}^{\text{inv}}\right) \cdot \boldsymbol{e}_z$$
$$D_{i,\text{inv}}^{\text{Mele}} = \left(\boldsymbol{F}_{\rho l} + \boldsymbol{F}_{m_\rho}^{\text{inv}}\right) \cdot \boldsymbol{e}_x$$
$$D_{P,\text{inv}}^{\text{Mele}} = \boldsymbol{F}_{S_e}^{\text{inv}} \cdot \boldsymbol{e}_x$$

Transonic flows

$$L_{\text{inv}}^{\text{Mele}} = \left(\boldsymbol{F}_{\rho l} + \boldsymbol{F}_{m_\rho}^{\text{trans,inv}}\right) \cdot \boldsymbol{e}_z$$
$$D_{i,\text{inv}}^{\text{Mele}} = \left(\boldsymbol{F}_{\rho l} + \boldsymbol{F}_{m_\rho}^{\text{trans,inv}}\right) \cdot \boldsymbol{e}_x$$
$$D_{P,\text{inv}}^{\text{Mele}} = \boldsymbol{F}_{S_e}^{\text{inv}} \cdot \boldsymbol{e}_x$$

with

$$\boldsymbol{F}_{\rho l} = -\int_\Omega \rho \boldsymbol{l} \mathrm{d}v$$

$$\boldsymbol{F}_{m_\rho}^{\text{inv}} = \frac{1}{\mathcal{N}-1}\int_\Omega \boldsymbol{r} \times \left(\nabla\left(\frac{q^2}{2}\right) \times \nabla\rho\right)_{fw} \mathrm{d}v + \frac{1}{\mathcal{N}-1}\int_\Omega \boldsymbol{r} \times \left(\nabla\left(\frac{q^2}{2}\right) \times \nabla\rho\right)_{ud} \mathrm{d}v$$

$$\boldsymbol{F}_{m_\rho}^{\text{trans,inv}} = \oint_{\partial\Omega_{sw}} \left(\rho\frac{q^2}{2}\boldsymbol{n}_{sw} - \rho\boldsymbol{q}\left(\boldsymbol{q}\cdot\boldsymbol{n}_{sw}\right)\right)\mathrm{d}S + \int_{\Omega_{sw}} \rho\boldsymbol{l}\mathrm{d}v + \frac{1}{\mathcal{N}-1}\int_{\Omega\setminus\Omega_{sw}} \boldsymbol{r}^{\text{sym}} \times \left(\nabla\left(\frac{q^2}{2}\right) \times \nabla\rho\right)_{fw} \mathrm{d}v + \frac{1}{\mathcal{N}-1}\int_{\Omega\setminus\Omega_{sw}} \boldsymbol{r}^{\text{sym}} \times \left(\nabla\left(\frac{q^2}{2}\right) \times \nabla\rho\right)_{ud} \mathrm{d}v + \frac{1}{\mathcal{N}-1}\oint_{\partial\Omega_{sw}} \boldsymbol{r}^{\text{sym}} \times \left(\boldsymbol{n}_{sw}^{\text{sym}} \times \frac{q^2}{2}\nabla\rho\Big|_{fw}\right)\mathrm{d}S + \frac{1}{\mathcal{N}-1}\oint_{\partial\Omega_{sw}} \boldsymbol{r}^{\text{sym}} \times \left(\boldsymbol{n}_{sw}^{\text{sym}} \times \frac{q^2}{2}\nabla\rho\Big|_{ud}\right)\mathrm{d}S$$

$$\boldsymbol{F}_{S_e}^{\text{inv}} = -\frac{1}{\mathcal{N}-1}\oint_{S_e} \boldsymbol{r} \times \left(\boldsymbol{n} \times \rho\boldsymbol{l}_{fw}\right)\mathrm{d}S$$

Then it has successfully been tested on the OAT15A airfoil and the NASA CRM wing-fuselage configuration. With this new formulation, the evolution of the terms of the decomposition with respect to the size of the integration domain does not depend anymore on the location of the

reference point, unlike the initial formulation (see subsection 2.1.3).

Yet, it has been noticed that the new Lamb-vector-based formulation systematically underestimates the lift-induced drag and overestimates the profile drag when compared to the tried-and-tested drag decomposition of Destarac and Van der Vooren [21]. It means that, in these two decompositions, the phenomenological sources of each drag contribution are not exactly the same. As it happens, the physical role of compressibility in lift and drag is still not identified in the Lamb-vector-based formulation. Unfortunately, the mathematical expressions of the terms of Mele *et al.*'s decomposition are difficult to interpret phenomenologically. That is why it is necessary to develop a new formulation more related to former theories, able to identify the role of compressibility in lift and drag, and which could at once improve the decomposition.

Chapter 4

Development of a Transonic Lamb-Vector-Based Formulation Identifying the Role of Compressibility in Lift and Drag

The physical role of the compressibility term $\boldsymbol{F}_{m_\rho}$ in the lift and the lift-induced drag has never been identified in the decomposition proposed by Mele *et al.* [31, 32, 36]. The aim of this chapter is then to understand the physical role played by the compressibility of the flow in lift and drag. By doing so, it may also allow for a better phenomenological interpretation of the other terms of the decomposition in compressible flows. For simplicity, all the mathematical developments are carried out on the original formulation of Mele *et al.* [31, 32, 36] while the reference-point-invariant version is used for the numerical applications.

In the first section, the first step is to find the links between Mele *et al.*'s formulation and the classical theories of Kutta, Joukowski, Maskell and Betz in transonic flows. Indeed, those analyses were the first to relate the lift, the lift-induced drag and the profile drag to their physical sources and the links with Mele *et al.*'s formulation may help understand the role of compressibility. During the process, a compressibility correction term is identified in the expressions. By means of a theoretical asymptotic study and numerical simulations, it is shown that the magnitude of this correction progressively tends to zero in the far field.

In the second section, Mele *et al.*'s formulation is revised in order to shape a new decomposition completely equivalent to the classical theories in transonic flows. This decomposition is called the ONERA decomposition and is naturally independent of the location of the reference point [39]. It is finally applied to practical test cases and compared to the transonic Lamb-vector-based decomposition developed by Mele *et al.* [36] and the thermodynamic decomposition of Destarac and Van der Vooren [21].

In the third section, it is shown that the aerodynamic force can be equivalently decomposed in transonic flows by means of a formulation embedding the three classical theories in a single expression. This formulation is called the Kutta-Joukowski-Maskell-Betz (KJMB) formulation and is applied to practical test cases in order to be compared to the drag decomposition of Destarac and Van der Vooren [21]. Then, the results provided by the ONERA formulation, the formulation of Mele *et al.* [31, 32, 36] and the formulation of Destarac and Van der Vooren [21] are all compared to one another. Finally, the physical role of compressibility in the ONERA and KJMB decompositions is investigated.

4.1 Identification of the role of compressibility through the links with classical theories

In the present section, the Lamb-vector-based decomposition into lift, lift-induced drag and profile drag proposed by Mele *et al.* [31, 32, 36] is analysed. In particular, the role of compressibility in lift and drag is investigated in transonic flows.

First of all, it is necessary to rigorously derive the transonic formulation previously introduced by Mele *et al.* [36]. Actually, they developed their formulation within the frame of transonic flows governed by the RANS equations, considering that the solution is differentiable across shock waves. Hence, in the following momentum balance, the shock waves are this time modeled as discontinuities. Then, an additional contribution to the force involving the jump of the flow quantities on the shock wave surface is identified and $\boldsymbol{F}_{m_\rho}$ is re-expressed in its transonic version $\boldsymbol{F}_{m_\rho}^{\text{trans}}$.

Indeed, Mele and Tognaccini [31] initially defined the lift and the lift-induced drag as the sum of $\boldsymbol{F}_{\rho l}$ and $\boldsymbol{F}_{m_\rho}$ in subsonic flows. Later on, Mele *et al.* [36] defined it as the sum of $\boldsymbol{F}_{\rho l}$ and $\boldsymbol{F}_{m_\rho}^{\text{trans}}$ (defined in (3.2.36)) in transonic flows. Their proposals were actually supported by numerical results. Yet, nothing suggests in the expressions of $\boldsymbol{F}_{m_\rho}$ and $\boldsymbol{F}_{m_\rho}^{\text{trans}}$ that they should contribute to the lift and the lift-induced drag. That is why a theoretical analysis is conducted in order to understand why they should be added to $\boldsymbol{F}_{\rho l}$ in the definition of the lift and the lift-induced drag. To do so, the links with the Kutta-Joukowski lift theorem and Maskell's lift-induced drag formula are investigated.

Similarly, Mele *et al.* [31, 32, 36] initially identified $\boldsymbol{F}_{S_e}$ to be responsible for the profile drag and no lift. In practice, the viscous-turbulent term $\boldsymbol{F}_\tau$ is negligible and was not accounted for. Those observations were again confirmed by numerical results. Here, a theoretical analysis is carried out on the sum of $\boldsymbol{F}_{S_e}$ and $\boldsymbol{F}_\tau$ in order to find a link with Betz's profile drag formula.

4.1.1 Derivation of Mele *et al.*'s formulation in transonic flows

In the following analysis, Mele *et al.*'s formulation will be derived in transonic flows. The flow field is then characterized by the presence of shock waves. In fact, because of the fluid acceleration on the wing, a shock wave usually appears on the suction side. In practice, a shock wave is a layer of very small thickness: it is more or less the same order of magnitude as the mean free path of the gas molecules [103]. Yet, the Navier-Stokes equations come from continuum mechanics, and hence they are not adapted to predict the internal structure of shock waves (see e.g. [41] p. 550-551 or [104] p. 353). To bypass this issue, it is common to represent a shock wave with a surface or line of discontinuity (denoted SW in Fig.4.1) on which the Rankine-Hugoniot relations apply [41, 53, 78, 104]: mass, momentum and energy conservation. To derive the transonic formulation, it is then necessary to account for the presence of those discontinuities.

The fluid domain Ω is divided in three sub-volumes Ω_1, Ω_2 and Ω_3 as shown in Fig.4.1. By proceeding to a Lamb-vector-based momentum balance in each sub-volume (see Appendix C), the transonic version of the Lamb-vector-based formula is obtained:

$$\boxed{\boldsymbol{F} = \boldsymbol{F}_{\rho l} + \boldsymbol{F}_{m_\rho} + \boldsymbol{F}_{S_e} + \boldsymbol{F}_\tau + \boldsymbol{F}_{\text{SW}}} \tag{4.1.1}$$

where

$$\boldsymbol{F}_{\text{SW}} = -\int_{\text{SW}} [\![\boldsymbol{\tau}]\!] \cdot \boldsymbol{N} \mathrm{d}S - \frac{1}{\mathcal{N}-1} \int_{\text{SW}} \boldsymbol{r} \times \left(\boldsymbol{N} \times [\![\nabla p + \rho \nabla \left(\frac{q^2}{2} \right)]\!] \right) \mathrm{d}S \tag{4.1.2}$$

Hence the appearance of the additional contribution $\boldsymbol{F}_{\text{SW}}$ is directly caused by the discontinuity of the shock wave since it contains the jump of the flow quantities at the shock surface SW. This term has never been noticed previously, hence it raises the question whether adding its contribution to $\boldsymbol{F}_{m_\rho}$ might mitigate the discrepancies noticed by Mele and Tognaccini [31] in

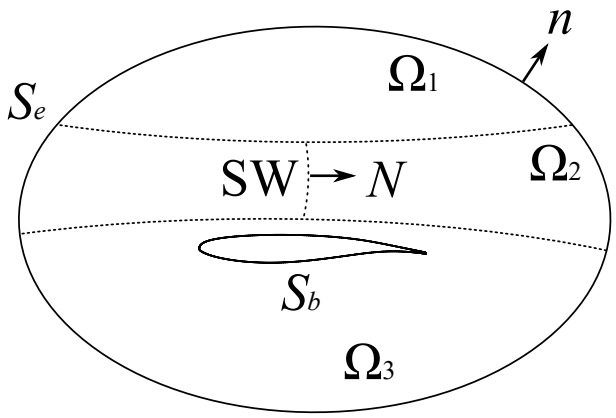

Figure 4.1: Partition of the fluid domain in transonic flows

transonic flows (see Fig.1.13). Unfortunately, $\boldsymbol{F}_{\mathrm{SW}}$ is tough to evaluate in practice because the shock wave detection is not an easy task and the numerical scheme is only first order accurate in this region. Furthermore, the derivatives of the flow quantities are no longer defined in the classical sense but rather in the sense of distributions with the jump of the flow quantities across SW. The next step is then to find an equivalent form of $\boldsymbol{F}_{\mathrm{SW}}$ which avoids the integration on SW.

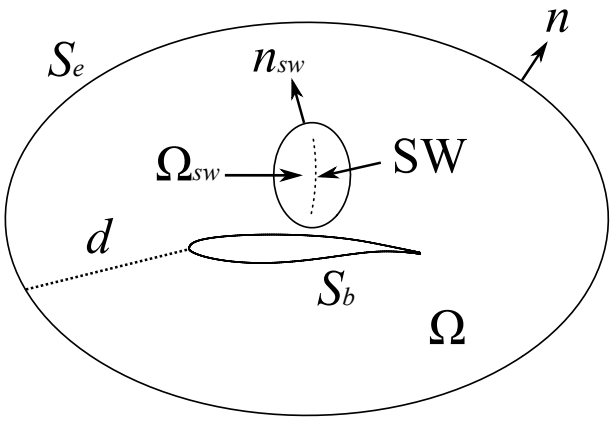

Figure 4.2: Fluid domains and boundaries in transonic flows

The new expression of $\boldsymbol{F}_{\mathrm{SW}}$ is derived in Appendix D. It comprises only integrations in the shock wave volume Ω_{sw} (see Fig.4.2), on its contour $\partial\Omega_{sw}$, and no integration on SW:

$$\begin{aligned}\boldsymbol{F}_{\mathrm{SW}} = &\int_{\Omega_{sw}} \boldsymbol{m}_\rho \mathrm{d}v + \oint_{\partial\Omega_{sw}} \left(\rho\frac{q^2}{2}\boldsymbol{n}_{sw} - \rho\boldsymbol{q}\left(\boldsymbol{q}\cdot\boldsymbol{n}_{sw}\right)\right)\mathrm{d}S \\ &+ \frac{1}{\mathcal{N}-1}\oint_{\partial\Omega_{sw}} \boldsymbol{r}\times\left(\boldsymbol{n}_{sw}\times\frac{q^2}{2}\nabla\rho\right)\mathrm{d}S + \int_{\Omega_{sw}}\rho\boldsymbol{l}\mathrm{d}v \end{aligned} \tag{4.1.3}$$

where $\boldsymbol{n}_{sw}$ denotes the unit normal pointing outside Ω_{sw} (see Fig.4.2) and $\boldsymbol{m}_\rho$ is defined as

$$\boldsymbol{m}_\rho = \frac{\boldsymbol{r}}{\mathcal{N}-1}\times\left(\nabla\rho\times\nabla\left(\frac{q^2}{2}\right)\right) \tag{4.1.4}$$

Yet, Mele and Tognaccini [31] precisely observed that the numerical inaccuracies in transonic flows come from the integration of $\boldsymbol{m}_\rho$ in Ω_{sw}. Therefore, it is more convenient to merge $\boldsymbol{F}_{\mathrm{SW}}$

with $\boldsymbol{F}_{m_\rho}$ in order to avoid the integration of $\boldsymbol{m}_\rho$ in Ω_{sw}:

$$\boldsymbol{F}_{m_\rho} + \boldsymbol{F}_{\mathrm{SW}} = -\int_{\Omega\setminus\Omega_{sw}} \boldsymbol{m}_\rho \mathrm{d}v + \oint_{\partial\Omega_{sw}} \left(\rho\frac{q^2}{2}\boldsymbol{n}_{sw} - \rho\boldsymbol{q}\left(\boldsymbol{q}\cdot\boldsymbol{n}_{sw}\right)\right)\mathrm{d}S + \frac{1}{\mathcal{N}-1}\oint_{\partial\Omega_{sw}} \boldsymbol{r}\times\left(\boldsymbol{n}_{sw}\times\frac{q^2}{2}\nabla\rho\right)\mathrm{d}S + \int_{\Omega_{sw}} \rho\boldsymbol{l}\mathrm{d}v \tag{4.1.5}$$

The right-hand side of (4.1.5) is nothing but the transonic version $\boldsymbol{F}_{m_\rho}^{\mathrm{trans}}$ of the term $\boldsymbol{F}_{m_\rho}$ first introduced by Mele *et al.* [36] (see relation (3.2.36)):

$$\boldsymbol{F}_{m_\rho} + \boldsymbol{F}_{\mathrm{SW}} = \boldsymbol{F}_{m_\rho}^{\mathrm{trans}} \tag{4.1.6}$$

In the end, this cumbersome mathematical step is paramount because it leads to the appearance of $\boldsymbol{F}_{\mathrm{SW}}$ in (4.1.1). Then, it provides an elegant, rigorous derivation of $\boldsymbol{F}_{m_\rho}^{\mathrm{trans}}$, and hence of Mele *et al.*'s formulation in transonic flows. Besides, the presence of $\boldsymbol{F}_{\mathrm{SW}}$ illustrates in mathematical terms that Mele and Tognaccini's formulation [31] might be not complete in the presence of shock wave discontinuities. Hence, the aerodynamic force summarizes as

$$\boxed{\boldsymbol{F} = \boldsymbol{F}_{\rho l} + \boldsymbol{F}_{m_\rho}^{\mathrm{trans}} + \boldsymbol{F}_{S_e} + \boldsymbol{F}_{\tau}} \tag{4.1.7}$$

and can now be used in transonic flows. The next step consists in analysing how (4.1.7) is related to the Kutta-Joukowski theorem and Maskell's formula through $\boldsymbol{F}_{\rho l}$ and $\boldsymbol{F}_{m_\rho}^{\mathrm{trans}}$ and to Betz's formula through $\boldsymbol{F}_{S_e}$ and $\boldsymbol{F}_{\tau}$.

4.1.2 Analysis of the links with the Kutta-Joukowski theorem and Maskell's formula

In incompressible flows, the existing links between the Lamb-vector-based formula, the Kutta-Joukowski lift theorem and Maskell's lift-induced drag formula were already identified by several authors [47, 75, 81, 92]. In particular, it has been shown in subsection 1.3.4 that the Lamb-vector-based formula is related to those theories through the vortex force $\boldsymbol{F}_{\rho l}$ which hence explains why this term is responsible for the lift and the lift-induced drag in incompressible flows.

In compressible regime, Mele and Tognaccini [31] noticed in numerical simulations that $\boldsymbol{F}_{m_\rho}$ contributes to the lift in two-dimensional flows, and Mele *et al.* [32] observed that it also contributes to the lift-induced drag in three-dimensional flows. Yet, it has never been conducted any theoretical analysis effectively proving that $\boldsymbol{F}_{m_\rho}$ is related to the lift and the lift-induced drag. In fact, one must first understand why the vortex force $\boldsymbol{F}_{\rho l}$ is not sufficient anymore in this case. That is why it is necessary to find the links between Mele *et al.*'s formulation [31, 32, 36], the Kutta-Joukowski theorem and Maskell's formula in compressible flows, in order to identify the role of $\boldsymbol{F}_{m_\rho}$ in the lift and the lift-induced drag.

Subsonic flows

Let us first consider the case of a subsonic flow. In this case, no shock wave is present in the flow and $\Omega_{sw} = \varnothing$. In compressible flows, $\boldsymbol{F}_{\rho l}$ is defined as follows:

$$\boldsymbol{F}_{\rho l} = -\int_{\Omega} \rho\boldsymbol{l}\mathrm{d}v = \int_{\Omega} \rho\boldsymbol{q}\times\boldsymbol{\omega}\mathrm{d}v \tag{4.1.8}$$

In steady conditions, the acceleration of a fluid particle $\boldsymbol{a}$ is given by

$$\rho\boldsymbol{a} = \nabla\cdot(\rho\boldsymbol{q}\otimes\boldsymbol{q}) = \rho\boldsymbol{l} + \rho\nabla\left(\frac{q^2}{2}\right) \tag{4.1.9}$$

such that

$$\rho \boldsymbol{l} = \nabla \cdot \left(\rho \boldsymbol{q} \otimes \boldsymbol{q} - \rho \frac{q^2}{2} \boldsymbol{I} \right) + \frac{q^2}{2} \nabla \rho \tag{4.1.10}$$

By using the Gauss theorem (A.5), the volume integral of the first term on the right-hand side of (4.1.10) can be transformed into a surface integral on S_e ($\boldsymbol{q} = \boldsymbol{0}$ on S_b due to the no-slip condition). $\boldsymbol{F}_{\rho l}$ is then expressed in the following form:

$$\boldsymbol{F}_{\rho l} = \oint_{S_e} \left(\rho \frac{q^2}{2} \boldsymbol{n} - \rho \boldsymbol{q} \left(\boldsymbol{q} \cdot \boldsymbol{n} \right) \right) \mathrm{d}S - \int_\Omega \frac{q^2}{2} \nabla \rho \mathrm{d}v \tag{4.1.11}$$

The next step consists in decomposing the velocity vector as $\boldsymbol{q} = \boldsymbol{U}_\infty + \delta \boldsymbol{q}$. By introducing this decomposition in the surface integral, it is possible to write $\boldsymbol{F}_{\rho l}$ as follows:

$$\begin{aligned} \boldsymbol{F}_{\rho l} = & \oint_{S_e} \rho \left(\boldsymbol{U}_\infty \cdot \delta \boldsymbol{q} \right) \boldsymbol{n} \mathrm{d}S - \oint_{S_e} \rho \delta \boldsymbol{q} \left(\boldsymbol{U}_\infty \cdot \boldsymbol{n} \right) \mathrm{d}S \\ & - \oint_{S_e} \rho \boldsymbol{U}_\infty \left(\boldsymbol{U}_\infty \cdot \boldsymbol{n} \right) \mathrm{d}S - \oint_{S_e} \rho \boldsymbol{U}_\infty \left(\delta \boldsymbol{q} \cdot \boldsymbol{n} \right) \mathrm{d}S \\ & + \oint_{S_e} \rho \frac{\delta q^2}{2} \boldsymbol{n} \mathrm{d}S - \oint_{S_e} \rho \delta \boldsymbol{q} \left(\delta \boldsymbol{q} \cdot \boldsymbol{n} \right) \mathrm{d}S \\ & + \frac{U_\infty^2}{2} \oint_{S_e} \rho \boldsymbol{n} \mathrm{d}S - \int_\Omega \frac{q^2}{2} \nabla \rho \mathrm{d}v \end{aligned} \tag{4.1.12}$$

According to the rule of the double cross product, the first line of (4.1.12) is equal to

$$\boldsymbol{U}_\infty \times \oint_{S_e} \boldsymbol{n} \times \rho \delta \boldsymbol{q} \mathrm{d}S$$

while the second line is equal to zero due to the steady continuity equation:

$$- \oint_{S_e} \rho \boldsymbol{U}_\infty \left(\boldsymbol{U}_\infty \cdot \boldsymbol{n} \right) \mathrm{d}S - \oint_{S_e} \rho \boldsymbol{U}_\infty \left(\delta \boldsymbol{q} \cdot \boldsymbol{n} \right) \mathrm{d}S = - \left(\oint_{S_e} \rho \boldsymbol{q} \cdot \boldsymbol{n} \mathrm{d}S \right) \boldsymbol{U}_\infty = \boldsymbol{0} \tag{4.1.13}$$

Then, $\boldsymbol{F}_{\rho l}$ becomes

$$\begin{aligned} \boldsymbol{F}_{\rho l} = & \boldsymbol{U}_\infty \times \oint_{S_e} \boldsymbol{n} \times \rho \delta \boldsymbol{q} \mathrm{d}S \\ & + \oint_{S_e} \rho \frac{\delta q^2}{2} \boldsymbol{n} \mathrm{d}S - \oint_{S_e} \rho \delta \boldsymbol{q} \left(\delta \boldsymbol{q} \cdot \boldsymbol{n} \right) \mathrm{d}S \\ & + \frac{U_\infty^2}{2} \oint_{S_e} \rho \boldsymbol{n} \mathrm{d}S - \int_\Omega \frac{q^2}{2} \nabla \rho \mathrm{d}v \end{aligned} \tag{4.1.14}$$

The first line of (4.1.14) is a Kutta-Joukowski formula involving the local density ρ instead of ρ_∞:

$$\oint_{S_e} \boldsymbol{n} \times \rho \delta \boldsymbol{q} \mathrm{d}S = \rho_\infty \boldsymbol{\Gamma}^* \tag{4.1.15}$$

where $\boldsymbol{\Gamma}^*$ is a circulation vector which accounts for compressibility effects. Using the far-wake symmetries introduced previously, it is possible to show that

$$\boldsymbol{\Gamma}^* \cdot \boldsymbol{e}_x = 0 \tag{4.1.16}$$

$$\boldsymbol{\Gamma}^* \cdot \boldsymbol{e}_z = 0 \tag{4.1.17}$$

Hence the first line of (4.1.14) contributes solely to the lift. On the contrary, the second line contributes to the lift and the drag. Considering that the inlet and lateral parts of S_e are located

far from the aircraft skin, it is possible to limit the integrals containing the velocity perturbation δq^2 and $\delta \boldsymbol{q}\,(\delta \boldsymbol{q} \cdot \boldsymbol{n})$ to the wake plane W on which $\boldsymbol{n} = \boldsymbol{e}_x$. In fact, $\delta \boldsymbol{q}$ asymptotically decays at least as $r^{-(\mathcal{N}-1)}$ outside the wake [63]. Hence, knowing that $\mathrm{d}S \propto r^{\mathcal{N}-1}$, the integrands in the second line of (4.1.14) behave as $r^{-(\mathcal{N}-1)}$ outside the wake and the integrals become negligible on the inlet and lateral parts of S_e. In this case, by projecting onto the x and z-directions, $\boldsymbol{F}_{\rho l}$ becomes

$$\begin{aligned}\boldsymbol{F}_{\rho l} = &-\rho_\infty U_\infty \left(\Gamma^* + \delta\Gamma^*\right) \boldsymbol{e}_z \\ &+ \left(\frac{1}{2}\int_W \rho \left(v^2 + w^2 - u^2\right) \mathrm{d}S\right) \boldsymbol{e}_x \\ &+ \frac{U_\infty^2}{2} \oint_{S_e} \rho \boldsymbol{n} \mathrm{d}S - \int_\Omega \frac{q^2}{2} \nabla\rho \mathrm{d}v\end{aligned} \tag{4.1.18}$$

with

$$\boldsymbol{\Gamma}^* = \oint_{S_e} \boldsymbol{n} \times \frac{\rho}{\rho_\infty} \delta\boldsymbol{q} \mathrm{d}S = -\Gamma^* \boldsymbol{e}_y \tag{4.1.19}$$

$$\delta\Gamma^* = \frac{1}{U_\infty} \int_W \frac{\rho}{\rho_\infty} uw \mathrm{d}S \tag{4.1.20}$$

In (4.1.18), the first line is the compressible counterpart of the generalized Kutta-Joukowski theorem already presented in (1.3.53) in its incompressible form: this time, Γ^* and $\delta\Gamma^*$ account for the compressibility of the flow with the presence of ρ/ρ_∞ in the integrals. The term $\delta\Gamma^*$ was previously identified by Schmitz [92] in incompressible flows and is nothing but a wake-induced lift penalty ($u, w \leq 0$ in the wake between the two tip vortices, so that $-\delta\Gamma^* \leq 0$ too). The second line is a compressible version of Maskell's lift-induced drag formula already identified in (1.3.54) in incompressible flows: here the integral contains the local density ρ instead of ρ_∞. Anyways, having that

$$\lim_{S_e \to \infty} \rho = \rho_\infty \tag{4.1.21}$$

$$\lim_{S_e \to \infty} u = 0 \tag{4.1.22}$$

the first line progressively returns to the classical Kutta-Joukowski theorem and yields the total lift [56, 57], while the second line returns to the original Maskell's formula and yields the lift-induced drag [12]. Finally, the third line is present only in compressible flows and accounts for compressibility effects. In conclusion, it can be deduced from (4.1.18) that $\boldsymbol{F}_{\rho l}$ is related to the lift and the lift-induced drag in compressible flows as well, although it is not their unique source. Indeed, $\boldsymbol{F}_{\rho l}$ also involves compressible terms containing the density and its gradient which suggests that it contributes only to part of the total lift and lift-induced drag. In this instance, the contribution of $\boldsymbol{F}_{m_\rho}$ is essential. In subsonic flows, $\boldsymbol{F}_{m_\rho}$ can be expressed as follows:

$$\boldsymbol{F}_{m_\rho} = \int_\Omega \frac{q^2}{2} \nabla\rho \mathrm{d}v + \frac{1}{\mathcal{N}-1} \oint_{S_e} \boldsymbol{r} \times \left(\boldsymbol{n} \times \frac{q^2}{2} \nabla\rho\right) \mathrm{d}S \tag{4.1.23}$$

When adding (4.1.23) to (4.1.18), the sum of $\boldsymbol{F}_{\rho l}$ and $\boldsymbol{F}_{m_\rho}$ is given by

$$\begin{aligned}\boldsymbol{F}_{\rho l} + \boldsymbol{F}_{m_\rho} = &-\rho_\infty U_\infty \left(\Gamma^* + \delta\Gamma^*\right) \boldsymbol{e}_z \\ &+ \left(\frac{1}{2}\int_W \rho \left(v^2 + w^2 - u^2\right) \mathrm{d}S\right) \boldsymbol{e}_x \\ &+ \frac{U_\infty^2}{2} \oint_{S_e} \rho \boldsymbol{n} \mathrm{d}S + \frac{1}{\mathcal{N}-1} \oint_{S_e} \boldsymbol{r} \times \left(\boldsymbol{n} \times \frac{q^2}{2} \nabla\rho\right) \mathrm{d}S\end{aligned} \tag{4.1.24}$$

The first integral in the third line of (4.1.24) is re-expressed upon applying the second DMT (A.2) in order to obtain

$$\boxed{\begin{aligned}\boldsymbol{F}_{\rho l}+\boldsymbol{F}_{m_\rho} = &\underbrace{-\rho_\infty U_\infty\left(\Gamma^*+\delta\Gamma^*\right)\boldsymbol{e}_z}_{\text{Compressible KJ theorem}}\\ &+\underbrace{\left(\frac{1}{2}\int_W \rho\left(v^2+w^2-u^2\right)\mathrm{d}S\right)\boldsymbol{e}_x}_{\text{Compressible Maskell's formula}}\\ &+\boldsymbol{F}_{\nabla\rho}\end{aligned}} \tag{4.1.25}$$

where

$$\boldsymbol{F}_{\nabla\rho}=\frac{1}{\mathcal{N}-1}\oint_{S_e}\boldsymbol{r}\times\left(\boldsymbol{n}\times\frac{q^2-U_\infty^2}{2}\nabla\rho\right)\mathrm{d}S \tag{4.1.26}$$

is a compressibility correction which asymptotic behaviour is investigated in Appendix E:

$$\lim_{S_e\to\infty}\boldsymbol{F}_{\nabla\rho}=\boldsymbol{0} \tag{4.1.27}$$

This results suggests that, at least in the far field, the lift component of $\boldsymbol{F}_{\rho l}+\boldsymbol{F}_{m_\rho}$ is equivalent to the Kutta-Joukowski lift theorem while its drag component corresponds to Maskell's lift-induced drag formula. Hence, according to (4.1.18), it means that $\boldsymbol{F}_{\rho l}$ is equal to the total lift and lift-induced drag minus the lift and lift-induced drag generated by compressibility phenomena. It explains why the relative contribution of $\boldsymbol{F}_{\rho l}$ decreases as the Mach number increases (see [31, 89, 90] for instance). With the addition of $\boldsymbol{F}_{m_\rho}$, the total lift and lift-induced drag are then recovered.

Transonic flows

The preceding analysis has been conducted in subsonic flows on the contributions of $\boldsymbol{F}_{\rho l}$ and $\boldsymbol{F}_{m_\rho}$. In transonic flows, with the presence of shock waves, it is necessary to use the transonic expression $\boldsymbol{F}_{m_\rho}^{\text{trans}}$ instead of $\boldsymbol{F}_{m_\rho}$. In this case, it is more convenient to analyse the sum $\boldsymbol{F}_{\rho l}+\boldsymbol{F}_{m_\rho}^{\text{trans}}$ directly. Starting over from (4.1.4), (4.1.5) and (4.1.6), $\boldsymbol{F}_{m_\rho}^{\text{trans}}$ is expressed as follows:

$$\begin{aligned}\boldsymbol{F}_{m_\rho}^{\text{trans}}=&\frac{1}{\mathcal{N}-1}\int_{\Omega\setminus\Omega_{sw}}\boldsymbol{r}\times\left(\nabla\left(\frac{q^2}{2}\right)\times\nabla\rho\right)\mathrm{d}v+\oint_{\partial\Omega_{sw}}\left(\rho\frac{q^2}{2}\boldsymbol{n}_{sw}-\rho\boldsymbol{q}\left(\boldsymbol{q}\cdot\boldsymbol{n}_{sw}\right)\right)\mathrm{d}S\\ &+\frac{1}{\mathcal{N}-1}\oint_{\partial\Omega_{sw}}\boldsymbol{r}\times\left(\boldsymbol{n}_{sw}\times\frac{q^2}{2}\nabla\rho\right)\mathrm{d}S+\int_{\Omega_{sw}}\rho\boldsymbol{l}\mathrm{d}v\end{aligned} \tag{4.1.28}$$

where $\boldsymbol{n}_{sw}$ is the unit normal pointing outside Ω_{sw}. Hence, the sum with $\boldsymbol{F}_{\rho l}$ yields

$$\begin{aligned}\boldsymbol{F}_{\rho l}+\boldsymbol{F}_{m_\rho}^{\text{trans}}=&-\int_{\Omega\setminus\Omega_{sw}}\rho\boldsymbol{l}\mathrm{d}v+\frac{1}{\mathcal{N}-1}\int_{\Omega\setminus\Omega_{sw}}\boldsymbol{r}\times\left(\nabla\left(\frac{q^2}{2}\right)\times\nabla\rho\right)\mathrm{d}v\\ &+\oint_{\partial\Omega_{sw}}\left(\rho\frac{q^2}{2}\boldsymbol{n}_{sw}-\rho\boldsymbol{q}\left(\boldsymbol{q}\cdot\boldsymbol{n}_{sw}\right)\right)\mathrm{d}S\\ &+\frac{1}{\mathcal{N}-1}\oint_{\partial\Omega_{sw}}\boldsymbol{r}\times\left(\boldsymbol{n}_{sw}\times\frac{q^2}{2}\nabla\rho\right)\mathrm{d}S\end{aligned} \tag{4.1.29}$$

By using the first DMT (A.1), it is possible to express the second volume integral of (4.1.29) as

$$\begin{aligned}\frac{1}{\mathcal{N}-1}\int_{\Omega\setminus\Omega_{sw}}\boldsymbol{r}\times\left(\nabla\left(\frac{q^2}{2}\right)\times\nabla\rho\right)\mathrm{d}v=&\int_{\Omega\setminus\Omega_{sw}}\frac{q^2}{2}\nabla\rho\mathrm{d}v\\ &+\frac{1}{\mathcal{N}-1}\oint_{S_e}\boldsymbol{r}\times\left(\boldsymbol{n}\times\frac{q^2}{2}\nabla\rho\right)\mathrm{d}S\\ &-\frac{1}{\mathcal{N}-1}\oint_{\partial\Omega_{sw}}\boldsymbol{r}\times\left(\boldsymbol{n}_{sw}\times\frac{q^2}{2}\nabla\rho\right)\mathrm{d}S\end{aligned} \tag{4.1.30}$$

such that $\boldsymbol{F}_{\rho l} + \boldsymbol{F}_{m_\rho}^{\text{trans}}$ becomes

$$\begin{aligned}\boldsymbol{F}_{\rho l} + \boldsymbol{F}_{m_\rho}^{\text{trans}} = &- \int_{\Omega\setminus\Omega_{sw}} \left(\rho\boldsymbol{l} - \frac{q^2}{2}\nabla\rho\right) \mathrm{d}v \\ &+ \oint_{\partial\Omega_{sw}} \left(\rho\frac{q^2}{2}\boldsymbol{n}_{sw} - \rho\boldsymbol{q}\left(\boldsymbol{q}\cdot\boldsymbol{n}_{sw}\right)\right) \mathrm{d}S \\ &+ \frac{1}{\mathcal{N}-1}\oint_{S_e} \boldsymbol{r}\times\left(\boldsymbol{n}\times\frac{q^2}{2}\nabla\rho\right) \mathrm{d}S \end{aligned} \tag{4.1.31}$$

Then, relation (4.1.10) implies that

$$\frac{q^2}{2}\nabla\rho - \rho\boldsymbol{l} = \nabla\cdot\left(\rho\frac{q^2}{2}\boldsymbol{I} - \rho\boldsymbol{q}\otimes\boldsymbol{q}\right) \tag{4.1.32}$$

and by using the generalized Gauss theorem (A.5), it is possible to transform the volume integral of (4.1.31) into a surface integral on S_e and $\partial\Omega_{sw}$:

$$\begin{aligned}-\int_{\Omega\setminus\Omega_{sw}} \left(\rho\boldsymbol{l} - \frac{q^2}{2}\nabla\rho\right) \mathrm{d}v = &\oint_{S_e} \left(\rho\frac{q^2}{2}\boldsymbol{n} - \rho\boldsymbol{q}\left(\boldsymbol{q}\cdot\boldsymbol{n}\right)\right) \mathrm{d}S \\ &- \oint_{\partial\Omega_{sw}} \left(\rho\frac{q^2}{2}\boldsymbol{n}_{sw} - \rho\boldsymbol{q}\left(\boldsymbol{q}\cdot\boldsymbol{n}_{sw}\right)\right) \mathrm{d}S \end{aligned} \tag{4.1.33}$$

As a consequence, $\boldsymbol{F}_{\rho l} + \boldsymbol{F}_{m_\rho}^{\text{trans}}$ is simplified as follows:

$$\boldsymbol{F}_{\rho l} + \boldsymbol{F}_{m_\rho}^{\text{trans}} = \oint_{S_e} \left(\rho\frac{q^2}{2}\boldsymbol{n} - \rho\boldsymbol{q}\left(\boldsymbol{q}\cdot\boldsymbol{n}\right)\right) \mathrm{d}S + \frac{1}{\mathcal{N}-1}\oint_{S_e} \boldsymbol{r}\times\left(\boldsymbol{n}\times\frac{q^2}{2}\nabla\rho\right) \mathrm{d}S \tag{4.1.34}$$

In (4.1.34), the first surface integral is exactly the same as that derived in (4.1.11) for $\boldsymbol{F}_{\rho l}$ in subsonic flows. With the same decomposition of the velocity vector $\boldsymbol{q} = \boldsymbol{U}_\infty + \delta\boldsymbol{q}$, and following the same steps as before, it is possible to demonstrate the links between $\boldsymbol{F}_{\rho l} + \boldsymbol{F}_{m_\rho}^{\text{trans}}$, the Kutta-Joukowski theorem and Maskell's formula in transonic flows:

$$\boxed{\begin{aligned}\boldsymbol{F}_{\rho l} + \boldsymbol{F}_{m_\rho}^{\text{trans}} = &\underbrace{-\rho_\infty U_\infty\left(\Gamma^* + \delta\Gamma^*\right)\boldsymbol{e}_z}_{\text{Compressible KJ theorem}} \\ &+ \underbrace{\left(\frac{1}{2}\int_W \rho\left(v^2 + w^2 - u^2\right)\mathrm{d}S\right)\boldsymbol{e}_x}_{\text{Compressible Maskell's formula}} \\ &+ \boldsymbol{F}_{\nabla\rho}\end{aligned}} \tag{4.1.35}$$

In conclusion, it has been shown that $\boldsymbol{F}_{\rho l} + \boldsymbol{F}_{m_\rho}$ and $\boldsymbol{F}_{\rho l} + \boldsymbol{F}_{m_\rho}^{\text{trans}}$ are linked to the Kutta-Joukowski theorem and Maskell's formula in subsonic and transonic flows. The Kutta-Joukowski theorem relates the lift to the circulation on S_e and Maskell's formula relates the lift-induced drag to the transverse kinetic energy on W. On the contrary, $\boldsymbol{F}_{\rho l}$, $\boldsymbol{F}_{m_\rho}$ and $\boldsymbol{F}_{m_\rho}^{\text{trans}}$ evaluate the volume contributions of the Lamb vector and the quantity $\frac{q^2}{2}\nabla\rho$ close to the aircraft. Hence, Mele *et al.*'s formulation [31, 32, 36] provides new insights on the local physical sources of the lift and the lift-induced drag in compressible flows. In this case, the contribution of $\boldsymbol{F}_{\rho l}$ is not sufficient to correctly predict the lift and the lift-induced drag. Indeed, as in the incompressible case, $\boldsymbol{F}_{\rho l}$ represents the contribution coming from the Lamb vector, hence the vorticity generated in boundary layers. It is then related to the viscous character of the flow [65]. In compressible flows, its impact in lift and lift-induced drag gradually weakens in favour of $\boldsymbol{F}_{m_\rho}$ (or $\boldsymbol{F}_{m_\rho}^{\text{trans}}$ in transonic flows) which represents the lift and the lift-induced drag generated by the density gradient in compressions and expansions. In the next analysis, the link between Mele *et al.*'s formulation and Betz's profile drag formula will be investigated in compressible flows.

4.1.3 Analysis of the link with Betz's formula

In fact, the link was already known in incompressible flows [18, 75, 78] (see subsection 1.3.4). For the sake of thoroughness, the viscous stresses are not neglected here so that the contribution of $\boldsymbol{F}_\tau$ is included in the profile drag. Therefore, the profile drag is given by the sum of $\boldsymbol{F}_{S_e}$ and $\boldsymbol{F}_\tau$ in this case:

$$\boldsymbol{F}_{S_e} = -\frac{1}{\mathcal{N}-1}\oint_{S_e} \boldsymbol{r}\times(\boldsymbol{n}\times\rho\boldsymbol{l})\,\mathrm{d}S \tag{4.1.36}$$

$$\boldsymbol{F}_\tau = \oint_{S_e} \boldsymbol{\tau}\cdot\boldsymbol{n}\mathrm{d}S + \frac{1}{\mathcal{N}-1}\oint_{S_e} \boldsymbol{r}\times(\boldsymbol{n}\times\nabla\cdot\boldsymbol{\tau})\,\mathrm{d}S \tag{4.1.37}$$

Then, with the Navier-Stokes equations written as

$$\rho\boldsymbol{l} - \nabla\cdot\boldsymbol{\tau} = -\nabla P + \frac{q^2}{2}\nabla\rho \tag{4.1.38}$$

where $P = p + \rho q^2/2$, it is possible to write $\boldsymbol{F}_{S_e} + \boldsymbol{F}_\tau$ as follows:

$$\begin{aligned}\boldsymbol{F}_{S_e} + \boldsymbol{F}_\tau = &\oint_{S_e} \boldsymbol{\tau}\cdot\boldsymbol{n}\mathrm{d}S + \frac{1}{\mathcal{N}-1}\oint_{S_e} \boldsymbol{r}\times(\boldsymbol{n}\times\nabla P)\,\mathrm{d}S\\ &- \frac{1}{\mathcal{N}-1}\oint_{S_e} \boldsymbol{r}\times\left(\boldsymbol{n}\times\frac{q^2}{2}\nabla\rho\right)\mathrm{d}S\end{aligned} \tag{4.1.39}$$

Using the second DMT (A.2), the second integral of (4.1.39) can be simplified:

$$\frac{1}{\mathcal{N}-1}\oint_{S_e} \boldsymbol{r}\times(\boldsymbol{n}\times\nabla P)\,\mathrm{d}S = -\oint_{S_e} P\boldsymbol{n}\mathrm{d}S = \oint_{S_e}(P_\infty - P)\,\boldsymbol{n}\mathrm{d}S \tag{4.1.40}$$

where $P_\infty = p_\infty + \rho_\infty U_\infty^2/2$. Moreover, using the definition (4.1.26) of $\boldsymbol{F}_{\nabla\rho}$ it is possible to replace the last integral of (4.1.39):

$$\begin{aligned}-\frac{1}{\mathcal{N}-1}\oint_{S_e} \boldsymbol{r}\times\left(\boldsymbol{n}\times\frac{q^2}{2}\nabla\rho\right)\mathrm{d}S &= -\boldsymbol{F}_{\nabla\rho} - \frac{1}{\mathcal{N}-1}\oint_{S_e} \boldsymbol{r}\times\left(\boldsymbol{n}\times\frac{U_\infty^2}{2}\nabla\rho\right)\mathrm{d}S\\ &= -\boldsymbol{F}_{\nabla\rho} + \frac{U_\infty^2}{2}\oint_{S_e}\rho\boldsymbol{n}\mathrm{d}S\\ &= -\boldsymbol{F}_{\nabla\rho} - \frac{U_\infty^2}{2}\oint_{S_e}(\rho_\infty-\rho)\,\boldsymbol{n}\mathrm{d}S\end{aligned} \tag{4.1.41}$$

where the second DMT (A.2) has been applied to $\frac{U_\infty^2}{2}\nabla\rho$. Finally, $\boldsymbol{F}_{S_e} + \boldsymbol{F}_\tau$ is written as follows:

$$\boxed{\boldsymbol{F}_{S_e} + \boldsymbol{F}_\tau = \underbrace{\oint_{S_e} \boldsymbol{\tau}\cdot\boldsymbol{n}\mathrm{d}S + \oint_{S_e}(P_\infty - P)\,\boldsymbol{n}\mathrm{d}S - \frac{U_\infty^2}{2}\oint_{S_e}(\rho_\infty-\rho)\,\boldsymbol{n}\mathrm{d}S}_{\text{Compressible Betz's formula}} - \boldsymbol{F}_{\nabla\rho}} \tag{4.1.42}$$

Here, the contribution of $\boldsymbol{\tau}$ is introduced in the compressible Betz's formula even if its magnitude is always negligible in high Re flows. Then, it has been shown that $\boldsymbol{F}_{S_e} + \boldsymbol{F}_\tau$ is equal to a compressible Betz's formula minus the same compressibility correction $\boldsymbol{F}_{\nabla\rho}$ discovered in the previous analysis.

First identified by Betz [8], $P_\infty - P$ is recovered in the latter expression. In this case, P contains the local density ρ instead of ρ_∞. Yet, unlike the compressible expressions of the Kutta-Joukowski theorem and Maskell's formula, the compressible Betz's formula involves the additional contribution

$$-\frac{U_\infty^2}{2}\oint_{S_e}(\rho_\infty-\rho)\,\boldsymbol{n}\mathrm{d}S$$

This term has no equivalent in the incompressible profile drag definition and represents the variations in kinetic energy due to the density variations of a fluid flowing at U_∞. In fact, in compressible flows, it seems that the profile drag can no longer be evaluated with the losses in P only, and variations in P may also come from variations in density occuring in compressions and expansions. Hence, it seems that the additional contribution withdraws the part of the variations in P induced by the compressibility. This term will be investigated in subsection 4.3.3.

4.2 Definition of a transonic Lamb-vector-based decomposition directly related to classical theories

It has been shown that the Lamb-vector-based aerodynamic force decomposition developed by Mele *et al.* [31, 32, 36] is related to the classical analyses of Kutta, Joukowski, Maskell and Betz. Hence, it is now easier to understand why the lift, the lift-induced drag and the profile drag computed in Mele *et al.*'s numerical applications are almost always in agreement with former formulations from the literature.

Nevertheless it has been observed in section 3.3.3 that their decomposition underestimates the lift-induced drag and overestimates the profile drag when compared to the thermodynamic decomposition of Destarac and Van der Vooren [21]. Besides, mathematically speaking, their decomposition is not strictly equivalent to the classical analyses. Indeed, although it progressively disappears in the far field, a compressibility correction term has been identified in the final expression. The aim of this section is then to develop a new Lamb-vector-based decomposition which is directly equivalent to the classical analyses: this new decomposition is called the ONERA decomposition. In the process, the ONERA decomposition unexpectedly turns out to be naturally invariant to the location of the reference point. The ONERA decomposition is finally applied to practical test cases and compared to the decompositions of Mele *et al.* [36] and Destarac and Van der Vooren [21].

4.2.1 Presentation of the new decomposition

The previous mathematical developments showed that $\boldsymbol{F}_{\rho l} + \boldsymbol{F}_{m_\rho}^{\text{trans}}$ are linked to the Kutta-Joukowski lift theorem and Maskell's lift-induced drag formula and that $\boldsymbol{F}_{S_e} + \boldsymbol{F}_\tau$ is related to Betz's profile drag formula. Thus, it better explains why Mele *et al.*'s aerodynamic force decomposition [36]

$$\boxed{\begin{aligned} L^{\text{Mele}} &= \boldsymbol{e}_z \cdot \left(\boldsymbol{F}_{\rho l} + \boldsymbol{F}_{m_\rho}^{\text{trans}} \right) && (4.2.1)\\ D_i^{\text{Mele}} &= \boldsymbol{e}_x \cdot \left(\boldsymbol{F}_{\rho l} + \boldsymbol{F}_{m_\rho}^{\text{trans}} \right) && (4.2.2)\\ D_P^{\text{Mele}} &= \boldsymbol{e}_x \cdot \boldsymbol{F}_{S_e} && (4.2.3) \end{aligned}}$$

often provides satisfying results in transonic flows ($\boldsymbol{F}_\tau$ is negligible in high Re flows). However, in some cases (e.g. on the NASA CRM in section 3.3.3), the decomposition provided by this formulation is not correct when compared to the robust thermodynamic method of Destarac and Van der Vooren [21]. This might be due to the fact that the compressibility correction $\boldsymbol{F}_{\nabla\rho}$ is not negligible in the near field and hence that Mele *et al.*'s decomposition is not equivalent to the classical analyses there. The equivalence is indeed achieved only in the far field where the magnitude of $\boldsymbol{F}_{\nabla\rho}$ tends to zero. Unfortunately, the dissipation of the trailing vortices caused by the viscous diffusion and the numerical scheme in the far field induces a transfer from the lift-induced drag to the profile drag [96] and reduces the accuracy of the decomposition.

It is therefore necessary to develop a new decomposition which is directly equivalent to the classical analyses even in the near field. It has been shown previously that the decomposition of Mele *et al.* [36] can be equivalently written as follows:

$$\boldsymbol{F}_{\rho l} + \boldsymbol{F}_{m_\rho}^{\text{trans}} = \underbrace{-\rho_\infty U_\infty \left(\Gamma^* + \delta\Gamma^*\right) \boldsymbol{e}_z}_{\text{Compressible KJ theorem}} + \overbrace{\left(\frac{1}{2} \int_W \rho \left(v^2 + w^2 - u^2 \right) \mathrm{d}S \right) \boldsymbol{e}_x}^{\text{Compressible Maskell's formula}} + \boldsymbol{F}_{\nabla\rho} \qquad (4.2.4)$$

$$\boldsymbol{F}_{S_e} + \boldsymbol{F}_\tau = \underbrace{\oint_{S_e} \boldsymbol{\tau} \cdot \boldsymbol{n} \mathrm{d}S + \oint_{S_e} \left(P_\infty - P\right) \boldsymbol{n} \mathrm{d}S - \frac{U_\infty^2}{2} \oint_{S_e} \left(\rho_\infty - \rho\right) \boldsymbol{n} \mathrm{d}S}_{\text{Compressible Betz's formula}} - \boldsymbol{F}_{\nabla\rho} \qquad (4.2.5)$$

In order to obtain a decomposition completely equivalent to the classical analyses, it is then necessary to subtract $\boldsymbol{F}_{\nabla\rho}$ from $\boldsymbol{F}_{\rho l} + \boldsymbol{F}_{m_\rho}^{\text{trans}}$ and add it to $\boldsymbol{F}_{S_e} + \boldsymbol{F}_\tau$. The new decomposition called ONERA decomposition is then defined as follows:

$$\boxed{\begin{aligned} L^{\text{ONERA}} &= \boldsymbol{e}_z \cdot \left(\boldsymbol{F}_{\rho l} + \boldsymbol{F}_{m_\rho}^{\text{trans}} - \boldsymbol{F}_{\nabla\rho}\right) \\ D_i^{\text{ONERA}} &= \boldsymbol{e}_x \cdot \left(\boldsymbol{F}_{\rho l} + \boldsymbol{F}_{m_\rho}^{\text{trans}} - \boldsymbol{F}_{\nabla\rho}\right) \\ D_P^{\text{ONERA}} &= \boldsymbol{e}_x \cdot \left(\boldsymbol{F}_{S_e} + \boldsymbol{F}_\tau + \boldsymbol{F}_{\nabla\rho}\right) \end{aligned}} \tag{4.2.6}$$

$$\tag{4.2.7}$$

$$\tag{4.2.8}$$

It is crucial to note that no approximation has been introduced in the ONERA decomposition. Its expression is an exact formula and the total force $\boldsymbol{F}$ is conserved:

$$\boldsymbol{F} = \boldsymbol{F}_{\rho l} + \boldsymbol{F}_{m_\rho}^{\text{trans}} \quad -\boldsymbol{F}_{\nabla\rho} \quad + \boldsymbol{F}_{S_e} + \boldsymbol{F}_\tau \quad +\boldsymbol{F}_{\nabla\rho} \tag{4.2.9}$$

The ONERA decomposition is strictly equivalent to the classical analyses of Kutta, Joukowski, Maskell and Betz, no matter the location of S_e: it allows for an integration in a better refined part of the grid and hence improves the accuracy of the decomposition. Besides, this equivalence with the classical analyses enables to interpret differently the physical sources of lift, lift-induced drag and profile drag in compressible flows (a physical analysis is presented in subsection 4.3.3). Another key advantage is that the ONERA decomposition is naturally invariant to the location of the reference point chosen for the computation of moment transformations.

4.2.2 Proof of the direct invariance to the location of the reference point

The aim of the present analysis is to demonstrate this invariance. To do so, let us consider a shift $\hat{\boldsymbol{r}} = \boldsymbol{r} - \boldsymbol{r}_0$. In this case, it is possible to write the ONERA decomposition as follows:

$$\begin{aligned} \boldsymbol{F}_{\rho l} + \boldsymbol{F}_{m_\rho}^{\text{trans}} - \boldsymbol{F}_{\nabla\rho} = &- \int_{\Omega\setminus\Omega_{sw}} \rho\boldsymbol{l}\,\mathrm{d}v + \frac{1}{\mathcal{N}-1}\int_{\Omega\setminus\Omega_{sw}} \hat{\boldsymbol{r}} \times \left(\nabla\left(\frac{q^2}{2}\right) \times \nabla\rho\right)\mathrm{d}v \\ &+ \oint_{\partial\Omega_{sw}} \left(\rho\frac{q^2}{2}\boldsymbol{n}_{sw} - \rho\boldsymbol{q}\left(\boldsymbol{q}\cdot\boldsymbol{n}_{sw}\right)\right)\mathrm{d}S \\ &+ \frac{1}{\mathcal{N}-1}\oint_{\partial\Omega_{sw}} \hat{\boldsymbol{r}} \times \left(\boldsymbol{n}_{sw} \times \frac{q^2}{2}\nabla\rho\right)\mathrm{d}S \\ &- \frac{1}{\mathcal{N}-1}\oint_{S_e} \hat{\boldsymbol{r}} \times \left(\boldsymbol{n} \times \frac{q^2-U_\infty^2}{2}\nabla\rho\right)\mathrm{d}S \\ &+ \frac{\boldsymbol{r}_0}{\mathcal{N}-1} \times \left[\int_{\Omega\setminus\Omega_{sw}} \nabla\left(\frac{q^2}{2}\right) \times \nabla\rho\,\mathrm{d}v - \oint_{S_e} \boldsymbol{n} \times \frac{q^2-U_\infty^2}{2}\nabla\rho\,\mathrm{d}S\right. \\ &\left. + \oint_{\partial\Omega_{sw}} \boldsymbol{n}_{sw} \times \frac{q^2}{2}\nabla\rho\,\mathrm{d}S\right] \end{aligned} \tag{4.2.10}$$

and

$$\begin{aligned} \boldsymbol{F}_{S_e} + \boldsymbol{F}_\tau + \boldsymbol{F}_{\nabla\rho} = &\oint_{S_e} \boldsymbol{\tau}\cdot\boldsymbol{n}\mathrm{d}S + \frac{1}{\mathcal{N}-1}\oint_{S_e} \hat{\boldsymbol{r}} \times \left(\boldsymbol{n} \times \left(\nabla\cdot\boldsymbol{\tau} - \rho\boldsymbol{l}\right)\right)\mathrm{d}S \\ &+ \frac{1}{\mathcal{N}-1}\oint_{S_e} \hat{\boldsymbol{r}} \times \left(\boldsymbol{n} \times \frac{q^2-U_\infty^2}{2}\nabla\rho\right)\mathrm{d}S \\ &+ \frac{\boldsymbol{r}_0}{\mathcal{N}-1} \times \oint_{S_e} \boldsymbol{n} \times \left(\nabla\cdot\boldsymbol{\tau} - \rho\boldsymbol{l} + \frac{q^2-U_\infty^2}{2}\nabla\rho\right)\mathrm{d}S \end{aligned} \tag{4.2.11}$$

Let us now analyse the last lines of the two preceding equations. In the last line of (4.2.10), it is possible to write the first integral as

$$\int_{\Omega\setminus\Omega_{sw}} \nabla\left(\frac{q^2}{2}\right) \times \nabla\rho\,\mathrm{d}v = \int_{\Omega\setminus\Omega_{sw}} \nabla \times \left(\frac{q^2}{2}\nabla\rho\right)\mathrm{d}v \tag{4.2.12}$$

and using the generalized Gauss theorem (A.5), it is possible to show that

$$\int_{\Omega\setminus\Omega_{sw}} \nabla\times\left(\frac{q^2}{2}\nabla\rho\right)\mathrm{d}v = \oint_{S_e} \boldsymbol{n}\times\frac{q^2}{2}\nabla\rho\,\mathrm{d}S - \oint_{\partial\Omega_{sw}} \boldsymbol{n}_{sw}\times\frac{q^2}{2}\nabla\rho\,\mathrm{d}S \tag{4.2.13}$$

such that

$$\begin{aligned}\boldsymbol{F}_{\rho l}+\boldsymbol{F}^{\text{trans}}_{m_\rho}-\boldsymbol{F}_{\nabla\rho} = &-\int_{\Omega\setminus\Omega_{sw}}\rho\boldsymbol{l}\mathrm{d}v+\frac{1}{\mathcal{N}-1}\int_{\Omega\setminus\Omega_{sw}}\hat{\boldsymbol{r}}\times\left(\nabla\left(\frac{q^2}{2}\right)\times\nabla\rho\right)\mathrm{d}v\\ &+\oint_{\partial\Omega_{sw}}\left(\rho\frac{q^2}{2}\boldsymbol{n}_{sw}-\rho\boldsymbol{q}\left(\boldsymbol{q}\cdot\boldsymbol{n}_{sw}\right)\right)\mathrm{d}S\\ &+\frac{1}{\mathcal{N}-1}\oint_{\partial\Omega_{sw}}\hat{\boldsymbol{r}}\times\left(\boldsymbol{n}_{sw}\times\frac{q^2}{2}\nabla\rho\right)\mathrm{d}S\\ &-\frac{1}{\mathcal{N}-1}\oint_{S_e}\hat{\boldsymbol{r}}\times\left(\boldsymbol{n}\times\frac{q^2-U_\infty^2}{2}\nabla\rho\right)\mathrm{d}S\\ &+\frac{\boldsymbol{r}_0}{\mathcal{N}-1}\times\frac{U_\infty^2}{2}\oint_{S_e}\boldsymbol{n}\times\nabla\rho\mathrm{d}S\end{aligned} \tag{4.2.14}$$

Using the Stokes theorem (A.6) with $\partial S_e=\varnothing$ (S_e is closed) and knowing that S_e is not crossed by any line of discontinuity, it is possible to show that

$$\oint_{S_e}\boldsymbol{n}\times\nabla\rho\mathrm{d}S=\boldsymbol{0} \tag{4.2.15}$$

and $\boldsymbol{F}_{\rho l}+\boldsymbol{F}^{\text{trans}}_{m_\rho}-\boldsymbol{F}_{\nabla\rho}$ is finally written as follows:

$$\begin{aligned}\boldsymbol{F}_{\rho l}+\boldsymbol{F}^{\text{trans}}_{m_\rho}-\boldsymbol{F}_{\nabla\rho} = &-\int_{\Omega\setminus\Omega_{sw}}\rho\boldsymbol{l}\mathrm{d}v+\frac{1}{\mathcal{N}-1}\int_{\Omega\setminus\Omega_{sw}}\hat{\boldsymbol{r}}\times\left(\nabla\left(\frac{q^2}{2}\right)\times\nabla\rho\right)\mathrm{d}v\\ &+\oint_{\partial\Omega_{sw}}\left(\rho\frac{q^2}{2}\boldsymbol{n}_{sw}-\rho\boldsymbol{q}\left(\boldsymbol{q}\cdot\boldsymbol{n}_{sw}\right)\right)\mathrm{d}S\\ &+\frac{1}{\mathcal{N}-1}\oint_{\partial\Omega_{sw}}\hat{\boldsymbol{r}}\times\left(\boldsymbol{n}_{sw}\times\frac{q^2}{2}\nabla\rho\right)\mathrm{d}S\\ &-\frac{1}{\mathcal{N}-1}\oint_{S_e}\hat{\boldsymbol{r}}\times\left(\boldsymbol{n}\times\frac{q^2-U_\infty^2}{2}\nabla\rho\right)\mathrm{d}S\end{aligned} \tag{4.2.16}$$

To address the last line of (4.2.11), one must first write the Navier-Stokes equations (4.1.38) and notice that

$$\oint_{S_e}\boldsymbol{n}\times\left(\nabla\cdot\boldsymbol{\tau}-\rho\boldsymbol{l}+\frac{q^2-U_\infty^2}{2}\nabla\rho\right)\mathrm{d}S=\oint_{S_e}\boldsymbol{n}\times\nabla\left(P-\frac{U_\infty^2}{2}\rho\right)\mathrm{d}S \tag{4.2.17}$$

Using again the Stokes theorem (A.6) on the closed surface S_e, it is possible to show that

$$\oint_{S_e}\boldsymbol{n}\times\nabla\left(P-\frac{U_\infty^2}{2}\rho\right)\mathrm{d}S=\boldsymbol{0} \tag{4.2.18}$$

The last line of (4.2.11) vanishes and

$$\begin{aligned}\boldsymbol{F}_{S_e}+\boldsymbol{F}_\tau+\boldsymbol{F}_{\nabla\rho} = &\oint_{S_e}\boldsymbol{\tau}\cdot\boldsymbol{n}\mathrm{d}S+\frac{1}{\mathcal{N}-1}\oint_{S_e}\hat{\boldsymbol{r}}\times\left(\boldsymbol{n}\times\left(\nabla\cdot\boldsymbol{\tau}-\rho\boldsymbol{l}\right)\right)\mathrm{d}S\\ &+\frac{1}{\mathcal{N}-1}\oint_{S_e}\hat{\boldsymbol{r}}\times\left(\boldsymbol{n}\times\frac{q^2-U_\infty^2}{2}\nabla\rho\right)\mathrm{d}S\end{aligned} \tag{4.2.19}$$

Therefore, the ONERA formulation naturally provides the same force decomposition whatever the reference point ($\boldsymbol{r}$ or $\hat{\boldsymbol{r}}$) chosen for the computation of moment transformations.

4.2.3 Comparison with Destarac and Van der Vooren's formulation

Although the ONERA decomposition is theoretically independent of the location of the reference point, the numerical errors made in the computation of the integrals make it slightly dependent in practice. That is why the integrals involved in the ONERA decomposition (4.2.6), (4.2.7) and (4.2.8) will be evaluated using the flow symmetrization method presented in section 3.1. Then, neglecting $\boldsymbol{F}_\tau$ in high Re flows, the reference-point-invariant ONERA decomposition is given by

$$\boxed{\begin{aligned} L_{\text{inv}}^{\text{ONERA}} &= \left(\boldsymbol{F}_{\rho l} + \boldsymbol{F}_{m_\rho}^{\text{trans,inv}} - \boldsymbol{F}_{\nabla\rho}^{\text{inv}}\right)\cdot\boldsymbol{e}_z && (4.2.20)\\ D_{i,\text{inv}}^{\text{ONERA}} &= \left(\boldsymbol{F}_{\rho l} + \boldsymbol{F}_{m_\rho}^{\text{trans,inv}} - \boldsymbol{F}_{\nabla\rho}^{\text{inv}}\right)\cdot\boldsymbol{e}_x && (4.2.21)\\ D_{P,\text{inv}}^{\text{ONERA}} &= \left(\boldsymbol{F}_{S_e}^{\text{inv}} + \boldsymbol{F}_{\nabla\rho}^{\text{inv}}\right)\cdot\boldsymbol{e}_x && (4.2.22)\end{aligned}}$$

with

$$\begin{aligned}\boldsymbol{F}_{\nabla\rho}^{\text{inv}} = &\frac{1}{\mathcal{N}-1}\oint_{S_e}\boldsymbol{r}\times\left(\boldsymbol{n}\times\frac{q^2-U_\infty^2}{2}\nabla\rho\Big|_{fw}\right)\mathrm{d}S\\ &+\frac{1}{\mathcal{N}-1}\oint_{S_e}\boldsymbol{r}\times\left(\boldsymbol{n}\times\frac{q^2-U_\infty^2}{2}\nabla\rho\Big|_{ud}\right)\mathrm{d}S\end{aligned} \tag{4.2.23}$$

The reference-point-invariant ONERA decomposition is now applied to transonic flows around the OAT15A airfoil at $M_\infty = 0.72$, $Re = 3\times10^6$ and $\alpha = 2°$ and around the NASA CRM in cruise flight conditions: $M_\infty = 0.85$, $Re = 5\times10^6$ and $C_L \approx 0.5$. The evolution of the reference-point-invariant Mele *et al.*'s decomposition defined in (3.2.38), (3.2.39) and (3.2.40) is also shown for comparison. Both formulations provide the same total drag so only the total drag computed by the ONERA formulation will be shown here. They are finally compared to the reference Destarac and Van der Vooren's thermodynamic formulation [21] (superscript VdV).

OAT15A airfoil

The evolution of the drag on the OAT15A airfoil with respect to the size of the integration domain is displayed in Fig.4.3a. The total drag computed by the ONERA formulation is almost always constant and equal to the thermodynamic prediction: some discrepancies due to numerical errors are reported for $d/c = 5.5$.

The evolution of the lift is presented in Fig.4.3b. Here, the lift predicted by Mele *et al.*'s formulation is always constant while that predicted by the ONERA formulation becomes constant only for $d/c \geq 2$. Anyways, both expressions eventually yield the same value when the size of the integration domain is increased: indeed, the lift component of $\boldsymbol{F}_{\nabla\rho}$ vanishes in the far field of the airfoil.

The decomposition of the drag is shown in Fig.4.4. Even though there is theoretically no lift-induced drag in two-dimensional flows, the evolutions of $C_{D_{i,\text{inv}}}^{\text{Mele}}$ and $C_{D_{i,\text{inv}}}^{\text{ONERA}}$ are investigated because their magnitude is not negligible in the near field (see Fig.4.4a): as already said in subsection 2.2.3, it might come from a slight thrust contribution from the Lamb vector. It can be seen that $C_{D_{i,\text{inv}}}^{\text{ONERA}}$ is always closer to zero than $C_{D_{i,\text{inv}}}^{\text{Mele}}$ although the gap between the two curves progressively shrinks as the size of the integration domain is increased. Similarly, it can be seen that $C_{D_{P,\text{inv}}}^{\text{ONERA}}$ is always closer to $C_{D_P}^{\text{VdV}}$ than $C_{D_{P,\text{inv}}}^{\text{Mele}}$ (see Fig.4.4b). It suggests that the ONERA drag decomposition is in slightly better agreement with the decomposition of Destarac and Van der Vooren [21], although the difference becomes very tiny as the drag component of $\boldsymbol{F}_{\nabla\rho}$ tends to zero in the far field.

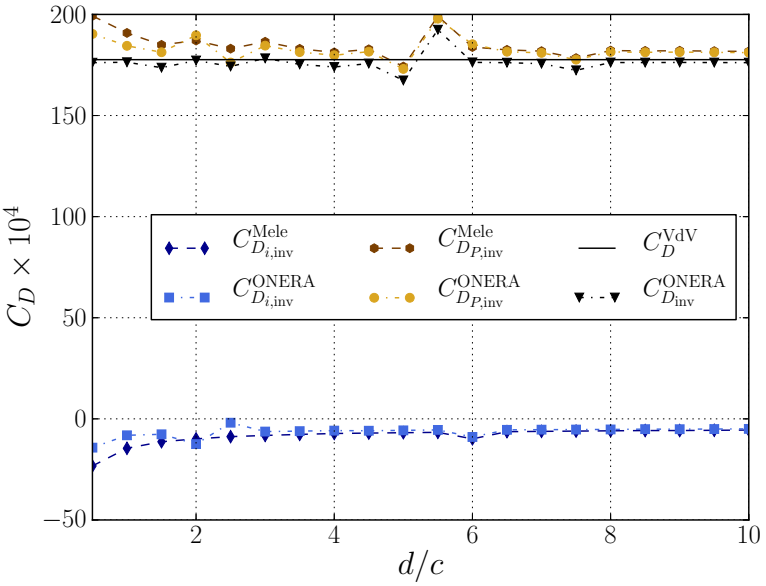

(a) Drag

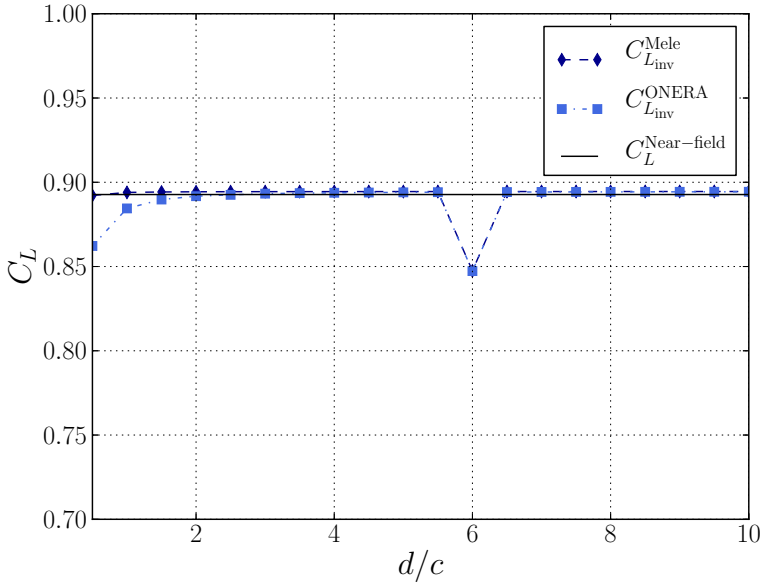

(b) Lift

Figure 4.3: Evolution of the aerodynamic force breakdown with respect to the size of the integration domain: comparison between the reference-point-invariant ONERA formulation, the reference-point-invariant Mele *et al.*'s formulation and Destarac and Van der Vooren's formulation [21] on the OAT15A airfoil, $M_\infty = 0.72$, $Re = 3 \times 10^6$, $\alpha = 2°$

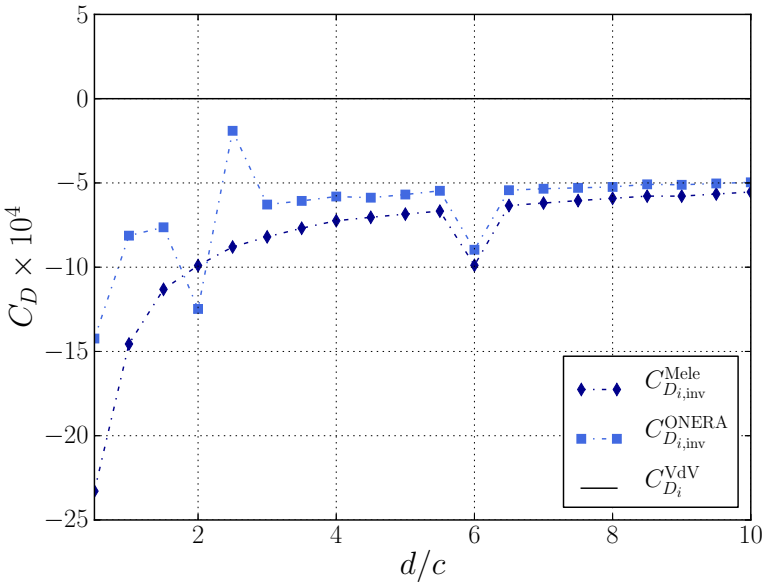

(a) Lift-induced drag

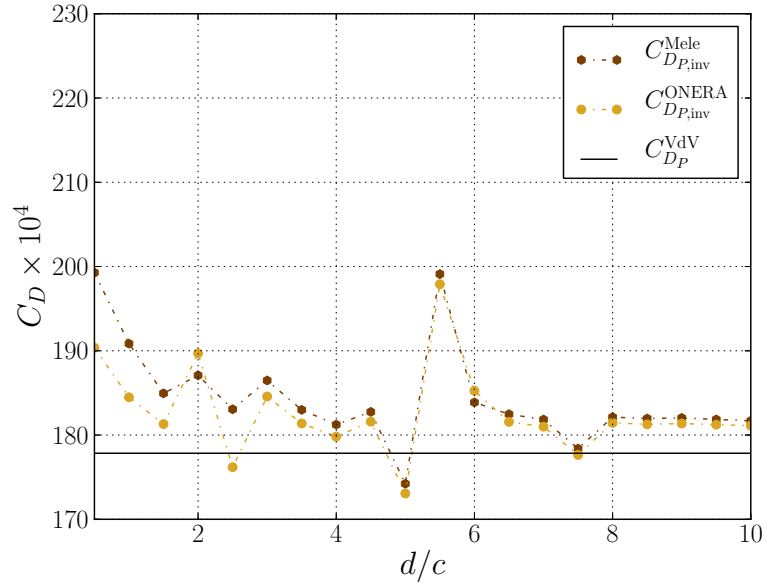

(b) Profile drag

Figure 4.4: Evolution of the lift-induced drag and the profile drag with respect to the size of the integration domain: comparison between the reference-point-invariant ONERA formulation, the reference-point-invariant Mele *et al.*'s formulation and Destarac and Van der Vooren's formulation [21] on the OAT15A airfoil, $M_\infty = 0.72$, $Re = 3 \times 10^6$, $\alpha = 2°$

NASA Common Research Model

The evolution of the drag on the NASA CRM with respect to the size of the integration domain is given in Fig.4.5a. The total drag predicted by the ONERA formulation is constant and equal to the thermodynamic value for $d/c_{ref} \geq 1$. The slight discrepancies occuring for $d/c_{ref} \leq 1$ are due to numerical errors.

The evolution of the lift is shown in Fig.4.5b. The lift evolutions are different in this case, due to the subtraction of $\boldsymbol{F}_{\nabla\rho}$ in the ONERA formulation: $C_{L_{\text{inv}}}^{\text{Mele}}$ decreases while $C_{L_{\text{inv}}}^{\text{ONERA}}$ increases. Both converge to the same value, which again confirms that the lift component of $\boldsymbol{F}_{\nabla\rho}$ disappears in the far field of the aircraft.

Regarding the drag decomposition, the lift-induced drag computed by the ONERA formulation is always higher than that computed by Mele *et al.*'s formulation. On the contrary, the profile drag computed by the ONERA formulation is always lower. It confirms that the drag component of $\boldsymbol{F}_{\nabla\rho}$ is not neglibible in the near field of the aircraft, at least for $d/c_{ref} \leq 2$. The evolution of the lift-induced drag is better perceived in Fig.4.6a. The predictions given by the ONERA formulation and Mele *et al.*'s formulation are compared to those of Destarac and Van der Vooren [21]: $C_{D_{i,\text{inv}}}^{\text{ONERA}}$ is always closer to $C_{D_i}^{\text{VdV}}$ than $C_{D_{i,\text{inv}}}^{\text{Mele}}$. Moreover, $C_{D_{i,\text{inv}}}^{\text{ONERA}}$ becomes constant starting from $d/c_{ref} = 0.6$, i.e. much faster than $C_{D_{i,\text{inv}}}^{\text{Mele}}$ which stabilizes at $d/c_{ref} = 2$. As already said, the increase in lift-induced drag is mostly caused by a still significant contribution of the Lamb vector in the near wake [18, 32, 81], likely coming from the rolling-up of the vortex sheet into two tip vortices [85, 105]. This increase also comes from $\boldsymbol{F}_{\nabla\rho}$: hence $C_{D_{i,\text{inv}}}^{\text{ONERA}}$ is less sensitive to the size of the integration domain than $C_{D_{i,\text{inv}}}^{\text{Mele}}$ since, in $C_{D_{i,\text{inv}}}^{\text{ONERA}}$, the contribution of $\boldsymbol{F}_{\nabla\rho}$ is subtracted from $\boldsymbol{F}_{\rho l} + \boldsymbol{F}_{m_\rho}^{\text{trans}}$. The evolution of the profile drag is shown in Fig.4.6b. $C_{D_{P,\text{inv}}}^{\text{ONERA}}$ is again always closer to $C_{D_P}^{\text{VdV}}$ than $C_{D_{P,\text{inv}}}^{\text{Mele}}$. Here, the bumpy aspect of the $C_{D_{P,\text{inv}}}^{\text{ONERA}}$ curve is caused by numerical errors in the computation of the vorticity on S_e.

In conclusion, a new ONERA decomposition has been developed in order to mathematically match the classical analyses of Kutta, Joukowski, Maskell and Betz in compressible flows. By doing so, the local phenomenological sources of the lift, the lift-induced drag and the profile drag carried by this formulation have been identified. In particular, it has been shown that the compressibility contributes to the lift and the lift-induced drag in the regions characterized by a density gradient, i.e. in compressions and expansions. The ONERA decomposition has then successfully been tested in transonic flows around the OAT15A airfoil and the NASA CRM aircraft configuration. It has been observed that the predicted lift is more sensitive to the size of the integration domain than that computed by Mele *et al*'s formulation [31, 32, 36]. Anyways, both predictions converge to the same value in the far field. Regarding the drag, the agreement with the reference Destarac and Van der Vooren's decomposition [21] is enhanced by using the ONERA decomposition instead of Mele *et al*'s decomposition. This is especially the case on the NASA CRM, suggesting that the compressibility correction $\boldsymbol{F}_{\nabla\rho}$ is not negligible in the near field. Therefore, it seems that the ONERA decomposition is better suited in the case of compressible flows around aircraft configurations. In the end, the ONERA decomposition has several advantages: it is strictly equivalent to the classical analyses, it is theoretically independent of the location of the reference point, and it improves the evaluation of the drag decomposition of typical industrial aircrafts. In the following, its equivalent form based on the theories of Kutta, Joukowski, Maskell and Betz will be analysed.

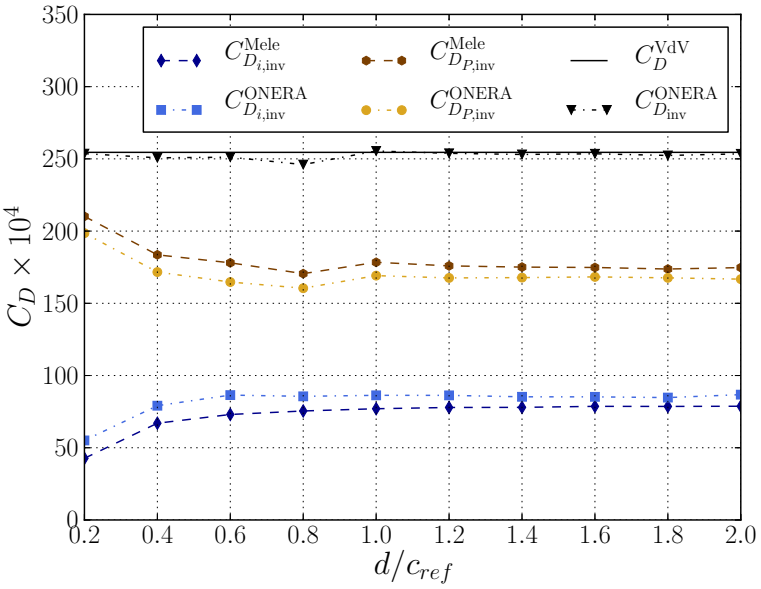

(a) Drag

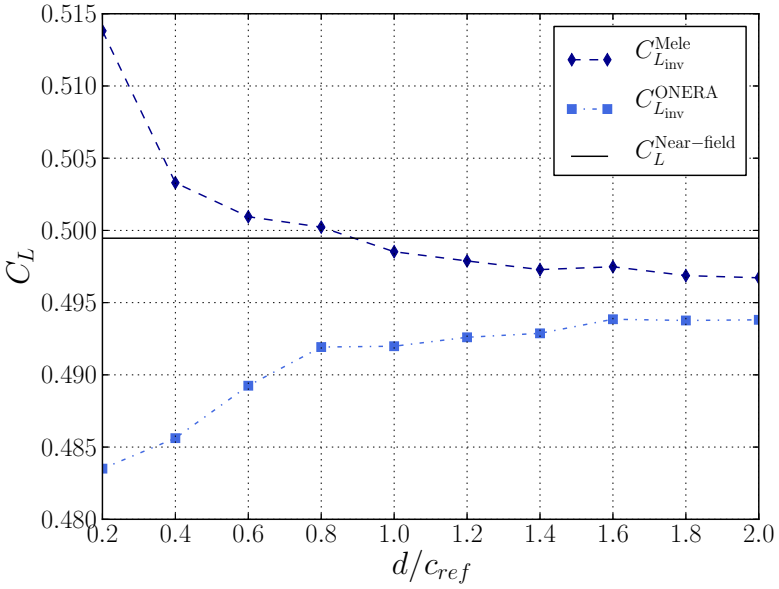

(b) Lift

Figure 4.5: Evolution of the aerodynamic force breakdown with respect to the size of the integration domain: comparison between the reference-point-invariant ONERA formulation, the reference-point-invariant Mele *et al.*'s formulation and Destarac and Van der Vooren's formulation [21] on the NASA CRM, $M_\infty = 0.85$, $Re = 5 \times 10^6$, $C_L \approx 0.5$

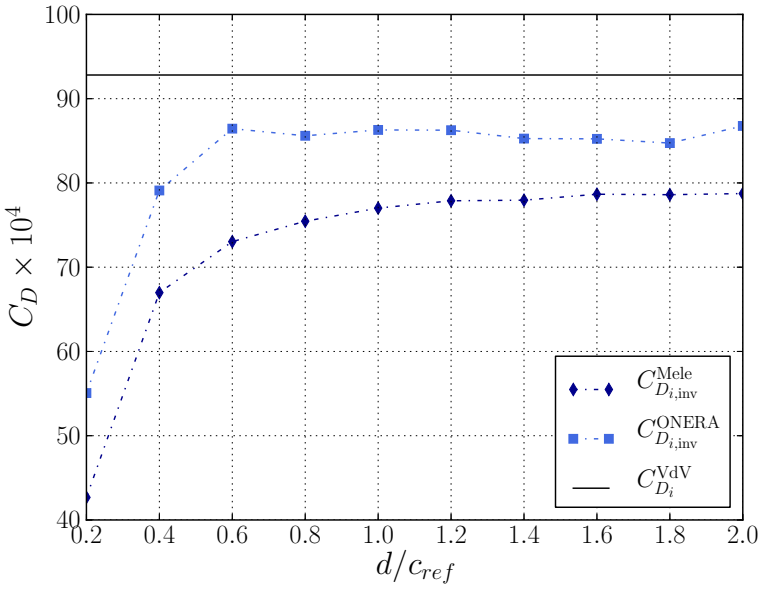

(a) Lift-induced drag

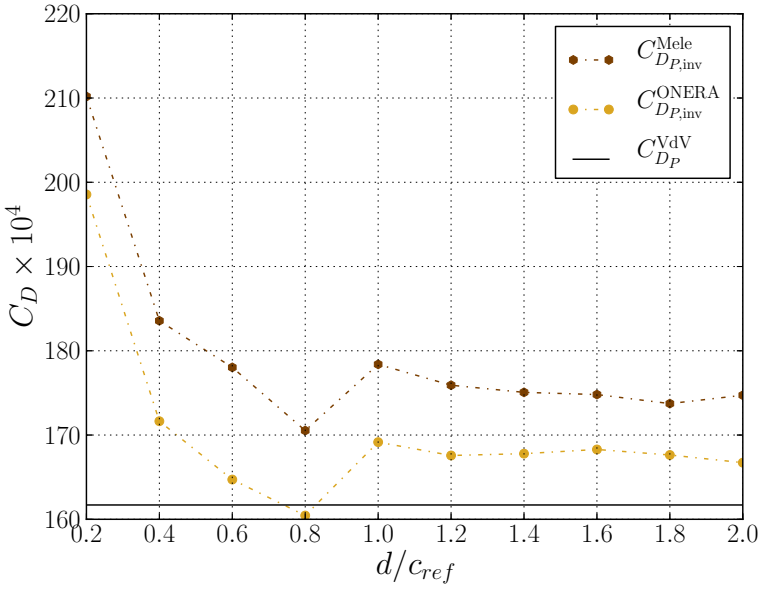

(b) Profile drag

Figure 4.6: Evolution of the lift-induced drag and the profile drag with respect to the size of the integration domain: comparison between the reference-point-invariant ONERA formulation, the reference-point-invariant Mele *et al.*'s formulation and Destarac and Van der Vooren's formulation [21] on the NASA CRM, $M_\infty = 0.85$, $Re = 5 \times 10^6$, $C_L \approx 0.5$

4.3 Analysis of the equivalent Kutta-Joukowski-Maskell-Betz formulation

In the present section, the focus is given to the Kutta-Joukowski-Maskell-Betz (KJMB) formulation, which is mathematically equivalent to the ONERA formulation presented earlier. The goal of this analysis is to find out whether this unprecedented formulation related to classical aerodynamics can accurately predict and decompose the aerodynamic force exerted on an aircraft in cruise flight conditions.

First of all, the KJMB formulation is derived starting from the definition of the ONERA formulation. Then, it is shown that the KJMB formulation summarizes in a single expression the classical analyses of Kutta, Joukowski, Maskell and Betz in compressible flows.

The KJMB formulation is later applied to the same practical test cases as before: the OAT15A airfoil and the NASA CRM. Once again, its drag decomposition is compared to that of Destarac and Van der Vooren [21]. A comparative study with the reference-point-invariant versions of the ONERA formulation and Mele *et al.*'s formulation is also conducted.

Finally, a phenomenological analysis is carried out on the compressible Betz's profile drag expression, in order to gain a better understanding of the role of compressibility in the ONERA and KJMB decompositions. It consists in analysing in more details the role of the term involving density variations in lift and drag.

4.3.1 Presentation of the formulation

In the previous analyses, the ONERA decomposition has been developed in order to be mathematically equivalent to the Kutta-Joukowski theorem, Maskell's formula and Betz's formula. Yet, it has been decided that the lateral parts of S_e are not too close to the aircraft so that the integrals containing the velocity perturbation $\delta\boldsymbol{q}$ reduce to a wake integration on W only. Here, this hypothesis is lifted in order to avoid interpolating the flow solution onto W, since the interpolation may introduce errors in the assessment of the aerodynamic force. Consequently, for the lift and the lift-induced drag, it is necessary to start over from the expression of $\boldsymbol{F}_{\rho l} + \boldsymbol{F}_{m_\rho}^{\text{trans}}$ given in (4.1.34):

$$\boldsymbol{F}_{\rho l} + \boldsymbol{F}_{m_\rho}^{\text{trans}} = \oint_{S_e} \left(\rho \frac{q^2}{2} \boldsymbol{n} - \rho \boldsymbol{q} \left(\boldsymbol{q} \cdot \boldsymbol{n} \right) \right) \mathrm{d}S + \frac{1}{\mathcal{N}-1} \oint_{S_e} \boldsymbol{r} \times \left(\boldsymbol{n} \times \frac{q^2}{2} \nabla \rho \right) \mathrm{d}S \tag{4.3.1}$$

Then, using the definition (4.1.26) of $\boldsymbol{F}_{\nabla\rho}$, it is possible to write $\boldsymbol{F}_{\rho l} + \boldsymbol{F}_{m_\rho}^{\text{trans}} - \boldsymbol{F}_{\nabla\rho}$ as follows:

$$\begin{aligned} \boldsymbol{F}_{\rho l} + \boldsymbol{F}_{m_\rho}^{\text{trans}} - \boldsymbol{F}_{\nabla\rho} &= \oint_{S_e} \left(\rho \frac{q^2}{2} \boldsymbol{n} - \rho \boldsymbol{q} \left(\boldsymbol{q} \cdot \boldsymbol{n} \right) \right) \mathrm{d}S + \frac{1}{\mathcal{N}-1} \frac{U_\infty^2}{2} \oint_{S_e} \boldsymbol{r} \times \left(\boldsymbol{n} \times \nabla \rho \right) \mathrm{d}S \\ &= \oint_{S_e} \left(\rho \frac{q^2}{2} \boldsymbol{n} - \rho \boldsymbol{q} \left(\boldsymbol{q} \cdot \boldsymbol{n} \right) \right) \mathrm{d}S - \frac{U_\infty^2}{2} \oint_{S_e} \rho \boldsymbol{n} \mathrm{d}S \end{aligned} \tag{4.3.2}$$

where the second DMT (A.2) has been applied to ρ. Then, the velocity vector is once again decomposed as $\boldsymbol{q} = \boldsymbol{U}_\infty + \delta\boldsymbol{q}$ and the first integral of (4.3.2) is transformed by following the same steps that led from (4.1.11) to (4.1.14):

$$\begin{aligned} \oint_{S_e} \left(\rho \frac{q^2}{2} \boldsymbol{n} - \rho \boldsymbol{q} \left(\boldsymbol{q} \cdot \boldsymbol{n} \right) \right) \mathrm{d}S = \boldsymbol{U}_\infty \times \oint_{S_e} \boldsymbol{n} \times \rho \delta\boldsymbol{q} \mathrm{d}S \\ + \oint_{S_e} \rho \frac{\delta q^2}{2} \boldsymbol{n} \mathrm{d}S - \oint_{S_e} \rho \delta\boldsymbol{q} \left(\delta\boldsymbol{q} \cdot \boldsymbol{n} \right) \mathrm{d}S \\ + \frac{U_\infty^2}{2} \oint_{S_e} \rho \boldsymbol{n} \mathrm{d}S \end{aligned} \tag{4.3.3}$$

Finally, by replacing in (4.3.2), it is possible to equivalently express $\boldsymbol{F}_{\rho l} + \boldsymbol{F}_{m_\rho}^{\text{trans}} - \boldsymbol{F}_{\nabla\rho}$ as follows:

$$\boxed{\boldsymbol{F}_{\rho l} + \boldsymbol{F}_{m_\rho}^{\text{trans}} - \boldsymbol{F}_{\nabla\rho} = \boldsymbol{F}_{\text{KJ}} + \boldsymbol{F}_{\text{MSK}}} \tag{4.3.4}$$

with

$$\boxed{\begin{aligned} \boldsymbol{F}_{\text{KJ}} &= \boldsymbol{U}_\infty \times \oint_{S_e} \boldsymbol{n} \times \rho\delta\boldsymbol{q}\mathrm{d}S + \left(\oint_{S_e} \rho\left(\frac{\delta q^2}{2} n_z - w\left(\delta\boldsymbol{q}\cdot\boldsymbol{n}\right)\right)\mathrm{d}S\right)\boldsymbol{e}_z \qquad (4.3.5)\\ \boldsymbol{F}_{\text{MSK}} &= \left(\oint_{S_e} \rho\left(\frac{\delta q^2}{2} n_x - u\left(\delta\boldsymbol{q}\cdot\boldsymbol{n}\right)\right)\mathrm{d}S\right)\boldsymbol{e}_x \qquad (4.3.6)\end{aligned}}$$

Here, $\boldsymbol{F}_{\text{KJ}}$ and $\boldsymbol{F}_{\text{MSK}}$ correspond to the Kutta-Joukowski lift theorem and Maskell's lift-induced drag formula when S_e is close to the aircraft. If the lateral parts of S_e are relegated far from the aircraft, then $\boldsymbol{F}_{\text{KJ}}$ and $\boldsymbol{F}_{\text{MSK}}$ reduce to more familiar expressions:

$$\boldsymbol{F}_{\text{KJ}} = -\rho_\infty U_\infty \left(\Gamma^* + \delta\Gamma^*\right)\boldsymbol{e}_z \tag{4.3.7}$$

$$\boldsymbol{F}_{\text{MSK}} = \left(\frac{1}{2}\int_W \rho\left(v^2 + w^2 - u^2\right)\mathrm{d}S\right)\boldsymbol{e}_x \tag{4.3.8}$$

with Γ^* and $\delta\Gamma^*$ defined in (4.1.19) and (4.1.20).

For the profile drag, it is necessary to start over from the expression of $\boldsymbol{F}_{S_e} + \boldsymbol{F}_\tau$ given in (4.1.42) and notice that

$$\boxed{\boldsymbol{F}_{S_e} + \boldsymbol{F}_\tau + \boldsymbol{F}_{\nabla\rho} = \boldsymbol{F}_{\text{BETZ}}} \tag{4.3.9}$$

with

$$\boxed{\boldsymbol{F}_{\text{BETZ}} = \oint_{S_e} \boldsymbol{\tau}\cdot\boldsymbol{n}\mathrm{d}S + \oint_{S_e}\left(P_\infty - P\right)\boldsymbol{n}\mathrm{d}S - \frac{U_\infty^2}{2}\oint_{S_e}\left(\rho_\infty - \rho\right)\boldsymbol{n}\mathrm{d}S} \tag{4.3.10}$$

$\boldsymbol{F}_{\text{BETZ}}$ is the compressible Betz's profile drag formula established in (4.1.42).

Finally, when adding up (4.3.4) and (4.3.9), the aerodynamic force $\boldsymbol{F}$ exerted on the aircraft is recovered:

$$\boldsymbol{F} = \boldsymbol{F}_{\text{KJ}} + \boldsymbol{F}_{\text{MSK}} + \boldsymbol{F}_{\text{BETZ}} \tag{4.3.11}$$

As for the ONERA decomposition, the latter formulation is an exact expression since no approximation has been introduced in the derivations. Then, it can be seen that (4.3.11) summarizes in the same expression the classical theories of Kutta, Joukowski, Maskell and Betz. Besides, this relation holds from subsonic to transonic flows although these theories were initially developed in incompressible flows. The KJMB decomposition is then defined as follows:

$$\boxed{\begin{aligned} L^{\text{KJMB}} &= \boldsymbol{e}_z\cdot\boldsymbol{F}_{\text{KJ}} \qquad (4.3.12)\\ D_i^{\text{KJMB}} &= \boldsymbol{e}_x\cdot\boldsymbol{F}_{\text{MSK}} \qquad (4.3.13)\\ D_P^{\text{KJMB}} &= \boldsymbol{e}_x\cdot\boldsymbol{F}_{\text{BETZ}} \qquad (4.3.14)\end{aligned}}$$

4.3.2 Comparison with the Lamb-vector-based approaches and Destarac and Van der Vooren's formulation

The KJMB decomposition is now tested on the OAT15A airfoil at $M_\infty = 0.72$, $Re = 3\times10^6$ and $\alpha = 2°$ and on the NASA CRM in cruise flight conditions: $M_\infty = 0.85$, $Re = 5\times10^6$ and $C_L \approx 0.5$.

First of all, the evolution of the decomposition with respect to the size of the integration domain is investigated. In the same time, a comparison is made with the reference Destarac and Van der Vooren's decomposition [21]. Eventually, the KJMB decomposition is also compared to the reference-point-invariant versions of the ONERA formulation and Mele *et al.*'s formulation.

OAT15A airfoil

The evolution of the drag on the OAT15A airfoil is shown in Fig.4.7a. In this case, the total drag computed by the KJMB formulation is always in perfect agreement with the thermodynamic value.

The lift evolution is presented in Fig.4.7b. Like $C_{L_{\text{inv}}}^{\text{ONERA}}$, C_L^{KJMB} reaches the near-field prediction as soon as $d/c \geq 2$ and remains constant afterwards, although a numerical error is reported at $d/c = 6$.

Regarding the drag breakdown, like in the ONERA decomposition and Mele *et al.*'s decomposition, the KJMB decomposition overestimates the profile drag, and the lift-induced drag is not exactly equal to zero (see Fig.4.8). Nevertheless, $C_{D_i}^{\text{KJMB}}$ is anyhow closer to zero than $C_{D_{i,\text{inv}}}^{\text{Mele}}$ and $C_{D_{i,\text{inv}}}^{\text{ONERA}}$ (see Fig.4.4a). Similarly, $C_{D_P}^{\text{KJMB}}$ is closer to $C_{D_P}^{\text{VdV}}$ than $C_{D_{P,\text{inv}}}^{\text{Mele}}$ and $C_{D_{P,\text{inv}}}^{\text{ONERA}}$ (see Fig.4.4b). The ONERA and KJMB formulations being mathematically equivalent, the discrepancies observed when comparing their respective results may come from numerical errors. Again, it is expected that $C_{D_i}^{\text{KJMB}}$ tends to zero and $C_{D_P}^{\text{KJMB}}$ tends to $C_{D_P}^{\text{VdV}}$ only in the extreme far field.

Those observations are confirmed by the results listed in Table 4.1 for $d/c = 10$. In this case, the total drag computed by the KJMB formulation is exactly equal to the near-field drag, and the computed lift is in better agreement with the near-field lift than the ONERA formulation and Mele *et al.*'s formulation. Hence, the KJMB formulation slightly outperforms the two formulations based on the Lamb vector in this two-dimensional case.

Formulation	$C_{D_i} \times 10^4$	$C_{D_P} \times 10^4$	$C_D \times 10^4$	C_L
Destarac and Van der Vooren [21]	0.00	177.63	177.63	–
Mele *et al.* invariant	-5.54	181.69	176.15	0.89452
ONERA invariant	-4.96	181.11	176.15	0.89436
Kutta-Joukowski-Maskell-Betz	-2.88	180.72	177.84	0.89324
Near-field	–	–	177.84	0.89272

Table 4.1: Comparison between the various aerodynamic force breakdown formulations on the OAT15A airfoil, $M_\infty = 0.72$, $Re = 3 \times 10^6$, $\alpha = 2°$ and $d/c = 10$.

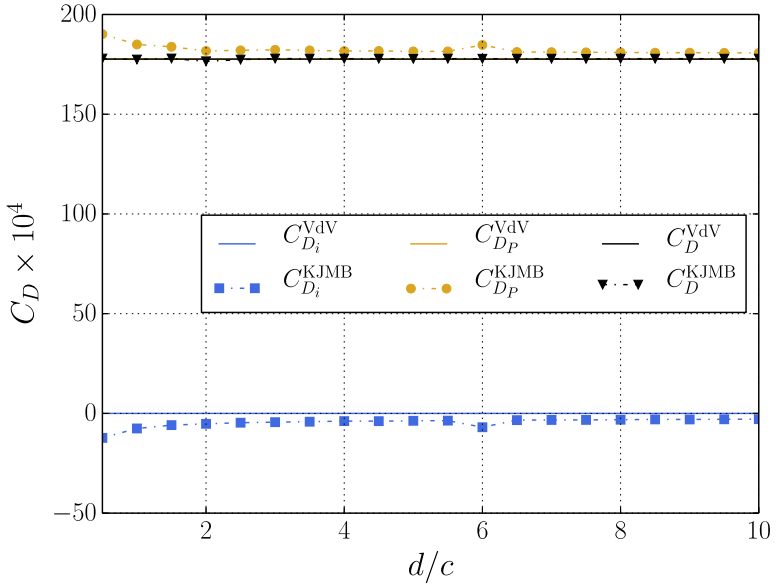

(a) Drag

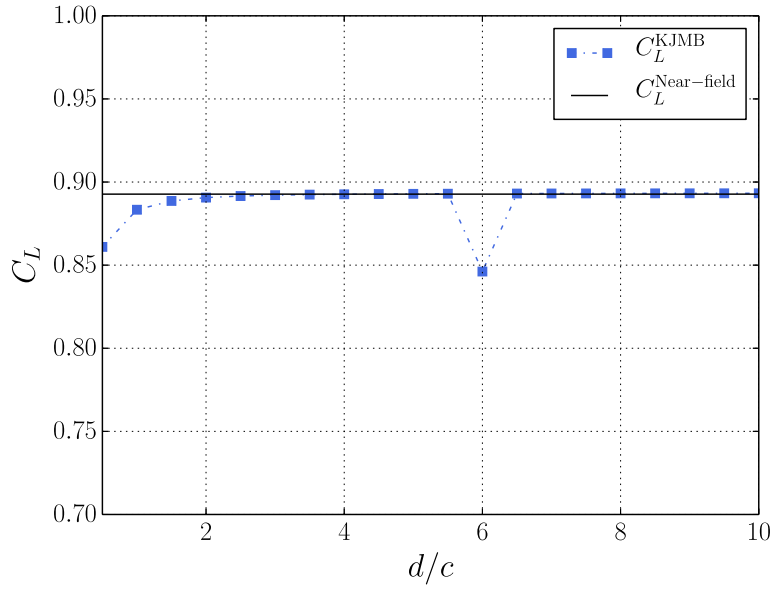

(b) Lift

Figure 4.7: Evolution of the aerodynamic force breakdown with respect to the size of the integration domain: comparison between the KJMB formulation and Destarac and Van der Vooren's formulation [21] on the OAT15A airfoil, $M_\infty = 0.72$, $Re = 3 \times 10^6$, $\alpha = 2°$

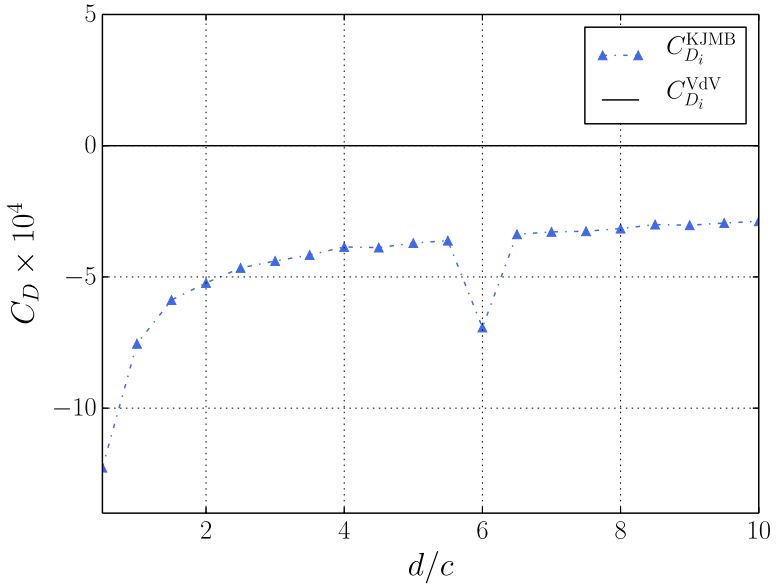

(a) Lift-induced drag

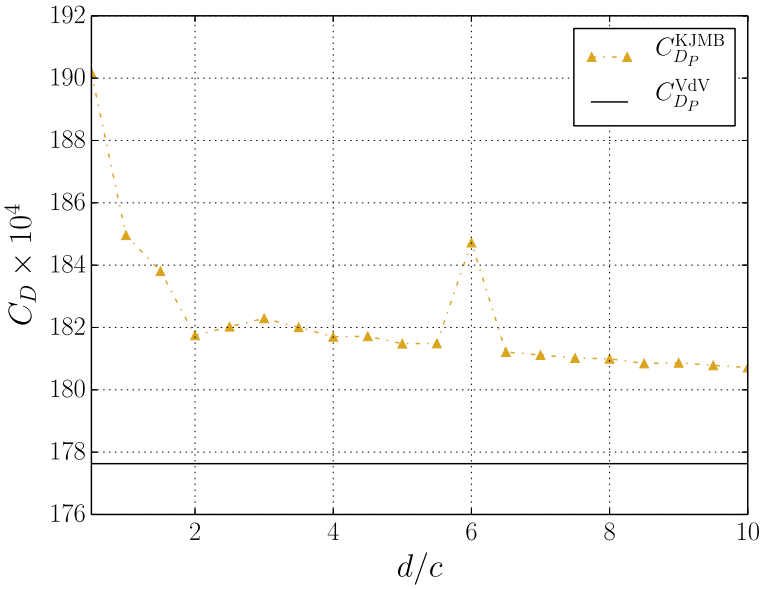

(b) Profile drag

Figure 4.8: Evolution of the lift-induced drag and the profile drag with respect to the size of the integration domain: comparison between the KJMB formulation and Destarac and Van der Vooren's formulation [21] on the OAT15A airfoil, $M_\infty = 0.72$, $Re = 3 \times 10^6$, $\alpha = 2°$

NASA Common Research Model

The evolution of the drag on the NASA CRM is shown in Fig.4.9a. Once again, the total drag computed by the KJMB formulation is always in perfect agreement with the thermodynamic prediction.

The evolution of the lift is presented in Fig.4.9b. The agreement with the near-field prediction is very satisfying starting from $d/c_{ref} = 0.8$ and is almost perfect for $d/c_{ref} \geq 1.6$. It confirms that the Kutta-Joukowski theorem can be used to measure the lift in viscous transonic flows. Here it is expected that the KJMB formulation gives the same values as the ONERA formulation, yet the total lift and drag predictions of the KJMB formulation are more accurate (see Fig.4.5). The gaps are again likely imputable to numerical errors in the assessment of the integrals.

The decomposition of the drag is illustrated in Fig.4.10. As for the ONERA decomposition and Mele *et al.*'s decomposition, the lift-induced drag increases in the near field (see Fig.4.10a) while the profile drag decreases (see Fig.4.10b). However, the agreement with the thermodynamic decomposition of Destarac and Van der Vooren [21] seems better in the KJMB decomposition. $C_{D_i}^{\text{KJMB}}$ and $C_{D_P}^{\text{KJMB}}$ respectively reach their maximum and minimum value at $d/c_{ref} = 1$. For $d/c_{ref} \geq 1$, it can be seen that $C_{D_P}^{\text{KJMB}}$ slightly increases while $C_{D_i}^{\text{KJMB}}$ slightly decreases, keeping C_D^{KJMB} constant. This is the transfer from the lift-induced drag to the profile drag caused by the viscous and numerical dissipations. Yet, this transfer has surpringly not been noticed in the ONERA decomposition, which proved to be less sensitive to the size of the integration domain in the far field (see Fig.4.6). No satisfying explanation has been found until now to explain this difference.

Additional results are listed in Table 4.2 for $d/c_{ref} = 1$. Taking the decomposition of Destarac and Van der Vooren [21] as reference, it is clear that the ONERA and KJMB decompositions outperform by far Mele *et al.*'s decomposition. Indeed, the lift-induced drag is increased by almost 10 counts with the ONERA decomposition and is then in much greater agreement with the thermodynamic value: it is 6 counts lower for the ONERA decomposition and 15 counts lower for Mele *et al.*'s decomposition. The agreement is even better for the KJMB decomposition with a lift-induced drag prediction only 5 counts lower than the thermodynamic value. Similarly, the profile drag values computed by the ONERA and KJMB decompositions are also closer to that computed by the thermodynamic approach.

Formulation	$C_{D_i} \times 10^4$	$C_{D_P} \times 10^4$	$C_D \times 10^4$	C_L
Destarac and Van der Vooren [21]	92.81	161.70	254.51	–
Mele *et al.* invariant	77.01	178.39	255.40	0.49852
ONERA invariant	86.29	169.11	255.40	0.49198
Kutta-Joukowski-Maskell-Betz	87.26	167.63	254.89	0.49698
Near-field	–	–	254.70	0.49946

Table 4.2: Comparison between the various aerodynamic force breakdown formulations on the NASA CRM, $M_\infty = 0.85$, $Re = 5 \times 10^6$, $C_L \approx 0.5$ and $d/c_{ref} = 1$.

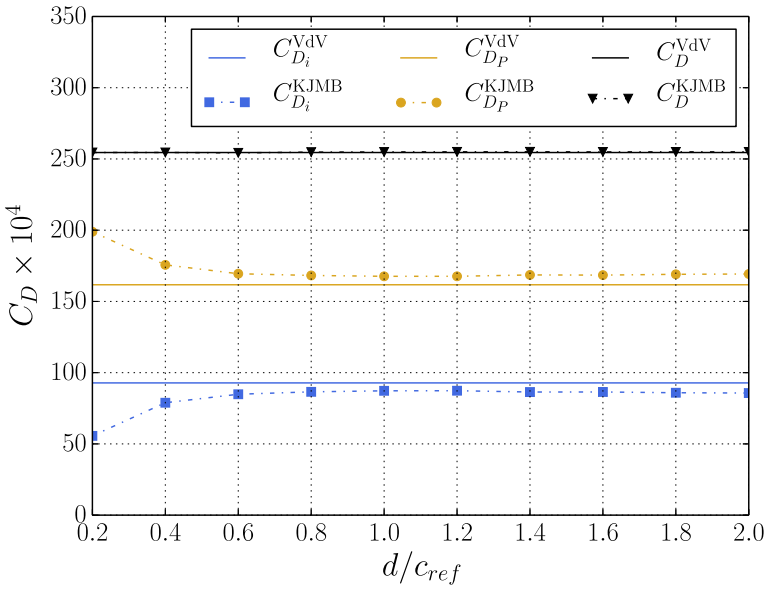

(a) Drag

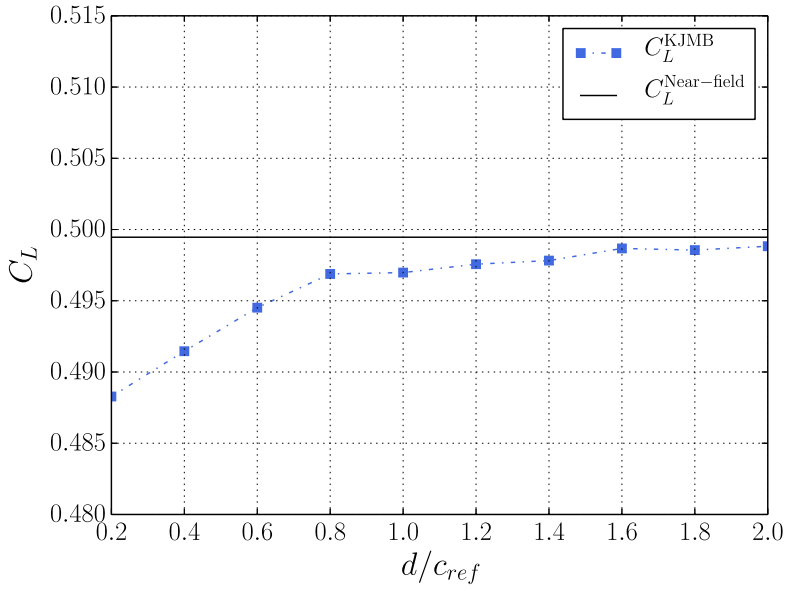

(b) Lift

Figure 4.9: Evolution of the aerodynamic force breakdown with respect to the size of the integration domain: comparison between the KJMB formulation and Destarac and Van der Vooren's formulation [21] on the NASA CRM, $M_\infty = 0.85$, $Re = 5 \times 10^6$, $C_L \approx 0.5$

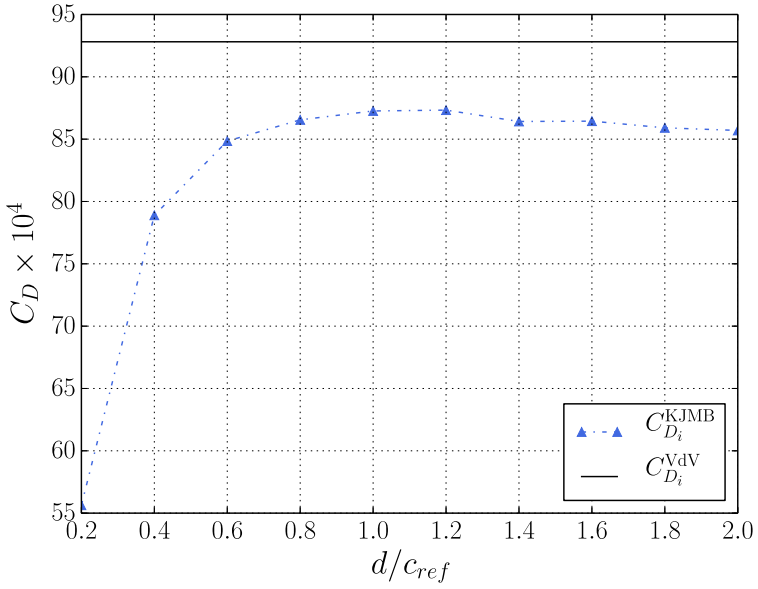

(a) Lift-induced drag

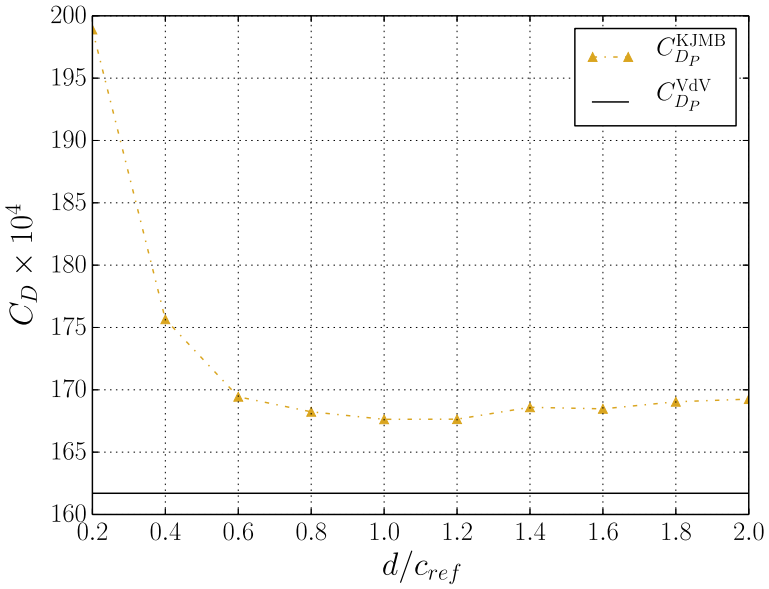

(b) Profile drag

Figure 4.10: Evolution of the lift-induced drag and the profile drag with respect to the size of the integration domain: comparison between the KJMB formulation and Destarac and Van der Vooren's formulation [21] on the NASA CRM, $M_\infty = 0.85$, $Re = 5 \times 10^6$, $C_L \approx 0.5$

4.3.3 Phenomenological analysis of the role of compressibility in the KJMB and ONERA decompositions

Hence, the KJMB formulation is completely suited to predict and decompose the aerodynamic force exerted on an aircraft in cruise flight with intricate physics at work. The numerical results also confirm the equivalence between the ONERA and KJMB decompositions shown in subsection 4.3.1. Hence, it gives the opportunity to identify the role of compressibility in the lift, the lift-induced drag and the profile drag in the ONERA decomposition. Indeed, the ONERA decomposition may now be interpreted with the physical quantities involved in the KJMB decomposition, rather than with the Lamb vector and the density gradient. In the following analysis, the focus is first given to the compressible Betz's profile drag formula because the compressibility appears explicitly in its expression (4.3.10).

With (4.3.14), it has been shown in the KJMB decomposition that the profile drag corresponds to a compressible Betz's formula. This extension to compressible flows is unprecedented and the physics at stake are not fully understood yet. Hence, the aim of the present analysis is to identify the role of compressibility by establishing the links between this formula and its incompressible version. For this purpose, $\boldsymbol{F}_{\mathrm{BETZ}}$ is decomposed into

$$\boldsymbol{F}_{\mathrm{BETZ}} = \oint_{S_e} \boldsymbol{\tau}\cdot\boldsymbol{n}\mathrm{d}S + \boldsymbol{F}_{\Delta P} + \boldsymbol{F}_{\Delta\rho} \tag{4.3.15}$$

with

$$\boldsymbol{F}_{\Delta P} = -\oint_{S_e} \Delta P\boldsymbol{n}\mathrm{d}S = \oint_{S_e} (P_\infty - P)\,\boldsymbol{n}\mathrm{d}S \tag{4.3.16}$$

$$\boldsymbol{F}_{\Delta\rho} = \frac{U_\infty^2}{2}\oint_{S_e} \Delta\rho\boldsymbol{n}\mathrm{d}S = \frac{U_\infty^2}{2}\oint_{S_e} (\rho - \rho_\infty)\,\boldsymbol{n}\mathrm{d}S \tag{4.3.17}$$

where $\Delta P = P - P_\infty$ and $\Delta\rho = \rho - \rho_\infty$. As mentioned in subsection 1.1.1, Betz initially defined the profile drag as the total pressure losses $P_\infty - P$ in incompressible flows [8]. In compressible flows however, the contribution of $\boldsymbol{F}_{\Delta\rho}$ must be accounted for. Hence Betz's definition does not hold anymore. In fact, it is necessary to identify the physical role of $\boldsymbol{F}_{\Delta\rho}$ in compressible flows. It is possible to relate the compressible Betz's formula $\boldsymbol{F}_{\mathrm{BETZ}}$ to its incompressible version $\boldsymbol{F}_{\mathrm{BETZ}}^{\mathrm{incomp}}$:

$$\boldsymbol{F}_{\mathrm{BETZ}} = \boldsymbol{F}_{\mathrm{BETZ}}^{\mathrm{incomp}} - \oint_{S_e} (\rho - \rho_\infty)\,\frac{q^2 - U_\infty^2}{2}\boldsymbol{n}\mathrm{d}S \tag{4.3.18}$$

with

$$\boldsymbol{F}_{\mathrm{BETZ}}^{\mathrm{incomp}} = \oint_{S_e} \boldsymbol{\tau}\cdot\boldsymbol{n}\mathrm{d}S + \oint_{S_e}\left[P_\infty - \left(p + \frac{1}{2}\rho_\infty q^2\right)\right]\boldsymbol{n}\mathrm{d}S \tag{4.3.19}$$

In (4.3.18), the sum of $\boldsymbol{F}_{\Delta P}$ and $\boldsymbol{F}_{\Delta\rho}$ is equal to the incompressible profile drag expression $\boldsymbol{F}_{\mathrm{BETZ}}^{\mathrm{incomp}}$ established by Betz [8] plus a correction term containing the density and kinetic energy perturbations. This correction term is expected to vanish in the far field of the aircraft. Hence, in order to understand the role of compressibility in the profile drag, it is necessary to examine the evolution of $\boldsymbol{F}_{\Delta P}$, $\boldsymbol{F}_{\Delta\rho}$ and $\boldsymbol{F}_{\mathrm{BETZ}}^{\mathrm{incomp}}$ with respect to the size of the integration domain. In addition to the profile drag, the analysis will also allow to identify how the compressibility contributes to the lift and the lift-induced drag in the KJMB and ONERA decompositions. For this purpose, it is necessary to combine (4.3.2), (4.3.4), and the definition (4.3.17) of $\boldsymbol{F}_{\Delta\rho}$ in order to write

$$\boldsymbol{F}_{\rho l} + \boldsymbol{F}_{m_\rho}^{\mathrm{trans}} - \boldsymbol{F}_{\nabla\rho} = \boldsymbol{F}_{\mathrm{KJ}} + \boldsymbol{F}_{\mathrm{MSK}} = \oint_{S_e}\left(\rho\frac{q^2}{2}\boldsymbol{n} - \rho\boldsymbol{q}\,(\boldsymbol{q}\cdot\boldsymbol{n})\right)\mathrm{d}S - \boldsymbol{F}_{\Delta\rho} \tag{4.3.20}$$

Hence, with (4.2.6), (4.2.7), (4.3.12) and (4.3.13), there is:

$$L^{\text{ONERA}} = L^{\text{KJMB}} = \boldsymbol{e}_z \cdot \oint_{S_e} \left(\rho \frac{q^2}{2} \boldsymbol{n} - \rho \boldsymbol{q} \left(\boldsymbol{q} \cdot \boldsymbol{n} \right) \right) \mathrm{d}S - L_{\Delta\rho} \tag{4.3.21}$$

$$D_i^{\text{ONERA}} = D_i^{\text{KJMB}} = \boldsymbol{e}_x \cdot \oint_{S_e} \left(\rho \frac{q^2}{2} \boldsymbol{n} - \rho \boldsymbol{q} \left(\boldsymbol{q} \cdot \boldsymbol{n} \right) \right) \mathrm{d}S - D_{\Delta\rho} \tag{4.3.22}$$

Besides, with (4.2.8), (4.3.9), (4.3.14) and (4.3.15), there is:

$$D_P^{\text{ONERA}} = D_P^{\text{KJMB}} = D_{\text{BETZ}} = \boldsymbol{e}_x \cdot \oint_{S_e} \boldsymbol{\tau} \cdot \boldsymbol{n} \mathrm{d}S + D_{\Delta P} + D_{\Delta\rho} \tag{4.3.23}$$

The analysis of $\boldsymbol{F}_{\Delta\rho}$ will then allow to gain more insights on all the contributors of the aerodynamic force, in both decompositions.

The evolution of $\boldsymbol{F}_{\text{BETZ}}$ is shown in Fig.4.11. It can be seen that the lift component of $\boldsymbol{F}_{\Delta P}$ is positive and not equal to zero. It means that the variations in P are not only responsible for a drag contribution in compressible flows, but also for a lift contribution. Actually, $C_{L_{\Delta\rho}}$ exactly balances $C_{L_{\Delta P}}$, which suggests that the lift contribution produced by the variations in P actually come from density variations. It is illustrated in Fig.4.12: the losses in P on the suction side of the wing (see Fig.4.12a in green) exactly coincide with the decrease in density caused by the fluid expansion in this region (see Fig.4.12b in purple). This expansion is responsible for part of the lift in compressible flows. Indeed, according to (4.3.21), the flow expansion on the suction side leading to $L_{\Delta\rho} \leq 0$ contributes to the lift. Hence, both in the ONERA and KJMB decompositions, (4.3.21) reveals that the compressibility plays a role in the lift through $\boldsymbol{F}_{\Delta\rho}$, i.e. through the density variations occuring in compressions and expansions. In $C_{L_{\text{BETZ}}}$, $C_{L_{\Delta P}}$ is instead cancelled by $C_{L_{\Delta\rho}}$, therefore guaranteeing that $\boldsymbol{F}_{\text{BETZ}}$ is only a drag contribution: the profile drag contributions D_P^{ONERA} and D_P^{KJMB} according to (4.3.23). Finally, the lift component of the correction term identified in (4.3.18) effectively disappears in the far field since $C_{L_{\text{BETZ}}}^{\text{incomp}}$ quickly converges to zero and the $C_{L_{\text{BETZ}}}$ curve.

Regarding the drag, $C_{D_{\Delta P}}$ and $C_{D_{\Delta\rho}}$ have once again complementary evolutions: for $d/c_{ref} \geq 0.6$, $C_{D_{\text{BETZ}}}$ remains almost constant. Notably, the decrease in $C_{D_{\Delta P}}$ is always compensated by the increase in $C_{D_{\Delta\rho}}$. Yet, it is not trivial to understand this increase since $\frac{U_\infty^2}{2}\Delta\rho$ is evaluated on S_e, which is itself defined by the distance d to the aircraft surface S_b (see Fig.2.2). Consequently, the boundaries of S_e follow the shape of the aircraft and intersect alternatively compression and expansion zones away from the leading and trailing edges (see Fig.4.13). That is why it makes it difficult to interpret the behaviour of $C_{D_{\Delta\rho}}$. To do so, it is necessary to analyse the quantity $\frac{U_\infty^2}{2}\Delta\rho$ in the vicinity of the aircraft. As seen in Fig.4.12b, compressions occuring at the nose, the wing leading edge and the bottom part of the aircraft increase the fluid density (in orange), hence increase P (see Fig.4.12a in orange), and generate a drag contribution. That is why $C_{D_{\Delta P}} \geq C_{D_{\text{BETZ}}}$ and $C_{D_{\Delta\rho}} \leq 0$ for $d/c_{ref} \leq 1.3$. In $C_{D_{\text{BETZ}}}$, $C_{D_{\Delta P}}$ is however compensated by $C_{D_{\Delta\rho}}$ such that those compression-induced density variations do not contribute to the profile drag. Rather, they contribute to the lift-induced drag. Indeed, $D_{\Delta\rho}$ is negative in the compressions occuring at the nose and the leading edge (where $n_x \leq 0$), and then contributes to the lift-induced drag according to (4.3.22). Hence, both in the ONERA and KJMB decompositions, (4.3.22) suggests that the compressibility also plays a role in the lift-induced drag through $\boldsymbol{F}_{\Delta\rho}$.

The evolution of $\boldsymbol{F}_{\Delta\rho}$ with respect to the location of S_e (see Fig.4.11) is directly related to the compressions and expansions occuring in the vicinity of the aircraft. The positive contribution to the profile drag for $d/c_{ref} \geq 1.3$ corresponds to S_e crossing in the same time the expansion (see Fig.4.13 in blue) caused by the fuselage upstream of the wing (where $n_x \leq 0$) and the compression (in red) near the tail of the fuselage (where $n_x \geq 0$). Anyways, it has been shown that $C_{D_{\Delta\rho}}$ represents the variations in P induced by density variations and that it always balances $C_{D_{\Delta P}}$. As in the incompressible case, it means that the profile drag computed by $\boldsymbol{F}_{\text{BETZ}}$ comes

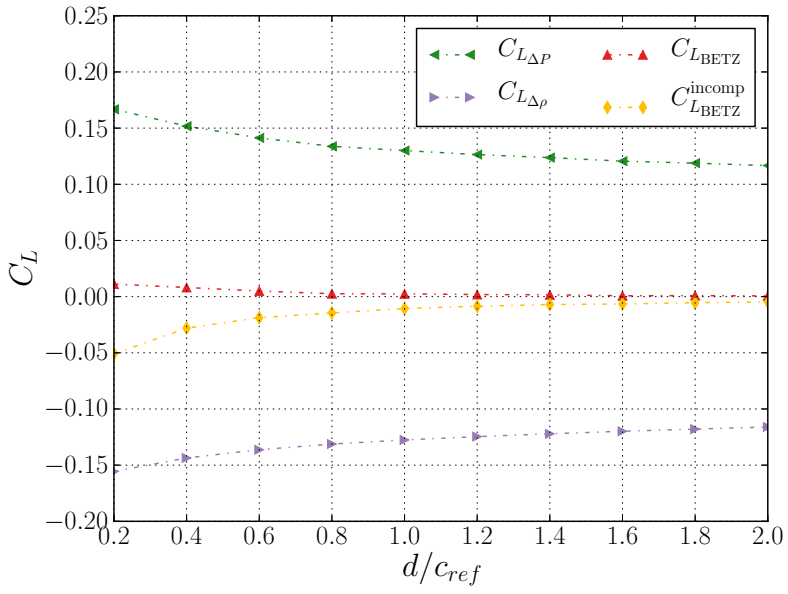

(a) Lift

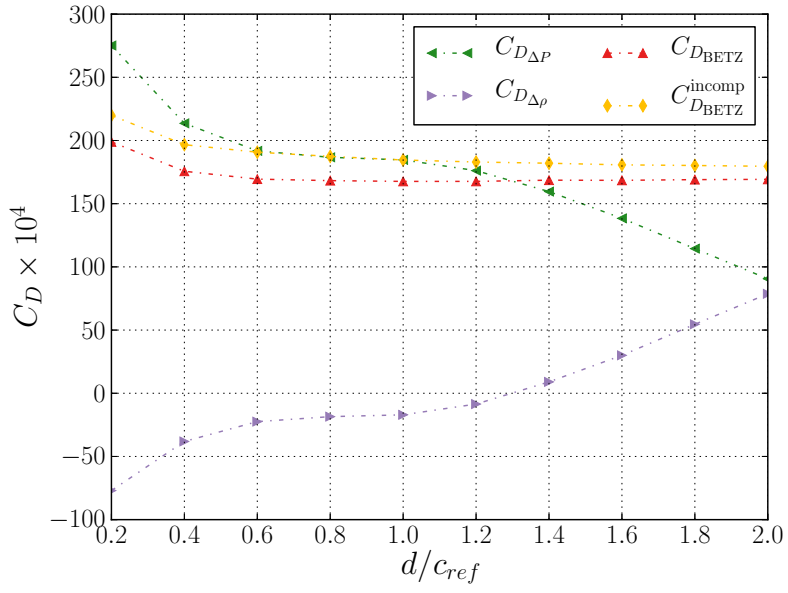

(b) Drag

Figure 4.11: Breakdown of $\boldsymbol{F}_{\text{BETZ}}$ on the NASA CRM, $M_\infty = 0.85$, $Re = 5 \times 10^6$, $C_L \approx 0.5$

from the losses in P induced by losses in static pressure and kinetic energy only. These losses occur in boundary layers and wakes (see Fig.4.12a). This interpretation is confirmed by $C^{\text{incomp}}_{D_{\text{BETZ}}}$ converging to the same value as $C_{D_{\text{BETZ}}}$ in the far field (see Fig.4.11b). It also proves that the drag component of the correction term identified in (4.3.18) vanishes in the far field. In conclusion, the incompressible Betz's profile drag formula $\boldsymbol{F}^{\text{incomp}}_{\text{BETZ}}$ [8] still holds in compressible flows, provided that S_e is located sufficiently far from the aircraft.

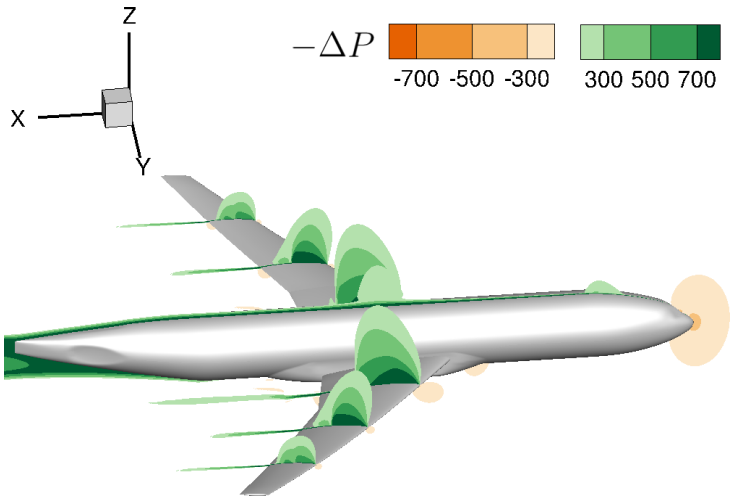

(a) ΔP

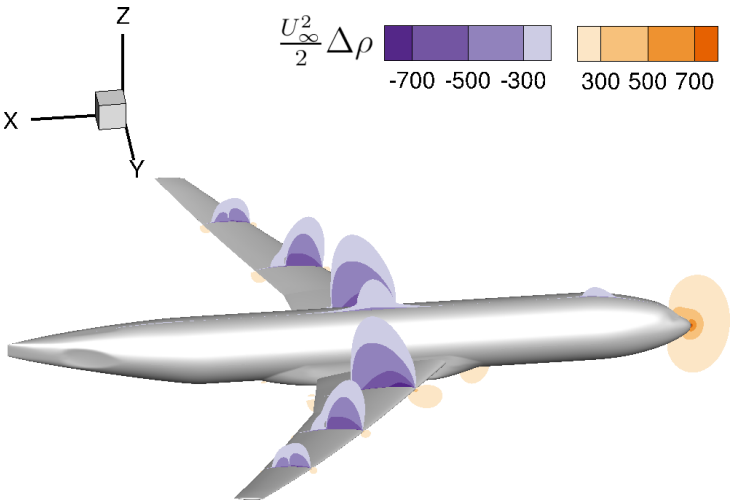

(b) $\frac{U_\infty^2}{2}\Delta\rho$

Figure 4.12: Visualisations of the contributors of $\boldsymbol{F}_{\text{BETZ}}$ on the NASA CRM, $M_\infty = 0.85$, $Re = 5 \times 10^6$, $C_L \approx 0.5$

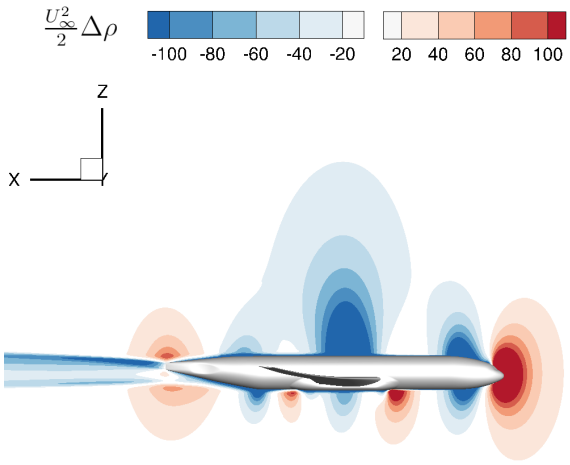

(a) $y/c_{ref} = 0$

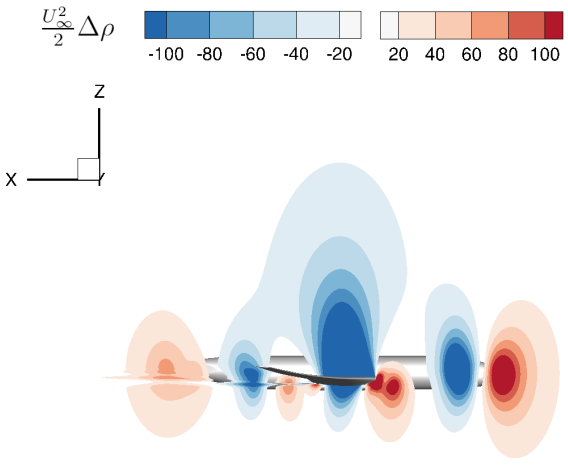

(b) $y/c_{ref} = 0.5$

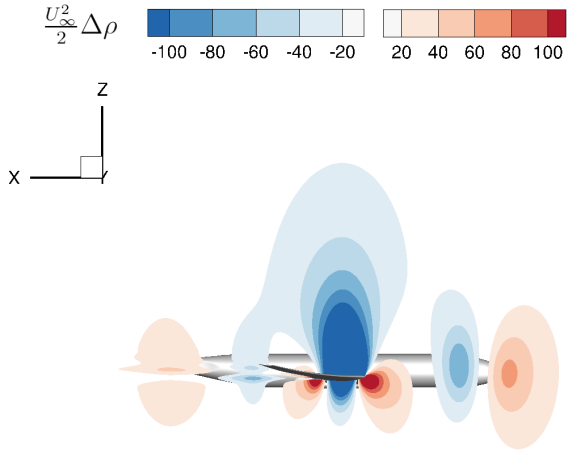

(c) $y/c_{ref} = 1$

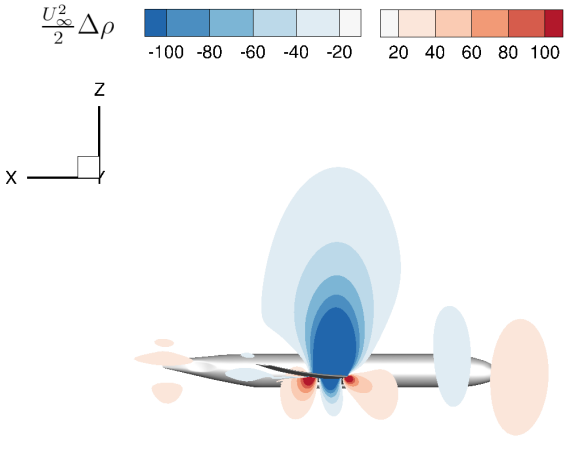

(d) $y/c_{ref} = 1.5$

Figure 4.13: Visualisations of $\frac{U_\infty^2}{2}\Delta\rho$ on the NASA CRM, $M_\infty = 0.85$, $Re = 5 \times 10^6$, $C_L \approx 0.5$

Chapter summary

The role of the compressibility term $\boldsymbol{F}_{m_\rho}$ has been investigated by highlighting the links between Mele *et al.*'s Lamb-vector-based decomposition [31, 32, 36] and pioneering theories from classical aerodynamics. In particular, it has been shown that the sum of $\boldsymbol{F}_{\rho l}$ and $\boldsymbol{F}_{m_\rho}$ (or $\boldsymbol{F}_{m_\rho}^{\text{trans}}$) yields to compressible versions of the Kutta-Joukowski lift theorem and Maskell's lift-induced drag formula. Similarly, it has been shown that the sum of $\boldsymbol{F}_{S_e}$ and $\boldsymbol{F}_\tau$ leads to a compressible version of Betz's profile drag formula. Additionally, a compressibility correction term vanishing in the far field has been discovered. Then, the total lift has been reconnected to the circulation generated by the wings, the lift-induced drag to the kinetic energy of the trailing vortices, and the profile drag to the losses in $P = p + \rho q^2/2$. For the profile drag however, an additional contribution withdrawing the variations in P induced by the compressibility of the flow explicitly appears in the expression.

Then, starting from the transonic formulation developed by Mele *et al.* [36], the ONERA formulation has been devised in order to be mathematically equivalent to the classical analyses of Kutta, Joukowski, Maskell and Betz:

$$\boxed{\begin{aligned} L^{\text{ONERA}} &= \left(\boldsymbol{F}_{\rho l} + \boldsymbol{F}_{m_\rho}^{\text{trans}} - \boldsymbol{F}_{\nabla\rho}\right)\cdot\boldsymbol{e}_z \\ D_i^{\text{ONERA}} &= \left(\boldsymbol{F}_{\rho l} + \boldsymbol{F}_{m_\rho}^{\text{trans}} - \boldsymbol{F}_{\nabla\rho}\right)\cdot\boldsymbol{e}_x \\ D_P^{\text{ONERA}} &= \left(\boldsymbol{F}_{S_e} + \boldsymbol{F}_\tau + \boldsymbol{F}_{\nabla\rho}\right)\cdot\boldsymbol{e}_x \end{aligned}}$$

with

$$\boxed{\begin{aligned} \boldsymbol{F}_{\rho l} &= -\int_\Omega \rho\boldsymbol{l}\,\mathrm{d}v \\ \boldsymbol{F}_{m_\rho}^{\text{trans}} &= \frac{1}{\mathcal{N}-1}\int_{\Omega\setminus\Omega_{sw}} \boldsymbol{r}\times\left(\nabla\left(\frac{q^2}{2}\right)\times\nabla\rho\right)\mathrm{d}v + \oint_{\partial\Omega_{sw}}\left(\rho\frac{q^2}{2}\boldsymbol{n}_{sw} - \rho\boldsymbol{q}\,(\boldsymbol{q}\cdot\boldsymbol{n}_{sw})\right)\mathrm{d}S \\ &\quad + \frac{1}{\mathcal{N}-1}\oint_{\partial\Omega_{sw}}\boldsymbol{r}\times\left(\boldsymbol{n}_{sw}\times\frac{q^2}{2}\nabla\rho\right)\mathrm{d}S + \int_{\Omega_{sw}}\rho\boldsymbol{l}\,\mathrm{d}v \\ \boldsymbol{F}_{\nabla\rho} &= \frac{1}{\mathcal{N}-1}\oint_{S_e}\boldsymbol{r}\times\left(\boldsymbol{n}\times\frac{q^2-U_\infty^2}{2}\nabla\rho\right)\mathrm{d}S \\ \boldsymbol{F}_{S_e} &= -\frac{1}{\mathcal{N}-1}\oint_{S_e}\boldsymbol{r}\times(\boldsymbol{n}\times\rho\boldsymbol{l})\,\mathrm{d}S \\ \boldsymbol{F}_\tau &= \oint_{S_e}\boldsymbol{\tau}\cdot\boldsymbol{n}\mathrm{d}S + \frac{1}{\mathcal{N}-1}\oint_{S_e}\boldsymbol{r}\times(\boldsymbol{n}\times\nabla\cdot\boldsymbol{\tau})\,\mathrm{d}S \end{aligned}}$$

Indeed, the terms of this new decomposition are still based on the Lamb vector and the density gradient, yet they are nothing but alternative expressions of the compressible versions of the Kutta-Joukowski lift theorem, Maskell's lift-induced drag formula and Betz's profile drag formula. As a consequence, the obtained decomposition is naturally independent of the location of the reference point everywhere in the flow field. The ONERA formulation has been successfully tested on the OAT15A airfoil and the NASA CRM. Particularly on the NASA CRM, it has been shown that, compared to Mele *et al.*'s formulation [36], the ONERA formulation provides a drag decomposition in much better agreement with Destarac and Van der Vooren's thermodynamic approach [21]. Hence, the ONERA formulation is more robust and better suited for applications to industrial aircrafts.

Finally, starting over from the ONERA formulation, the equivalent Kutta-Joukowski-Maskell-Betz (KJMB) formulation has been derived. This formulation can predict and decompose the aerodynamic force with an expression embedding in the same equation the compressible versions

of the Kutta-Joukowski theorem, Maskell's formula and Betz's formula:

$$\boxed{\begin{aligned} L^{\mathrm{KJMB}} &= \boldsymbol{e}_z \cdot \boldsymbol{F}_{\mathrm{KJ}} \\ D_i^{\mathrm{KJMB}} &= \boldsymbol{e}_x \cdot \boldsymbol{F}_{\mathrm{MSK}} \\ D_P^{\mathrm{KJMB}} &= \boldsymbol{e}_x \cdot \boldsymbol{F}_{\mathrm{BETZ}} \end{aligned}}$$

with

$$\boxed{\begin{aligned} \boldsymbol{F}_{\mathrm{KJ}} &= \boldsymbol{U}_\infty \times \oint_{S_e} \boldsymbol{n} \times \rho \delta \boldsymbol{q} \mathrm{d}S + \left(\oint_{S_e} \rho \left(\frac{\delta q^2}{2} n_z - w \left(\delta \boldsymbol{q} \cdot \boldsymbol{n} \right) \right) \mathrm{d}S \right) \boldsymbol{e}_z \\ \boldsymbol{F}_{\mathrm{MSK}} &= \left(\oint_{S_e} \rho \left(\frac{\delta q^2}{2} n_x - u \left(\delta \boldsymbol{q} \cdot \boldsymbol{n} \right) \right) \mathrm{d}S \right) \boldsymbol{e}_x \\ \boldsymbol{F}_{\mathrm{BETZ}} &= \oint_{S_e} \boldsymbol{\tau} \cdot \boldsymbol{n} \mathrm{d}S + \oint_{S_e} \left(P_\infty - P \right) \boldsymbol{n} \mathrm{d}S - \frac{U_\infty^2}{2} \oint_{S_e} \left(\rho_\infty - \rho \right) \boldsymbol{n} \mathrm{d}S \end{aligned}}$$

Then, the KJMB decomposition has successfully been applied to the OAT15A airfoil and the NASA CRM. Particularly on the NASA CRM, it has been shown that the lift is better predicted with the KJMB formulation than with the ONERA formulation, although they are mathematically equivalent. Moreover it has been shown that, compared to Mele *et al.*'s formulation [36] and the ONERA formulation, the KJMB formulation provides a drag decomposition in even better agreement with Destarac and Van der Vooren's approach [21]. In the end, a physical analysis of the variations in P has shown that, in compressible flows, one part of the lift and the lift-induced drag comes from the variations in density caused by compressions and expansions. On the contrary, it has shown that the profile drag corresponds to the losses in P induced only by the decrease in static pressure and kinetic energy in the wake.

In conclusion, two innovative formulations have been developed. The ONERA formulation is based on local flow quantities, the Lamb vector and the density gradient, while the KJMB formulation is based on global flow quantities, the circulation around the wings, the kinetic energy of the vortices, and the losses in pressure and kinetic energy in the wake. Notably, the discovery of the KJMB formulation enables to bridge the gap between classical incompressible aerodynamics and the study of highly complex transonic flows. The equivalence between these two formulations has enabled to better understand the physical roles of the Lamb vector and the density gradient in lift and drag. Besides, both formulations have shown their ability to accurately predict and decompose the aerodynamic force into lift, lift-induced drag and profile drag on a typical industrial aircraft in cruise flight. However, the breakdown of the profile drag into viscous and wave contributions is still not achieved. That is why it is now necessary to develop a method that can extract the wave drag from the profile drag.

Chapter 5

Lamb-Vector-Based Wave Drag Extraction by Shock Wave Wake Identification

In Mele *et al.*'s formulation [31, 32, 36], the ONERA formulation and the KJMB formulation, it has been shown that the profile drag varies when increasing the size of the integration domain. In particular, it has been observed that the profile drag decreases in the near field with the rolling-up of the vortex sheet. Hence, unlike Destarac and Van der Vooren's approach [21], the wave contribution to the profile drag cannot be evaluated on the contour of the shock wave volume since it would be overestimated. For the same reason, it cannot either be evaluated on a shock wake plane directly downstream of the shock wave as already observed in several studies [36, 91]. Thus, the aim of this chapter is to find a method for extracting the wave drag in the wake of the aircraft.

First of all, it is necessary to investigate the relations between the Lamb-vector-based formulations (Mele *et al.*'s and ONERA formulations) and former wave drag extraction methods in order to check whether the wave drag can be evaluated with the Lamb vector. To do so, a theoretical study is conducted in the shock wave wake in order to emphasize the link between Mele *et al.*'s formulation [31, 32, 36] and Oswatitsch's wave drag formula [40, 41]. Then, another theoretical analysis is carried out in order to highlight the links between the ONERA formulation, the KJMB formulation and Destarac and Van der Vooren's wave drag formula [21].

Then, with the observations made in the first part, it becomes clear that the wave drag must be extracted from the profile drag in the wake of the shock wave. To do so, it is necessary to identify the part of the wake coming from the shock wave and to separate it from the viscous wake coming from the boundary layers: this is done by means of a physical criterion based on entropy and vorticity. The separation of the shock wave wake and the viscous wake is then illustrated around the NACA0012 airfoil.

Finally, two Lamb-vector-based wave drag formulae are presented: the first one is based on the wave drag definition proposed by Mele *et al.* [36] while the second one is based on the profile drag expression given in the ONERA formulation. Additionally, another wave drag formula based on the profile drag expression given in the KJMB formulation is presented. A numerical comparative study of those three formulae and the thermodynamic methods of Oswatitsch, Destarac and Van der Vooren is then conducted on two-dimensional and three-dimensional configurations.

5.1 Theoretical comparison between the Lamb-vector-based formulations and thermodynamic wave drag extraction methods

In this section, the focus is given to the links between the Lamb-vector-based formulations and the thermodynamic approaches of Oswatitsch [40, 41], Destarac and Van der Vooren [21]. In fact, the thermodynamic approaches were the first to predict the wave drag and it is fundamental to identify the similarities and differences with the formulations based on the Lamb vector in order to find out where the drag predictions might differ or become equal to each other.

First of all, the link between Mele *et al.*'s profile drag definition [31, 32, 36] and Oswatitsch's wave drag formula [40, 41] is established with a theoretical study of $\boldsymbol{F}_{S_e}$ in the shock wave wake.

Then, by considering the same hypotheses as Destarac and Van der Vooren [21], a similar analysis of $\boldsymbol{F}_{S_e} + \boldsymbol{F}_{\nabla\rho}$ and $\boldsymbol{F}_{\mathrm{BETZ}}$ is conducted. It reveals the existing relation between the profile drag expression of the ONERA formulation, the profile drag expression of the KJMB formulation, and Destarac and Van der Vooren's wave drag formula.

In the end, the theoretical speculations made in the first two parts are validated through a numerical simulation around the NACA0012 airfoil. This simulation is performed on an Euler (inviscid) flow in order to ensure that the wake downstream of the airfoil comes from the presence of the shock wave only.

5.1.1 Link with Oswatitsch's formula

In the first chapter of this dissertation, it has been shown that Oswatitsch's formula is a surface integral which relates the profile drag to the entropy generated in boundary layers and across shock waves (see subsection 1.1.3). Should this integration be performed directly downstream of the shock wave, one will obtain the wave drag. In order to find the links between the Lamb-vector-based profile drag definition of Mele *et al.* [31, 32, 36] and Oswatitsch's wave drag formula [40, 41], it is then necessary to find a way to express the Lamb vector with the entropy. This is done by means of the Crocco-Vazsonyi equation.

The flow inside and outside the shock wave wake is considered almost inviscid ($Re \to \infty$). Hence, the contribution of the viscous-stress tensor $\boldsymbol{\tau}$ is negligible and the Crocco-Vazsonyi equation is given by

$$\rho\boldsymbol{l} = \rho T\nabla s - \rho\nabla H \tag{5.1.1}$$

Denoting $\Delta s = s - s_\infty$ and $\Delta H = H - H_\infty$, it is also possible to write

$$\rho\boldsymbol{l} = \rho T\nabla\left(\Delta s\right) - \rho\nabla\left(\Delta H\right) \tag{5.1.2}$$

Moreover, across a steady shock, the total specific enthalpy H is conserved. Additionally, the flow is steady, almost inviscid, and thermal effects are negligible [40], hence the flow remains isenthalpic between the upstream far field and the region just upstream of the shock. Therefore, ΔH represents in this case the difference in total specific enthalpy between the upstream far field and the wake of the shock wave. With the aforementioned arguments, it is then clear that $\Delta H = 0$ everywhere in the flow. Using the perfect gas relation

$$p = \rho RT \tag{5.1.3}$$

where R is the perfect gas constant, the Crocco-Vazsonyi equation may now be written as follows:

$$\rho\boldsymbol{l} = \nabla\left(\rho T\Delta s\right) - \frac{\Delta s}{R}\nabla p \tag{5.1.4}$$

To analyse the wave drag, one must first start from the expression of the profile drag. In the decomposition proposed by Mele *et al.* [31, 32, 36], the profile drag is given by the x-component of $\boldsymbol{F}_{S_e}$:

$$D_P^{\mathrm{Mele}} = \boldsymbol{F}_{S_e}\cdot\boldsymbol{e}_x = \boldsymbol{e}_x\cdot\left(-\frac{1}{\mathcal{N}-1}\oint_{S_e}\boldsymbol{r}\times\left(\boldsymbol{n}\times\rho\boldsymbol{l}\right)\mathrm{d}S\right) \tag{5.1.5}$$

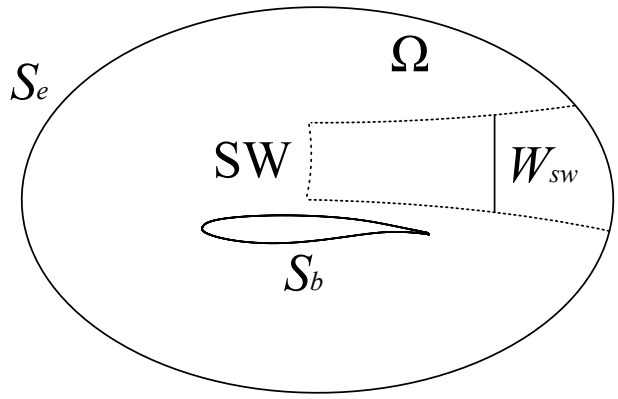

Figure 5.1: Definition of W_{sw}

By using (5.1.4), it is possible to re-express $\boldsymbol{F}_{S_e}$ with the entropy:

$$\begin{aligned}\boldsymbol{F}_{S_e} = &-\frac{1}{\mathcal{N}-1}\oint_{S_e} \boldsymbol{r}\times(\boldsymbol{n}\times\nabla(\rho T\Delta s))\,\mathrm{d}S \\ &+\frac{1}{\mathcal{N}-1}\oint_{S_e} \boldsymbol{r}\times\left(\boldsymbol{n}\times\frac{\Delta s}{R}\nabla p\right)\mathrm{d}S\end{aligned} \tag{5.1.6}$$

With the second DMT (A.2), the first integral can be simplified:

$$\boldsymbol{F}_{S_e} = \oint_{S_e} \rho T\Delta s\boldsymbol{n}\mathrm{d}S + \frac{1}{\mathcal{N}-1}\oint_{S_e} \boldsymbol{r}\times\left(\boldsymbol{n}\times\frac{\Delta s}{R}\nabla p\right)\mathrm{d}S \tag{5.1.7}$$

Knowing that $\boldsymbol{e}_x = \boldsymbol{U}_\infty/U_\infty$, it is then possible to write the profile drag D_P^{Mele} as follows:

$$\begin{aligned}D_P^{\text{Mele}} = &\frac{1}{U_\infty}\oint_{S_e}\rho T\Delta s\,(\boldsymbol{U}_\infty\cdot\boldsymbol{n})\,\mathrm{d}S \\ &+\boldsymbol{e}_x\cdot\left(\frac{1}{\mathcal{N}-1}\oint_{S_e}\boldsymbol{r}\times\left(\boldsymbol{n}\times\frac{\Delta s}{R}\nabla p\right)\mathrm{d}S\right)\end{aligned} \tag{5.1.8}$$

The temperature may be written as $T = T_\infty + \Delta T$ in the latter expression:

$$\begin{aligned}D_P^{\text{Mele}} = &\frac{T_\infty}{U_\infty}\oint_{S_e}\Delta s\,(\rho\boldsymbol{U}_\infty\cdot\boldsymbol{n})\,\mathrm{d}S \\ &+\frac{1}{U_\infty}\oint_{S_e}\Delta s\Delta T\,(\rho\boldsymbol{U}_\infty\cdot\boldsymbol{n})\,\mathrm{d}S \\ &+\boldsymbol{e}_x\cdot\left(\frac{1}{\mathcal{N}-1}\oint_{S_e}\boldsymbol{r}\times\left(\boldsymbol{n}\times\frac{\Delta s}{R}\nabla p\right)\mathrm{d}S\right)\end{aligned} \tag{5.1.9}$$

Then, with the decomposition of the velocity vector $\boldsymbol{q} = \boldsymbol{U}_\infty + \delta\boldsymbol{q}$, the first integral can be re-expressed:

$$\begin{aligned}D_P^{\text{Mele}} = &\frac{T_\infty}{U_\infty}\oint_{S_e}\Delta s\,(\rho\boldsymbol{q}\cdot\boldsymbol{n})\,\mathrm{d}S - \frac{T_\infty}{U_\infty}\oint_{S_e}\Delta s\,(\rho\delta\boldsymbol{q}\cdot\boldsymbol{n})\,\mathrm{d}S \\ &+\boldsymbol{e}_x\cdot\oint_{S_e}\rho\Delta s\Delta T\boldsymbol{n}\mathrm{d}S + \boldsymbol{e}_x\cdot\left(\frac{1}{\mathcal{N}-1}\oint_{S_e}\boldsymbol{r}\times\left(\boldsymbol{n}\times\frac{\Delta s}{R}\nabla p\right)\mathrm{d}S\right)\end{aligned} \tag{5.1.10}$$

In (5.1.10), the first integral is Oswatitsch's profile drag formula (see subsection 1.1.3). Yet, $\Delta s = 0$ outside the shock wave wake in the case of an inviscid transonic flow. Hence, the

integrals are limited to the shock wake plane W_{sw} (see Fig.5.1). Then, the link between Mele *et al.*'s profile drag definition [31, 32, 36] and Oswatitsch's wave drag formula [40, 41] is obtained:

$$\boxed{D_P^{\text{Mele}} = D_w^{\text{Osw}} + D_{\delta \boldsymbol{q} \Delta s} + D_{\Delta s \Delta T} + D_{\Delta s \nabla p}} \tag{5.1.11}$$

with

$$D_w^{\text{Osw}} = \frac{T_\infty}{U_\infty} \int_{W_{sw}} \Delta s \, (\rho \boldsymbol{q} \cdot \boldsymbol{n}) \, \mathrm{d}S \tag{5.1.12}$$

$$D_{\delta \boldsymbol{q} \Delta s} = -\frac{T_\infty}{U_\infty} \int_{W_{sw}} \Delta s \, (\rho \delta \boldsymbol{q} \cdot \boldsymbol{n}) \, \mathrm{d}S \tag{5.1.13}$$

$$D_{\Delta s \Delta T} = \boldsymbol{e}_x \cdot \int_{W_{sw}} \rho \Delta s \Delta T \boldsymbol{n} \mathrm{d}S \tag{5.1.14}$$

$$D_{\Delta s \nabla p} = \boldsymbol{e}_x \cdot \left(\frac{1}{\mathcal{N} - 1} \int_{W_{sw}} \boldsymbol{r} \times \left(\boldsymbol{n} \times \frac{\Delta s}{R} \nabla p \right) \mathrm{d}S \right) \tag{5.1.15}$$

The other terms of (5.1.11) are expected to vanish in the far wake of the shock wave. First of all, Δs is generally small provided that the shock is not too strong. Besides, according to Oswatitsch [40], it is reasonable to assume a *"slightly perturbed parallel flow"* in the far wake. Indeed, with turbulence and viscous effects (although limited in this case), there is

$$\lim_{W_{sw} \to \infty} \Delta s \, (\delta \boldsymbol{q} \cdot \boldsymbol{n}) = \lim_{W_{sw} \to \infty} u \Delta s = 0 \tag{5.1.16}$$

since u is small far downstream. Additionally, the temperature T returns to T_∞. Hence,

$$\lim_{W_{sw} \to \infty} \Delta s \Delta T = (T_\infty - T_\infty) \, \Delta s = 0 \tag{5.1.17}$$

Moreover, in transonic flows, the shock wave is weakly curved and almost straight, so that the tangential pressure gradient $\boldsymbol{n} \times \nabla p$ is small and progressively disappears as well. As a consequence,

$$\lim_{W_{sw} \to \infty} D_{\delta \boldsymbol{q} \Delta s} = 0 \tag{5.1.18}$$

$$\lim_{W_{sw} \to \infty} D_{\Delta s \Delta T} = 0 \tag{5.1.19}$$

$$\lim_{W_{sw} \to \infty} D_{\Delta s \nabla p} = 0 \tag{5.1.20}$$

so that

$$D_P^{\text{Mele}} = D_w^{\text{Osw}} \tag{5.1.21}$$

in the far wake. All these speculations will be confirmed by numerical results in subsection 5.1.3. In the next analysis, the focus is given to the profile drag expressions of the ONERA and KJMB formulations, and the links with Destarac and Van der Vooren's wave drag formula [21].

5.1.2 Link with Destarac and Van der Vooren's approach

Oswatitsch's formula is one of the first definitions of the wave drag and is actually a linearization of the formula later developed by Destarac and Van der Vooren [21]. Then, through its link with Oswatitsch's formula, D_P^{Mele} is somewhat linked to Destarac and Van der Vooren's approach as well. In the following, however, the focus is on the profile drag expressions of the ONERA and KJMB formulations.

The approach of Destarac and Van der Vooren is based on the assumption that no trailing vorticity is present in the wake, hence the drag only comes from irreversible processes (see subsection 1.1.5). Moreover, the viscous stresses are neglected and the pressure is assumed to be

equal to its freestream value. In this case, the profile drag D_P^{VdV} is expressed with the irreversible velocity deficit $\Delta\overline{u}$:

$$D_P^{\mathrm{VdV}} = -\oint_{S_e} \Delta\overline{u}\,(\rho\boldsymbol{q}\cdot\boldsymbol{n})\,\mathrm{d}S \tag{5.1.22}$$

In the ONERA and KJMB formulations, the force decomposition is the same since both formulations are mathematically equivalent, but they are based on different physical quantities. In the case of an inviscid flow, the viscous stresses are negligible. Hence the profile drag is given by

$$D_P^{\mathrm{ONERA}} = \boldsymbol{e}_x\cdot(\boldsymbol{F}_{S_e}+\boldsymbol{F}_{\nabla\rho}) = \boldsymbol{F}_{\mathrm{BETZ}}\cdot\boldsymbol{e}_x = D_P^{\mathrm{KJMB}} \tag{5.1.23}$$

with

$$\begin{aligned}\boldsymbol{F}_{S_e}+\boldsymbol{F}_{\nabla\rho} = &-\frac{1}{\mathcal{N}-1}\oint_{S_e}\boldsymbol{r}\times(\boldsymbol{n}\times\rho\boldsymbol{l})\,\mathrm{d}S\\ &+\frac{1}{\mathcal{N}-1}\oint_{S_e}\boldsymbol{r}\times\left(\boldsymbol{n}\times\frac{q^2-U_\infty^2}{2}\nabla\rho\right)\mathrm{d}S\end{aligned} \tag{5.1.24}$$

$$\boldsymbol{F}_{\mathrm{BETZ}} = \oint_{S_e}(P_\infty-P)\,\boldsymbol{n}\mathrm{d}S - \frac{U_\infty^2}{2}\oint_{S_e}(\rho_\infty-\rho)\,\boldsymbol{n}\mathrm{d}S \tag{5.1.25}$$

Here, it is more convenient to express $\boldsymbol{F}_{\mathrm{BETZ}}$ with the static pressure for the analysis to follow:

$$\boldsymbol{F}_{\mathrm{BETZ}} = \oint_{S_e}(p_\infty-p)\,\boldsymbol{n}\mathrm{d}S - \oint_{S_e}\rho\frac{q^2-U_\infty^2}{2}\boldsymbol{n}\mathrm{d}S \tag{5.1.26}$$

Then, reminding that $\boldsymbol{e}_x = \boldsymbol{U}_\infty/U_\infty$, the profile drag $D_P^{\mathrm{ONERA}} = D_P^{\mathrm{KJMB}}$ is expressed with the x-component of $\boldsymbol{F}_{\mathrm{BETZ}}$:

$$D_P^{\mathrm{ONERA}} = D_P^{\mathrm{KJMB}} = \boldsymbol{e}_x\cdot\oint_{S_e}(p_\infty-p)\,\boldsymbol{n}\mathrm{d}S - \oint_{S_e}\rho\frac{q^2-U_\infty^2}{2U_\infty}(\boldsymbol{U}_\infty\cdot\boldsymbol{n})\,\mathrm{d}S \tag{5.1.27}$$

Let us now analyse the second term of (5.1.27). First of all, it is possible to re-express it as follows:

$$-\oint_{S_e}\rho\frac{q^2-U_\infty^2}{2U_\infty}(\boldsymbol{U}_\infty\cdot\boldsymbol{n})\,\mathrm{d}S = -\oint_{S_e}\rho\,(q-U_\infty)\,\frac{q+U_\infty}{2U_\infty}(\boldsymbol{U}_\infty\cdot\boldsymbol{n})\,\mathrm{d}S \tag{5.1.28}$$

To find the link with Destarac and Van der Vooren's formula [21], it is necessary to consider the same hypotheses as those they made in the far wake:

- $v = w = 0$
- $p = p_\infty$

In this specific case, the flow in the wake is parallel to the x-axis and the velocity q simplifies as follows (see subsection 1.1.5):

$$U_{irr} = U_\infty + \Delta\overline{u} \tag{5.1.29}$$

Hence, (5.1.28) becomes

$$\begin{aligned}-\oint_{S_e}\rho\frac{U_{irr}^2-U_\infty^2}{2U_\infty}(\boldsymbol{U}_\infty\cdot\boldsymbol{n})\,\mathrm{d}S &= -\oint_{S_e}\Delta\overline{u}\left(1+\frac{\Delta\overline{u}}{2U_\infty}\right)(\rho\boldsymbol{U}_\infty\cdot\boldsymbol{n})\,\mathrm{d}S\\ &= -\oint_{S_e}\Delta\overline{u}\,(\rho\boldsymbol{U}_\infty\cdot\boldsymbol{n})\,\mathrm{d}S - \boldsymbol{e}_x\cdot\oint_{S_e}\rho\frac{\Delta\overline{u}^2}{2}\boldsymbol{n}\mathrm{d}S\end{aligned} \tag{5.1.30}$$

The next step consists in adding and subtracting the term

$$-\oint_{S_e}\rho\frac{U_{irr}^2-U_\infty^2}{2U_\infty}(\boldsymbol{U}_\infty\cdot\boldsymbol{n})\,\mathrm{d}S$$

to (5.1.27) in order to obtain

$$D_P^{\text{ONERA}} = D_P^{\text{KJMB}} = \boldsymbol{e}_x \cdot \oint_{S_e} (p_\infty - p)\,\boldsymbol{n}\mathrm{d}S - \oint_{S_e} \rho \frac{U_{irr}^2 - U_\infty^2}{2U_\infty} (\boldsymbol{U}_\infty \cdot \boldsymbol{n})\,\mathrm{d}S - \oint_{S_e} \rho \frac{q^2 - U_{irr}^2}{2U_\infty} (\boldsymbol{U}_\infty \cdot \boldsymbol{n})\,\mathrm{d}S \tag{5.1.31}$$

Then, by introducing (5.1.30) into (5.1.31), it is possible to write

$$D_P^{\text{ONERA}} = D_P^{\text{KJMB}} = \boldsymbol{e}_x \cdot \oint_{S_e} (p_\infty - p)\,\boldsymbol{n}\mathrm{d}S - \oint_{S_e} \Delta\overline{u}\,(\rho \boldsymbol{U}_\infty \cdot \boldsymbol{n})\,\mathrm{d}S - \oint_{S_e} \rho \frac{q^2 + \Delta\overline{u}^2 - U_{irr}^2}{2U_\infty} (\boldsymbol{U}_\infty \cdot \boldsymbol{n})\,\mathrm{d}S \tag{5.1.32}$$

Using (5.1.29) and the decomposition of the velocity vector $\boldsymbol{q} = \boldsymbol{U}_\infty + \delta\boldsymbol{q}$, the latter expression is re-expressed as follows:

$$\begin{aligned} D_P^{\text{ONERA}} = D_P^{\text{KJMB}} = &- \oint_{S_e} \Delta\overline{u}\,(\rho \boldsymbol{q} \cdot \boldsymbol{n})\,\mathrm{d}S + \boldsymbol{e}_x \cdot \oint_{S_e} (p_\infty - p)\,\boldsymbol{n}\mathrm{d}S \\ &+ \oint_{S_e} \Delta\overline{u}\,(\rho\delta\boldsymbol{q} \cdot \boldsymbol{n})\,\mathrm{d}S \\ &- \oint_{S_e} (u - \Delta\overline{u})\,(\rho \boldsymbol{U}_\infty \cdot \boldsymbol{n})\,\mathrm{d}S - \boldsymbol{e}_x \cdot \oint_{S_e} \rho \frac{\delta q^2}{2} \boldsymbol{n}\mathrm{d}S \end{aligned} \tag{5.1.33}$$

In (5.1.33), the first integral represents Destarac and Van der Vooren's profile drag formula [21]. Moreover, the flow is inviscid and transonic, so the integrals containing u, $\Delta\overline{u}$ and δq^2 are limited to the shock wake plane W_{sw}. Finally, considering that the lateral parts of S_e are far enough from the aircraft, the integral containing the pressure difference $p_\infty - p$ can also be limited to W_{sw}. Consequently, the link with the wave drag computed by Destarac and Van der Vooren's formula [21] is obtained:

$$\boxed{D_P^{\text{ONERA}} = D_P^{\text{KJMB}} = D_w^{\text{VdV}} + D_{\Delta p} + D_{\delta\boldsymbol{q}\Delta\overline{u}}} \tag{5.1.34}$$

with

$$D_w^{\text{VdV}} = - \int_{W_{sw}} \Delta\overline{u}\,(\rho \boldsymbol{q} \cdot \boldsymbol{n})\,\mathrm{d}S \tag{5.1.35}$$

$$D_{\Delta p} = \boldsymbol{e}_x \cdot \int_{W_{sw}} (p_\infty - p)\,\boldsymbol{n}\mathrm{d}S \tag{5.1.36}$$

$$D_{\delta\boldsymbol{q}\Delta\overline{u}} = \int_{W_{sw}} \Delta\overline{u}\,(\rho\delta\boldsymbol{q} \cdot \boldsymbol{n})\,\mathrm{d}S - \boldsymbol{e}_x \cdot \int_{W_{sw}} \rho \frac{\delta q^2}{2} \boldsymbol{n}\mathrm{d}S - \int_{W_{sw}} (u - \Delta\overline{u})\,(\rho \boldsymbol{U}_\infty \cdot \boldsymbol{n})\,\mathrm{d}S \tag{5.1.37}$$

The other terms of (5.1.34) are expected to vanish in the far wake of the shock wave. First of all, in $D_{\Delta p}$, the pressure p progressively returns to its freestream value p_∞:

$$\lim_{W_{sw} \to \infty} p = p_\infty \tag{5.1.38}$$

Moreover, v and w tend to zero and u tends to $\Delta\overline{u}$. Hence, in $D_{\delta\boldsymbol{q}\Delta\overline{u}}$, there is

$$\begin{aligned} \lim_{W_{sw} \to \infty} \left[\Delta\overline{u}\,(\delta\boldsymbol{q} \cdot \boldsymbol{n}) - \boldsymbol{e}_x \cdot \frac{\delta q^2}{2} \boldsymbol{n} \right] &= \lim_{W_{sw} \to \infty} \left[u\Delta\overline{u} - \frac{\delta q^2}{2} \right] \\ &= \lim_{W_{sw} \to \infty} \left[\Delta\overline{u}^2 - \frac{\Delta\overline{u}^2 + v^2 + w^2}{2} \right] \\ &= \lim_{W_{sw} \to \infty} \frac{\Delta\overline{u}^2}{2} = 0 \end{aligned} \tag{5.1.39}$$

and

$$\lim_{W_{sw}\to\infty} \left[(u-\Delta\overline{u})\,(\boldsymbol{U}_\infty\cdot\boldsymbol{n})\right] = (\Delta\overline{u}-\Delta\overline{u})\,U_\infty = 0 \tag{5.1.40}$$

As a consequence,

$$\lim_{W_{sw}\to\infty} D_{\Delta p} = 0 \tag{5.1.41}$$

$$\lim_{W_{sw}\to\infty} D_{\delta\boldsymbol{q}\Delta\overline{u}} = 0 \tag{5.1.42}$$

so that

$$D_P^{\text{ONERA}} = D_P^{\text{KJMB}} = D_w^{\text{VdV}} \tag{5.1.43}$$

in the far wake. The aforementioned results will be confirmed in the next subsection with a numerical transonic Euler simulation around the NACA0012 airfoil.

5.1.3 Numerical study in the inviscid wake of a NACA0012 airfoil

In fact, in this case, the lift-induced drag and the viscous drag are equal to zero, hence the total drag exerted on the airfoil is equal to the wave drag only. The aim of this numerical application is to find out whether the theoretical speculations made earlier in the shock wave wake are correct. In particular, it is necessary to check whether the expressions of the profile drag based on the Lamb vector predict the same drag as Oswatitsch's and Destarac and Van der Vooren's wave drag formulae. To do so, the evolution of the different drag contributors is investigated in the shock wave wake. The location of the shock wake plane W_{sw} is defined by the position x_W downstream of the trailing edge. In the following charts, the near-field drag (equal to the wave drag in this case) is taken as reference value.

The analysis of (5.1.11) is illustrated in Fig.5.2. In Fig.5.2a, the profile drag computed by the reference-point-invariant version of Mele *et al.*'s formulation is compared to the near-field drag and Oswatitsch's wave drag. It can be seen that the difference in drag computed by the three formulae is always less than one drag count. Moreover, Mele *et al.*'s profile drag quickly converges to the constant value predicted by Oswatitsch's formula which confirms the speculation made in (5.1.21). The other terms of (5.1.11) are displayed in Fig.5.2b: their magnitude is always less than one drag count. Besides, $D_{\Delta s\nabla p} \simeq 0$ and the two other drag contributors tend to zero which gives further support to the validity of (5.1.21) in the far wake.

The analysis of (5.1.34) is illustrated in Fig.5.3. In Fig.5.3a, the profile drag computed by the reference-point-invariant version of the ONERA formulation and that computed by the KJMB formulation are compared to the near-field drag and Destarac and Van der Vooren's wave drag. This time, the difference in drag is more pronounced in the very near wake (3 to 4 drag counts) but the profile drag computed by the ONERA and KJMB formulations quickly returns to that computed by Destarac and Van der Vooren's formula. Once again, the predicted drag becomes invariant to x_W in the far wake. Then, the speculation made in (5.1.43) seems correct. The other terms of (5.1.34) are shown in Fig.5.3b: $D_{\Delta p}$ and $D_{\delta\boldsymbol{q}\Delta\overline{u}}$ both tend to zero in the far wake. Even more compelling, they seem to always compensate each other (the reason is still not clear), suggesting that (5.1.43) should hold in the near wake as well. As a matter of fact, the difference with D_w^{VdV} noticed for $x_W/c \leq 20$ may be explained with various arguments:

- $D_{P,\text{inv}}^{\text{ONERA}}$ and D_P^{KJMB} are computed on the closed surface S_e, in this case a rectangle with the plane W as its dowstream boundary. Hence, the difference may come from contributions on W located outside the wake when W is close to the trailing edge. Then, those contributions gradually disappear as W retreats further downstream.

- It could instead/also be due to the fact that the hypotheses made in the derivation of (5.1.34) hold only far enough in the shock wave wake.

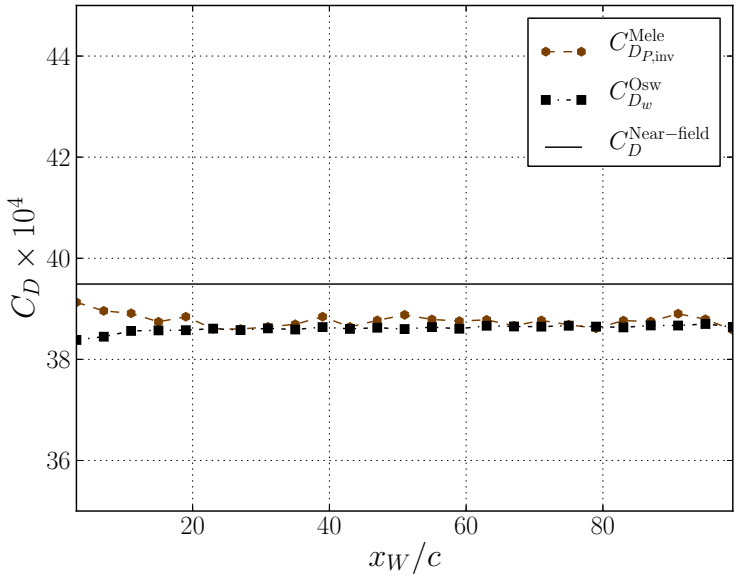

(a) Mele *et al.*'s profile drag VS Oswatitsch's wave drag

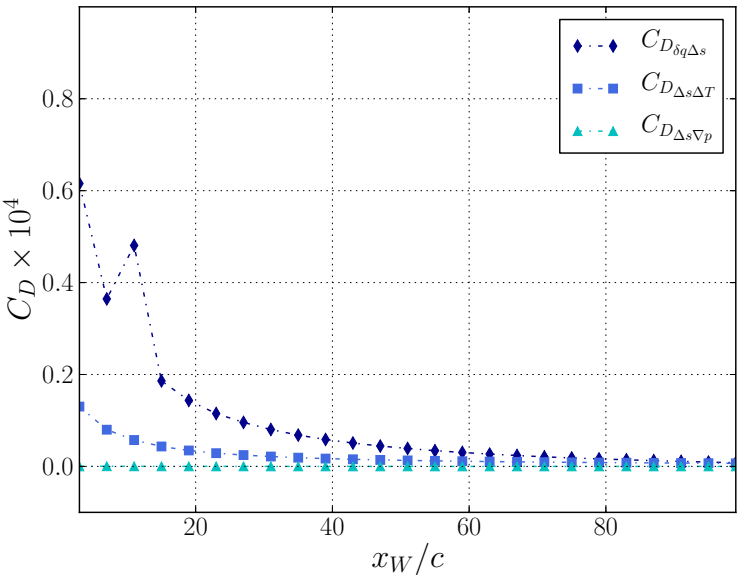

(b) Other terms of (5.1.11)

Figure 5.2: Evolution of the profile drag computed by Mele *et al.*'s definition [31, 32, 36] and the wave drag computed by Oswatitsch's formula [40, 41] in the wake of the NACA0012 airfoil, $M_\infty = 0.72$, $Re \to \infty$, $\alpha = 2°$

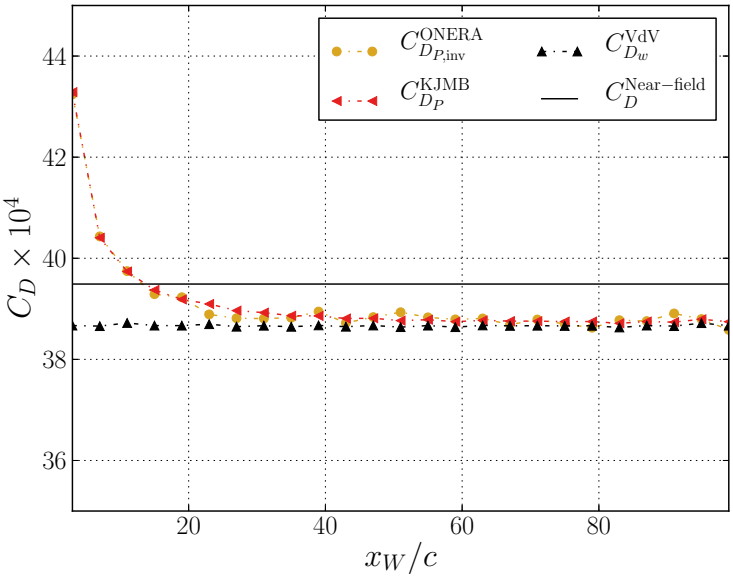

(a) ONERA/KJMB profile drag VS Destarac and Van der Vooren's wave drag

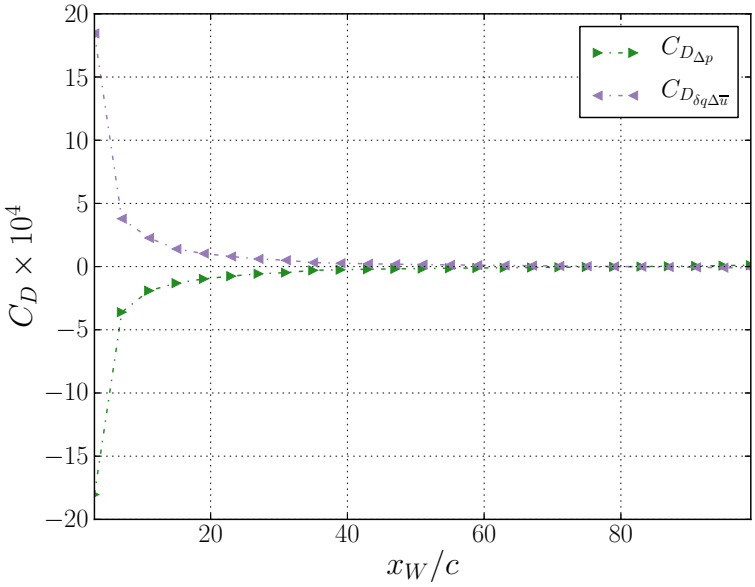

(b) Other terms of (5.1.34)

Figure 5.3: Evolution of the profile drag computed by the ONERA and KJMB formulations and the wave drag computed by Destarac and Van der Vooren's formula [21] in the wake of the NACA0012 airfoil, $M_\infty = 0.72$, $Re \to \infty$, $\alpha = 2°$

5.2 Identification of the shock wave wake in the flow solution

In the shock wave wake, it has been shown that the Lamb-vector-based expressions of the profile drag progressively become equivalent to the wave drag computed by the thermodynamic approaches of Oswatitsch [40, 41] and Destarac and Van der Vooren [21]. Then, it seems that an evaluation of the wave drag using the Lamb vector is possible. In fact, the equivalence between the Lamb-vector-based formulations and the thermodynamic approaches is achieved only in the far wake of the shock wave. Yet, in viscous flows, the shock wave wake quickly merges with the wake of the boundary layer, therefore making it impossible to distinguish the wave drag and the viscous drag.

Hence, it appears necessary to perform the integration closer to the shock. Unfortunately, Mele *et al.* [36] and Ostieri and Tognaccini [91, 106] noticed that the wave drag is overestimated when the plane of integration is located too close to the shock. That is why choice is made to integrate on a plane located not too close to the shock, but not too far in the wake in order to avoid the entrainment of the shock wave wake into the viscous wake. To do so, a physical criterion able to identify the shock wave wake is defined: two filters based on entropy and vorticity enable to delineate it from the spurious regions (characterized by the production of numerical drag) and the viscous wake. Then, the region selected by the criterion is shown in a viscous flow around the NACA0012 airfoil.

5.2.1 Definition of a physical criterion based on entropy and vorticity

In the first place, the criterion used to separate the shock wave wake from the viscous wake has been inspired from the one developed by Kusunose [45]. His criterion was based on the magnitude of the Lamb vector in the wake of the aircraft: when the magnitude of the Lamb vector is less than a specific value, the cell is considered to be part of the shock wave wake.

In the present study, rather than the Lamb vector, the physical quantity used to distinguish the viscous wake and the shock wave wake is the vorticity. Besides, it has also appeared paramount to exclude all spurious contributions from the selected region. In fact, inaccuracies in the numerical simulation may generate an additional unphysical drag contribution outside the wake. To avoid the spurious regions, the physical quantity used to delimit the physical wake is the entropy. In the end, the physical criterion developed here is very similar to the one proposed by Toubin [107] for the identification of an extended shock wave volume.

Unlike Toubin, the criterion is here intended for use on a surface rather than a volume. Hence, the location of the surface in the wake must be specified. In this regard, it has been observed that the integration should not be performed too close nor too far from the shock wave. Then the shock wake plane W_{sw} is defined as follows:

$$x_W = \begin{cases} x_{te} + c/10 & \text{in RANS flows around airfoils} \\ x_{te} + c & \text{in Euler flows around airfoils} \\ x_{wt} & \text{in RANS flows around wings or aircrafts} \end{cases} \tag{5.2.1}$$

where the subscript te refers to the trailing edge and wt to the wing tip. Then, a cell is tagged as belonging to W_{sw} if:

1. The entropy increment satisfies $\Delta s \geq \beta_{\Delta s}$ in order to avoid the spurious regions.
2. The vorticity modulus $||\boldsymbol{\omega}||$ is such that $||\boldsymbol{\omega}||c_{ref}/U_\infty \leq \beta_\omega$ to avoid the wake of the boundary layer.
3. The cell does not belong to the boundary layer region.

Here, $\beta_{\Delta s}$ and β_ω are two thresholds to be specified empirically. They must be chosen so that the criterion is applicable to any configuration, and for a wide variety of flow conditions. That

is why the criterion uses the normalized vorticity modulus instead of its gross value. Regarding the entropy, the threshold must be low enough to capture the shock wave wake, but high enough to avoid the entropy generated in spurious regions. In the following, these thresholds will be set with an application to a viscous flow around the NACA0012 airfoil.

5.2.2 Illustration with the viscous flow around a NACA0012 airfoil

In order to calibrate the parameters and test the criterion on a typical transonic case, a RANS simulation has been performed on the NACA0012 airfoil at $M_\infty = 0.72$, $Re = 3 \times 10^6$, and $\alpha = 2°$ ($C_L \approx 0.5$). Fig.5.4 illustrates the vorticity and the entropy generated within the shock wave and the boundary layer. The shock wake plane W_{sw} is positioned at $x_W = x_{te} + c/10$.

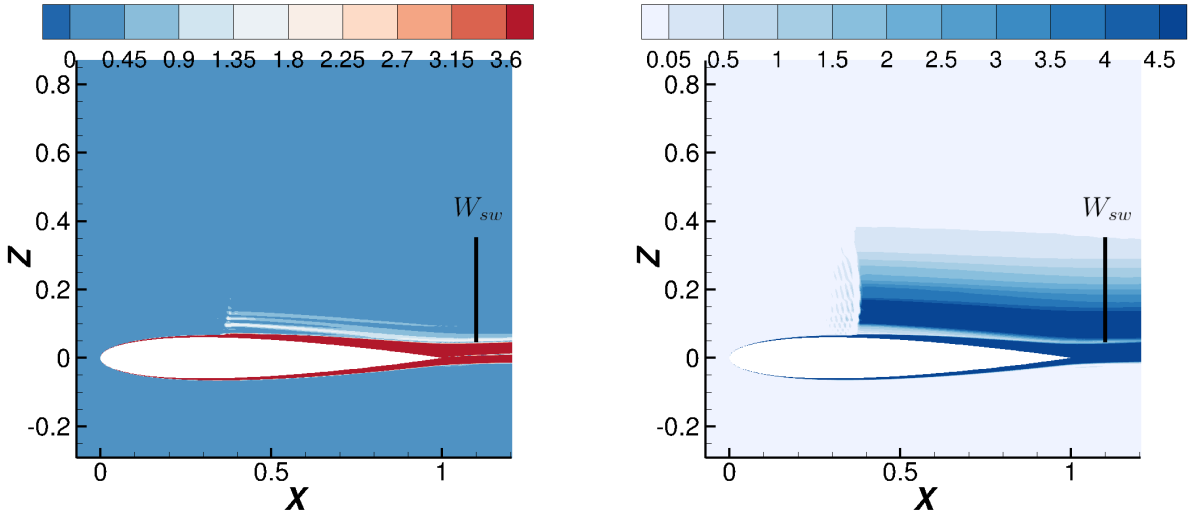

(a) Vorticity filter

(b) Entropy filter

Figure 5.4: Illustration of W_{sw} past the NACA0012 airfoil, $M_\infty = 0.72$, $Re = 3 \times 10^6$, $C_L \approx 0.5$

A contour of the normalized vorticity $||\boldsymbol{\omega}||c_{ref}/U_\infty$ is provided in Fig.5.4a. It is clear that the shock wave generates much less vorticity than the boundary layer, due to the fact that the transonic shock is almost straight. Hence, it confirms that the vorticity is the key for distinguishing the shock wave wake from the viscous wake. In the present case, the threshold has been set at $\beta_\omega = 1.8$.

The goal is now to find the upper boundary of the shock wave wake. A contour of the entropy increment Δs is proposed in Fig.5.4b. Here again, the entropy generated by the presence of the shock wave enables to clearly distinguish the shock wave wake from regions located outside the wake. In the present case, the threshold has been set at $\beta_{\Delta s} = 0.05$ in order to capture as much as possible the wake of the shock wave.

In the end, the approach chosen here for the evaluation of the wave drag is not very different from that of Mele *et al.* [36]. Yet, the shock wake plane W_{sw} is not located directly downstream of the shock wave, but rather further in the wake this time. Moreover, the boundaries of W_{sw} are now defined by means of the two filters based on entropy and vorticity, which was not the case in Mele *et al.*'s study.

In the following, various wave drag formulations will be tested. Among these ones, two definitions are based on the Lamb vector and one is based on the profile drag expression of the KJMB formulation. Additionally, the Lamb-vector-based wave drag definition proposed by Ostieri and Tognaccini [91] will be examined. The applications will be held on the NACA0012 airfoil, the OAT15A airfoil, the ONERA M6 wing and the NASA CRM.

5.3 Wave drag extraction using the Lamb vector in the shock wave wake

In this section, the four wave drag formulations described earlier are first presented. The aim of this analysis is to compare them to one another in order to identify which ones are the most robust for extracting the wave drag, and which ones must be definitively discarded.

To do so, the formulations are first tested on simple airfoils in order to find out whether their predictions on the shock wake plane match the predictions of the thermodynamic approaches of Oswatitsch [40, 41] and Destarac and Van der Vooren [21]. After this analysis, only the definitions that have given satisfaction are retained for the next applications.

Then, the remaining formulations are tested this time on the ONERA M6 wing and the NASA CRM in order to investigate their validity in three-dimensional flows around geometries of increasing complexity. In particular, the focus is given to the ability of the remaining formulations to deal with the wing sweep of the ONERA M6 wing and the wing of the NASA CRM.

5.3.1 Presentation of the final wave drag definitions

Several force decompositions have been analysed in this dissertation so far: Mele *et al.*'s decomposition [31, 32, 36], the ONERA decomposition and the KJMB decomposition. The aim of this subsection is to develop a specific wave drag extraction method for each of these decompositions.

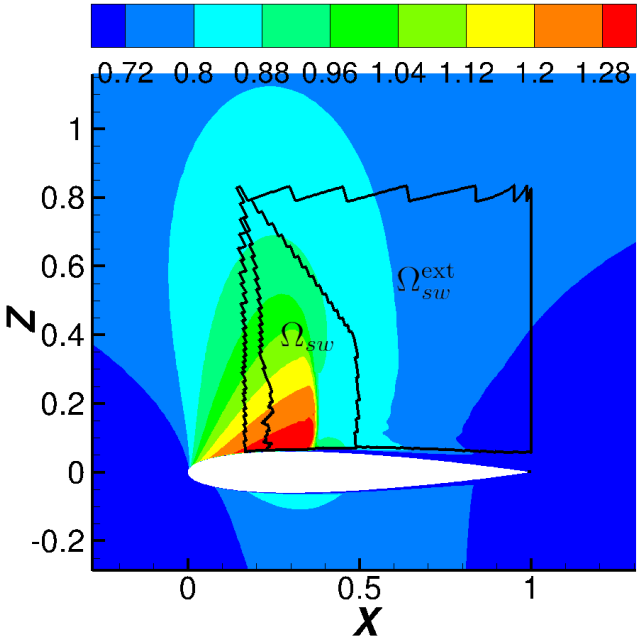

Figure 5.5: Definition of Ω_{sw} and Ω_{sw}^{ext} on the NACA0012 airfoil, $M_\infty = 0.72$, $Re = 3 \times 10^6$, $C_L \approx 0.5$

First of all, Toubin [107] showed that, in the thermodynamic approaches of Oswatitsch, Destarac and Van der Vooren, the wave drag can either be evaluated on the shock wake plane W_{sw} or on the contour of the shock wave volume Ω_{sw} (see Fig.5.5). Indeed, she considered a streamtube enclosing the shock wave and its wake and assumed that the flow in there is isentropic and isenthalpic. Under those hypotheses, she demonstrated that Δs and $\Delta \overline{u}$ remain constant on a streamline, so that the wave drag is independent of the location of W_{sw} in the shock wave wake. Hence, Oswatitsch's formula and Destarac and Van der Vooren's formula can be equivalently

expressed as follows:

$$D_w^{\mathrm{Osw}} = \frac{T_\infty}{U_\infty} \oint_{\partial\Omega_{sw}} \Delta s \, (\rho \boldsymbol{q} \cdot \boldsymbol{n}) \, \mathrm{d}S \tag{5.3.1}$$

$$D_w^{\mathrm{VdV}} = -\oint_{\partial\Omega_{sw}} \Delta \overline{u} \, (\rho \boldsymbol{q} \cdot \boldsymbol{n}) \, \mathrm{d}S \tag{5.3.2}$$

On the contrary, this invariance property is not fulfilled by the Lamb vector. Then, the wave drag computed by the term $\boldsymbol{F}_{S_e}$ may well not be the same depending on the surface chosen for integration. Very recently, Ostieri and Tognaccini [91] proposed to evaluate the wave drag by computing the contribution of $\boldsymbol{F}_{S_e}$ on the contour of an extended shock wave volume $\Omega_{sw}^{\mathrm{ext}}$ (see Fig.5.5):

$$D_w^{\mathrm{Ostieri}} = \boldsymbol{e}_x \cdot \left(-\frac{1}{\mathcal{N}-1} \oint_{\partial\Omega_{sw}^{\mathrm{ext}}} \boldsymbol{r} \times (\boldsymbol{n} \times \rho \boldsymbol{l}) \, \mathrm{d}S \right) \tag{5.3.3}$$

For the other formulations, the wave drag is evaluated on the shock wake plane W_{sw} defined by the criterion presented earlier. A first formulation called ONERA1 uses the Lamb vector and is based on Mele *et al.*'s expression of the profile drag with $\boldsymbol{F}_{S_e}$ [31, 32, 36]. A second definition called ONERA2 uses the Lamb vector and the density gradient, and is based on the expression of the profile drag expression using $\boldsymbol{F}_{S_e} + \boldsymbol{F}_{\nabla\rho}$ in the ONERA formulation. Then, a third and last definition not using the Lamb vector is based on the profile drag expression of the KJMB formulation:

$$D_w^{\mathrm{ONERA1}} = \boldsymbol{e}_x \cdot \left(-\frac{1}{\mathcal{N}-1} \int_{W_{sw}} \boldsymbol{r} \times (\boldsymbol{n} \times \rho \boldsymbol{l}) \, \mathrm{d}S \right) \tag{5.3.4}$$

$$D_w^{\mathrm{ONERA2}} = \boldsymbol{e}_x \cdot \left(\frac{1}{\mathcal{N}-1} \int_{W_{sw}} \boldsymbol{r} \times \left(\boldsymbol{n} \times \left(\frac{q^2 - U_\infty^2}{2} \nabla\rho - \rho \boldsymbol{l} \right) \right) \mathrm{d}S \right) \tag{5.3.5}$$

$$D_w^{\mathrm{KJMB}} = \boldsymbol{e}_x \cdot \left(\int_{W_{sw}} (P_\infty - P) \, \boldsymbol{n} \mathrm{d}S - \frac{U_\infty^2}{2} \int_{W_{sw}} (\rho_\infty - \rho) \, \boldsymbol{n} \mathrm{d}S \right) \tag{5.3.6}$$

Again, it is important to note that D_w^{ONERA1} is very similar to the wave drag expression proposed by Mele *et al.* [36] but here, W_{sw} is located downstream of the trailing edge and its definition is addressed by a physical criterion.

It should also be noted that the Lamb-vector-based wave drag expressions introduce the position vector $\boldsymbol{r}$ on $\partial\Omega_{sw}^{\mathrm{ext}}$ and W_{sw} which do not necessarily satisfy the symmetry properties expected in subsections 2.3.1 and 2.3.2. Hence, the wave drag will be evaluated with the corresponding invariant expressions of those definitions:

$$D_{w,\mathrm{inv}}^{\mathrm{Ostieri}} = \boldsymbol{e}_x \cdot \left(-\frac{1}{\mathcal{N}-1} \oint_{\partial\Omega_{sw}^{\mathrm{ext}}} \boldsymbol{r}^{\mathrm{sym}} \times (\boldsymbol{n}^{\mathrm{sym}} \times \rho \boldsymbol{l}_{fw}) \, \mathrm{d}S \right) \tag{5.3.7}$$

$$D_{w,\mathrm{inv}}^{\mathrm{ONERA1}} = \boldsymbol{e}_x \cdot \left(-\frac{1}{\mathcal{N}-1} \int_{W_{sw}} \boldsymbol{r}^{\mathrm{sym}} \times (\boldsymbol{n}^{\mathrm{sym}} \times \rho \boldsymbol{l}_{fw}) \, \mathrm{d}S \right) \tag{5.3.8}$$

$$\begin{aligned} D_{w,\mathrm{inv}}^{\mathrm{ONERA2}} = \boldsymbol{e}_x \cdot \Bigg(& -\frac{1}{\mathcal{N}-1} \int_{W_{sw}} \boldsymbol{r}^{\mathrm{sym}} \times (\boldsymbol{n}^{\mathrm{sym}} \times \rho \boldsymbol{l}_{fw}) \, \mathrm{d}S \\ & + \frac{1}{\mathcal{N}-1} \int_{W_{sw}} \boldsymbol{r}^{\mathrm{sym}} \times \left(\boldsymbol{n}^{\mathrm{sym}} \times \left. \frac{q^2 - U_\infty^2}{2} \nabla\rho \right|_{fw} \right) \mathrm{d}S \Bigg) \end{aligned} \tag{5.3.9}$$

In the following, the KJMB wave drag definition and the formulations based on the Lamb vector will be applied to airfoils, the ONERA M6 wing and the NASA CRM. In particular, their predictions will be compared to those of the thermodynamic definitions of Oswatitsch [40, 41] and Destarac and Van der Vooren [21].

5.3.2 Application to airfoils

The wave drag formulations are applied to the NACA0012 airfoil and the OAT15A airfoil for various lift coefficients in order to find out whether the definitions can be considered reliable on any kind of airfoil and for a wide variety of flow conditions. For the NACA0012 airfoil, the lift coefficient is low (it ranges from 0.08 to 0.5) while for the OAT15A airfoil, it is high (it ranges from 0.72 to 0.93): it allows to analyse the behaviour of the various wave drag formulations in low-lift conditions, cruise flight conditions (when $C_L \approx 0.5$) and high-lift conditions.

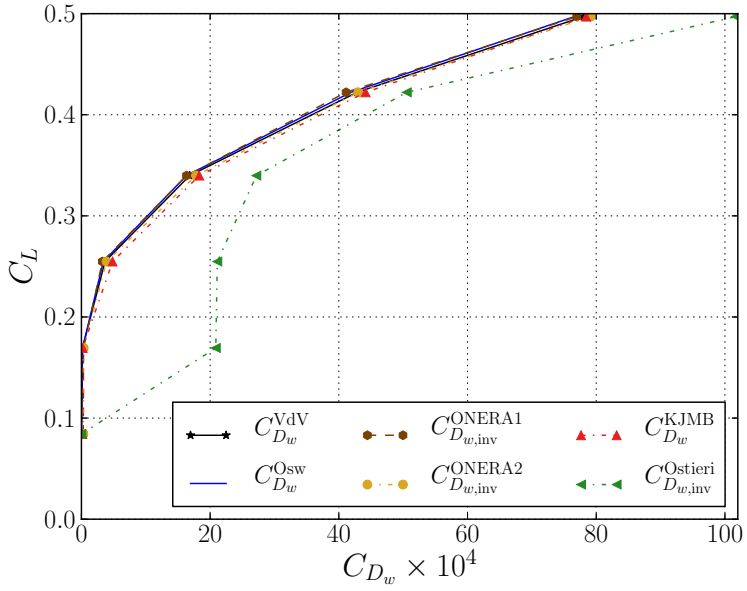

Figure 5.6: Wave drag coefficient VS lift coefficient on the NACA0012 airfoil, $M_\infty = 0.72$, $Re = 3 \times 10^6$

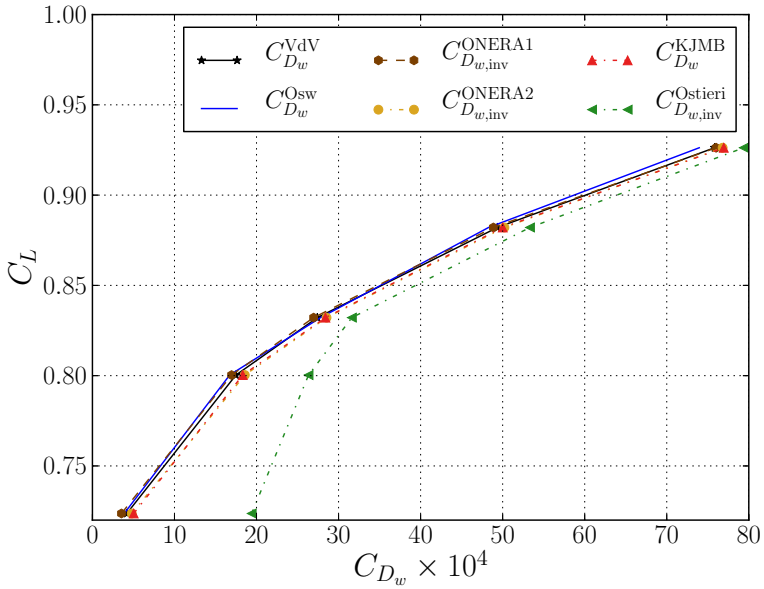

Figure 5.7: Wave drag coefficient VS lift coefficient on the OAT15A airfoil, $M_\infty = 0.724$, $Re = 3 \times 10^6$

The evolution of the wave drag coefficient versus the lift coefficient is shown in Figs.5.6 and 5.7. First of all, it is seen that the predictions of Oswatitsch's formula [40, 41] are always in perfect agreement with those of Destarac and Van der Vooren's formula [21] even when the strength of the shock wave increases at high C_L: in fact Oswatitsch's formula is a Taylor expansion of Destarac and Van der Vooren's formula but still constitutes a fine alternative for wave drag evaluation in transonic flows.

Regarding the Lamb-vector-based approaches, it is clear that Ostieri's formulation does not provide satisfying results. Indeed, its predictions are already way off the expected values at very low C_L. Then, it seems to progressively follow the same trend as the other formulations when increasing the C_L, but the gap is never completely overtaken. For this reason, Ostieri's formulation will be discarded. On the contrary, the predictions of the ONERA1 and ONERA2 definitions are always in very good agreement with those of the thermodynamic approaches. Hence, it is the first time that the wave drag is correctly evaluated using the Lamb vector in viscous flows. It should be noted that the ONERA1 and ONERA2 definitions are very different from the thermodynamic definitions regarding the physical content, but they still predict the same wave drag which is quite promising. Besides, the wave drag expression based on the KJMB formulation also yields very good results, which provides another unprecedented definition of the wave drag so far.

5.3.3 Application to the ONERA M6 wing and the NASA Common Research Model

Predictions on the ONERA M6 wing

Three-dimensional RANS computations were conducted on the ONERA M6 wing. The flight conditions are summarized in Table 5.1 and the wave drag results are listed in Table 5.2. Although the agreement with the thermodynamic approaches is not as good as in the two-dimensional cases, the results are still reasonably close. The difficulty here is the presence of several shock waves which form a lambda pattern on the wing (see Fig.F.11).

	Case 1	Case 2	Case 3	Case 4	Case 5
M_∞	0.6	0.699	0.84	0.8803	0.88400
Re	10×10^6	11.74×10^6	12×10^6	11.78×10^6	11.71×10^6
α	3°	3.06°	3.06°	2.05°	0.03°

Table 5.1: Flight conditions for the ONERA M6 wing.

	Case 1	Case 2	Case 3	Case 4	Case 5
Destarac and Van der Vooren [21]	0.00	2.58	28.85	57.83	38.58
Oswatitsch [40, 41]	0.00	2.61	28.17	57.44	38.33
ONERA1 invariant	0.01	0.03	20.29	50.92	38.55
ONERA2 invariant	0.01	0.04	21.46	57.84	43.25
Kutta-Joukowski-Maskell-Betz	0.03	0.08	21.64	55.74	41.24

Table 5.2: Wave drag predictions (in counts) on the ONERA M6 wing.

Moreover, the wing sweep angle makes it tough to find a suitable wake plane for wave drag computation. As mentioned earlier, the wake plane W_{sw} is located at $x_W = x_{wt}$ in this case. A potential refinement would be to integrate on a wake plane which follows the shape of the wing trailing edge.

Sensitivity to the sweep angle

Such a wake plane can be defined for $y_W \leq y_{wt}$ by choosing

$$x_W = x_{wt} - (y_{wt} - y_W) \,/\, \tan\theta \tag{5.3.10}$$

where θ is the sweep angle between W_{sw} (see Fig.5.8 in grey) and the vertical black line downstream of the trailing edge. Unfortunately, a strong sensitivity with respect to θ was evidenced, which underlines the drawbacks of the Lamb-vector-based wave drag definitions compared to the thermodynamic approaches. The results on the NASA CRM are presented in Fig.5.9. Only $C_{D_w}^{\text{KJMB}}$ seems to converge to the correct value as W_{sw} is tilted towards the wing trailing edge. Unexpectedly, $C_{D_w}^{\text{ONERA2}}$ and $C_{D_w}^{\text{KJMB}}$ are not always equal to each other although the profile drag expressions from which they are inspired are mathematically equivalent. The discrepancy might be due to numerical errors in the computation of the Lamb vector and/or the density gradient. It suggests that $C_{D_w}^{\text{KJMB}}$ may be the most reliable wave drag definition in this case.

The same θ sensitivity study was conducted on the ONERA M6 wing. The results for Cases 3, 4 and 5 are shown in Figs.5.10, 5.11 and 5.12. In this case, the wave drag computed by the ONERA2 and KJMB formulations with $\theta = 0°$ are sometimes in good agreement with the expected value (see Figs.5.11 and 5.12) and sometimes not (see Fig.5.10): it depends on the flight conditions, which is an additional issue. Nevertheless, it seems that the optimal sweep angle for W_{sw} is $\theta = 20°$ in this case, since the ONERA1, ONERA2 and KJMB definitions all predict a value in reasonable agreement with the thermodynamic approaches.

In the end, three unprecedented wave drag formulations have been presented and applied to transonic flows around airfoils, a wing and a commercial aircraft wing-body configuration. All yield very good results on airfoils but difficulties have been encountered regarding three-dimensional configurations due to the sweep angle of the wings. In conclusion, it seems that, except the thermodynamic approaches, the most satisfying wave drag definition is the one based on the KJMB formulation. Indeed, this is the only one able to provide a correct value on the NASA CRM when W_{sw} exactly follows the shape of the trailing edge (the wing sweep angle is 26°), while the other formulations either overestimate or underestimate way too much the wave drag in this case.

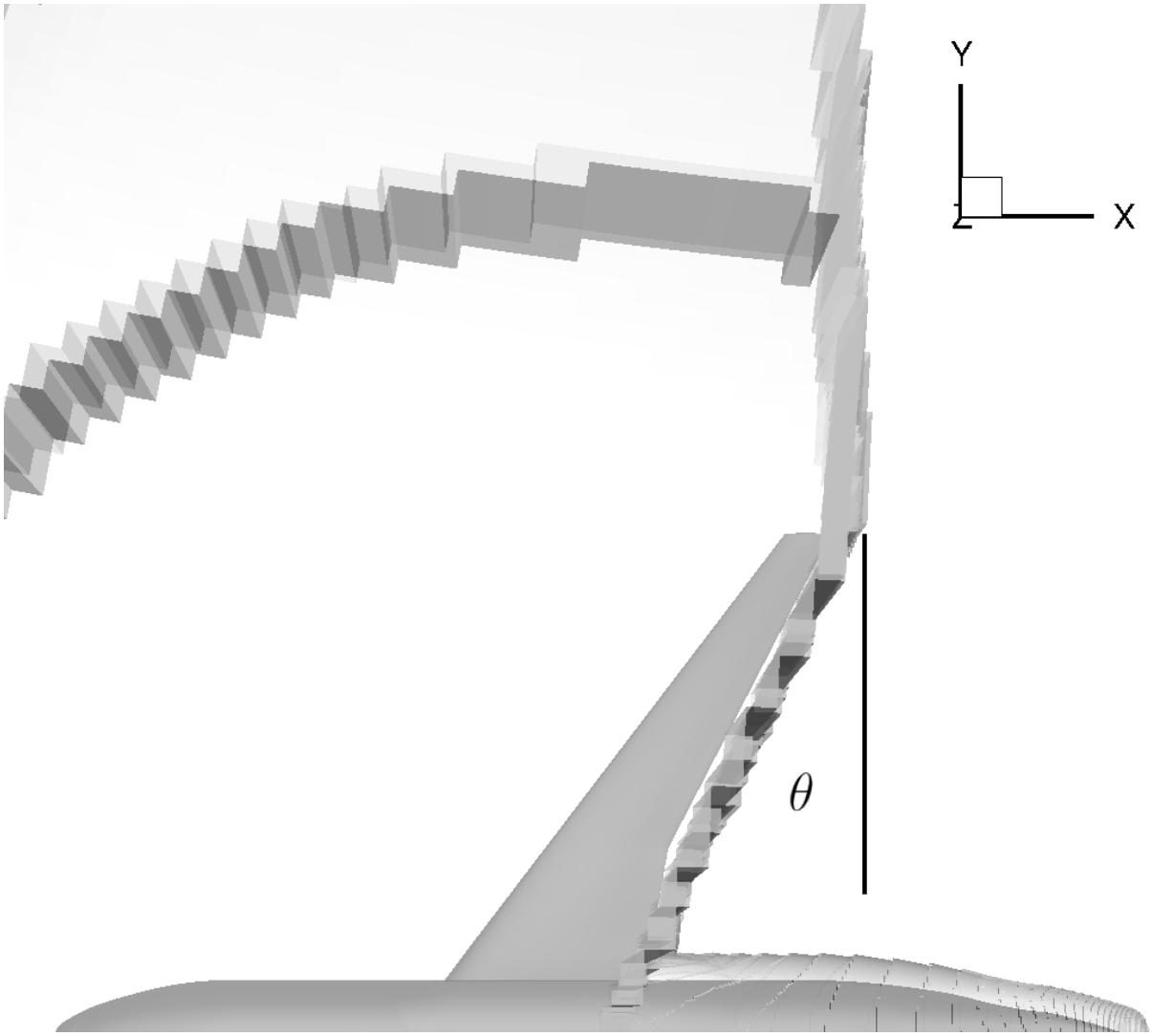

Figure 5.8: Illustration of W_{sw} and the angle θ made with the vertical line on the NASA CRM

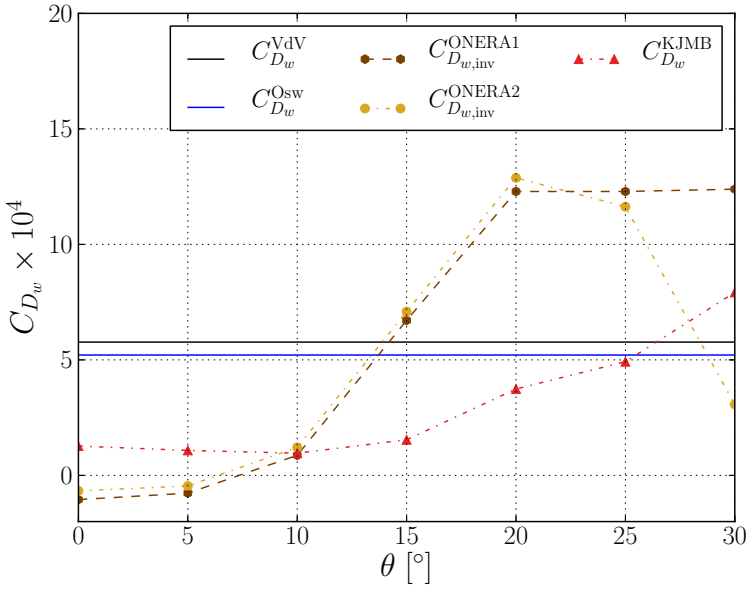

Figure 5.9: Sensitivity of C_{D_w} with respect to θ on the NASA CRM, $M_\infty = 0.85$, $Re = 5 \times 10^6$, $C_L \approx 0.5$

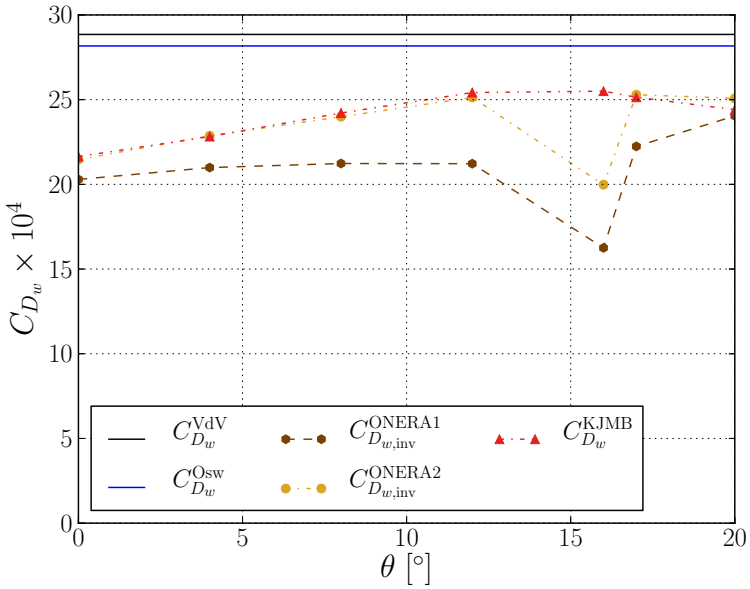

Figure 5.10: Sensitivity of C_{D_w} with respect to θ on the ONERA M6 wing, $M_\infty = 0.84$, $Re = 12 \times 10^6$, $\alpha = 3.06°$

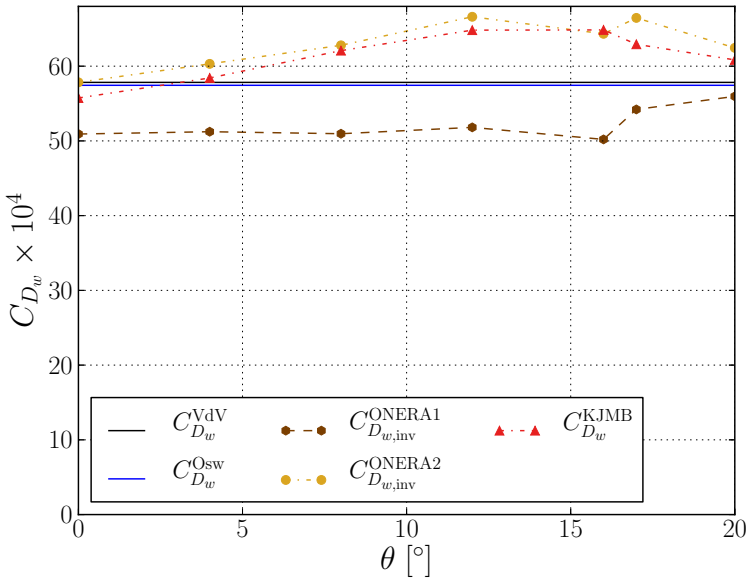

Figure 5.11: Sensitivity of C_{D_w} with respect to θ on the ONERA M6 wing, $M_\infty = 0.8803$, $Re = 11.78 \times 10^6$, $\alpha = 2.05°$

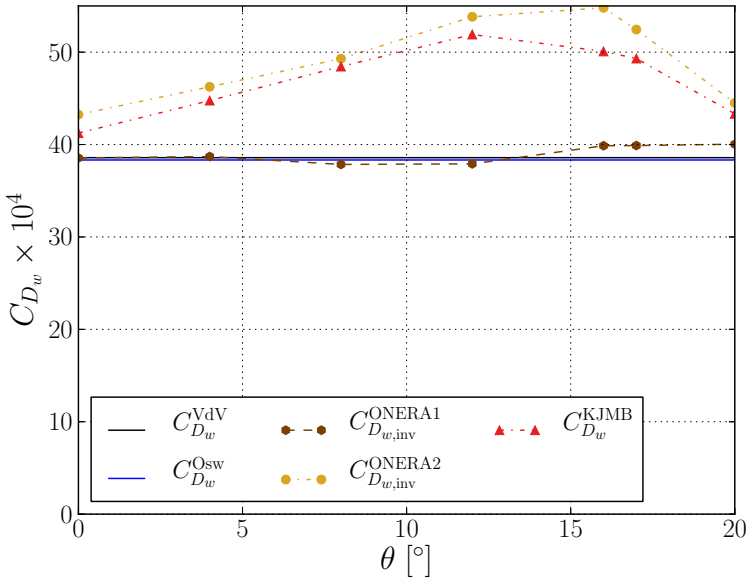

Figure 5.12: Sensitivity of C_{D_w} with respect to θ on the ONERA M6 wing, $M_\infty = 0.884$, $Re = 11.71 \times 10^6$, $\alpha = 0.03°$

Chapter summary

In this chapter, the focus has been given to the extraction of the wave drag using the Lamb vector. In fact, the various force decompositions previously developed in this dissertation were only able to provide the profile drag, i.e. the sum of the wave drag and the viscous drag. Consequently, the aim of the chapter has consisted in extracting the wave drag from the profile drag.

In the first step, several theoretical links have been emphasized between the Lamb-vector-based formulations and former thermodynamic methods: the links between Mele *et al.*'s formulation [31, 32, 36] and Oswatitsch's formula [40, 41], and those between the ONERA and KJMB formulations and Destarac and Van der Vooren's formula [21]. Those theoretical analyses have allowed to confirm that the wave drag can be evaluated with the Lamb vector, provided that the integration is performed far enough from the shock wave.

Yet, knowing that the shock wave wake progressively merges with the viscous wake further downstream, the second step has consisted in identifying the part of the wake coming from the presence of the shock wave. To do so, a physical criterion has been proposed in order to define a shock wake plane which allows to extract the wave drag before it becomes undistinguishable from the viscous drag. This physical criterion is based on entropy and vorticity. The entropy filter enables to avoid the spurious regions outside the physical wake, while the vorticity filter allows to delineate the shock wave wake from the vortical wake of the boundary layer.

Then, three novel wave drag definitions have been presented. Two are based on the Lamb vector, among which one is inspired from Mele *et al.*'s profile drag definition [31, 32, 36] and one is inspired from the profile drag expression of the ONERA formulation. The third one is based on the profile drag definition of the KJMB formulation:

$$\boxed{\begin{aligned} D_w^{\text{ONERA1}} &= \boldsymbol{e}_x \cdot \left(-\frac{1}{\mathcal{N}-1} \int_{W_{sw}} \boldsymbol{r} \times (\boldsymbol{n} \times \rho \boldsymbol{l}) \, \mathrm{d}S \right) \\ D_w^{\text{ONERA2}} &= \boldsymbol{e}_x \cdot \left(\frac{1}{\mathcal{N}-1} \int_{W_{sw}} \boldsymbol{r} \times \left(\boldsymbol{n} \times \left(\frac{q^2 - U_\infty^2}{2} \nabla \rho - \rho \boldsymbol{l} \right) \right) \mathrm{d}S \right) \\ D_w^{\text{KJMB}} &= \boldsymbol{e}_x \cdot \left(\int_{W_{sw}} (P_\infty - P) \, \boldsymbol{n} \mathrm{d}S - \frac{U_\infty^2}{2} \int_{W_{sw}} (\rho_\infty - \rho) \, \boldsymbol{n} \mathrm{d}S \right) \end{aligned}}$$

with the shock wake plane W_{sw} defined as follows:

$$\boxed{x_W = \begin{cases} x_{te} + c/10 & \text{in RANS flows around airfoils} \\ x_{te} + c & \text{in Euler flows around airfoils} \\ x_{wt} & \text{in RANS flows around wings or aircrafts} \end{cases}}$$

and

$$\boxed{\begin{aligned} &\Delta s \geq \beta_{\Delta s} \\ &||\boldsymbol{\omega}|| c_{ref} / U_\infty \leq \beta_\omega \\ &\text{cell} \notin \text{boundary layer region} \end{aligned}}$$

Those three wave drag definitions have been compared to the thermodynamic approaches and to Ostieri and Tognaccini's Lamb-vector-based formula [91]. The applications to the NACA0012 airfoil and the OAT15A airfoil have proved the great potential of the three novel wave drag definitions and have allowed to discard Ostieri and Tognaccini's approach. Yet, some difficulties have been encountered on the ONERA M6 wing and the NASA CRM regarding the wing sweep angle, which suggests that the computation of the wave drag using the Lamb vector still requires further developments.

General Discussion

The first goal of this thesis was to develop a Lamb-vector-based aerodynamic force decomposition which is invariant to the location of the reference point and to the size of the integration domain everywhere in the flow field. Then, the second goal was to phenomenologically interpret the terms of the decomposition by identifying the role of compressibility in lift and drag. The third objective was to develop a method for extracting the wave drag from the profile drag. Finally, the last goal was to implement it in a post-processing code and to test it on various configurations. All those steps have been addressed in the preceding chapters. The outcome of the work carried out so far may now be examined and discussed before concluding this dissertation.

Regarding the invariance

Before developing an invariant Lamb-vector-based force decomposition, it has been necessary to investigate how the terms of Mele *et al.*'s formulation [31, 32, 36] are impacted by a change in the location of the reference point, and by an increase in the size of the integration domain. This first step has evidenced the sensitivity of the decomposition to those two parameters in the near field, its invariance in the far field, and also demonstrated that the invariance is ensured as soon as the flow progressively satisfies symmetries in the far field.

The study of these symmetries has also paved the way towards the development of a reference-point-invariant version of Mele *et al.*'s formulation: by symmetrizing each flow quantity involved in the integrals. This new formulation has then been tested on several configurations, and the complete invariance to the location of the reference point has been achieved. Nevertheless, the force decomposition computed by the reference-point-invariant formulation is still sensitive to the size of the integration domain.

Later on, another reference-point-invariant Lamb-vector-based formulation has been developed: the ONERA formulation. The decomposition provided by this formulation is theoretically totally invariant to the location of the reference point. Yet, numerical errors are made by the post-processing code in the computation of the integrals, and the invariance is not completely guaranteed in practice. To remedy this issue, the very same symmetrization procedure has been employed on the integrals of the formulation. Unfortunately, the force decomposition computed by the ONERA formulation is still sensitive to the size of the integration domain as well.

To address the uncertainty regarding the choice of the integration domain, it has appeared necessary to draw good practice recommendations from the numerical results and to set default parameters. In fact, in order to obtain a satisfying drag decomposition into lift-induced drag and profile drag, these results have suggested that:

- For the study of airfoils, the distance d between S_e and S_b is set at $d/c = 10$.
- For the study of wings or aircrafts, the distance d between S_e and S_b is set at $d/c_{ref} = 1$.

Of course, the issue of the sentivity to the size of the integration domain is not solved upon defining such default parameters. Rather, it allows the user to obtain an optimal drag decomposition with the Lamb-vector-based formulations and the KJMB formulation.

Regarding the phenomenological interpretation

In this thesis, the role of compressibility in lift and drag has been identified by emphasizing the links between Mele *et al.*'s decomposition [31, 32, 36] and the classical theories of Kutta, Joukowski, Maskell and Betz. Then, this theoretical analysis has allowed to phenomenologically interpret all the terms of the decomposition and hence to better understand why the decomposition established by Wu *et al.* [75] in incompressible flows is not valid anymore in compressible flows. Yet, Mele *et al.*'s decomposition is not exactly equivalent to the classical theories of Kutta, Joukowski, Maskell and Betz, due to the presence of a compressibility correction term.

With the development of the ONERA formulation, the decomposition is now strictly equivalent to the classical theories. Moreover, its equivalent KJMB formulation encompasses these three classical theories in a single expression and bridges the gap between classical incompressible aerodynamics and the study of complex transonic flows. Finally, the ONERA and KJMB formulations have successfully been applied to airfoils and a commercial aircraft configuration.

Hence, the role of compressibility is better identified in the decomposition provided by these two formulations, which are then much easier to interpret phenomenologically than Mele *et al.*'s decomposition. Yet, although the role of compressibility has been clearly highlighted in the lift, its role in the lift-induced drag and the profile drag deserves to be analysed more thoroughly.

Regarding the wave drag

It has been shown that the KJMB formulation and the formulations based on the Lamb vector can be used for predicting the wave drag. Indeed, their connections with the approaches developed by Oswatitsch [40, 41] and by Destarac and Van der Vooren [21] have been evidenced. However, they seemed to correctly predict the wave drag only in the wake. Unfortunately, the wakes of the shock wave and the boundary layer progressively merge downstream and the corresponding drag contributions become ever more difficult to distinguish.

To circumvent this issue, a method has been developed allowing to extract the wave drag in the very near wake where the two wakes are still not merged. For this purpose, default parameters have been set for the definition of the shock wake plane of integration W_{sw}:

- For airfoils, $x_W = x_{te} + c/10$ in viscous flows while $x_W = x_{te} + c$ in inviscid flows.
- For wings or aircrafts in viscous flows, $x_W = x_{wt}$.
- The physical thresholds are set at $\beta_{\Delta s} = 0.05$ and $\beta_\omega = 1.8$.

This approach has given very satisfying wave drag predictions on airfoils. However difficulties remain on swept wings, due to the sensitivity to the location of the shock wake plane, which suggests that the present method has not completely solved the wave drag problem, and that further developments should be undertaken. Among these, potential improvements could be made by interpolating the solution onto a shock wake plane shaped in order to best fit the geometry of the wing trailing edge, or by developing a hybrid vortical/thermodynamic wave drag definition.

Regarding the numerical implementation

The KJMB formulation and the formulations using the Lamb vector have been implemented in the ONERA FORTRAN code *ffd01*. This code now calculates the aerodynamic force from CFD solutions converged on structured grids with the near-field approach, Destarac and Van der Vooren's formulation [21], the KJMB formulation and the two Lamb-vector-based formulations, among which only the last three allow for a far-field estimation of the lift.

The only limitation observed with the formulations using the Lamb vector is the extended computational time compared to other methods. In fact, they require the computation of several gradients and curls that are presently calculated from scratch for each term of the decomposition. A better implementation could be achieved by computing them only once in a specific routine, store them in big matrices, and call these matrices in the routines aimed at computing the terms of the decomposition.

Conclusion and Perspectives

Synthesis

At the beginning of this dissertation, several questions were still left unanswered regarding the Lamb-vector-based formulation. Hence, the aim of this thesis has been to address those questions and to provide solid answers as much as possible. The main achieved objectives of this work are summarized here:

- The sensitivity of Mele *et al.*'s Lamb-vector-based decomposition [31, 32, 36] to the location of the reference point has been clearly emphasized in the near field.
- Its invariance in the far field has been related to the progressive appearance of far-field symmetries in the flow.
- The study of those symmetries has allowed to develop a reference-point-invariant version of Mele *et al.*'s decomposition.
- The role of compressibility in lift and drag has been evidenced by identifying the links between Mele *et al.*'s formulation and the classical theories of Kutta, Joukowski, Maskell and Betz, therefore providing a phenomenological interpretation of the terms of the decomposition in compressible flows.
- A new Lamb-vector-based force decomposition (the ONERA formulation) strictly equivalent to the classical theories has been devised and successfully tested on airfoils and a commercial aircraft configuration. Compared to Mele *et al.*'s decomposition, the new drag breakdown into lift-induced drag and profile drag has proved to be in better agreement with Destarac and Van der Vooren's approach [21]. This new decomposition has later been made completely invariant to the location of the reference point.
- Another brand new aerodynamic force decomposition (the KJMB formulation) embedding the classical theories in a single equation has also been developed and successfully applied to airfoils and the same commercial aircraft configuration. This formulation extends the field of application of the classical theories to viscous transonic aerodynamics. Besides, compared to the ONERA decomposition and Mele *et al.*'s decomposition, its drag breakdown has proved to be in even better agreement with Destarac and Van der Vooren's approach [21].
- Later, the ability of the Lamb-vector-based formulations and the KJMB formulation to predict the wave drag has been confirmed by identifying the links with Oswatitsch's formula [40, 41] and Destarac and Van der Vooren's formula [21].
- Finally, a method for extracting the wave drag from the profile drag has been implemented in the very near wake upon defining a physical criterion used to separate the shock wave wake from the viscous wake. The application of this method to the Lamb-vector-based formulations and the KJMB formulation has notably provided very accurate wave drag predictions on airfoils.

Perspectives

Although a lot of positive achievements can be drawn from this thesis, the Lamb-vector-based formulations and the KJMB formulation may still be subject to improvements and discoveries. Hereafter are summarized several points that are still worth investigating in the future:

Regarding the invariance to the size of the integration domain

Throughout the analyses conducted on the Lamb-vector-based formulations and the KJMB formulation, it has been observed that the lift-induced drag increases in the near field (while the profile drag decreases), then reaches a maximum (while the profile drag reaches a minimum) and later decreases (while the profile drag increases) because of the dissipation of the vortices in the wake.

In order to achieve or at least tend towards the invariance to the size of the integration domain, several possibilities exist:

1. Find an invariant vortical quantity upon which establish a new drag decomposition, even if the only invariant quantity found so far is the fluid momentum (see subsection 2.2.2). There might be particular flow physics to account for in order to find this invariant quantity: it could be found by analysing the Navier-Stokes equations together with Helmholtz vorticity transport equation, since the Lamb vector and the density gradient appear in both. Although the analysis seems difficult, this possibility is interesting because it would lead to a better understanding of the vorticity dynamics at stake in the rolling-up of the vortex sheet.

2. Use a vorticity confinement technique in order to counterbalance the numerical dissipation of the vortices responsible for the transfer from the lift-induced drag to the profile drag in the wake. By doing so, the lift-induced drag would reach a maximum and remain constant further downstream, so that the size of the integration domain could be chosen arbitrarily once this maximum value has been reached. Yet, the physical existence of such a flow solution could be questioned by proceeding this way.

Regarding the wave drag

Further investigations could be made concerning the case of unswept wings in both inviscid and viscous flows. On a theoretical point of view, the previously proposed method for extracting the wave drag could be adapted to better fit the analysis of the more complex geometries of swept wings and aircrafts.

Regarding the domain of application

In this study, the Lamb-vector-based formulations and the KJMB formulation have been applied to subsonic and transonic aerodynamics. In particular, the focus has been given to steady flows in order to simplify the resolution of the important issues raised in the introduction of this dissertation.

Yet, several authors have proposed formulations able to decompose the aerodynamic force in unsteady flows [75, 88, 95, 108]. It could be interesting to pursue these works and address the same sensitivity issues in unsteady flows as those encountered in steady flows. It could allow one to apply the Lamb-vector-based formulations to rotating frames such as turbomachines, rotorcrafts and also flight conditions characterized by flow separation or transonic buffet.

Another axis of research could concern the decomposition of the aerodynamic force in supersonic flows. It would imply to adapt the grid topology, with grid lines following the shape of the characteristics in order to avoid a significant increase in spurious drag. Mele and Tognaccini [31] already analysed the case of the NACA0012 airfoil. It would be worth investigating the

decomposition provided by the ONERA and the KJMB formulations in this case around wings and fighter aircraft configurations.

The possibility to achieve a drag-thrust bookkeeping with those formulations could also be of interest: Russo *et al.* [109] already studied the case of an actuator disk in incompressible flows. It could be interesting to carry on their work, extend the analysis to compressible flows, apply it to other models such as body force, and even use it in turbomachinery.

Besides, it would be appealing to apply the ONERA and the KJMB formulations to disruptive configurations in order to obtain a phenomenological force breakdown analysis on these new geometries: the box wing, on which Mele *et al.*'s formulation [31, 32, 36] has already been tested [110], blended-wing-body configurations and so on.

From a practical point of view, it could be interesting to investigate the possibility to use the Lamb-vector-based formulations and the KJMB formulation in wind-tunnel tests. For sure, it would imply to have technologies able to probe the flow very close to the skin of the model, or to adapt the formulation and thoroughly define the boundaries of the control volume. For this purpose, the KJMB formulation seems to be the most suitable method since it contains only surface integrals.

Finally, it is important to remind that the Lamb-vector-based formulations and the KJMB formulation can be applied to hydrodynamics as well, unlike Destarac and Van der Vooren's approach [21] which is valid only for perfect gases. Their use in hydrodynamics could in the end lead to a hydrodynamic force decomposition on foils, boats or submarines.

Regarding the numerical implementation

For the moment, the gradients and curls are recalculated in each routine aimed at computing a term of the decomposition involving the Lamb vector or the density gradient. Consequently, the computational time spent by the routines coding the Lamb-vector-based formulations is much more important than that spent by those coding the KJMB formulation and Destarac and Van der Vooren's approach [21].

In order to reduce the computational time spent with the Lamb-vector-based formulations, two possibilities stand out:

1. Calculate the derivatives of the density and the velocity vector in a specific routine and call the computed values in those aimed at computing the terms of the decomposition. Hence, the derivatives would be calculated only once and kept in computer memory.

2. Directly calculate and extract the derivatives from the CFD solver. In this case, it would imply to modify the input strategy of the post-processing code since *ffd01* is formatted to receive only the five conservative variables (density, momentum in the x, y, z-directions and total energy) plus the turbulent viscosity in RANS computations. Nevertheless, the user could benefit from this approach since the derivatives could be computed more accurately with the frequently implemented high-order capabilities of CFD solvers.

Appendices

A Integral theorems

This appendix presents the main integral theorems used in the mathematical demonstrations of this dissertation. Let $\boldsymbol{f}$ be a differentiable vector field, ϕ be a differentiable scalar field, Ω be a domain bounded by $\partial\Omega$ and S be a surface bounded by ∂S. The derivative moment transformations state that in a $\mathcal{N}$-dimensional space with $\mathcal{N} = 2$ or 3:

$$\int_\Omega \boldsymbol{f}\mathrm{d}v = \frac{1}{\mathcal{N}-1}\int_\Omega \boldsymbol{r}\times(\nabla\times\boldsymbol{f})\,\mathrm{d}v - \frac{1}{\mathcal{N}-1}\oint_{\partial\Omega}\boldsymbol{r}\times(\boldsymbol{n}\times\boldsymbol{f})\,\mathrm{d}S \tag{A.1}$$

$$\int_S \phi\boldsymbol{n}\mathrm{d}S = -\frac{1}{\mathcal{N}-1}\int_S \boldsymbol{r}\times(\boldsymbol{n}\times\nabla\phi)\,\mathrm{d}S + \frac{1}{\mathcal{N}-1}\oint_{\partial S}\phi\boldsymbol{r}\times\mathbf{d}\boldsymbol{r} \tag{A.2}$$

where $\boldsymbol{n}$ is the unit normal pointing outside the fluid and $\mathbf{d}\boldsymbol{r}$ is the unit vector tangential to S.

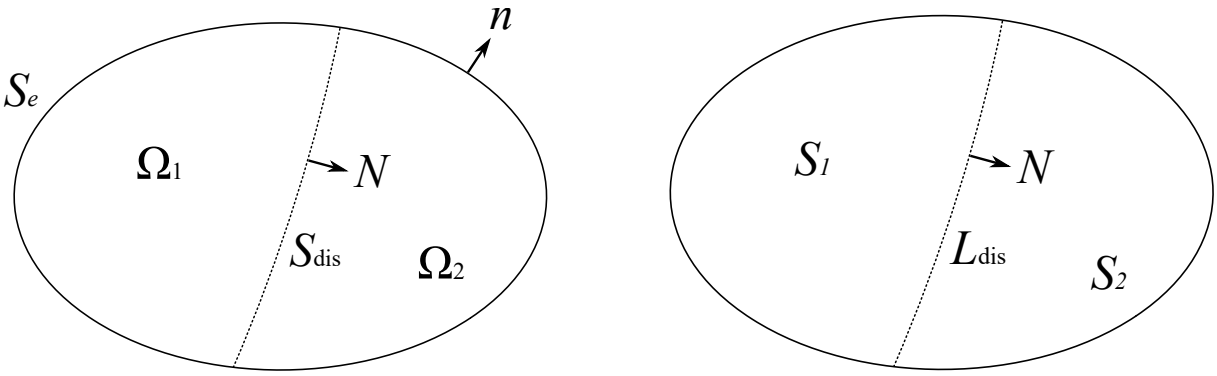

(a) Discontinuous volume

(b) Discontinuous surface

Figure A.1: Discontinuous domain of integration

In the presence of a discontinuity, $\boldsymbol{f}$ and ϕ are no longer differentiable in the whole domain Ω or on the whole surface S. In this case, Ω is split into $\Omega_1 \cup \Omega_2$ with Ω_1 and Ω_2 separated by a surface of discontinuity S_{dis} and S is split into $S_1 \cup S_2$ with S_1 and S_2 separated by a line of discontinuity L_{dis} (see Fig.A.1). Denoting $\boldsymbol{N}$ the unit normal on the discontinuity pointing from region 1 to 2, $[\![\boldsymbol{f}]\!] = \boldsymbol{f}_2 - \boldsymbol{f}_1$ and $[\![\phi]\!] = \phi_2 - \phi_1$, the application of (A.1) to Ω_1 and Ω_2 and (A.2) to S_1 and S_2 yields

$$\begin{aligned}\int_\Omega \boldsymbol{f}\mathrm{d}v = {}& \frac{1}{\mathcal{N}-1}\int_\Omega \boldsymbol{r}\times(\nabla\times\boldsymbol{f})\,\mathrm{d}v - \frac{1}{\mathcal{N}-1}\oint_{\partial\Omega}\boldsymbol{r}\times(\boldsymbol{n}\times\boldsymbol{f})\,\mathrm{d}S \\ & + \frac{1}{\mathcal{N}-1}\int_{S_{\text{dis}}}\boldsymbol{r}\times(\boldsymbol{N}\times[\![\boldsymbol{f}]\!])\,\mathrm{d}S\end{aligned} \tag{A.3}$$

$$\int_S \phi\boldsymbol{n}\mathrm{d}S = -\frac{1}{\mathcal{N}-1}\int_S \boldsymbol{r}\times(\boldsymbol{n}\times\nabla\phi)\,\mathrm{d}s + \frac{1}{\mathcal{N}-1}\oint_{\partial S}\phi\boldsymbol{r}\times\mathbf{d}\boldsymbol{r} - \frac{1}{\mathcal{N}-1}\int_{L_{\text{dis}}}[\![\phi]\!]\boldsymbol{r}\times\mathbf{d}\boldsymbol{r} \tag{A.4}$$

Those identities are independent of the magnitude of $\boldsymbol{r}_0$: a shift $\boldsymbol{r} \to \boldsymbol{r} + \boldsymbol{r}_0$ gives birth to several additional terms that cancel each other according to the Gauss theorem. However, the right-hand side integrals individually depend on the choice of $\boldsymbol{r}_0$.

Similarly, it is possible to generalize the Gauss and Stokes theorems in the presence of discontinuities inside the integration domain. Let $\mathcal{F}$ be a tensor of any rank. Denoting $[\![\mathcal{F}]\!] = \mathcal{F}_2 - \mathcal{F}_1$ and letting $\circ$ be any permissible operation:

$$\int_\Omega \nabla\circ\mathcal{F}\mathrm{d}v = \oint_{\partial\Omega}\boldsymbol{n}\circ\mathcal{F}\mathrm{d}S - \int_{S_{\text{dis}}}\boldsymbol{N}\circ[\![\mathcal{F}]\!]\mathrm{d}S \tag{A.5}$$

$$\int_S (\boldsymbol{n}\times\nabla)\circ\mathcal{F}\mathrm{d}S = \oint_{\partial S}\mathbf{d}\boldsymbol{r}\circ\mathcal{F} - \int_{L_{\text{dis}}}\mathbf{d}\boldsymbol{r}\circ[\![\mathcal{F}]\!] \tag{A.6}$$

B Symmetry properties of the velocity vector derivatives and the density gradient

This appendix demonstrates the symmetry properties satisfied by the velocity vector and the density gradient in the far field. The derivatives of the velocity vector with respect to the x, y and z-coordinates are defined as follows:

$$\frac{\partial \boldsymbol{q}}{\partial x}(x,y,z) = \lim_{\varepsilon \to 0} \frac{\boldsymbol{q}(x+\varepsilon,y,z) - \boldsymbol{q}(x,y,z)}{\varepsilon} \tag{B.1a}$$

$$\frac{\partial \boldsymbol{q}}{\partial y}(x,y,z) = \lim_{\varepsilon \to 0} \frac{\boldsymbol{q}(x,y+\varepsilon,z) - \boldsymbol{q}(x,y,z)}{\varepsilon} \tag{B.1b}$$

$$\frac{\partial \boldsymbol{q}}{\partial z}(x,y,z) = \lim_{\varepsilon \to 0} \frac{\boldsymbol{q}(x,y,z+\varepsilon) - \boldsymbol{q}(x,y,z)}{\varepsilon} \tag{B.1c}$$

with $\varepsilon > 0$. Therefore, using the symmetry properties (2.3.4a) and (2.3.4b) of the velocity vector in the far wake, it is possible to derive those of its derivatives in $(x,-y,z)$:

$$\begin{aligned}\frac{\partial \boldsymbol{q}}{\partial x}(x,-y,z) &= \lim_{\varepsilon \to 0} \frac{\boldsymbol{q}(x+\varepsilon,-y,z) - \boldsymbol{q}(x,-y,z)}{\varepsilon} \\ &= \lim_{\varepsilon \to 0} \boldsymbol{S}_y \cdot \frac{\boldsymbol{q}(x+\varepsilon,y,z) - \boldsymbol{q}(x,y,z)}{\varepsilon} = \boldsymbol{S}_y \cdot \frac{\partial \boldsymbol{q}}{\partial x}(x,y,z)\end{aligned} \tag{B.2a}$$

$$\begin{aligned}\frac{\partial \boldsymbol{q}}{\partial y}(x,-y,z) &= \lim_{\varepsilon \to 0} \frac{\boldsymbol{q}(x,-y+\varepsilon,z) - \boldsymbol{q}(x,-y,z)}{\varepsilon} \\ &= \lim_{\varepsilon \to 0} \frac{\boldsymbol{q}(x,-(y-\varepsilon),z) - \boldsymbol{q}(x,-y,z)}{\varepsilon} \\ &= \lim_{\varepsilon \to 0} \boldsymbol{S}_y \cdot \frac{\boldsymbol{q}(x,y-\varepsilon,z) - \boldsymbol{q}(x,y,z)}{\varepsilon} = -\boldsymbol{S}_y \cdot \frac{\partial \boldsymbol{q}}{\partial y}(x,y,z)\end{aligned} \tag{B.2b}$$

$$\begin{aligned}\frac{\partial \boldsymbol{q}}{\partial z}(x,-y,z) &= \lim_{\varepsilon \to 0} \frac{\boldsymbol{q}(x,-y,z+\varepsilon) - \boldsymbol{q}(x,-y,z)}{\varepsilon} \\ &= \lim_{\varepsilon \to 0} \boldsymbol{S}_y \cdot \frac{\boldsymbol{q}(x,y,z+\varepsilon) - \boldsymbol{q}(x,y,z)}{\varepsilon} = \boldsymbol{S}_y \cdot \frac{\partial \boldsymbol{q}}{\partial z}(x,y,z)\end{aligned} \tag{B.2c}$$

and similarly those of its derivatives in $(x,y,-z)$:

$$\frac{\partial \boldsymbol{q}}{\partial x}(x,y,-z) = \boldsymbol{S}_y \cdot \frac{\partial \boldsymbol{q}}{\partial x}(x,y,z) \tag{B.3a}$$

$$\frac{\partial \boldsymbol{q}}{\partial y}(x,y,-z) = \boldsymbol{S}_y \cdot \frac{\partial \boldsymbol{q}}{\partial y}(x,y,z) \tag{B.3b}$$

$$\frac{\partial \boldsymbol{q}}{\partial z}(x,y,-z) = -\boldsymbol{S}_y \cdot \frac{\partial \boldsymbol{q}}{\partial z}(x,y,z) \tag{B.3c}$$

The derivatives of the density field with respect to the x, y and z-coordinates are defined as follows:

$$\frac{\partial \rho}{\partial x}(x,y,z) = \lim_{\varepsilon \to 0} \frac{\rho(x+\varepsilon,y,z) - \rho(x,y,z)}{\varepsilon} \tag{B.4a}$$

$$\frac{\partial \rho}{\partial y}(x,y,z) = \lim_{\varepsilon \to 0} \frac{\rho(x,y+\varepsilon,z) - \rho(x,y,z)}{\varepsilon} \tag{B.4b}$$

$$\frac{\partial \rho}{\partial z}(x,y,z) = \lim_{\varepsilon \to 0} \frac{\rho(x,y,z+\varepsilon) - \rho(x,y,z)}{\varepsilon} \tag{B.4c}$$

Therefore, using the symmetry properties (2.3.5a) and (2.3.5b) of the density field in the far

wake, it is possible to derive those of its derivatives in $(x, -y, z)$:

$$\frac{\partial \rho}{\partial x}(x, -y, z) = \frac{\partial \rho}{\partial x}(x, y, z) \tag{B.5a}$$

$$\frac{\partial \rho}{\partial y}(x, -y, z) = -\frac{\partial \rho}{\partial y}(x, y, z) \tag{B.5b}$$

$$\frac{\partial \rho}{\partial z}(x, -y, z) = \frac{\partial \rho}{\partial z}(x, y, z) \tag{B.5c}$$

and similarly those of its derivatives in $(x, y, -z)$:

$$\frac{\partial \rho}{\partial x}(x, y, -z) = \frac{\partial \rho}{\partial x}(x, y, z) \tag{B.6a}$$

$$\frac{\partial \rho}{\partial y}(x, y, -z) = \frac{\partial \rho}{\partial y}(x, y, z) \tag{B.6b}$$

$$\frac{\partial \rho}{\partial z}(x, y, -z) = -\frac{\partial \rho}{\partial z}(x, y, z) \tag{B.6c}$$

Finally, using (2.3.19a), it is possible to express the symmetries of the density derivatives in $(-x, y, z)$:

$$\frac{\partial \rho}{\partial x}(-x, y, z) = -\frac{\partial \rho}{\partial x}(x, y, z) \tag{B.7a}$$

$$\frac{\partial \rho}{\partial y}(-x, y, z) = \frac{\partial \rho}{\partial y}(x, y, z) \tag{B.7b}$$

$$\frac{\partial \rho}{\partial z}(-x, y, z) = \frac{\partial \rho}{\partial z}(x, y, z) \tag{B.7c}$$

It should be noted that the derivatives of the kinetic energy $\frac{q^2}{2}$ satisfy the same symmetries in the far field as those of the density derivatives.

C Lamb-vector-based momentum balance in transonic flows

In this appendix, the mathematical developments leading to the transonic version of the Lamb-vector-based formulation are presented. In particular, a Lamb-vector-based momentum balance is performed in a control volume which comprises a shock wave discontinuity. To do so,

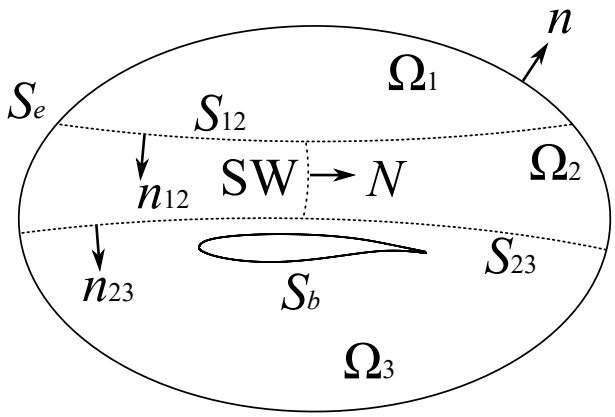

Figure C.1: Partition of the control volume in transonic flows

the control volume Ω is split into three sub-volumes $\Omega = \Omega_1 \cup \Omega_2 \cup \Omega_3$ as shown in Fig.C.1. The steady Navier-Stokes equations write as follows:

$$\rho \boldsymbol{l} + \rho \nabla \left(\frac{q^2}{2} \right) = -\nabla p + \nabla \cdot \boldsymbol{\tau} \tag{C.1}$$

The steady Helmholtz equations are found by applying the curl operator to the latter relation:

$$-\nabla \times (\rho \boldsymbol{l}) + \nabla \left(\frac{q^2}{2} \right) \times \nabla \rho = -\nabla \times (\nabla \cdot \boldsymbol{\tau}) \tag{C.2}$$

Then, by taking the cross product between the position vector $\boldsymbol{r}$ and the Helmholtz equations in Ω_1, it is possible to write

$$-\frac{1}{\mathcal{N}-1} \int_{\Omega_1} \boldsymbol{r} \times (\nabla \times (\rho \boldsymbol{l}))\, \mathrm{d}v + \boldsymbol{F}_{m_{\rho_1}} = -\frac{1}{\mathcal{N}-1} \int_{\Omega_1} \boldsymbol{r} \times (\nabla \times (\nabla \cdot \boldsymbol{\tau}))\, \mathrm{d}v \tag{C.3}$$

By applying the first DMT (A.1) to the volume integrals, and then the Gauss theorem (A.5), the Lamb-vector-based momentum balance in Ω_1 is written as follows:

$$\boxed{\boldsymbol{F}_{\rho l_1} + \boldsymbol{F}_{m_{\rho_1}} + \boldsymbol{F}_{S_{e1}} + \boldsymbol{F}_{\tau_1} = \boldsymbol{0}} \tag{C.4}$$

with

$$\boldsymbol{F}_{\rho l_1} = -\int_{\Omega_1} \rho \boldsymbol{l} \mathrm{d}v \tag{C.5}$$

$$\boldsymbol{F}_{m_{\rho_1}} = \frac{1}{\mathcal{N}-1} \int_{\Omega_1} \boldsymbol{r} \times \left(\nabla \left(\frac{q^2}{2} \right) \times \nabla \rho \right) \mathrm{d}v \tag{C.6}$$

$$\boldsymbol{F}_{S_{e1}} = -\frac{1}{\mathcal{N}-1} \int_{S_{12}} \boldsymbol{r} \times (\boldsymbol{n}_{12} \times \rho \boldsymbol{l})\, \mathrm{d}S - \frac{1}{\mathcal{N}-1} \int_{\partial\Omega_1 \setminus S_{12}} \boldsymbol{r} \times (\boldsymbol{n} \times \rho \boldsymbol{l})\, \mathrm{d}S \tag{C.7}$$

$$\begin{aligned} \boldsymbol{F}_{\tau_1} = &\int_{S_{12}} \boldsymbol{\tau} \cdot \boldsymbol{n}_{12} \mathrm{d}S + \frac{1}{\mathcal{N}-1} \int_{S_{12}} \boldsymbol{r} \times (\boldsymbol{n}_{12} \times \nabla \cdot \boldsymbol{\tau})\, \mathrm{d}S \\ &+ \int_{\partial\Omega_1 \setminus S_{12}} \boldsymbol{\tau} \cdot \boldsymbol{n} \mathrm{d}S + \frac{1}{\mathcal{N}-1} \int_{\partial\Omega_1 \setminus S_{12}} \boldsymbol{r} \times (\boldsymbol{n} \times \nabla \cdot \boldsymbol{\tau})\, \mathrm{d}S \end{aligned} \tag{C.8}$$

Again, by taking the cross product between the position vector $\boldsymbol{r}$ and the Helmholtz equations in Ω_2, it is possible to write

$$-\frac{1}{\mathcal{N}-1}\int_{\Omega_2}\boldsymbol{r}\times(\nabla\times(\rho\boldsymbol{l}))\,\mathrm{d}v+\boldsymbol{F}_{m_{\rho 2}}=-\frac{1}{\mathcal{N}-1}\int_{\Omega_2}\boldsymbol{r}\times(\nabla\times(\nabla\cdot\boldsymbol{\tau}))\,\mathrm{d}v \tag{C.9}$$

This time Ω_2 contains the shock wave discontinuity SW. When applying the first generalized DMT (A.3) to the volume integrals, and then the Gauss theorem (A.5), the latter relation is transformed as follows:

$$\begin{aligned}\boldsymbol{F}_{\rho l_2}+\boldsymbol{F}_{m_{\rho 2}}+\boldsymbol{F}_{S_{e2}}+\frac{1}{\mathcal{N}-1}\int_{\mathrm{SW}}\boldsymbol{r}\times(\boldsymbol{N}\times[\![\rho\boldsymbol{l}]\!])\,\mathrm{d}S=-\boldsymbol{F}_{\tau_2}+\frac{1}{\mathcal{N}-1}\int_{\mathrm{SW}}\boldsymbol{r}\times(\boldsymbol{N}\times[\![\nabla\cdot\tau]\!])\,\mathrm{d}S\\+\int_{\mathrm{SW}}[\![\boldsymbol{\tau}]\!]\cdot\boldsymbol{N}\mathrm{d}S\end{aligned} \tag{C.10}$$

Finally, by using the steady Navier-Stokes equations, the Lamb-vector-based momentum balance in Ω_2 becomes

$$\boxed{\begin{aligned}\boldsymbol{F}_{\rho l_2}+\boldsymbol{F}_{m_{\rho 2}}+\boldsymbol{F}_{S_{e2}}+\boldsymbol{F}_{\tau_2}=\frac{1}{\mathcal{N}-1}\int_{\mathrm{SW}}\boldsymbol{r}\times\left(\boldsymbol{N}\times[\![\nabla p+\rho\nabla\left(\frac{q^2}{2}\right)]\!]\right)\mathrm{d}S\\+\int_{\mathrm{SW}}[\![\boldsymbol{\tau}]\!]\cdot\boldsymbol{N}\mathrm{d}S\end{aligned}} \tag{C.11}$$

with

$$\boldsymbol{F}_{\rho l_2}=-\int_{\Omega_2}\rho\boldsymbol{l}\mathrm{d}v \tag{C.12}$$

$$\boldsymbol{F}_{m_{\rho 2}}=\frac{1}{\mathcal{N}-1}\int_{\Omega_2}\boldsymbol{r}\times\left(\nabla\left(\frac{q^2}{2}\right)\times\nabla\rho\right)\mathrm{d}v \tag{C.13}$$

$$\begin{aligned}\boldsymbol{F}_{S_{e2}}=&\frac{1}{\mathcal{N}-1}\int_{S_{12}}\boldsymbol{r}\times(\boldsymbol{n}_{12}\times\rho\boldsymbol{l})\,\mathrm{d}S-\frac{1}{\mathcal{N}-1}\int_{S_{23}}\boldsymbol{r}\times(\boldsymbol{n}_{23}\times\rho\boldsymbol{l})\,\mathrm{d}S\\&-\frac{1}{\mathcal{N}-1}\int_{\partial\Omega_2\setminus(S_{12}\cup S_{23})}\boldsymbol{r}\times(\boldsymbol{n}\times\rho\boldsymbol{l})\,\mathrm{d}S\end{aligned} \tag{C.14}$$

$$\begin{aligned}\boldsymbol{F}_{\tau_2}=&-\int_{S_{12}}\boldsymbol{\tau}\cdot\boldsymbol{n}_{12}\mathrm{d}S-\frac{1}{\mathcal{N}-1}\int_{S_{12}}\boldsymbol{r}\times(\boldsymbol{n}_{12}\times\nabla\cdot\boldsymbol{\tau})\,\mathrm{d}S\\&+\int_{S_{23}}\boldsymbol{\tau}\cdot\boldsymbol{n}_{23}\mathrm{d}S+\frac{1}{\mathcal{N}-1}\int_{S_{23}}\boldsymbol{r}\times(\boldsymbol{n}_{23}\times\nabla\cdot\boldsymbol{\tau})\,\mathrm{d}S\\&+\int_{\partial\Omega_2\setminus(S_{12}\cup S_{23})}\boldsymbol{\tau}\cdot\boldsymbol{n}\mathrm{d}S+\frac{1}{\mathcal{N}-1}\int_{\partial\Omega_2\setminus(S_{12}\cup S_{23})}\boldsymbol{r}\times(\boldsymbol{n}\times\nabla\cdot\boldsymbol{\tau})\,\mathrm{d}S\end{aligned} \tag{C.15}$$

Eventually, by taking the cross product between the position vector $\boldsymbol{r}$ and the Helmholtz equations in Ω_3, the following relation is obtained:

$$-\frac{1}{\mathcal{N}-1}\int_{\Omega_3}\boldsymbol{r}\times(\nabla\times(\rho\boldsymbol{l}))\,\mathrm{d}v+\boldsymbol{F}_{m_{\rho 3}}=-\frac{1}{\mathcal{N}-1}\int_{\Omega_3}\boldsymbol{r}\times(\nabla\times(\nabla\cdot\boldsymbol{\tau}))\,\mathrm{d}v \tag{C.16}$$

This time Ω_3 encloses the skin surface S_b. Here, the no-slip condition ensures that the Lamb vector is zero on S_b. Therefore, when applying the first DMT (A.1) to the volume integrals, and then the Gauss theorem (A.5), it is possible to write

$$\boldsymbol{F}_{\rho l_3}+\boldsymbol{F}_{m_{\rho 3}}+\boldsymbol{F}_{S_{e3}}=-\int_{\Omega_3}\nabla\cdot\boldsymbol{\tau}\mathrm{d}v-\frac{1}{\mathcal{N}-1}\oint_{\partial\Omega_3}\boldsymbol{r}\times(\boldsymbol{n}\times\nabla\cdot\boldsymbol{\tau})\,\mathrm{d}S \tag{C.17}$$

$$\iff\boldsymbol{F}_{\rho l_3}+\boldsymbol{F}_{m_{\rho 3}}+\boldsymbol{F}_{S_{e3}}+\boldsymbol{F}_{\tau_3}=-\oint_{S_b}\boldsymbol{\tau}\cdot\boldsymbol{n}\mathrm{d}S-\frac{1}{\mathcal{N}-1}\oint_{S_b}\boldsymbol{r}\times(\boldsymbol{n}\times\nabla\cdot\boldsymbol{\tau})\,\mathrm{d}S \tag{C.18}$$

Having that $\nabla \cdot \boldsymbol{\tau} = \nabla p$ on S_b due to the no-slip condition, and using the second DMT (A.2) for the pressure, it is therefore possible to express the Lamb-vector-based momentum balance in Ω_3 as follows:

$$\boxed{\boldsymbol{F}_{\rho l_3} + \boldsymbol{F}_{m_{\rho 3}} + \boldsymbol{F}_{S_{e3}} + \boldsymbol{F}_{\tau_3} = -\oint_{S_b} (-p\boldsymbol{I} + \boldsymbol{\tau}) \cdot \boldsymbol{n} \mathrm{d}S = \boldsymbol{F}} \tag{C.19}$$

with

$$\boldsymbol{F}_{\rho l_3} = -\int_{\Omega_3} \rho \boldsymbol{l} \mathrm{d}v \tag{C.20}$$

$$\boldsymbol{F}_{m_{\rho 3}} = \frac{1}{\mathcal{N}-1} \int_{\Omega_3} \boldsymbol{r} \times \left(\nabla \left(\frac{q^2}{2} \right) \times \nabla \rho \right) \mathrm{d}v \tag{C.21}$$

$$\boldsymbol{F}_{S_{e3}} = \frac{1}{\mathcal{N}-1} \int_{S_{23}} \boldsymbol{r} \times (\boldsymbol{n}_{23} \times \rho \boldsymbol{l}) \, \mathrm{d}S - \frac{1}{\mathcal{N}-1} \int_{\partial\Omega_3 \setminus S_{23}} \boldsymbol{r} \times (\boldsymbol{n} \times \rho \boldsymbol{l}) \, \mathrm{d}S \tag{C.22}$$

$$\begin{aligned} \boldsymbol{F}_{\tau_3} = &-\int_{S_{23}} \boldsymbol{\tau} \cdot \boldsymbol{n}_{23} \mathrm{d}S - \frac{1}{\mathcal{N}-1} \int_{S_{23}} \boldsymbol{r} \times (\boldsymbol{n}_{23} \times \nabla \cdot \boldsymbol{\tau}) \, \mathrm{d}S \\ &+ \int_{\partial\Omega_3 \setminus S_{23}} \boldsymbol{\tau} \cdot \boldsymbol{n} \mathrm{d}S + \frac{1}{\mathcal{N}-1} \int_{\partial\Omega_3 \setminus S_{23}} \boldsymbol{r} \times (\boldsymbol{n} \times \nabla \cdot \boldsymbol{\tau}) \, \mathrm{d}S \end{aligned} \tag{C.23}$$

Finally, by summing altogether the momentum balances in each sub-volume (C.4), (C.11) and (C.19), the Lamb-vector-based formulation in transonic flows is obtained:

$$\boxed{\boldsymbol{F} = \boldsymbol{F}_{\rho l} + \boldsymbol{F}_{m_\rho} + \boldsymbol{F}_{S_e} + \boldsymbol{F}_{\tau} + \boldsymbol{F}_{\mathrm{SW}}} \tag{C.24}$$

with

$$\boldsymbol{F}_{\rho l} = -\int_{\Omega} \rho \boldsymbol{l} \mathrm{d}v \tag{C.25}$$

$$\boldsymbol{F}_{m_\rho} = \frac{1}{\mathcal{N}-1} \int_{\Omega} \boldsymbol{r} \times \left(\nabla \left(\frac{q^2}{2} \right) \times \nabla \rho \right) \mathrm{d}v \tag{C.26}$$

$$\boldsymbol{F}_{S_e} = -\frac{1}{\mathcal{N}-1} \oint_{S_e} \boldsymbol{r} \times (\boldsymbol{n} \times \rho \boldsymbol{l}) \, \mathrm{d}S \tag{C.27}$$

$$\boldsymbol{F}_{\tau} = \oint_{S_e} \boldsymbol{\tau} \cdot \boldsymbol{n} \mathrm{d}S + \frac{1}{\mathcal{N}-1} \oint_{S_e} \boldsymbol{r} \times (\boldsymbol{n} \times \nabla \cdot \boldsymbol{\tau}) \, \mathrm{d}S \tag{C.28}$$

$$\boldsymbol{F}_{\mathrm{SW}} = -\int_{\mathrm{SW}} [\![\boldsymbol{\tau}]\!] \cdot \boldsymbol{N} \mathrm{d}S - \frac{1}{\mathcal{N}-1} \int_{\mathrm{SW}} \boldsymbol{r} \times \left(\boldsymbol{N} \times [\![\nabla p + \rho \nabla \left(\frac{q^2}{2} \right)]\!] \right) \mathrm{d}S \tag{C.29}$$

D Equivalent expression of F_{SW}

In this appendix, an equivalent expression of the term F_{SW} is derived in order to avoid the integration of the jump of the flow quantities on the shock wave surface SW. By using the first generalized DMT (A.3) and the generalized Gauss theorem (A.5) in the shock wave region Ω_{sw} (see Fig.4.2), it is possible to express $\boldsymbol{F}_{\mathrm{SW}}$ as follows:

$$\begin{aligned}\boldsymbol{F}_{\mathrm{SW}} = &\int_{\Omega_{sw}} \nabla\cdot\boldsymbol{\tau}\mathrm{d}v - \oint_{\partial\Omega_{sw}} \boldsymbol{\tau}\cdot\boldsymbol{n}_{sw}\mathrm{d}S - \int_{\Omega_{sw}} \left(\nabla p + \rho\nabla\left(\frac{q^2}{2}\right)\right)\mathrm{d}v \\ &+ \frac{1}{\mathcal{N}-1}\int_{\Omega_{sw}} \boldsymbol{r}\times\left(\nabla\rho\times\nabla\left(\frac{q^2}{2}\right)\right)\mathrm{d}v \\ &- \frac{1}{\mathcal{N}-1}\oint_{\partial\Omega_{sw}} \boldsymbol{r}\times\left[\boldsymbol{n}_{sw}\times\left(\nabla p + \rho\nabla\left(\frac{q^2}{2}\right)\right)\right]\mathrm{d}S \end{aligned} \tag{D.1}$$

It is important to remind here that $\boldsymbol{n}_{sw}$ is the unit normal pointing outside Ω_{sw}. Using the steady Navier-Stokes equations

$$\rho\boldsymbol{l} + \rho\nabla\left(\frac{q^2}{2}\right) = -\nabla p + \nabla\cdot\boldsymbol{\tau} \tag{D.2}$$

$\nabla p + \rho\nabla\left(\frac{q^2}{2}\right)$ is replaced by $\nabla\cdot\boldsymbol{\tau} - \rho\boldsymbol{l}$ in the volume integral of the first line of (D.1) such that

$$\begin{aligned}\boldsymbol{F}_{\mathrm{SW}} = &-\oint_{\partial\Omega_{sw}} \boldsymbol{\tau}\cdot\boldsymbol{n}_{sw}\mathrm{d}S + \int_{\Omega_{sw}} \rho\boldsymbol{l}\mathrm{d}v + \int_{\Omega_{sw}} \boldsymbol{m}_\rho\mathrm{d}v \\ &- \frac{1}{\mathcal{N}-1}\oint_{\partial\Omega_{sw}} \boldsymbol{r}\times\left[\boldsymbol{n}_{sw}\times\left(\nabla p + \rho\nabla\left(\frac{q^2}{2}\right)\right)\right]\mathrm{d}S \end{aligned} \tag{D.3}$$

where $\boldsymbol{m}_\rho$ is defined as

$$\boldsymbol{m}_\rho = \frac{\boldsymbol{r}}{\mathcal{N}-1}\times\left(\nabla\rho\times\nabla\left(\frac{q^2}{2}\right)\right) \tag{D.4}$$

Let us have a closer look at the second line of (D.3). $\partial\Omega_{sw}$ is a closed surface which comprises the shock and its surroundings such that it does not cross the shock discontinuity. Hence, no line of discontinuity crosses $\partial\Omega_{sw}$. Having that

$$\nabla p + \rho\nabla\left(\frac{q^2}{2}\right) = \nabla\left(p + \rho\frac{q^2}{2}\right) - \frac{q^2}{2}\nabla\rho$$

and using the second DMT (A.2), $\boldsymbol{F}_{\mathrm{SW}}$ is now written in the following form:

$$\begin{aligned}\boldsymbol{F}_{\mathrm{SW}} = &\oint_{\partial\Omega_{sw}} (p\boldsymbol{I} - \boldsymbol{\tau})\cdot\boldsymbol{n}_{sw}\mathrm{d}S + \int_{\Omega_{sw}} \rho\boldsymbol{l}\mathrm{d}v + \int_{\Omega_{sw}} \boldsymbol{m}_\rho\mathrm{d}v \\ &+ \oint_{\partial\Omega_{sw}} \rho\frac{q^2}{2}\boldsymbol{n}_{sw}\mathrm{d}S + \frac{1}{\mathcal{N}-1}\oint_{\partial\Omega_{sw}} \boldsymbol{r}\times\left(\boldsymbol{n}_{sw}\times\frac{q^2}{2}\nabla\rho\right)\mathrm{d}S \end{aligned} \tag{D.5}$$

Let us now analyse the surface integral in the first line of (D.5). The generalized Gauss theorem (A.5) yields

$$\oint_{\partial\Omega_{sw}} (p\boldsymbol{I} - \boldsymbol{\tau})\cdot\boldsymbol{n}_{sw}\mathrm{d}S = \int_{\Omega_{sw}} (\nabla p - \nabla\cdot\boldsymbol{\tau})\,\mathrm{d}v + \int_{\mathrm{SW}} [\![p\boldsymbol{I} - \boldsymbol{\tau}]\!]\cdot\boldsymbol{N}\mathrm{d}S \tag{D.6}$$

With the equivalent form of the steady Navier-Stokes equations

$$\nabla\cdot(\rho\boldsymbol{q}\otimes\boldsymbol{q}) = -\nabla p + \nabla\cdot\boldsymbol{\tau}$$

$\nabla p - \nabla \cdot \boldsymbol{\tau}$ is replaced by $-\nabla \cdot (\rho \boldsymbol{q} \otimes \boldsymbol{q})$ in the volume integral of (D.6). Using once again the generalized Gauss theorem (A.5) in order to cast it to a surface integral, it is possible to write

$$\oint_{\partial\Omega_{sw}} (p\boldsymbol{I} - \boldsymbol{\tau}) \cdot \boldsymbol{n}_{sw} \mathrm{d}S = -\oint_{\partial\Omega_{sw}} \rho \boldsymbol{q} \, (\boldsymbol{q} \cdot \boldsymbol{n}_{sw}) \, \mathrm{d}S + \underbrace{\int_{\mathrm{SW}} [\![\rho \boldsymbol{q} \otimes \boldsymbol{q} + p\boldsymbol{I} - \boldsymbol{\tau}]\!] \cdot \boldsymbol{N} \mathrm{d}S}_{= \boldsymbol{0}} \tag{D.7}$$

The third term of (D.7) is always zero since

$$[\![\rho \boldsymbol{q} \otimes \boldsymbol{q} + p\boldsymbol{I} - \boldsymbol{\tau}]\!] \cdot \boldsymbol{N} = \boldsymbol{0}$$

on the shock wave SW. The introduction of (D.7) into (D.5) yields the desired form of $\boldsymbol{F}_{\mathrm{SW}}$:

$$\begin{aligned} \boldsymbol{F}_{\mathrm{SW}} = & \int_{\Omega_{sw}} \boldsymbol{m}_\rho \mathrm{d}v + \oint_{\partial\Omega_{sw}} \left(\rho \frac{q^2}{2} \boldsymbol{n}_{sw} - \rho \boldsymbol{q} \, (\boldsymbol{q} \cdot \boldsymbol{n}_{sw}) \right) \mathrm{d}S \\ & + \frac{1}{\mathcal{N} - 1} \oint_{\partial\Omega_{sw}} \boldsymbol{r} \times \left(\boldsymbol{n}_{sw} \times \frac{q^2}{2} \nabla \rho \right) \mathrm{d}S + \int_{\Omega_{sw}} \rho \boldsymbol{l} \mathrm{d}v \end{aligned} \tag{D.8}$$

E Asymptotic study of the compressibility correction $F_{\nabla\rho}$

This appendix is devoted to the asymptotic evolution of the compressibility correction $\boldsymbol{F}_{\nabla\rho}$ defined as

$$\boldsymbol{F}_{\nabla\rho} = \frac{1}{\mathcal{N}-1}\oint_{S_e} \boldsymbol{r} \times \left(\boldsymbol{n} \times \frac{q^2 - U_\infty^2}{2}\nabla\rho\right) \mathrm{d}S \tag{E.1}$$

$\boldsymbol{F}_{\nabla\rho}$ involves the kinetic energy perturbation, hence its asymptotic behaviour will be sought only in the wake, provided that the lateral surfaces are located sufficiently far from the aircraft. The asymptotic behaviour of the velocity perturbation in the wake was addressed by Batchelor [63] (p.352), Schlichting [111] (p.732) and White [112] (p.481) for two-dimensional planar wakes and three-dimensional circular wakes in incompressible flows. They both used the two-dimensional form of Navier-Stokes equations in the (x, z)-plane. In such conditions, and assuming that the same study can be held in the (x, y)-plane, the lateral extent of the planar wake behaves as $y, z = \mathcal{O}\left(x^{1/2}\right)$ while the longitudinal velocity perturbation behaves as $u = \mathcal{O}\left(x^{-1/2}\right)$. Hence the incompressible continuity equation yields $v, w = \mathcal{O}\left(x^{-1}\right)$. For circular wakes, $y, z = \mathcal{O}\left(x^{1/3}\right)$ while $u = \mathcal{O}\left(x^{-2/3}\right)$ which yields $v, w = \mathcal{O}\left(x^{-4/3}\right)$. Experimental studies conducted on three-dimensional wakes highlighted that the asymptotic behaviour of u becomes equivalent to that for circular wakes [113] in the far field. Furthermore, Kuo and Baldwin [114] observed that the lateral and vertical widths of the three-dimensional wake progressively increase as $x^{1/3}$ as in the case of a circular wake.

The aforementioned results were established in incompressible flows. Yet, the flows considered in this study are compressible. Here, the asymptotic behaviour will then be sought only in the wake far enough downstream such that compressibility effects become negligible. Indeed, consider the steady continuity equation:

$$\nabla \cdot (\rho \boldsymbol{q}) = 0 \Leftrightarrow \nabla \cdot \boldsymbol{q} = -\boldsymbol{q} \cdot \nabla (\ln \rho) \tag{E.2}$$

The local density can be written as follows [18]:

$$\rho = \rho_\infty e^{-\Delta s/R} \left(\frac{T}{T_\infty}\right)^{\frac{1}{\gamma-1}} \tag{E.3}$$

$$\text{with} \quad \frac{T}{T_\infty} = 1 + \frac{\gamma-1}{2} M_\infty^2 \left(1 - \frac{q^2}{U_\infty^2} + \frac{2\Delta H}{U_\infty^2}\right) \tag{E.4}$$

It is therefore possible to express (E.2) in terms of ∇s, ∇H and $\nabla\left(\frac{q^2}{2}\right)$:

$$\nabla \cdot \boldsymbol{q} = \frac{1}{R}\boldsymbol{q} \cdot \nabla s + \frac{1}{\gamma R T}\left(\boldsymbol{q} \cdot \nabla\left(\frac{q^2}{2}\right) - \boldsymbol{q} \cdot \nabla H\right) \tag{E.5}$$

In steady conditions, the evolution of $\frac{q^2}{2}$ along a streamline is given by

$$\boldsymbol{q} \cdot \nabla\left(\frac{q^2}{2}\right) = -\boldsymbol{q} \cdot \frac{\nabla p}{\rho} + \boldsymbol{q} \cdot \frac{\nabla \cdot \boldsymbol{\tau}}{\rho} \tag{E.6}$$

Using the Crocco-Vazsonyi equation

$$\rho \boldsymbol{\omega} \times \boldsymbol{q} = \rho T \nabla s - \rho \nabla H + \nabla \cdot \boldsymbol{\tau} \tag{E.7}$$

it is possible to express $\boldsymbol{q} \cdot (\nabla \cdot \boldsymbol{\tau})$ in terms of $\boldsymbol{q} \cdot \nabla s$ and $\boldsymbol{q} \cdot \nabla H$. Hence, (E.6) becomes

$$\boldsymbol{q} \cdot \nabla\left(\frac{q^2}{2}\right) = -\boldsymbol{q} \cdot \frac{\nabla p}{\rho} + \boldsymbol{q} \cdot \nabla H - T\boldsymbol{q} \cdot \nabla s \tag{E.8}$$

Combining (E.5) and (E.8), the steady continuity equation can be written as follows:

$$\nabla \cdot \boldsymbol{q} = -\boldsymbol{q} \cdot \frac{\nabla p}{\gamma p} + \frac{\gamma - 1}{\gamma R} \boldsymbol{q} \cdot \nabla s \tag{E.9}$$

Finally for an adiabatic steady flow, the evolution of the entropy along a streamline is solely driven by viscous effects:

$$\rho \boldsymbol{q} \cdot T \nabla s = \boldsymbol{\tau} : \nabla \boldsymbol{q} \tag{E.10}$$

Hence, (E.9) becomes

$$\nabla \cdot \boldsymbol{q} = \frac{1}{\gamma p} \left(-\boldsymbol{q} \cdot \nabla p + (\gamma - 1) \boldsymbol{\tau} : \nabla \boldsymbol{q} \right) \tag{E.11}$$

Wakes are free turbulent flows where it is common to assume that the pressure is nearly constant provided that the wake survey is performed sufficiently far downstream of the obstacle [111]. Hence it suggests that the streamwise pressure gradient can be neglected. Moreover, in high Re flows it is common to neglect the viscous effects in the far wake [28, 81] and the velocity gradients progressively vanish downstream. In those conditions, and according to (E.11),

$$\nabla \cdot \boldsymbol{q} = o(1) \tag{E.12}$$

and the flow in the far wake can effectively be assumed incompressible. This is consistent with Bradshaw's statement [115]: *"The most important feature of free shear layers, with the exception of the mixing layer or "half-jet," is that typical velocity and temperature differences decrease rapidly with streamwise distance, so that, for instance, an axisymmetric jet or wake becomes effectively incompressible a few tens of nozzle or body diameters downstream, unless the initial Mach number is extremely large"*. As a consequence, the results for the asymptotic behaviour of the velocity perturbation in planar and circular wakes presented above may be applied.

The asymptotic behaviour of $\boldsymbol{F}_{\nabla\rho}$ may now be investigated. In the far wake the local density is equal to its freestream value plus a small perturbation $\rho = \rho_\infty + \Delta\rho$ with $\Delta\rho = \mathcal{O}(x^{-\epsilon})$ and $\epsilon > 0$. Starting over from the definition of $\boldsymbol{F}_{\nabla\rho}$ in (E.1), and neglecting the x-derivatives, it is possible to write

$$\boldsymbol{F}_{\nabla\rho} = \frac{1}{\mathcal{N} - 1} \int_W \left(U_\infty u + \frac{u^2 + v^2 + w^2}{2} \right) \begin{pmatrix} y\,(\partial\rho/\partial y) + z\,(\partial\rho/\partial z) \\ -x\,(\partial\rho/\partial y) \\ -x\,(\partial\rho/\partial z) \end{pmatrix} \mathrm{d}S \tag{E.13}$$

Hence $\boldsymbol{F}_{\nabla\rho}$ is of the order of

$$\boldsymbol{F}_{\nabla\rho} = \frac{1}{\mathcal{N} - 1} \int_W \begin{pmatrix} \mathcal{O}\left(x^{-(\epsilon+\eta)}\right) \\ \mathcal{O}\left(x^{-\epsilon}\right) \\ \mathcal{O}\left(x^{-\epsilon}\right) \end{pmatrix} \mathrm{d}S \tag{E.14}$$

$$\text{with} \quad \eta = \begin{cases} \frac{1}{2} & \text{planar wake} \\ \frac{2}{3} & \text{circular wake} \end{cases}$$

Then, having that $\mathrm{d}S \propto x^\eta$ in the wake, $\boldsymbol{F}_{\nabla\rho}$ asymptotically behaves as

$$\boldsymbol{F}_{\nabla\rho} = \begin{pmatrix} \mathcal{O}\left(x^{-\epsilon}\right) \\ \mathcal{O}\left(x^{-\epsilon+\eta}\right) \\ \mathcal{O}\left(x^{-\epsilon+\eta}\right) \end{pmatrix} \tag{E.15}$$

Finally, due to the symmetrical character of u with respect to the planes $y = 0$ and $z = 0$ in the far wake (see relation (2.3.4)), the antisymmetrical character of $\partial\rho/\partial y$ with respect to the plane $y = 0$ (see relation (B.5b)), and the antisymmetrical character of $\partial\rho/\partial z$ with respect to the plane $z = 0$ in the far wake (see relation (B.6c)), the transverse and lift components disappear and $\boldsymbol{F}_{\nabla\rho}$ is theoretically expected to vanish when S_e retreats to infinity, in the case of a planar or a circular wake sufficiently far downstream of the obstacle:

$$\lim_{S_e \to \infty} \boldsymbol{F}_{\nabla\rho} = \boldsymbol{0} \tag{E.16}$$

F Presentation of the test cases

F.1 NACA0012 airfoil

Grids

The NACA0012 airfoil is a symmetrical airfoil for which the maximum thickness is 12% of the chord. In this study, three grid levels were tested in viscous and inviscid flows (see Figs.F.1 and F.2).

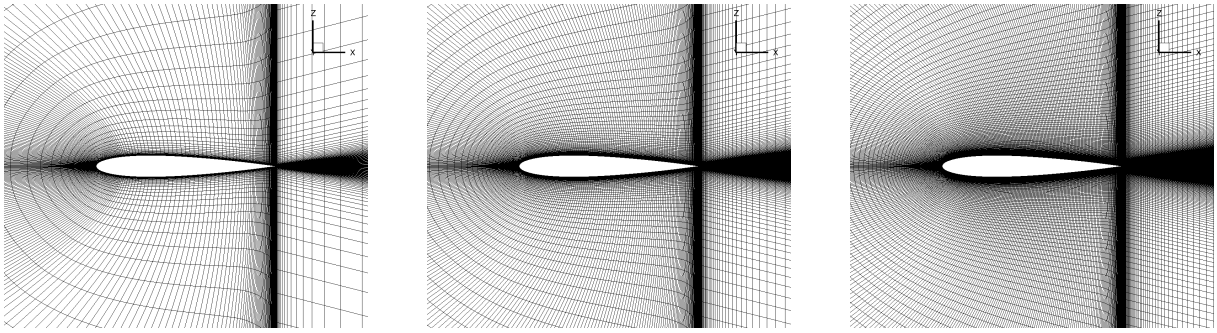

(a) Coarse grid (b) Intermediate grid (c) Fine grid

Figure F.1: Three grid levels of the NACA0012 airfoil for the analysis of RANS simulations

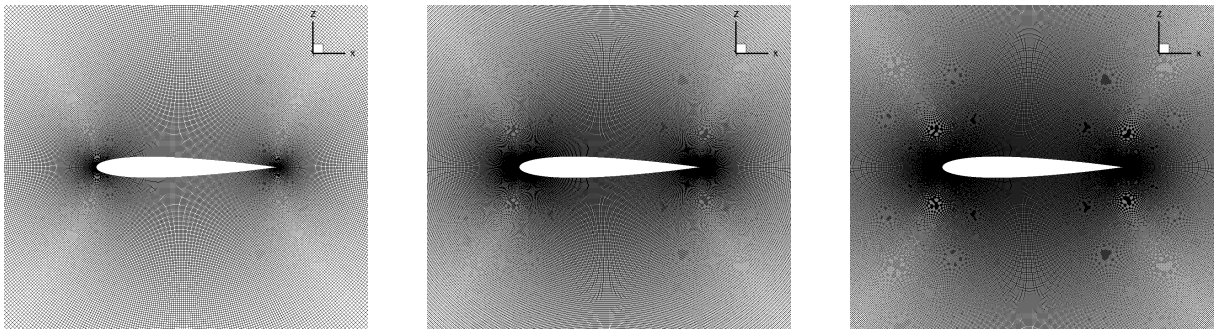

(a) Coarse grid (b) Intermediate grid (c) Fine grid

Figure F.2: Three grid levels of the NACA0012 airfoil for the analysis of Euler simulations

The grids used for the analysis of RANS simulations are indeed more refined in the boundary layer regions than those used for the analysis of Euler flows. Those grids are divided in two blocks: a C block containing the airfoil and the upstream region and an H block containing the wake. The coarse grid contains $301 \times 113 + 61 \times 225 = 47,738$ points, the intermediate grid contains $361 \times 217 + 141 \times 433 = 139,390$ points and the fine grid contains $417 \times 385 + 193 \times 769 = 308,962$ points. For the three grid levels, the $y+$ is always lower than 0.5 in order to accurately compute the gradients and hence the Lamb vector in the boundary layer, and the far field lies $50,000$ chords away from the airfoil surface.

Regarding the analysis of Euler flows, the grids are divided into 32 blocks of equal size. These grids are O-type grids. The coarse grid contains $65 \times 129 \times 32 = 268,320$ points, the intermediate grid contains $129 \times 129 \times 32 = 532,512$ points and the fine grid contains $129 \times 257 \times 32 = 1,060,896$ points. For the three grid levels, the far field lies 150 chords away from the airfoil surface.

Convergence

All the simulations on the NACA0012 airfoil were performed using Spalart-Allmaras turbulence model [116] (for the RANS simulations) and Jameson's numerical scheme [117] (cell-centered, 2nd and 4th order artificial viscosities) in the AIRBUS-SAFRAN-ONERA elsA solver [118]. The convergence is checked by looking at the lift and drag components computed by the elsA solver at each iteration and the evolution of the L_2-norm of the residuals (see Figs.F.3 and F.4). On Fig.F.3a, it is shown that the lift and drag computed by the elsA solver converge fast

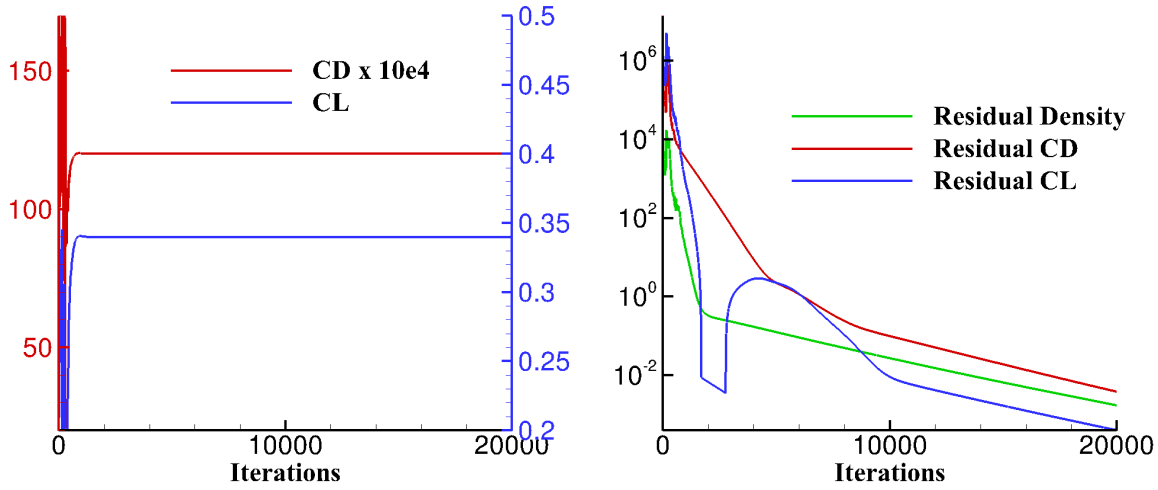

(a) Lift and drag convergence

(b) Residuals

Figure F.3: Convergence on the fine grid of the NACA0012 airfoil for the analysis of RANS simulations, $M_\infty = 0.72$, $Re = 3 \times 10^6$, $\alpha = 2°$

to their final value and remain constant until the end. On Fig.F.3b, one can notice that the L_2-norm of the density residual decreases by eight orders of magnitude between the first and the last iteration while the lift and drag residuals decrease by nine orders of magnitude, therefore guaranteeing a clean convergence of the computation. A visualization of the contours of the Mach number is displayed in Fig.F.5a. The flow around the NACA0012 airfoil is transonic and characterized by the presence of a shock wave on the suction side. Just downstream of the shock, the flow is subsonic which suggests that the shock is almost straight although its curvature is clearly visible at the edges. The presence of the shock also increases the boundary layer thickness downstream due to the adverse pressure gradient.

The same flight conditions were tested in the case of an Euler (inviscid) flow. Once again, the convergence of the lift and drag components calculated by the elsA solver is very fast (see Fig.F.4a). This time, the residuals decrease by more than twelve orders of magnitude which ensures a very clean convergence of the simulation (see Fig.F.4b). The same visualization of the contours of the Mach number is displayed in Fig.F.5b. In this case there is no boundary layer because the flow is inviscid. It can be seen that the shock wave is located further on the suction side than in the RANS simulation. Moreover, the strength of the shock seems greater since the Mach number just upstream of the shock is higher than in the RANS computation. The wave drag generated by the shock is then higher in the Euler case ($C_{D_w} \sim 40 \times 10^{-4}$) than in the RANS case ($C_{D_w} \sim 17 \times 10^{-4}$).

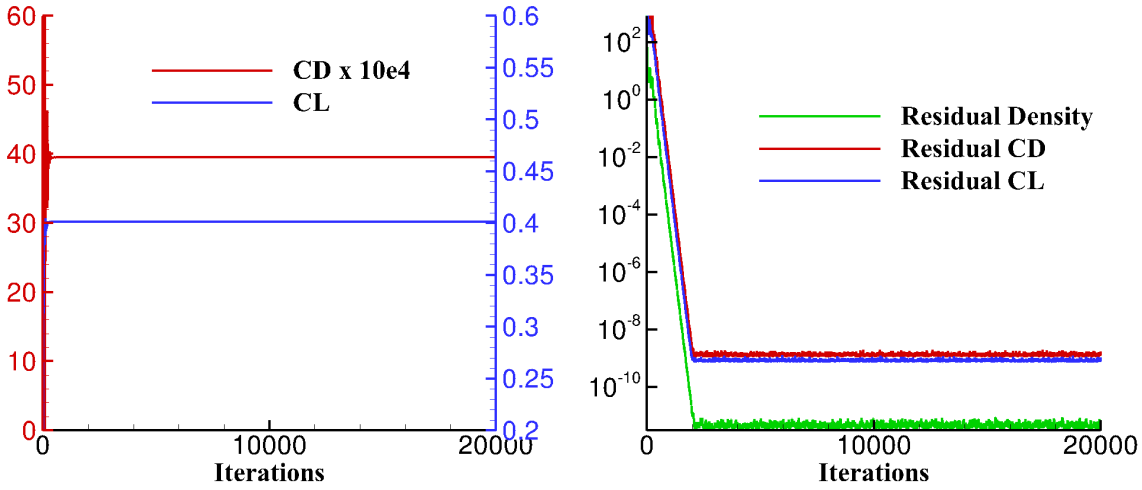

(a) Lift and drag convergence

(b) Residuals

Figure F.4: Convergence on the fine grid of the NACA0012 airfoil for the analysis of Euler simulations, $M_\infty = 0.72$, $Re \to \infty$, $\alpha = 2°$

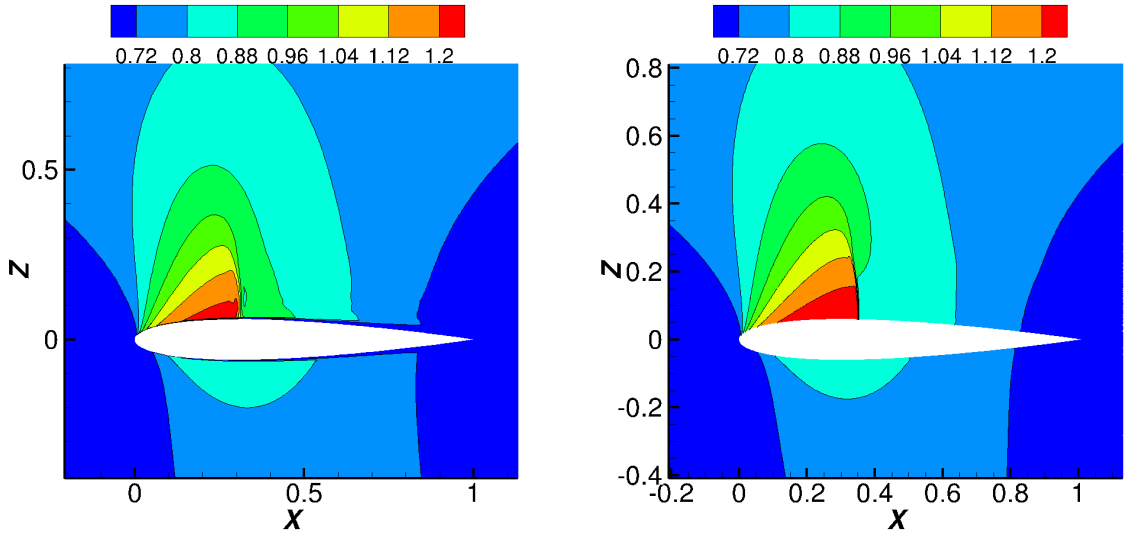

(a) $Re = 3 \times 10^6$

(b) $Re \to \infty$

Figure F.5: Contour of Mach number on the fine meshes of the NACA0012 airfoil, $M_\infty = 0.72$, $\alpha = 2°$

Grid studies

Table F.1 presents the computed lift and drag contributions on the three grid levels used in the study of RANS simulations. It can be seen that the grid refinement has much more impact on the Lamb-vector-based drag decompositions (ONERA and Mele *et al.*'s formulations [36]) than on the thermodynamic formulation of Destarac and Van der Vooren [21]. In fact, the use of Lamb-vector-based formulae implies the computation of the vorticity which can be inaccurate with coarse grids. Regarding the lift, for a given grid level the predictions are always in very good agreement. Moreover, the lift coefficient increases with the refinement. In conclusion, the results computed on the fine grid and the intermediate grid are very close to each other which suggests that the intermediate grid is fine enough to be used in the context of lift and drag analysis using

the Lamb vector.

Grid level	Coarse	Intermediate	Fine
		$C_{D_P} \times 10^4$	
ONERA invariant	126.54	122.83	122.12
Kutta-Joukowski-Maskell-Betz	123.27	121.97	121.82
Mele *et al.* invariant	125.67	122.83	122.51
Destarac and Van der Vooren [21]	120.46	120.03	120.06
		$C_D \times 10^4$	
ONERA invariant	123.26	119.48	119.93
Kutta-Joukowski-Maskell-Betz	121.62	120.21	120.04
Mele *et al.* invariant	123.26	119.48	119.93
Destarac and Van der Vooren [21]	120.46	120.03	120.06
Near-field	120.77	120.17	120.07
		C_L	
ONERA invariant	0.33454	0.33925	0.34054
Kutta-Joukowski-Maskell-Betz	0.33422	0.33895	0.34023
Mele *et al.* invariant	0.33464	0.33935	0.34057
Near-field	0.33385	0.33855	0.33983

Table F.1: Effect of the NACA0012 airfoil grid sizing on the force prediction and breakdown, $M_\infty = 0.72$, $Re = 3 \times 10^6$, $\alpha = 2°$, $d/c = 10$.

Grid level	Coarse	Intermediate	Fine
		$C_{D_w} \times 10^4$	
ONERA	39.07	37.23	37.28
Kutta-Joukowski-Maskell-Betz	40.61	40.23	39.77
Mele	39.19	37.35	37.40
Destarac and Van der Vooren [21]	38.58	38.37	38.54
		$C_D \times 10^4$	
Kutta-Joukowski-Maskell-Betz	39.96	39.81	39.54
Destarac and Van der Vooren [21]	38.58	38.37	38.54
Near-field	40.03	39.80	39.49
		C_L	
Kutta-Joukowski-Maskell-Betz	0.40084	0.40001	0.40166
Near-field	0.40105	0.40010	0.40107

Table F.2: Effect of the NACA0012 airfoil grid sizing on the force prediction and breakdown, $M_\infty = 0.72$, $Re \to \infty$, $\alpha = 2°$, $d/c = 10$ for C_D and C_L, $d/c = 1$ for C_{D_w}.

In the Euler case, the total drag is equal to the wave drag generated by the shock. As shown in Table F.2, the effect of the grid sizing on the Euler grid of the NACA0012 airfoil is weak due to the fact that all grids are fine. Again, the grid sizing has more impact on the Lamb-vector-based drag predictions for the same reasons as before. The results in total lift and drag computed by the ONERA and Mele *et al.*'s formulations [36] are not shown here because they cannot be used as such for the analysis of Euler flows. Indeed, it is necessary to add a vortex sheet at the airfoil skin to generate the lift since no vorticity is produced in inviscid flows [18]. Only the KJMB formulation is directly applicable to Euler conditions: the computed results are very satisfactory and are weakly sensitive to the grid refinement.

F.2 OAT15A airfoil

Grids

The OAT15A airfoil is a supercritical airfoil designed at ONERA and was used in numerous studies on the buffet onset in transonic flows [119, 120, 121, 122]. In this study, only RANS computations were performed on this airfoil and three grids were used, all having a C-block and an H-block as in the case of the NACA0012 airfoil (see Fig.F.6). The coarse grid contains $97\times289+61\times213 = 41,026$ points, the intermediate grid contains $385\times193+97\times425 = 115,530$ points and the fine grid contains $385 \times 385 + 193 \times 849 = 312,082$ points. For the three grid levels, the $y+$ is always lower than 0.5 and the far field lies 50,000 chords away from the airfoil surface.

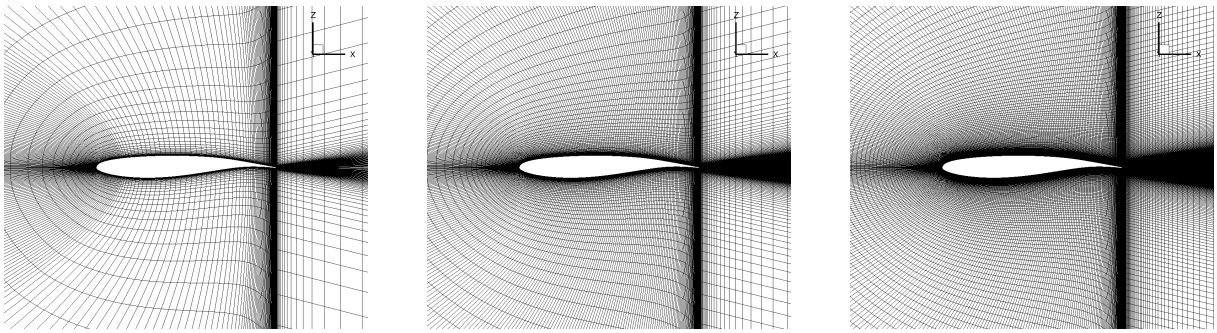

(a) Coarse grid (b) Intermediate grid (c) Fine grid

Figure F.6: Three grid levels of the OAT15A airfoil for the analysis of RANS simulations

Convergence

As for the NACA0012 airfoil, the simulations were performed using Spalart-Allmaras turbulence model and Jameson's numerical scheme. The convergence of a typical transonic flow is presented in Fig.F.7. Once again, the convergence of the lift and drag components is very fast

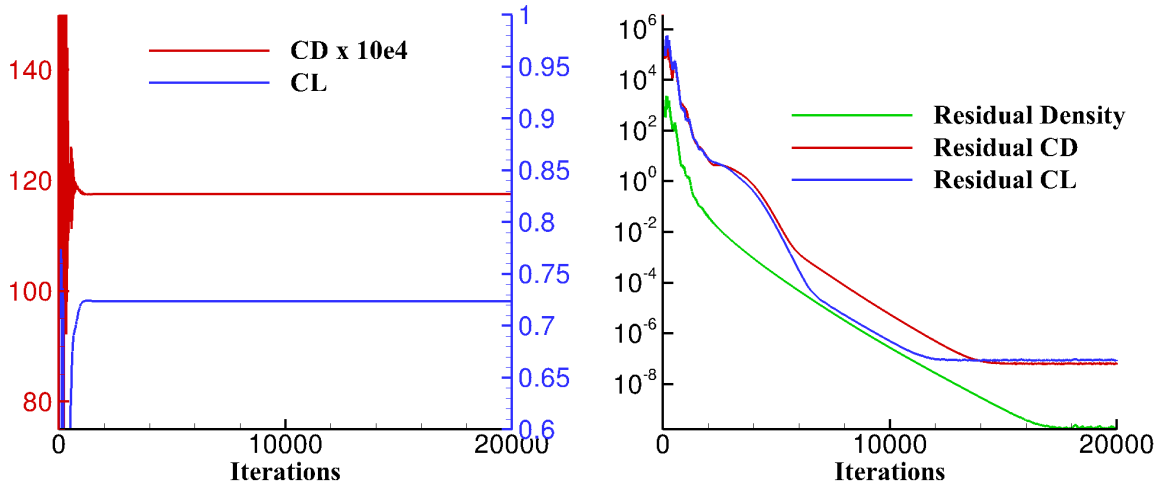

(a) Lift and drag convergence (b) Residuals

Figure F.7: Convergence on the fine grid of the OAT15A airfoil for the analysis of RANS simulations, $M_\infty = 0.724$, $Re = 3 \times 10^6$, $\alpha = 1.15°$

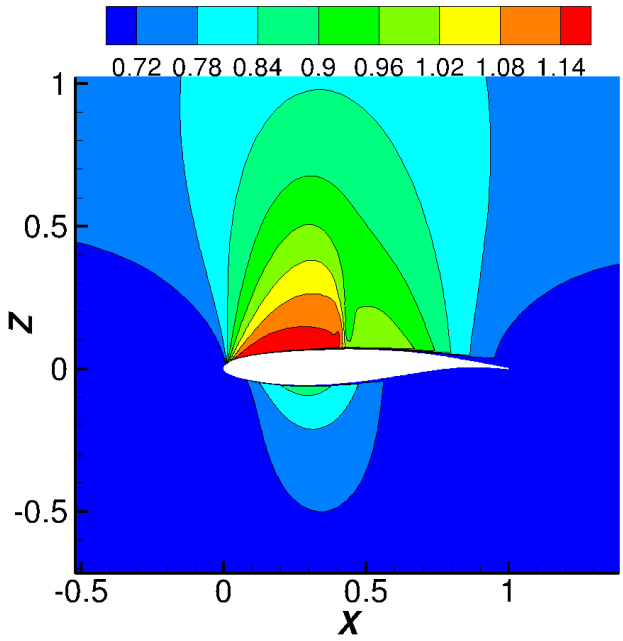

Figure F.8: Contour of Mach number on the fine mesh of the OAT15A airfoil, $M_\infty = 0.724$, $Re = 3 \times 10^6$, $\alpha = 1.15°$

and this time the convergence is even better since the residuals decrease by fourteen orders of magnitude between the first and the last iteration.

As shown in Fig.F.8, the flow around the airfoil produces a much weaker shock than in the case of the NACA0012 airfoil. In fact, a supercritical airfoil enables to reduce the strength of the transonic shock while producing enough lift to sustain the aircraft into air.

Grid studies

A grid convergence study was held on the three grid levels (see Table F.3). The coarsening of the grid has the same effects on the Lamb-vector-based formulations as before: the coarser the grid, the less accurate the drag prediction. The intermediate grid still yields a two-drag-count discrepancy between the Lamb-vector-based formulations and the near-field computation. Moreover the lift coefficient is more impacted by the grid refinement in this case than in the case of the NACA0012 airfoil. Therefore it is better to use the fine grid for the analysis of lift and drag using the Lamb vector.

In conclusion, regarding the two-dimensional cases, the recommendation is to use fine grids when one wants to assess the aerodynamic force with vorticity-based formulations. If one uses less refined grids, it is then recommended to use the thermodynamic formulation of Destarac and Van der Vooren [21] which is less sensitive to the grid refinement although it is unable to provide a far-field evaluation of the lift.

F.3 ONERA M6 wing

Grids

The M6 wing was designed at ONERA and tested in wind-tunnel experiments at low and high transonic Mach numbers in order to emphasize a lambda pattern drawn by the shock wave on the suction side [123]. In this study, two multiblock grids were used: a coarse grid of $3,800,000$ points and a fine grid of $10,200,000$ points (see Fig.F.9). Theses meshes were used by Mayeur *et al.* [124] in CFD computations in the elsA solver in order to compare their results to those

Grid level	Coarse	Intermediate	Fine
		$C_{D_P} \times 10^4$	
ONERA invariant	126.00	120.78	119.50
Kutta-Joukowski-Maskell-Betz	123.06	119.49	119.22
Mele *et al.* invariant	124.02	120.85	119.79
Destarac and Van der Vooren [21]	116.71	117.42	117.50
		$C_D \times 10^4$	
ONERA invariant	124.98	119.45	117.28
Kutta-Joukowski-Maskell-Betz	121.79	117.81	117.55
Mele *et al.* invariant	124.98	119.45	117.28
Destarac and Van der Vooren [21]	116.71	117.42	117.50
Near-field	119.68	117.79	117.55
		C_L	
ONERA invariant	0.71089	0.72017	0.72368
Kutta-Joukowski-Maskell-Betz	0.71341	0.72152	0.72382
Mele *et al.* invariant	0.71104	0.72046	0.72380
Near-field	0.71330	0.72137	0.72366

Table F.3: Effect of the OAT15A airfoil grid sizing on the force prediction and breakdown, $M_\infty = 0.724$, $Re = 3 \times 10^6$, $\alpha = 1.15°$, $d/c = 10$.

coming from wind-tunnel experiments. In both grids, the $y+$ is always close or below one and the far field lies 185 reference-chord lengths ($c_{ref} = 0.64607$ m) away from the wing surface.

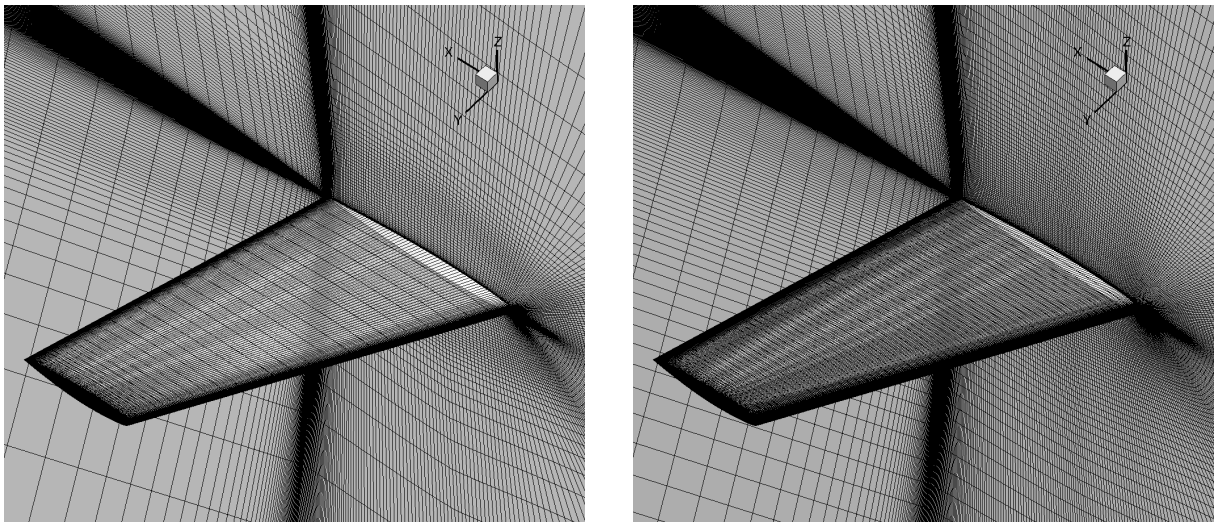

(a) Coarse grid (b) Fine grid

Figure F.9: Two grid levels of the ONERA M6 wing for the analysis of RANS simulations

Convergence

All the simulations on the M6 wing were performed using Spalart-Allmaras turbulence model and Roe's numerical scheme [125]. The convergence of the lift and drag components computed by the elsA solver is shown in Fig.F.10: both converge after less than $1,500$ iterations. The evolution of the L_2-norm of the residuals shows that they decrease by six to seven orders of magnitude between the first and the last iteration on the fine grid.

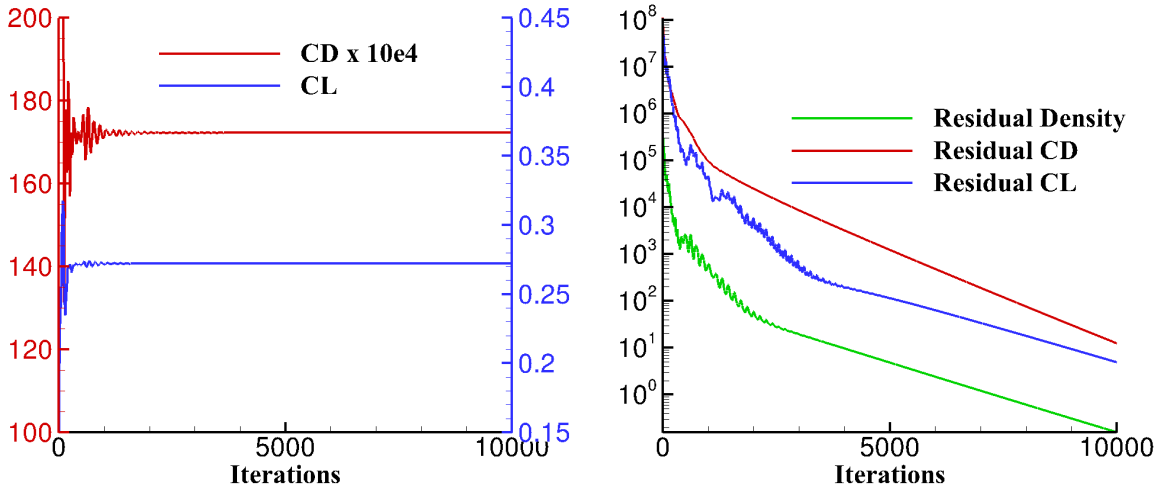

(a) Lift and drag convergence

(b) Residuals

Figure F.10: Convergence on the fine grid of the ONERA M6 wing for the analysis of RANS simulations, $M_\infty = 0.84$, $Re = 12 \times 10^6$, $\alpha = 3.06°$

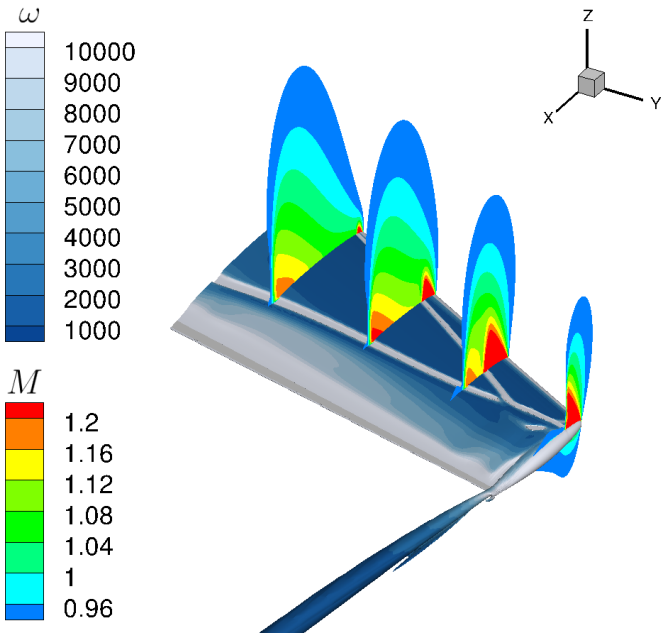

Figure F.11: Contour of Mach number and isosurface of Q-criterion coloured by the vorticity modulus ω on the fine mesh of the ONERA M6 wing, $M_\infty = 0.84$, $Re = 12 \times 10^6$, $\alpha = 3.06°$

Fig.F.11 displays the Mach number on several wing sections along the span and an isosurface of Q-criterion coloured by the modulus of the vorticity. The Q-criterion is used to identify the vortical regions, i.e. the regions where vortices are present. Therefore, the Q-criterion is high in regions where the rotation is dominant. On the contrary, the Q-criterion is weak in regions of pure deformation. Here, the wing-tip vortex is materialized by the Q-criterion isosurface and the vorticity decreases as the vortex extends in the wake. On the suction side, the feet of the shocks are characterized by a region of strong deformation where the Q-criterion is zero (grey lines): it can be seen that the shocks form a lambda pattern on the suction side, which implies that the fluid particles will go through two succesive shock waves as seen on the Mach contours.

Grid studies

The grid convergence study on the M6 wing is summarized in Table F.4. The results provided by the formulation of Destarac and Van der Vooren [21] suggest that the grid refinement has a greater impact on the lift-induced drag prediction: it increases by more than one drag count between the two grids while the profile drag decreases by 0.7 drag count, the total drag increasing itself by 0.64 drag count. Besides, it is clear that the near-field evaluation of the drag is much more impacted by the refinement since it decreases by three drag counts between the two grids. Once again, the Lamb-vector-based formulations are more sensitive to the refinement and the total drag increases by more than four drag counts.

Grid level	Coarse	Fine
	$C_{D_i} \times 10^4$	
ONERA invariant	50.85	52.33
Kutta-Joukowski-Maskell-Betz	55.33	54.72
Mele *et al.* invariant	47.46	51.17
Destarac and Van der Vooren [21]	60.48	61.82
	$C_{D_P} \times 10^4$	
ONERA invariant	115.18	118.50
Kutta-Joukowski-Maskell-Betz	119.17	117.38
Mele *et al.* invariant	118.57	119.66
Destarac and Van der Vooren [21]	109.87	109.17
	$C_D \times 10^4$	
ONERA invariant	166.03	170.83
Kutta-Joukowski-Maskell-Betz	174.50	172.10
Mele *et al.* invariant	166.03	170.83
Destarac and Van der Vooren [21]	170.35	170.99
Near-field	175.17	172.23
	C_L	
ONERA invariant	0.26806	0.27090
Kutta-Joukowski-Maskell-Betz	0.26781	0.27076
Mele *et al.* invariant	0.27013	0.27298
Near-field	0.26966	0.27209

Table F.4: Effect of the ONERA M6 wing grid sizing on the force prediction and breakdown, $M_\infty = 0.84$, $Re = 12 \times 10^6$, $\alpha = 3.06°$, $d/c_{ref} = 1$.

In this three-dimensional case, the lift coefficient is well predicted with both grids although the agreement between the various approaches is better when using the fine grid. The lift seems to be less sensitive to the grid refinement than the drag. Anyways, in this case, the use of a fine mesh is recommended if one chooses to evaluate the aerodynamic force with a formulation based on the Lamb vector, especially due to the discrepancies occuring on the drag component and its decomposition with the coarse mesh.

F.4 NASA Common Research Model

Grids

In order to show the maturity and applicability of the Lamb-vector-based force decomposition to industrial aircraft configurations, a RANS computation on the NASA Common Research Model (CRM) was performed. The simulation was carried out using Spalart-Allamaras turbulence model and Jameson's numerical scheme. The Mach number was set to $M_\infty = 0.85$, the

Reynolds number to $Re = 5 \times 10^6$ and the lift coefficient to $C_L \approx 0.5$ in order to match the transonic cruise flight conditions encountered by a high-capacity transport aircraft.

The four grids used in this study are the same as those used by Hue [72] in the fifth Drag Prediction Workshop (DPW): they correspond to the L2′, L3′, L4′ and L5′ grids introduced in Ref.[72]. Those meshes are all multiblock meshes and they differ from the L2, L3, L4 and L5 versions introduced by Vassberg [126] only by the added wing twist used to better match wind-tunnel experiments. The L2′ has a $y+ = 1.33$, the L3′ has a $y+ = 1$, the L4′ has a $y+ = 0.67$, the L5′ has a $y+ = 0.5$ and the far field always lies more than a hundred reference-chord lengths ($c_{ref} = 7.00532$ m) away from the aircraft surface. In this study, the grid used for the analysis of lift and drag prediction and breakdown is the L4′ refinement since it is already fine enough according to Hue's results [72].

Convergence

The convergence on the L4′ grid of the NASA CRM is shown in Fig.F.12. The computation required a much greater amount of iterations in order to guarantee a very clean convergence even if the lift and drag components computed by the elsA solver converge quite fast, after only $1,500$ iterations. In fact, the residuals decrease by thirteen orders of magnitude after $105,000$ iterations and remain constant afterwards.

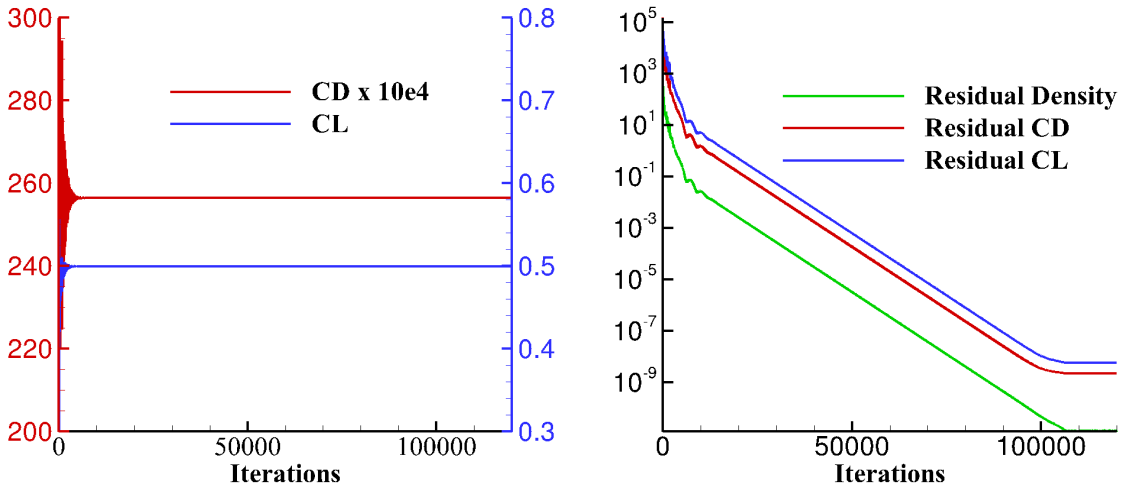

(a) Lift and drag convergence

(b) Residuals

Figure F.12: Convergence on the L4′ grid of the NASA CRM for the analysis of RANS simulations, $M_\infty = 0.85$, $Re = 5 \times 10^6$, $C_L \approx 0.5$

A visualization of the Mach number on the suction side of the wings and a Q-criterion isosurface coloured by the vorticity modulus are displayed in Fig.F.13. In this case, the wing is swept in the streamwise direction which enables to reduce the strength of the shock wave: the component of the Mach number normal to the leading edge is lower than the effective Mach number and the entropy jump is weaker. Moreover, the wing section is a supercritical airfoil which further reduces the strength of the shock wave: the maximum Mach number is around 1.08 whereas it was 1.3 in the case of the NACA0012 airfoil. The Q-criterion isosurface emphasizes three counter-rotating vortex pairs: the wing-tip vortices and two others generated by the tail of the aircraft. In the near wake, the wing-tip vortices progressively acquire their cylindrical shape as the vortex sheet rolls up. Regarding the two other vortex pairs, they may not show up in the presence of the horizontal tail plane and the vertical stabilizer.

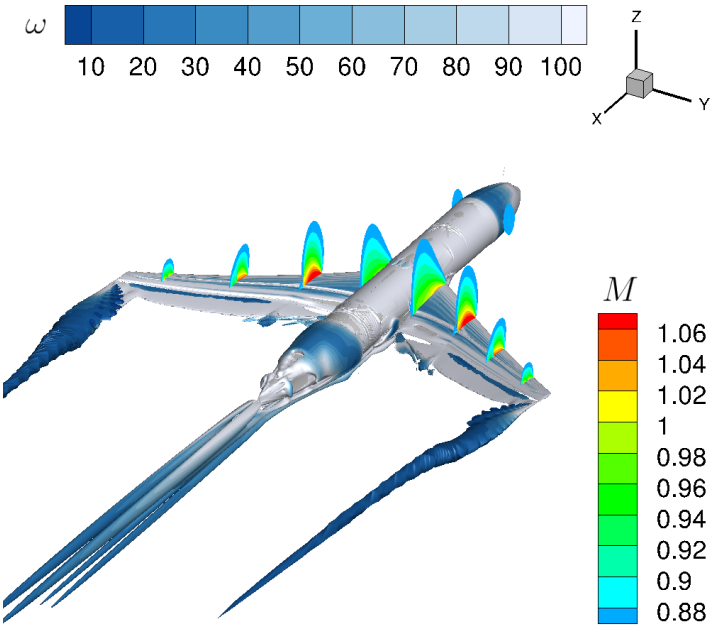

Figure F.13: Contour of Mach number and isosurface of Q-criterion coloured by the vorticity modulus ω on the L4′ grid of the NASA CRM, $M_\infty = 0.85$, $Re = 5 \times 10^6$, $C_L \approx 0.5$

Grid studies

The effect of the grid sizing on the NASA CRM is presented in Table F.5. It can be seen that the grid refinement has opposite effects on the lift-induced drag whether it is calculated by Lamb-vector-based approaches or the thermodynamic method of Destarac and Van der Vooren [21]: indeed, the ONERA and Mele *et al.*'s formulations [36] see their lift-induced drag component increase whereas Destarac and Van der Vooren's formulation sees its lift-induced drag component decrease. Reversely, the profile drag component computed by the ONERA, the KJMB and Mele *et al.*'s formulations decreases. Actually, the grid refinement allows for a better resolution of the vortices which explains why the lift-induced drag computed by Lamb-vector-based formulae increases. Yet, the ONERA and the KJMB formulations provide a drag decomposition in better agreement with the thermodynamic approach than Mele *et al.*'s formulation. Finally, the results obtained with the L4′ and L5′ grids suggest that the L4′ version is already a well refined grid and is fine enough for fine drag decomposition analyses.

Besides, it can be seen that the predicted lift increases with the grid refinement for the same reason as the lift-induced drag. The lift predicted by the ONERA formulation seems to be less accurate than that computed by Mele *et al.*'s formulation. Yet, the KJMB formulation (mathematically equivalent to the ONERA formulation) provides a better lift prediction when compared to the classical near-field approach. Finally, the results obtained with the L4′ and L5′ grids again suggest that the L4′ version is enough for a fine lift analysis.

Grid level	L2′	L3′	L4′	L5′
		$C_{D_i} \times 10^4$		
ONERA invariant	84.94	84.57	86.29	86.72
Kutta-Joukowski-Maskell-Betz	87.81	88.34	87.26	87.69
Mele *et al.* invariant	73.79	75.19	77.01	77.45
Destarac and Van der Vooren [21]	93.54	93.24	92.81	92.75
		$C_{D_P} \times 10^4$		
ONERA invariant	169.23	165.50	169.11	168.40
Kutta-Joukowski-Maskell-Betz	171.61	168.56	167.63	166.69
Mele *et al.* invariant	180.37	174.88	178.39	177.68
Destarac and Van der Vooren [21]	163.30	162.41	161.70	161.55
		$C_D \times 10^4$		
ONERA invariant	254.16	250.07	255.40	255.13
Kutta-Joukowski-Maskell-Betz	259.43	256.90	254.89	254.38
Mele *et al.* invariant	254.16	250.07	255.40	255.13
Destarac and Van der Vooren [21]	256.84	255.65	254.51	254.30
Near-field	258.38	256.34	254.70	254.35
		C_L		
ONERA invariant	0.48583	0.48933	0.49198	0.49446
Kutta-Joukowski-Maskell-Betz	0.49697	0.49741	0.49698	0.49768
Mele *et al.* invariant	0.49280	0.49610	0.49852	0.50088
Near-field	0.49967	0.49990	0.49946	0.49963

Table F.5: Effect of the NASA CRM grid sizing on the force prediction and breakdown, $M_\infty = 0.85$, $Re = 5 \times 10^6$, $C_L \approx 0.5$, $d/c_{ref} = 1$.

List of Figures

List of Tables

Bibliography

[1] I. Kroo, "Drag due to lift: Concepts for prediction and reduction," *Annual Review of Fluid Mechanics*, vol. 33, no. 1, pp. 587–617, 2001.

[2] B. Mele, L. Russo, and R. Tognaccini, "Drag bookkeeping on an aircraft with riblets and NLF control," *Aerospace Science and Technology*, vol. 98, p. 105714, 2020.

[3] Y. Fan and W. Li, "Review of far-field drag decomposition methods for aircraft design," *Journal of Aircraft*, vol. 56, no. 1, pp. 11–21, 2019.

[4] M. Ueno, K. Yamamoto, K. Tanaka, M. Murayama, and R. Tognaccini, "Far-field drag analysis of NASA Common Research Model simulation," *Journal of Aircraft*, vol. 50, no. 2, pp. 388–397, 2013.

[5] W. M. Kutta, "Auftriebskräfte in strömenden flüssigkeiten," *Illustrierte Aeronautische Mitteilungen*, vol. 6, no. 133, pp. 133–135, 1902.

[6] N. Joukowski, "On annexed vortices," *Proc. Phys. Section of the Natural Science Society*, vol. 13, no. 2, pp. 12–25, 1906.

[7] L. Prandtl, "Theory of lifting surfaces," Tech. Rep. NACA TN10, National Advisory Committee for Aeronautics, 1919.

[8] A. Betz, "A method for the direct determination of wing-section drag," Tech. Rep. NACA TM37, National Advisory Committee for Aeronautics, 1925.

[9] E. Maskell, "Progress towards a method for the measurement of the components of the drag of a wing of finite span," Tech. Rep. 72232, Procurement Executive, Ministry of Defence, Royal Aircraft Establishment, 1972.

[10] K. Nikfetrat, C. Van Dam, P. Vijgen, and I. Chang, "Prediction of drag at subsonic and transonic speeds using Euler methods," in *30th Aerospace Sciences Meeting and Exhibit*, p. 169, 1992.

[11] R. M. Cummings, M. B. Giles, and G. Shrinivas, "Analysis of the elements of drag in three-dimensional viscous and inviscid flows," in *14th Applied Aerodynamics Conference*, p. 2482, 1996.

[12] K. Kusunose, "Drag prediction based on a wake-integral method," in *16th AIAA Applied Aerodynamics Conference*, p. 2723, 1998.

[13] D. L. Hunt, R. M. Cummings, and M. B. Giles, "Wake integration for three-dimensional flowfield computations: applications," *Journal of Aircraft*, vol. 36, no. 2, pp. 366–373, 1999.

[14] C. P. Van Dam, "Recent experience with different methods of drag prediction," *Progress in Aerospace Sciences*, vol. 35, no. 8, pp. 751–798, 1999.

[15] M. B. Giles and R. M. Cummings, "Wake integration for three-dimensional flowfield computations: theoretical development," *Journal of Aircraft*, vol. 36, no. 2, pp. 357–365, 1999.

[16] D. Chao and C. Van Dam, "Wing drag prediction and decomposition," *Journal of Aircraft*, vol. 43, no. 1, pp. 82–90, 2006.

[17] K. Kusunose and J. P. Crowder, "Extension of wake-survey analysis method to cover compressible flows," *Journal of Aircraft*, vol. 39, no. 6, pp. 954–963, 2002.

[18] L. L. Kang, L. Russo, R. Tognaccini, J. Z. Wu, and W. D. Su, "Aerodynamic force breakdown in reversible and irreversible components by vortex force theory," *AIAA Journal*, vol. 57, no. 11, pp. 4623–4638, 2019.

[19] J. Van Der Vooren and J. Slooff, "CFD-based drag prediction: state-of-the-art, theory, prospects," *National Aerospace Lab., NLR, TP 90247 U*, 1992.

[20] D. Destarac, "Far-field/near-field drag balance and applications of drag extraction in CFD," *VKI Lecture Series*, vol. 2, pp. 3–7, 2003.

[21] D. Destarac and J. Van Der Vooren, "Drag/thrust analysis of jet-propelled transonic transport aircraft; definition of physical drag components," *Aerospace Science and Technology*, vol. 8, no. 6, pp. 545–556, 2004.

[22] F. Noca, D. Shiels, and D. Jeon, "Measuring instantaneous fluid dynamic forces on bodies, using only velocity fields and their derivatives," *Journal of Fluids and Structures*, vol. 11, no. 3, pp. 345–350, 1997.

[23] F. Noca, *On the evaluation of time-dependent fluid-dynamic forces on bluff bodies*. PhD thesis, California Institute of Technology, 1997.

[24] F. Noca, D. Shiels, and D. Jeon, "A comparison of methods for evaluating time-dependent fluid dynamic forces on bodies, using only velocity fields and their derivatives," *Journal of Fluids and Structures*, vol. 13, no. 5, pp. 551–578, 1999.

[25] G. Zhu, P. W. Bearman, and J. M. R. Graham, "Prediction of drag and lift using velocity and vorticity fields," *The Aeronautical Journal*, vol. 106, no. 1064, pp. 547–554, 2002.

[26] J. Z. Wu, Z. L. Pan, and X. Y. Lu, "Unsteady fluid-dynamic force solely in terms of control-surface integral," *Physics of Fluids*, vol. 17, no. 9, p. 098102, 2005.

[27] G. Zhu, P. W. Bearman, and J. M. R. Graham, "Prediction of drag and lift of wings from velocity and vorticity fields," *The Aeronautical Journal*, vol. 111, no. 1125, pp. 699–704, 2007.

[28] Y. T. Yang, R. K. Zhang, Y. R. An, and J. Z. Wu, "Steady vortex force theory and slender-wing flow diagnosis," *Acta Mechanica Sinica*, vol. 23, no. 6, pp. 609–619, 2007.

[29] J. Z. Wu, X. Y. Lu, and L. X. Zhuang, "Integral force acting on a body due to local flow structures," *Journal of Fluid Mechanics*, vol. 576, pp. 265–286, 2007.

[30] H. Lamb, "On the conditions for steady motion of a fluid," *Proceedings of the London Mathematical Society*, vol. 1, no. 1, pp. 91–93, 1877.

[31] B. Mele and R. Tognaccini, "Aerodynamic force by Lamb vector integrals in compressible flow," *Physics of Fluids*, vol. 26, no. 5, p. 056104, 2014.

[32] B. Mele, M. Ostieri, and R. Tognaccini, "Vorticity based breakdown of the aerodynamic force in three-dimensional compressible flows," *AIAA Journal*, vol. 54, no. 4, pp. 1198–1208, 2016.

[33] P. Curie, "Sur la symétrie dans les phénomènes physiques, symétrie d'un champ électrique et d'un champ magnétique," *Journal de Physique Théorique et Appliquée*, vol. 3, no. 1, pp. 393–415, 1894.

[34] C. Fournis, D. Bailly, and R. Tognaccini, "A reference point invariant Lamb vector based aerodynamic force breakdown in steady compressible flows," in *AIAA Scitech 2020 Forum*, 2020.

[35] C. Fournis, D. Bailly, and R. Tognaccini, "Definition of an invariant Lamb-vector-based aerodynamic force breakdown using far-field flow symmetries," *AIAA Journal*, vol. 59, no. 1, pp. 34–48, 2021.

[36] B. Mele, M. Ostieri, and R. Tognaccini, "Aircraft lift and drag decomposition in transonic flows," *Journal of Aircraft*, vol. 54, no. 5, pp. 1933–1944, 2017.

[37] C. Fournis, D. Bailly, and R. Tognaccini, "Compressibility correction to Kutta-Joukowski and Maskell formulas using vortex-force theory," *AIAA Journal*, vol. 59, no. 2, pp. 758–763, 2021.

[38] C. Fournis, D. Bailly, and R. Tognaccini, "An invariant vortex-force theory related to classical far-field analyses in transonic flows," in *AIAA Aviation 2021 Forum*, p. 2554, 2021.

[39] C. Fournis, D. Bailly, and R. Tognaccini, "Invariant vortex-force theory extending classical aerodynamic theories to transonic flows," *Submitted to AIAA Journal*.

[40] K. Oswatitsch, *Der luftwiderstand als integral des entropiestromes*. Vandenhoeck & Ruprecht, 1945.

[41] K. Oswatitsch, *Gas dynamics*, vol. 1. Academic Press, 1956.

[42] G. Taylor, "Note on the connection between the lift on an aërofoil in a wind and the circulation round it," *Phil. Trans. R. Soc. London A*, vol. 225, pp. 238–246, 1926.

[43] B. M. Jones, *The measurement of profile drag by the pitot-traverse method*. HM Stationery Office, 1936.

[44] K. Oswatitsch, "Der verdichtungsstoß bei der stationären umströmung flacher profile," *ZAMM-Journal of Applied Mathematics and Mechanics/Zeitschrift für Angewandte Mathematik und Mechanik*, vol. 29, no. 5, pp. 129–141, 1949.

[45] K. Kusunose, J. Crowder, and R. Watzlavick, "Wave drag extraction from profile drag based on a wake-integral method," in *37th Aerospace Sciences Meeting and Exhibit*, p. 275, 1999.

[46] L. Paparone and R. Tognaccini, "Computational fluid dynamics-based drag prediction and decomposition," *AIAA Journal*, vol. 41, no. 9, pp. 1647–1657, 2003.

[47] S. Schmitz and J. G. Coder, "Inviscid circulatory-pressure field derived from the incompressible Navier-Stokes equations," *AIAA Journal*, vol. 53, no. 1, pp. 33–41, 2015.

[48] S. Schmitz, "Drag decomposition using partial-pressure fields in the compressible Navier-Stokes equations," *AIAA Journal*, vol. 57, no. 5, pp. 2030–2038, 2019.

[49] J. G. Coder and S. Schmitz, "Thermodynamic decomposition of compressible wave drag in the Euler equations," in *AIAA Aviation 2019 Forum*, p. 2958, 2019.

[50] J. Z. Wu, L. Q. Liu, and T. S. Liu, "Fundamental theories of aerodynamic force in viscous and compressible complex flows," *Progress in Aerospace Sciences*, 2018.

[51] J. A. Ackroyd, B. P. Axcell, and A. Ruban, *Early developments of modern aerodynamics*. American Institute of Aeronautics and Astronautics / Butterworth-Heinemann, 2001.

[52] L. M. Milne-Thomson, *Theoretical aerodynamics*. General Publishing Company, 1973.

[53] J. John D. Anderson, *Fundamentals of aerodynamics*. MacGraw-Hill, Inc., 1991.

[54] L. W. Bryant and D. H. Williams, "An investigation of the flow of air around an aërofoil of infinite span," *Philosophical Transactions of the Royal Society of London. Series A, Containing Papers of a Mathematical or Physical Character*, vol. 225, no. 626-635, pp. 199–245, 1926.

[55] L. N. G. Filon, "The forces on a cylinder in a stream of viscous fluid," *Proceedings of the Royal Society of London. Series A, Containing Papers of a Mathematical and Physical Character*, vol. 113, no. 763, pp. 7–27, 1926.

[56] L. Q. Liu, J. Y. Zhu, and J. Z. Wu, "Lift and drag in two-dimensional steady viscous and compressible flow," *Journal of Fluid Mechanics*, vol. 784, pp. 304–341, 2015.

[57] L. Q. Liu, J. Z. Wu, W. D. Su, and L. L. Kang, "Lift and drag in three-dimensional steady viscous and compressible flow," *Physics of Fluids*, vol. 29, no. 11, p. 116105, 2017.

[58] J. C. Wu, "Theory for aerodynamic force and moment in viscous flows," *AIAA Journal*, vol. 19, no. 4, pp. 432–441, 1981.

[59] J. Z. Wu, J. M. Wu, and C. J. Wu, "A viscous compressible flow theory on the interaction between moving bodies and flow field in the (ω, ϑ) framework," *Fluid Dynamics Research*, vol. 3, no. 1-4, p. 203, 1988.

[60] J. Z. Wu and J. M. Wu, "Vortical sources of aerodynamic force and moment," Tech. Rep. 892346, SAE Technical Paper, 1989.

[61] J. Z. Wu and J. M. Wu, "Interactions between a solid surface and a viscous compressible flow field," *Journal of Fluid Mechanics*, vol. 254, pp. 183–211, 1993.

[62] M. Lighthill, "Boundary layer theory," 1963.

[63] G. K. Batchelor, *An introduction to fluid dynamics*. Cambridge University Press, 1967.

[64] J. Y. Zhu, T. S. Liu, L. Q. Liu, S. F. Zou, and J. Z. Wu, "Causal mechanisms in airfoil-circulation formation," *Physics of Fluids*, vol. 27, no. 12, p. 123601, 2015.

[65] T. S. Liu, S. Z. Wang, and G. W. He, "Explicit role of viscosity in generating lift," *AIAA Journal*, pp. 3990–3994, 2017.

[66] S. I. Green, "Wing tip vortices," in *Fluid vortices*, pp. 427–469, Springer, 1995.

[67] J. Wu, J. Hackett, and D. Lilley, "A generalized wake-integral approach for drag determination in three-dimensional flows," in *17th Aerospace Sciences Meeting*, p. 279, 1979.

[68] S. C. Smith, "A computational and experimental study of nonlinear aspects of induced drag," *NASA TP-3598*, 1996.

[69] M. Méheut, *Évaluation des composantes phénoménologiques de la traînée d'un avion à partir de résultats expérimentaux*. PhD thesis, Université de Lille 1, 2006.

[70] M. Méheut and D. Bailly, "Drag-breakdown methods from wake measurements," *AIAA Journal*, vol. 46, no. 4, pp. 847–862, 2008.

[71] K. Kusunose and J. Crowder, "Physical properties of Maskell's induced drag integral," in *39th Aerospace Sciences Meeting and Exhibit*, p. 421, 2001.

[72] D. Hue, "Fifth drag prediction workshop: ONERA investigations with experimental wing twist and laminarity," *Journal of Aircraft*, vol. 51, no. 4, pp. 1311–1322, 2014.

[73] P. R. Spalart, "On the far wake and induced drag of aircraft," *Journal of Fluid Mechanics*, vol. 603, pp. 413–430, 2008.

[74] P. G. Saffman, *Vortex dynamics*. Cambridge University Press, 1992.

[75] J. Z. Wu, H. Y. Ma, and M. D. Zhou, *Vorticity and vortex dynamics*. Springer Science & Business Media, 2007.

[76] H. Lamb, *Hydrodynamics*. Cambridge University Press, 1916.

[77] J. C. Wu, "Vorticity-moment theorem," in *Elements of vorticity aerodynamics*, pp. 75–94, Springer, 2018.

[78] J. Z. Wu, H. Y. Ma, and M. D. Zhou, *Vortical flows*, vol. 28. Springer, 2015.

[79] T. Von Kármán and W. R. Sears, "Airfoil theory for non-uniform motion," *Journal of the Aeronautical Sciences*, vol. 5, no. 10, pp. 379–390, 1938.

[80] J. Z. Wu and J. M. Wu, "Vorticity dynamics on boundaries," in *Advances in applied mechanics*, vol. 32, pp. 119–275, Elsevier, 1996.

[81] C. Marongiu, R. Tognaccini, and M. Ueno, "Lift and lift-induced drag computation by Lamb vector integration," *AIAA Journal*, vol. 51, no. 6, pp. 1420–1430, 2013.

[82] A. Holloway and T. Jeans, "Hydrodynamic impulse generated by slender bodies in viscous flow," *Ocean Engineering*, vol. 206, p. 106951, 2020.

[83] F. Mao, Y. P. Shi, and J. Z. Wu, "On a general theory for compressing process and aeroacoustics: Linear analysis," *Acta Mechanica Sinica*, vol. 26, no. 3, pp. 355–364, 2010.

[84] C. Marongiu and R. Tognaccini, "Far-field analysis of the aerodynamic force by Lamb vector integrals," *AIAA Journal*, vol. 48, no. 11, pp. 2543–2555, 2010.

[85] S. F. Zou, J. Z. Wu, A. K. Gao, L. Q. Liu, L. L. Kang, and Y. P. Shi, "On the concept and theory of induced drag for viscous and incompressible steady flow," *Physics of Fluids*, vol. 31, no. 6, p. 065106, 2019.

[86] L. Q. Liu, Y. P. Shi, J. Y. Zhu, W. D. Su, S. F. Zou, and J. Z. Wu, "Longitudinal-transverse aerodynamic force in viscous compressible complex flow," *Journal of Fluid Mechanics*, vol. 756, pp. 226–251, 2014.

[87] L. Q. Liu, J. Z. Wu, Y. P. Shi, and J. Y. Zhu, "A dynamic counterpart of Lamb vector in viscous compressible aerodynamics," *Fluid Dynamics Research*, vol. 46, no. 6, p. 061417, 2014.

[88] L. Q. Liu, *Unified theoretical foundations of lift and drag in viscous and compressible external flows*. Springer, 2017.

[89] C.-C. Chang and S.-Y. Lei, "An analysis of aerodynamic forces on a delta wing," *Journal of Fluid Mechanics*, vol. 316, pp. 173–196, 1996.

[90] C.-C. Chang, J.-Y. Su, and S.-Y. Lei, "On aerodynamic forces for viscous compressible flow," *Theoretical and Computational Fluid Dynamics*, vol. 10, no. 1-4, pp. 71–90, 1998.

[91] M. Ostieri and R. Tognaccini, "On a recently proposed vorticity-based definition of wave drag," *Journal of Aircraft*, vol. 55, no. 6, pp. 2521–2523, 2018.

[92] S. Schmitz, "Finite domain viscous correction to the Kutta-Joukowski theorem in incompressible flow," *AIAA Journal*, vol. 52, no. 9, pp. 2079–2083, 2014.

[93] J. C. Wu, C. Wang, and K. McAlister, "Wake-integral determination of aerodynamic drag, lift and moment in three-dimensional flows," in *40th AIAA Aerospace Sciences Meeting and Exhibit*, p. 555, 2002.

[94] A. K. Gao and J. Z. Wu, "A note on the galilean invariance of aerodynamic force theories in unsteady incompressible flows," *Acta Mechanica Sinica*, pp. 1–5, 2019.

[95] M. Ostieri, B. Mele, and R. Tognaccini, "Linear and nonlinear decomposition of aerodynamic force acting on an oscillating plate," *AIAA Journal*, vol. 56, no. 2, pp. 594–608, 2018.

[96] V. Schmitt and D. Destarac, "Recent progress in drag prediction and reduction for civil transport aircraft at ONERA," in *36th AIAA Aerospace Sciences Meeting and Exhibit*, p. 137, 1998.

[97] G. Batchelor, "Axial flow in trailing line vortices," *Journal of Fluid Mechanics*, vol. 20, no. 04, pp. 645–658, 1964.

[98] W. J. Devenport, M. C. Rife, S. I. Liapis, and G. J. Follin, "The structure and development of a wing-tip vortex," *Journal of Fluid Mechanics*, vol. 312, pp. 67–106, 1996.

[99] D. Sipp, L. Jacquin, and C. Cossu, "Self-adaptation and viscous selection in concentrated two-dimensional vortex dipoles," *Physics of Fluids*, vol. 12, no. 2, pp. 245–248, 2000.

[100] D. Fabre, *Instabilité et instationnarités dans les tourbillons: application aux sillages d'avions*. PhD thesis, Université Paris 6, 2002.

[101] T. Misaka, F. Holzäpfel, and T. Gerz, "Large-eddy simulation of aircraft wake evolution from roll-up until vortex decay," *AIAA Journal*, vol. 53, no. 9, pp. 2646–2670, 2015.

[102] L. Q. Liu, L. L. Kang, and J. Z. Wu, "Zonal structure of unbounded external-flow and aerodynamics," *Fluid Dynamics Research*, vol. 49, no. 4, p. 045508, 2017.

[103] M. Morduchow and P. A. Libby, "On a complete solution of the one-dimensional flow equations of a viscous, heat-conducting, compressible gas," *Journal of the Aeronautical Sciences*, vol. 16, no. 11, pp. 674–684, 1949.

[104] L. Landau and E. Lifshitz, *Course of theoretical physics. vol. 6: Fluid mechanics*. A. Wheaton & Co., 1959.

[105] C. W. Hamman, J. C. Klewicki, and R. M. Kirby, "On the Lamb vector divergence in Navier-Stokes flows," *Journal of Fluid Mechanics*, vol. 610, pp. 261–284, 2008.

[106] M. Ostieri, *Aerodynamic lift and drag breakdown in steady and unsteady flows*. PhD thesis, Università degli Studi di Napoli Federico II, 2017.

[107] H. Toubin, *Prediction and phenomenological breakdown of drag for unsteady flows.* PhD thesis, Université Pierre et Marie Curie, 2015.

[108] M. Ostieri, R. Tognaccini, D. Bailly, and D. Destarac, "Aerodynamic force and Lamb vector field in compressible unsteady flows," in *2018 AIAA Aerospace Sciences Meeting*, p. 0548, 2018.

[109] L. Russo, M. Ostieri, and R. Tognaccini, "Thrust extraction from vorticity fields in steady and unsteady flows," in *2018 Applied Aerodynamics Conference*, p. 3967, 2018.

[110] L. Russo, R. Tognaccini, and L. Demasi, "Box wing and induced drag: compressibility effects in subsonic and transonic regimes," *AIAA Journal*, pp. 1–16, 2020.

[111] H. Schlichting, *Boundary-layer theory.* McGraw-Hill, Inc., 1979.

[112] F. M. White, *Viscous fluid flow.* McGraw-Hill, Inc., 1991.

[113] N. Trentacoste and P. M. Sforza, "Some remarks on three-dimensional wakes and jets.," *AIAA Journal*, vol. 6, no. 12, pp. 2454–2456, 1968.

[114] Y. H. Kuo and L. V. Baldwin, "Diffusion and decay of turbulent elliptic wakes.," *AIAA Journal*, vol. 4, no. 9, pp. 1566–1572, 1966.

[115] P. Bradshaw, "Compressible turbulent shear layers," *Annual Review of Fluid Mechanics*, vol. 9, no. 1, pp. 33–52, 1977.

[116] P. Spalart and S. Allmaras, "A one-equation turbulence model for aerodynamic flows," in *30th Aerospace Sciences Meeting and Exhibit*, p. 439, 1992.

[117] A. Jameson, W. Schmidt, and E. Turkel, "Numerical solution of the Euler equations by finite volume methods using Runge Kutta time stepping schemes," in *14th Fluid and Plasma Dynamics Conference*, p. 1259, 1981.

[118] L. Cambier, S. Heib, and S. Plot, "The ONERA elsA CFD software: input from research and feedback from industry," *Mechanics & Industry*, vol. 14, no. 3, pp. 159–174, 2013.

[119] S. Deck, "Numerical simulation of transonic buffet over a supercritical airfoil," *AIAA Journal*, vol. 43, no. 7, pp. 1556–1566, 2005.

[120] L. Jacquin, P. Molton, S. Deck, B. Maury, and D. Soulevant, "Experimental study of shock oscillation over a transonic supercritical profile," *AIAA Journal*, vol. 47, no. 9, pp. 1985–1994, 2009.

[121] H. Toubin and D. Bailly, "Development and application of a new unsteady far-field drag decomposition method," *AIAA Journal*, vol. 53, no. 11, pp. 3414–3429, 2015.

[122] H. Toubin, D. Bailly, and M. Costes, "Improved unsteady far-field drag breakdown method and application to complex cases," *AIAA Journal*, vol. 54, no. 6, pp. 1907–1921, 2016.

[123] V. Schmitt and F. Charpin, "Pressure distributions on the ONERA-M6-wing at transonic Mach numbers," *Experimental Data Base for Computer Program Assessment*, AGARD Advisory Report AR-138, 1979.

[124] J. Mayeur, A. Dumont, D. Destarac, and V. Gleize, "Reynolds-averaged Navier-Stokes simulations on NACA0012 and ONERA-M6 wing with the ONERA elsA solver," *AIAA Journal*, pp. 2671–2687, 2016.

[125] P. L. Roe, "Approximate Riemann solvers, parameter vectors, and difference schemes," *Journal of Computational Physics*, vol. 43, no. 2, pp. 357–372, 1981.

[126] J. Vassberg, "A unified baseline grid about the Common Research Model wing/body for the fifth AIAA CFD drag prediction workshop," in *29th AIAA Applied Aerodynamics Conference*, p. 3508, 2011.